Computational fluid dynamics for non-conventional power cycles
Turbulence modelling of supercritical fluids and simulations of high-expansion turbines

Otero Rodriguez, G.J.

DOI

Publication date
2021

Document Version
Final published version

Citation (APA)

Important note
To cite this publication, please use the final published version (if applicable).
Please check the document version above.

Computational fluid dynamics for non-conventional power cycles:

TURBULENCE MODELLING OF SUPERCRITICAL FLUIDS AND SIMULATIONS OF HIGH-EXPANSION TURBINES

Dissertation

for the purpose of obtaining the degree of doctor
at Delft University of Technology
by the authority of the Rector Magnificus Prof. dr. ir. T.H.J.J. van der Hagen,
Chair of the Board of Doctorates,
to be defended publicly on
Wednesday, 24th of February 2021 at 12:30 hours

by

Gustavo Jose OTERO RODRIGUEZ

Master of Science in Mechanical Engineering,
Delft University of Technology, the Netherlands
born in Caracas, Venezuela.

This dissertation has been approved by the promotors.
Composition of the doctoral committee:

Rector Magnificus	Chairperson
Dr. R. Pecnik	Delft University of Technology, promotor
Prof.dr.ir. S. Klein	Delft University of Technology, promotor

Independent members:

Prof. T. Turunen Saaresti	Lappeenranta-Lahti University of Technology, Finland
Prof. P. Cinnella	Sorbonne University of Technology, France
Prof.dr.ir. H.C. de Lange	Eindhoven University of Technology
Prof.dr. S. Hickel	Delft University of Technology
Prof.dr. D.J.E.M. Roekaerts	Delft University of Technology

Reserve members:

Prof.dr.ir. B.J. Boersma	Delft University of Technology

---

[1]Author e-mail address: `gustavojoteror@gmail.com`

Para mi familia y mi esposa Daniela,
por siempre impulsarme más allá de mis limites.

Table of Contents

Summary

The global temperature rise, which directly results from greenhouse gases emitted by burning fossil fuels, requires humanity to harness renewable energy sources at an increased rate. However, renewable energy sources are either highly intermittent, such as wind and solar radiation, or available at low temperatures leading to low efficiencies of current thermal conversion systems.

Two exciting technologies that can alleviate the low thermal conversion efficiencies of power plants with low-temperature heat sources are supercritical carbon dioxide (s-CO_2) and organic Rankine cycles (ORCs). Compared to conventional power cycles, ORCs and s-CO_2 power cycles have different working media (e.g., CO_2 and hydrocarbons), such that the working fluid provides an additional degree of freedom to better adapt to low-grade heat sources. As a consequence, the power cycles have higher thermal efficiency and a more compact design.

However, the main difficulty in designing highly efficient components of these non-conventional power plants lies in the fact that the heat exchangers and the turbines operate either with fluids of high molecular complexity or with fluids in highly non-ideal thermodynamic conditions. These complexities make it challenging to accurately design efficient components with computational fluid dynamic (CFD) software that can reliably predict heat transfer and pressure losses in heat exchangers, and aerodynamic performance parameters in turbomachinery equipment.

The overall goals of this thesis are: to first gain knowledge on non-ideal fluid dynamics, and then use this insight to improve models used in computational fluid dynamic simulations to design power cycle components operating with non-conventional fluids. The two main components we consider are the heat exchanger and the turbine of the s-CO_2 power and the organic Rankine cycles, respectively. On the one hand, the two most important flow phenomena that heat exchanger designers need to balance are the heat transfer between two (or more) fluids and the pressure drop due to skin friction, both of which are strongly influenced by turbulence. However, knowledge is lacking on how to incorporate the non-ideal fluid behavior of supercritical fluids into modeling turbulence. On the other hand, the overall ORC efficiency depends on the turbine's design, which is challenging due to the intrinsic unsteady flow features and non-ideal thermodynamic effects. Currently, steady-state and quasi-three-dimensional computational fluid dynamics (CFD) simulations are used to analyze, design, and optimize ORC turbines. However, these calculations ignore several loss mechanisms that reduce the performance of the expander.

We organized this thesis into two parts that correspond to these obstacles: Part I deals

with turbulence modeling of supercritical fluids in heat exchangers, and Part II addresses the optimization of high-expansion ORC turbines with unsteady three-dimensional (3D) CFD simulations.

In Part I, we present a novel methodology for improving the ability of turbulence models to predict wall-bounded turbulent flows with sharp changes in fluid properties. Based on the recently derived semi-locally-scaled turbulent kinetic energy equation, we analytically derive a modification of the turbulent scalar equations' diffusion term. We apply these modifications to several turbulence models and test them for (1) heated fully-developed turbulent channel flows with variable properties and (2) upward heated turbulent pipe flows with CO_2 at supercritical pressure. The agreement of our simulations with results obtained by direct numerical simulations and experimental measurements shows that the modifications significantly improve the model accuracy for fluids with variable transport properties. However, heat transfer deterioration can occur in flows with strong buoyancy effects, for which the turbulence models would require additional adaptations to improve the turbulent heat flux and the buoyancy production.

Part II presents the first of its kind simulations of a high-expansion radial inflow ORC turbines using detailed unsteady 3D calculations. Additionally, we propose a design methodology for such a turbine where the 3D and unsteady flow field is taken into account by a detailed design assessment a posteriori. The Reynolds-averaged Navier-Stokes equations and a multi-parameter equation of state are coupled to investigate the expansion of an ORC turbine operating in the dense-gas region. To account for the unsteady stator-rotor interaction, a conservative flux assembling technique for non-matching 3D meshes is applied. We consider two rotor blade shapes, the original (or old) geometry from the expander of an ORC manufacturer, and a new design derived from our design methodology. The simulations indicate strong unsteady effects, especially in the rotor blade passage, for both geometries. Because of the highly supersonic flow at the stator exit, unsteady shock waves emanate from the trailing edge of the stator and interact downstream with a bow shock at the rotor leading edge and the viscous structures at the suction side of the blade. The flow field of the old rotor blade geometry indicates a large recirculation bubble at the suction side of the blade and strong 3D effects; a secondary flow is generated at the rotor leading edge close to the shroud. The new blade design has a smooth pressure distribution, decrease of viscous losses, and reduces the secondary flow in the rotor channel. Consequently, an increase in the power output is calculated by the simulation of the new ORC turbine stage. From the detailed assessment of the new blade, we strongly recommend accounting for 3D effects during the detailed blade design phase by including the radial-to-axial bend during the blade height distribution's derivation.

Samenvatting

Hernieuwbare energiebronnen zullen steeds meer ingezet moeten worden vanwege de wereldwijde temperatuurstijging, die veroorzaakt wordt door de broeikasgassen die vrijkomen bij de verbranding van fossiele brandstoffen. Echter, hernieuwbare energiebronnen fluctueren sterk, zoals windenergie en zonne-energie en hernieuwbare warmte is met name beschikbaar bij lagere temperaturen, wat resulteert in een laag omzettingsrendement naar elektriciteit in de huidige thermische energieconversie systemen.

Het rendement van elektriciteitscentrales op basis van lage temperatuur warmtebronnen kan aanzienlijk verbeterd worden door de toepassing van twee veelbelovende technologieën: (1) een cyclus waarin koolstofdioxide in een superkritische toestand als werkmedium wordt gebruikt (s-CO2) en (2) een Rankine cyclus waarin een organische werkmedium wordt toegepast (ORC). Het gebruik van een andere werkmedium dan conventionele vermogenscycli, geeft de mogelijkheid om het werkmedium aan te passen aan de lage temperatuur van de bronwarmte. Dit resulteert in een hoger thermisch rendement en een compacter ontwerp.

Het ontwerp van efficiënte componenten, zoals turbines en warmtewisselaars, voor deze niet-conventionele elektriciteitscentrales is complex doordat deze worden bedreven met werkmedia met een hoge moleculaire complexiteit of met werkmedia onder sterk niet-ideale thermodynamische condities. Deze factoren maken het zeer uitdagend om de warmteoverdracht en drukval in warmtewisselaars en de prestaties van turbines nauwkeurig berekenen met behulp van Computational Fluid Dynamic (CFD).

De algemene doelstellingen van dit proefschrift zijn: (1) kennis te verwerven ten aanzien van de vloeistofdynamica van niet-ideale werkmedia en (2) vervolgens om deze nieuwe kennis te gebruiken om modellen voor niet-conventionele werkmedia te verbeteren die in CFD simulaties worden gebruikt voor het ontwerpen van componenten voor vermogenscycli. De belangrijkste componenten die worden beschouwd zijn de warmtewisselaar en de turbine voor respectievelijk de s-CO2 cyclus en de ORC cyclus. De ontwerper moet bij het ontwerp van een warmtewisselaar twee belangrijke stromingsverschijnselen in balans brengen: de warmteoverdracht en de drukval. Beide verschijnselen worden sterk beïnvloed door turbulentie. Kennis ontbreekt echter over de invloed van het niet-ideale gedrag van superkritische media op turbulentie modellering. Voor de ORC cyclus hangt het rendement sterk af van het turbineontwerp. Het intrinsieke tijdsafhankelijke stromingsgedrag en de niet-ideale thermodynamische eigenschappen van het werkmedium maken dit tot een uitdaging. Momenteel worden stationaire en quasi-drie-dimensionale CFD simulaties gebruikt om ORC turbines te analyseren, te ontwerpen en te optimaliseren. Deze vereenvoudigde berekeningen verwaarlozen echter diverse mechanismen die

leiden tot een lagere performance van de turbine.

Dit proefschrift bestaat uit twee delen, corresponderend met de hierboven benoemde leemtes in kennis. Deel 1 beschrijft de turbulentie modellering van superkritische media in warmtewisselaars terwijl Deel 2 de optimalisatie van een ORC turbine met een hoge expansieverhouding behandelt, waarbij gebruik wordt gemaakt van tijdsafhankelijke driedimensionale (3D) CFD simulaties.

Deel 1 presenteert een nieuwe methodiek die leidt tot een verbetering van de voorspelling van turbulente stromingen in grenslagen met sterke veranderingen van mediumeigenschappen met behulp van turbulentiemodellering . Op analytische wijze wordt een aanpassing van de diffusie term in de turbulente scalaire transportvergelijking afgeleid op basis van een recent afgeleide vergelijking voor de semi-lokaal-geschaalde turbulente kinetische energie. We passen deze aanpassing toe op verschillende turbulentiemodellen en testen deze voor (1) een verwarmd kanaal met volledig ontwikkelde turbulente stroming met variabele mediumeigenschappen en (2) een opwaartse turbulente stroming van CO2 in een verwarmde buis onder superkritische druk. Vergelijking van onze simulaties met de resultaten die zijn verkregen met directe numerieke simulatie en experimentele metingen tonen aan dat de aangebrachte wijzigingen de nauwkeurigheid van turbulentie modellering voor media met variabele transporteigenschappen sterk verbetert. Echter een lagere warmteoverdracht kan optreden in stromingen met sterke invloed van de zwaartekracht,. hiervoor zullen turbulentiemodellen verder aangepast moeten worden om de berekening van de turbulente warmteflux en van de productie van turbulentie ten gevolge van de opwaartse kracht te verbeteren.

Deel 2 presenteert voor het eerst in de literatuur gedetailleerde tijdsafhankelijke 3D berekeningen van een radiale instroom ORC turbine met hoge expansieverhouding. Daarnaast bespreken we een ontwerpmethodiek voor een dergelijke turbine waar het tijdsafhankelijke 3D stromingsveld a posteriori wordt meegenomen.De expansie in een ORC turbine in het gebied nabij de verzadigingslijn en het kritieke punt van het werkmedium is onderzocht met behulp van de Reynolds-gemiddelde Navier-Stokes (RANS) vergelijkingen samen met een multi-parameter toestandsvergelijking . Bij het berekenen van de tijdsafhankelijke stator-rotor interactie ontstaan niet-conforme 3D-meshes in het CFD model. Er is hierbij een methodiek toegepast die er voor zorgt dat de flux behouden blijft op het grensvlak van de twee meshes. Twee verschillende ontwerpen voor turbine rotoren zijn geanalyseerd: (1) de originele (oude) geometrie van een ORC turbine producent en (2) een nieuw ontwerp, op basis van onze ontwerpmethodiek. De simulaties laten sterke tijdsafhankelijke effecten zien voor beide rotoren, met name in het gebied tussen de rotorbladen. Vanwege de sterk supersone stroming aan de uitgang van de stator ontstaan tijdsafhankelijke schokgolven aan de trailing edge (achterkant) van de stator. Stroomafwaarts treedt een wisselwerking op met een schokgolf (bow shock) aan de leadind edge (voorrand) van de rotor en met de viskeuze stromingsstructuren aan de zuigzijde van het blad. Het stromingsveld van het oude rotorblad laat een groot recirculatie gebied zien aan de zuigzijde van het blad en sterke 3D-effecten; een secundaire stroming wordt opgewekt aan de leading edge van de rotor, dicht bij het rotorhuis. Het nieuwe rotorblad heeft een gelijkmatige drukverdeling, geeft minder viskeuze verliezen en verkleint de secundaire stroming in het rotorkanaal. De berekening laat zien dat het nieuwe rotorkanaal meer

vermogen produceert. Op basis van een gedetailleerde beoordeling van het nieuwe blad bevelen we ten zeerste aan om 3D effecten mee te nemen in de detail ontwerpfase van een blad door de overgang van de radiale naar de axiale stromingsrichting mee te nemen bij het bepalen van bladhoogteverdeling.

Nomenclature

$\dot{m}$	mass flow
$\dot{Q}$	Heat
$\mathbf{F}$	Flux vector
$\mathbf{F}_c$	Euler flux vector
$\mathbf{F}_d$	Diffusive flux vector
$\mathbf{n}$	Normal vector
$\mathbf{r}$	Vector connecting control volumes
$\mathbf{s}_f$	Vector connecting the cell centroid and the face
$\mathbf{U}$	Conserved variables vector
$\mathbf{x}$	Position vector
A	Perpendicular flow area
A_p	Surface area of the pipe
B_k	Bouyancy production of TKE
C	Model constant
c_p	Specific heat capacity at constant pressure
$CD_{k\omega}$	Cross derivative of k and ω for SST model
D	Diameter
E	Total internal energy
Ec_τ	Friction based Eckert number $(= u_\tau^2/(\tilde{T}_w \tilde{c}_{p,w}))$
f	Model function

f_x	External body force
Fr	Froude number ($Fr = u/\sqrt{g\,D}$)
G	Mass flux ($G = \dot{m}/A$)
g	Gravitational acceleration
H	Specific enthalpy
h	Characteristic length (half channel height); Blade height
k	Turbulent kinetic energy
L	Pipe stream-wise length; Parameter of blade parametrization
M	Absolute Mach number
M_τ	Friction based Mach number
M_{rel}	Relative Mach number
N_b	Number of blades
N_d	Number of discrete elements
Nu	Nusselt number ($Nu = \frac{hD}{\lambda}$)
p	Pressure
P_k	Production of TKE
Pe_t	Turbulent Peclet number ($Pe_t = \mu_t/\mu\,Pr$)
Pr	Prandtl number ($Pr = c_p\mu/\lambda$)
Pr_t	Turbulent Prandtl number
$q"$	Heat flux ($q'' = \dot{Q}/A_p$)
q''	heat flux
R	Specific gas constant, radius
r	Radius/radial distance, edge thickness
Re	Reynolds number ($Re = GD/\mu$)
Re_τ	Friction Reynolds number ($Re_\tau = u_\tau\rho_w D/\mu_w$)
$Re_\tau^\star$	Semi-local Reynolds number ($Re_\tau^\star = Re_\tau\sqrt{\langle\rho\rangle/\rho_w}\mu_w/\langle\mu\rangle = u_\tau^\star\langle\rho\rangle\,D/\langle\mu\rangle$)
s	Thermodynamic entropy

s_{gen}	Entropy generation
S_{ij}	Strain rate tensor
s_{th}	Flow line or camber line distance
T	Temperature
t	Time
T_τ	Turbulent time scale
th	Blade thickness
u^{vD}	Van Driest velocity transformation $(= \int_0^{(u/u_\tau)} \sqrt{\rho/\rho_w}\, \partial\, (u/u_\tau))$
u_τ	Friction velocity $(u_\tau = \sqrt{\tau_w/\rho_w})$
$u_\tau^\star$	Semi-local friction velocity $(u_\tau^\star = \sqrt{\tau_w/\langle\rho\rangle})$
V	Volume
W	Blade channel width
x	Length, x-direction
y	Length, y-direction
y^+	Locally scaled wall distance $(y^+ = y/DRe_\tau)$
$y^\star$	Semi-locally scaled wall distance $(y^\star = y/DRe_\tau^\star)$
Z	Compressibility factor
z	Axial/stream-wise distance in the pipem z-direction
u	Velocity vector

Greek letters

α	Absolute velocity direction
α_f	Dot product between $\mathbf{n}_f$ and $\mathbf{s}_f$
α_t	Eddy diffusivity
β	Blade angle
β_T	Thermal expansion coefficient
δ	Stagger angle
δ_v	Viscous length scale

δ_{ij}	Kronecker delta
ϵ	TKE dissipation rate
η_{ise}	Isentropic efficiency
η_{ts}	Total-to-static efficiency
γ	Heat capacity ratio
γ_{IS}	Model parameter
κ	Von Karman constant ($\kappa = 0.41$)
λ	Thermal conductivity
∇	Vector differential operator
Ω	Physical domain
ω	TKE specific dissipation rate; Rotational speed
Φ	Volumetric heat source
ρ	Density
σ	Eddy viscosity model constant
τ	Shear stress, time period
τ_w	Wall-shear stress
ϑ	Specific volume
$\check{\nu}$	Spalart-Allmaras turbulent scalar
μ_γ	Turbulent to molecular viscosity ratio ($\mu_\gamma = \mu_t/\mu$)
μ_t	Eddy viscosity
μ	Dynamic viscosity

Subscripts

0	Inflow
b	Bulk
bc	Boundary condition
bf	Boundary face
c	Channel/pipe center

cv	Control volume
f	Face
if	Internal face
in	Inlet
L	Left-side face
nbr	Neighbour control volume
o	Total condition
out	Outlet
pc	Pseudo-critical
R	Right-side face
r	Radial/wall-normal direction; Rotor
red	Reduced
s	Stator
sf	Supermesh face
sr	Between stator and rotor
t	Turbulent
w	Wall
z	Axial/stream-wise direction

Acronyms

1D	One-dimensional
2D	Two-dimensional
3D	Three-dimensional
AFM	Algebraic flux model
ARS	Approximate Riemann solver
AUSM	Advection upstream splitting method
BCGSTAB	Bi-conjugate gradient stabilized method
CFD	Computational fluid dynamics

CO_2	Carbon dioxide
DNS	Direct numerical simulation
EoS	Equation of state
EVM	Eddy viscosity model
GGDH	Generalized gradient diffusion hypothesis
HTD	Heat transfer deterioration
LES	Large Eddy simulation
LUT	Look-up table
MK	Myong and Kasagi
NS	Navier-Stokes
ORC	Organic Rankine cycle
PR	Pressure ratio
Q3D	Quasi-three-dimensional
RANS	Reynolds-Averaged Navier-Stokes
RLE	Rotor leading edge
RTE	Rotor trailing edge
SA	Spalart-Allmaras
SLE	Stator leading edge
SST	Shear stress transport
STE	Stator trailing edge
TKE	Turbulent kinetic energy

Averaged operators

$\{\phi\}$	Favre averaging ($\phi = \{\phi\} + \phi''$ with $\langle\rho\rangle\{\phi\} = \langle\rho\phi\rangle$, $\langle\rho\rangle\{\phi''\} = 0$, $\langle\phi''\rangle \neq 0$)
$\langle\phi\rangle$	Reynolds averaging ($\phi = \langle\phi\rangle + \phi'$ with $\langle\phi'\rangle = 0$)

Variable scaling

ϕ	Wall-scaled variable
$\hat{\phi}$	Semi-locally-scaled quantity
$\tilde{\phi}$	Dimensional variable

1
Introduction

1.1 Non-conventional power cycles in the global energy scenario

Steam power plants and gas turbine power engines play a dominant role in our present-day electricity generation[1]. The concept behind both systems is equivalent: a thermodynamic power cycle[2]. Figure 1.1 depicts a basic schematic of a power cycle that consists of four processes. First (conditions 1-2), the fluid is compressed to a high pressure. Then (2-3), heat is added to the fluid. Later (3-4), the internal energy of the fluid is converted into mechanical power in an expander; the mechanical power is then converted into electricity by a generator. Finally (4-1), the fluid is cooled, and the whole process starts again.[^1] A fundamental distinction between a steam cycle (or Rankine cycle) and a gas turbine (or standard Brayton cycle) is the working medium; the Rankine cycle utilizes water while the Brayton cycle uses air. Moreover, the water in the Rankine cycle undergoes a phase transition at processes (2-3) and (4-1), while there is no phase change of the working fluid in the standard Brayton cycle. The heat source for such thermodynamic cycles is commonly the combustion of fossil fuels that generate greenhouse gas emissions[3].

The global temperature increase — a direct result of greenhouse gas levels in the atmosphere[4] — has sparked the pursuit of renewable energy sources and non-conventional power cycles. The scientific community and most governments around the world agree that a mitigation plan to stop climate change must be enforced[5]. For example, the Paris agreement aims to keep global warming below $\Delta T = 2°C$ by lowering greenhouse gas emissions[6]. The energy sector is the industry with by far the highest emissions[7]. Two possible solutions to reduce greenhouse gas emissions are (1) to shift towards renewable energy sources, such as solar radiation or wind energy, and (2) to improve the efficiency of the existing power plants.

A complete shift towards renewable energy sources is technically challenging[8]. In recent years, we have witnessed an increase of wind and solar energy around the world. The shift in policy and a boost of the production of essential equipment — such as photovoltaic cells and wind turbines — have allowed renewable energy to compete with coal power plants[9–11]. Both, however, are of a fluctuating nature, driven by weather as well as daily and seasonal cycles; other energy sources need to supply the gap in electricity demand.

Low-grade heat sources, such as waste heat recovery, biomass combustion, and geothermal energy, can supply a constant power load to the grid[12]. Waste heat recovery involves utilizing the excess heat from an industrial process, e.g., converting this waste heat into electrical power, which increases the overall system efficiency. Biomass combustion follows the same principle as burning fossil fuels, but instead, organic matter is burned to generate heat. A geothermal power plant extracts energy from the earth's core. These energy sources are available all year round and with virtually no fluctuation. But their low temperature, typically between 100 and 600 °C, is the main obstacle for their conversion into electricity with standard thermodynamic power cycles.

[^1]: Usually, gas turbine engines consist of an open system where the air is taken from the environment before the compression and the flue gases are discharged to the atmosphere after the expansion.
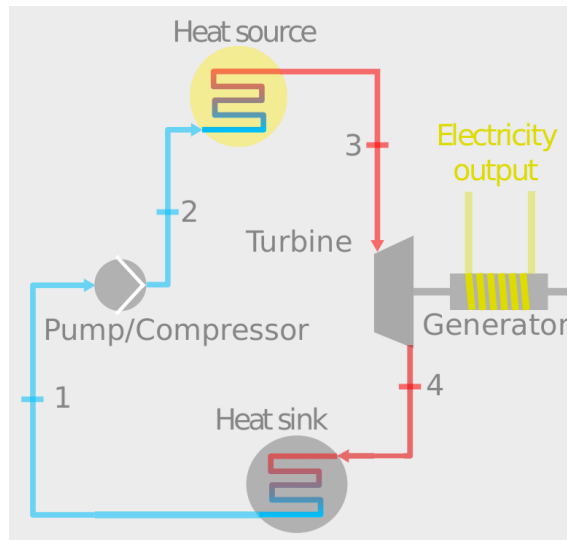
Figure 1.1: Power cycle schematic

Two innovative and exciting technologies that can fill the energy transition gap are the organic Rankine cycle (ORC) and the supercritical carbon dioxide (s-CO_2) Brayton cycle[12–14]. The peculiarity of these power systems lies in the working medium and the thermodynamic working conditions. These systems do not use traditional working fluids like air or water. Moreover, the working conditions are close to the fluid's thermodynamic critical point. The thermodynamic representation of the ORC and s-CO_2 cycles are depicted in figure 1.2 and 1.3, respectively. Research on this topic is relatively scarce if compared to the conventional Rankine and Brayton cycles. For this reason, this dissertation aims to advance the comprehension of these non-conventional power cycles.

1.1.1 Organic Rankine Cycle

Organic Rankine cycles are a viable alternative to steam based cycles for low-grade heat sources with temperature less than 500°C[13]. Such a system adopts an organic fluid (e.g., a hydrocarbon or refrigerant) as the working medium. This technology is mature enough to have commercial products.[2] As of 2017, the total installed capacity is more than 2.5 GW[15].

Utilizing an organic fluid instead of water in a Rankine cycle has several advantages. First, the working fluid selection adds an extra degree of freedom to the system design; the fluid can be determined from a technical, economic, or thermodynamic perspective[16]. And second, for low-power outputs, in the range of kW or a few MW, achieving an ef-

---

[2]Several ORC manufacturers are Triogen B.V. (the Netherlands), Turboden (Italy), and Ormat Technologies (USA), among others.
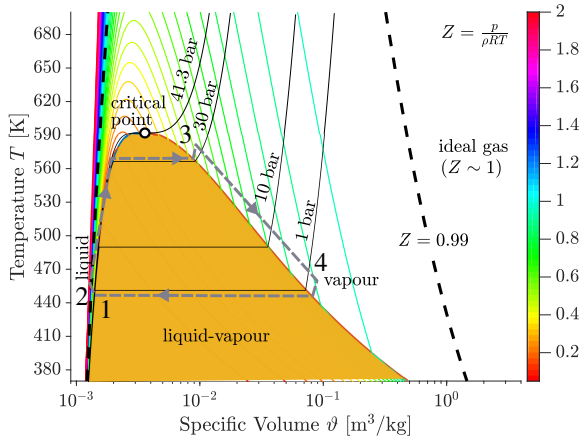
Figure 1.2: Temperature specific volume diagram of an organic fluid (toluene) with contour of the compressibility factor $Z = pV/RT$.

ficient and reliable organic expander is feasible. For a steam turbine, this is very challenging due to the small mass flow, the high-expansion ratio, and the possibility of wet expansion[13]. Therefore, an ORC has higher thermal efficiency for low-temperature heat sources if compared to a conventional steam Rankine cycle.

Another distinction of an ORC is the expansion process; this takes place close to the working fluid's critical point, in the dense-vapour region, where the ideal gas assumption is invalid (process 3-4 in figure 1.2). Therefore, to accurately describe organic fluids, complex equations of state are necessary[17]. Moreover, an organic fluid features a small specific enthalpy drop that results in a few expansion stages with a large pressure ratio. As a consequence, the turbine can have a highly supersonic flow at the stator exit. For these reasons, design diagrams and correlations of steam turbines are not suitable for ORC turbines.

1.1.2 Supercritical carbon dioxide cycle

Currently, engineers strive to replace the steam cycle with an s-CO$_2$ cycle to improve the efficiency of power plants. According to various sources, including the Department of Energy of the United States[18], the s-CO$_2$ power cycle can become the next-generation power cycle[19]. In such a system, carbon dioxide is used as the working fluid in the supercritical fluid region. Still, our fundamental understanding of flow physics in the supercritical region lags behind and thus poses a serious challenge.

The s-CO$_2$ cycle combines the advantages of the Rankine and Brayton cycles[14]. Figure 1.3 depicts the temperature entropy diagram of an s-CO$_2$ power cycle. First, the medium is compressed in the liquid-like region resulting in less compression work than its gas turbine counterpart. Second, unlike the steam cycle, the heat addition is performed
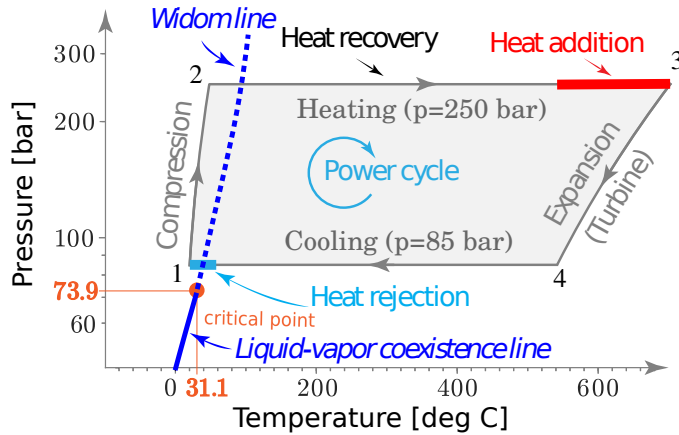
Figure 1.3: Supercritical Carbon Dioxide power cycle

at a variable temperature, giving more flexibility to the system to adapt to the heat source. Finally, as the exhaust temperature from the turbine is still high due to the low cycle pressure ratio (≈ 4), a large amount of heat is available for recuperation. All these advantages result in a higher thermal efficiency (up to $+5\Delta\%$) than a steam cycle[14].

The supercritical fluid region is the area in the thermodynamic state where the temperature and pressure are above than the critical point. At this thermodynamic state, extremely complex molecular interactions result in highly non-ideal behaviour of the fluid[20]. Along the Widom line in figure 1.3, where there is a second-order phase transition from an incompressible liquid to a highly dense gas, sharp variations in thermophysical properties are seen[21]. The high density in the supercritical region also raises the power density of the thermodynamic cycle, making the system relatively compact[14].

The field of application of s-CO_2 power cycles is broad. The original idea was to couple s-CO_2 power system with nuclear energy[22]. They can also be used for a low-grade heat source, like waste heat recovery and geothermal heat, or paired with concentrated solar power (CSP), which uses solar radiation as the heat source[23]. All these applications require a comprehensive understanding of fluid dynamics and heat transfer of supercritical fluids to correctly design and model the power cycle. However, we do not fully understand supercritical fluids, and the technical challenges are substantial. Therefore, no commercial system is yet available.[3]

1.2 Motivation

The main difficulties of these non-conventional power cycles, such as the ORC and the s-CO_2 cycle, are the thermodynamic representation of the fluid and the complex conditions

---

[3]Several pilot s-CO_2 power plants are being built and ran at the moment, for example in USA[25], China[26], and South Korea[27]. Moreover, Echogen[24] commercialized a trans-critical process with s-CO_2.

at which such systems work. Close to the critical point, the fluid does not follow the ideal gas law; for example, the compressibility factor (Z) is not constant and not equal to one as shown by figure 1.2 for an organic fluid near the critical point. Moreover, in the real-gas region, significant variations of the thermo-physical properties may occur.

Intimate knowledge of the systems is needed to harness as much energy as possible in non-conventional energy power cycles. Numerical simulations play an instrumental role for evaluating, seizing, and optimizing such cycles. However, current numerical models — developed for idealized flows — cannot capture the full complexity of these fluid flows. Therefore, more robust and accurate models for non-conventional power systems are needed to overcome their technical challenges; improving existing industrial processes, like power plants, and helping in the transition to renewable energy sources to ultimate decrease greenhouse gas emissions.

1.3 Objective

Ultimately, this thesis aims to improve the numerical modelling of non-ideal fluids for the non-conventional power cycles. We focus on the components that operate the closest to the critical point, where the strongest non-ideal phenomena are seen. The two flow guiding devices that we consider are the heat exchanger and the expander in the s-CO$_2$ cycle and the ORC, respectively.

For the seizing of any heat exchanger at a low cost, the two most important aspects a designer needs to balance are heat transfer between two (or more) fluids and the pressure drop due to frictional forces[28]. Both — for a high Reynolds number flow[4] — are influenced by turbulence.[5] However, there is currently a lack of knowledge on how turbulence is affected by non-ideal flows, e.g., in the supercritical region. Because of this fact, numerical models, used to design heat exchangers with a supercritical fluid, are unreliable and inaccurate[31].

In this thesis we will address the following research sub-questions related to turbulence modelling of supercritical fluids:

- How can turbulence models be improved to accurately solve flows with significant variations of thermo-physical properties, such as a supercritical fluid?

- How does the turbulent heat transfer model affect the overall modelling of supercritical fluids?

In terms of the design and performance prediction of ORC turbines, several degrees of complexity can be included. Several efforts in improving the predictive capability and understanding the flow features in ORC turbomachinery expanding non-ideal fluids have been conducted[32,33]; still, most computational fluid dynamic (CFD) simulations

---

[4]The Reynolds number is a dimensionless parameter defined as the ratio between the inertial to viscous force[29].

[5]Turbulence can be roughly defined as a state of fluid flow that is characterized by random and chaotic motions of varying length scales[30].

of ORC turbomachinery are under the assumption of steady-state. Most of the literature on ORC turbine design concentrate on delivering the geometry at the meridional plane, neglecting the span-wise direction. These two assumptions — steady-state flow field and span-wise symmetry — may be acceptable for an incompressible flow and a low-pressure-ratio turbine, but for an ORC turbine, where the flow is transonic and the pressure ratio may be large, these effects can become significant depending on the thermodynamic conditions, fluid, and turbine architecture.

The following research sub-questions are addressed in this dissertation related to ORC turbines:

- Which are the numerical methods needed to accurately simulate high-expansion ORC turbines by means of unsteady three-dimensional calculations?

- How do three-dimensional and unsteady effects impact the performance of high-expansion ORC turbines?

- How can we include the three-dimensional effects and the intrinsic unsteady flow in the design procedure of high-expansion ORC turbines?

1.4 Thesis outline

We organize the thesis into two parts with two and three chapters, respectively; each chapter addresses a research sub-question given above. A visual overview of the dissertation is shown in figure 1.4.

First, ***Part I*** aims to improve standard turbulence models to properly account for the effects of strong variation of thermo-physical properties, like the case of an s-CO_2 cycle heat exchanger. Consequently, a better prediction can be achieved of the pressure drop, the heat transfer coefficient, and other quantities of interest of supercritical flows. *Chapter 2* presents a novel methodology for improving eddy viscosity models for predicting wall-bounded turbulent flows with strong gradients of the thermo-physical properties; this methodology is validated with direct numerical simulation of variable property flows. In *Chapter 3*, we apply the derived density-corrected turbulence model to a heated turbulent pipe flow with s-CO_2 in an upward flow configuration. Moreover, this chapter also investigates the turbulent heat transfer models for supercritical flows.

Next, ***Part II*** focuses on the numerical representation of a high-expansion ORC expander using CFD. Currently, steady-state and quasi-three-dimensional simulations are used to design and to analyze the performance of ORC turbines. However, these calculations ignore several loss mechanisms — e.g., secondary flow, shock-shock, and/or shock-boundary layer interactions — that reduce the performance of the expander. In this part of the dissertation, we present detailed unsteady numerical simulations of high-expansion ORC turbines via three-dimensional calculations, including the real-gas effects. *Chapter 4* presents the numerical set-up for non-conventional turbomachinery simulations. We use this numerical framework for the simulation of high-expansion ORC turbines in the following chapters. *Chapter 5* includes a detailed unsteady numerical simulation, for the
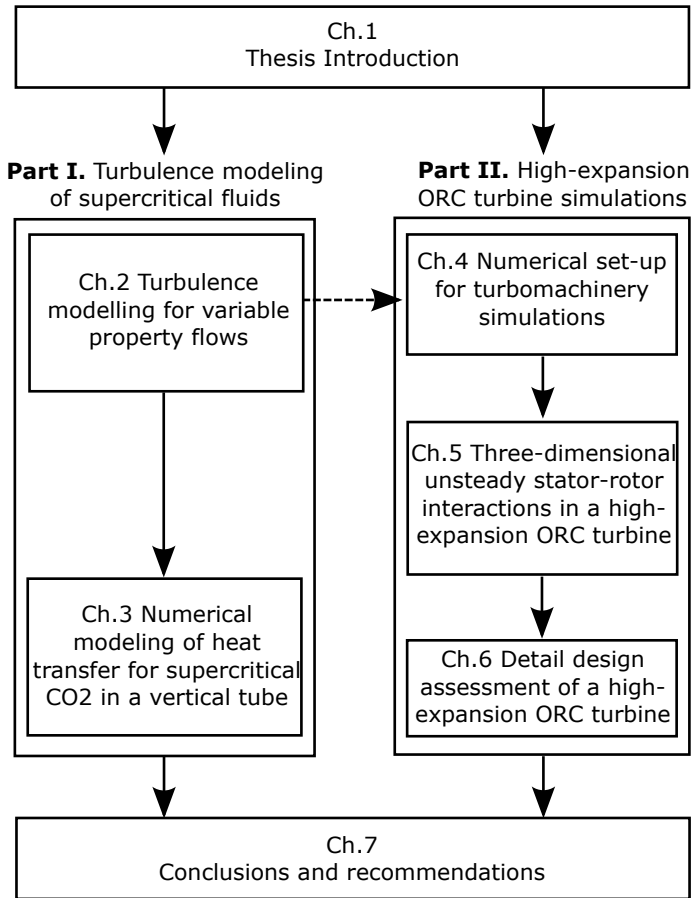
Figure 1.4: Dissertation overview

first time in the field, of a high-expansion ORC turbine via three-dimensional calculations. In *Chapter 6*, we proposed a design procedure for high-expansion ORC turbines, which includes the three-dimensional effects and the intrinsic unsteadiness of the flow; a detail design assessment is performed a posteriori. We apply this design methodology to the expansion process of a ORC manufacturer to generate a new turbine design.

The research included in this dissertation has been published in peer-reviewed scientific journals and was presented at several international conferences, see list of publications on page 159. At the end of this thesis, the reader can find the acknowledgements and a short biography from the author.

References

[1] Administration, U. E. I., 2019. Electricity explained, how electricity is generated. `https://www.eia.gov/energyexplained/electricity/how-electricity-is-generated.php`.

[2] Moran, M. J., Shapiro, H. N., Boettner, D. D., and Bailey, M. B., 2010. *Fundamentals of engineering thermodynamics*. John Wiley & Sons.

[3] Ritchie, H., and Roser, M., 2017. Fossil fuels. `https://ourworldindata.org/fossil-fuels`.

[4] Raupach, M. R., Marland, G., Ciais, P., Le Quéré, C., Canadell, J. G., Klepper, G., and Field, C. B., 2007. "Global and regional drivers of accelerating CO2 emissions". *Proceedings of the National Academy of Sciences,* **104**(24), pp. 10288–10293.

[5] Change, C., 2001. "Climate change". *Synthesis report*.

[6] Rogelj, J., Den Elzen, M., Höhne, N., Fransen, T., Fekete, H., Winkler, H., Schaeffer, R., Sha, F., Riahi, K., and Meinshausen, M., 2016. "Paris agreement climate proposals need a boost to keep warming well below 2 c". *Nature,* **534**(7609), p. 631.

[7] Olivier, J. G. J., Schire, K. M., and Peters, J. A. H. W., 2017. Trends in global CO2 and total greenhouse gas emissions. Tech. rep.

[8] Liang, X., 2016. "Emerging power quality challenges due to integration of renewable energy sources". *IEEE Transactions on Industry Applications,* **53**(2), pp. 855–866.

[9] Eurostat, 2017. Renewables energy statistics. `https://ec.europa.eu/eurostat/statistics-explained/index.php/Renewable_energy_statistics#Renewable_energy_produced_in_the_EU_increased_by_two_thirds_in_2007-2017`.

[10] SunRun, 2018. Cost of solar. `https://www.sunrun.com/solar-lease/cost-of-solar`.

[11] US Department of Energy, 2018. 2018 wind technologies market report. Tech. rep.

[12] Chen, H., Goswami, D. Y., and Stefanakos, E. K., 2010. "A review of thermodynamic cycles and working fluids for the conversion of low-grade heat". *Renewable and sustainable energy reviews,* **14**(9), pp. 3059–3067.

[13] Colonna, P., Casati, E., Trapp, C., Mathijssen, T., Larjola, J., Turunen-Saaresti, T., and Uusitalo, A., 2015. "Organic Rankine cycle power systems: From the concept to current technology, applications, and an outlook to the future". *J. Eng. Gas Turb. Power,* **137**(10), p. 100801.

[14] Ahn, Y., Bae, S. J., Kim, M., Cho, S. K., Baik, S., Lee, J. I., and Cha, J. E., 2015. "Review of supercritical co2 power cycle technology and current status of research and development". *Nuclear Engineering and Technology,* **47**(6), pp. 647–661.

[15] Tartière, T., and Astolfi, M., 2017. "A world overview of the organic Rankine cycle market". *Energy Procedia,* **129**, pp. 2–9.

[16] Feidt, M., Kheiri, A., Pelloux-Prayer, S., et al., 2014. "Performance optimization of low-temperature power generation by supercritical ORCs (organic Rankine cycles) using low gwp (global warming potential) working fluids". *Energy,* **67**, pp. 513–526.

[17] Colonna, P., Harinck, J., Rebay, S., and Guardone, A., 2008. "Real-gas effects in organic Rankine cycle turbine nozzles". *J. Propul. Power,* **24**(2), pp. 282–294.

[18] Irfan, U., 2015. Can carbone dioxide replace steam to generate power? https://www.scientificamerican.com/article/can-carbon-dioxide-replace-steam-to-generate-power/.

[19] Service, R., 2017. "Fossil power, guilt free.". *Science (New York, NY),* **356**(6340), p. 796.

[20] Yoon, S. H., Kim, J. H., Hwang, Y. W., Kim, M. S., Min, K., and Kim, Y., 2003. "Heat transfer and pressure drop characteristics during the in-tube cooling process of carbon dioxide in the supercritical region". *International Journal of Refrigeration,* **26**(8), pp. 857–864.

[21] Simeoni, G., Bryk, T., Gorelli, F., Krisch, M., Ruocco, G., Santoro, M., and Scopigno, T., 2010. "The widom line as the crossover between liquid-like and gas-like behaviour in supercritical fluids". *Nature Physics,* **6**(7), p. 503.

[22] Cabeza, L. F., de Gracia, A., Fernández, A. I., and Farid, M. M., 2017. "Supercritical CO2 as heat transfer fluid: A review". *Applied Thermal Engineering,* **125**, oct, pp. 799–810.

[23] Ma, Z., and Turchi, C. S., 2011. Advanced supercritical carbon dioxide power cycle configurations for use in concentrating solar power systems. Tech. rep., National Renewable Energy Lab.(NREL), Golden, CO (United States).

[24] Echogen power systems = https://www.echogen.com/, year = 2021 urldate = 2021.01.11.

[25] Wagman, D., 2018. This power plant runs on CO2. https://spectrum.ieee.org/energy/fossil-fuels/this-power-plant-runs-on-co2.

[26] Moullec, U. L., Qi, Z., Zhang, J., Zhou, P., Yang, Z., Wang, X., Chen, W., and Wang, S., 2019. "Shouhang-EDF: 10MWe supercritical CO2 cycle + CSP demostration project". In Proceedings of the 3rd European supercritical CO2 Conference, Paris, France.

[27] Cho, J., Shin, H., Cho, J., Choi, B., Roh, C., Lee, B., Lee, G., Ra, H.-S., and Baik, Y.-J., 2019. "Development and power generating operation of the supercritical carbon dioxide power cycle experimental test loop in kier". In 3rd European Conference on Supercritical CO2 (sCO2) Power Systems 2019: 19th-20th September 2019, pp. 116–124.

[28] Webb, R., 1981. "Performance evaluation criteria for use of enhanced heat transfer surfaces in heat exchanger design". *International Journal of Heat and Mass Transfer,* **24**(4), pp. 715–726.

[29] Reynolds, O., 1883. "Xxix. an experimental investigation of the circumstances which determine whether the motion of water shall be direct or sinuous, and of the law of resistance in parallel channels". *Philosophical Transactions of the Royal society of London*(174), pp. 935–982.

[30] Nelkin, M., 1992. "In what sense is turbulence an unsolved problem?". *Science,* **255**(5044), pp. 566–570.

[31] He, S., Kim, W., and Bae, J., 2008. "Assessment of performance of turbulence models in predicting supercritical pressure heat transfer in a vertical tube". *International Journal of Heat and Mass Transfer,* **51**(19-20), pp. 4659–4675.

[32] Harinck, J., Pasquale, D., Pecnik, R., van Buijtenen, J., and Colonna, P., 2013. "Performance improvement of a radial organic Rankine cycle turbine by means of automated computational fluid dynamic design". *Proc. IMechE, Part A: J. Power and Energy,* **227**(6), pp. 637–645.

[33] Bülten, B., Althaus, W., Weidner, E., and Stoff, H., 2015. "Experimental and numerical flow investigation of a centripetal supersonic turbine for organic rankine cycle applications". In 11th European Conference on Turbomachinery Fluid Dynamics & Thermodynamics, Madrid, Spain, Mar, pp. 23–27.

Part I

Turbulence modelling of supercritical fluids

The supercritical carbon dioxide (CO_2) Brayton cycle is a viable alternative to steam cycles, which results in higher thermal efficiency, more compact installation, and lower greenhouse gas emissions. Moreover, renewable energy technologies, such as solar energy and waste heat recovery, can benefit from the advantage of supercritical fluids, e.g., the high density near the critical point. However, these fluids deviate from ideal thermodynamic behavior and do not have a recognizable phase change. Furthermore, small changes of temperature or pressure in the supercritical region can produce strong gradients on the thermo-physical properties. Standard eddy viscosity models are incapable of accounting for the effects of strong variation of thermo-physical properties on the turbulence of supercritical fluids, which can cause considerable inaccuracies in predicting the pressure drop, the heat transfer coefficient, and other quantities of interest for supercritical fluid flows. This section aims to improve the modeling of supercritical fluids. First, in Chapter 2, we develop consistent modifications to make eddy viscosity models more reliable for wall-bounded turbulent flow with sharp gradients of the thermo-physical properties. Later, in Chapter 3, we implement these density-corrected turbulence models to our in-house solver to simulate an upward heated turbulent pipe flow with CO_2 at supercritical pressure.

2

Turbulence modelling for variable property flows

This chapter presents a novel methodology for improving the ability of eddy viscosity models to predict wall-bounded turbulent flows with strong gradients in the thermophysical properties, as is the case for fluids in the supercritical region. Common turbulence models for solving the Reynolds-averaged Navier-Stokes equations do not correctly account for variations in transport properties, such as density and viscosity, which can cause substantial inaccuracies in predicting important quantities of interest, including heat transfer and drag. Based on the semi-locally-scaled turbulent kinetic energy equation, introduced in [Pecnik and Patel, J. Fluid Mech. (2017), vol. 823, R1], we analytically derive a modification of the diffusion term of turbulent scalar equations. We apply this modification to five common eddy viscosity turbulence models and test them for a fully-developed turbulent channels with isothermal walls that are volumetrically heated, either by a uniform source or by viscous heating in supersonic flow conditions. The agreement with results obtained by direct numerical simulation shows that the modification significantly improves the accuracy of eddy viscosity models for fluids with variable transport properties.

2.1   Introduction

Turbulence plays a vital role in heat transfer and skin friction across the boundary layer in wall bounded flows. For engineers, it is therefore of paramount importance to accurately model turbulence during the design process of any flow guiding devices, such as heat exchangers with strongly cooled or heated flows, rocket propulsion systems, combustion chambers with chemically reacting flows, or turbomachinery flows with unconventional working fluids. In all these applications, strong heat transfer causes large temperature gradients and consequently large variations in density, viscosity, thermal conductivity, heat capacity, etc., which alter the conventional behaviour of turbulence. Despite decades of research, turbulent flows with variable thermo-physical properties are still far from being understood. Accordingly, turbulence models for engineering applications with large heat transfer rates are not able to provide accurate results for Nusselt numbers, pressure losses, or any other quantities of interest.

In the past, experiments and direct numerical simulations (DNS) have been performed to study turbulent flows over a wide range of Reynolds numbers for boundary layers, channel, pipes, among others[1–4]. However, these detailed measurements and simulations are limited to simple geometries, and as the Reynolds number increases, DNS become computationally more expensive. Because of this fact, turbulence models for simulations of the Reynolds-averaged Navier-Stokes (RANS) equations rely on a limited number of accurate data, and their development is additionally hampered by the lack of knowledge on how turbulence is affected by strong variations of thermo-physical properties. Since almost all turbulence models have been developed for incompressible flows, several extensions to include compressible effects have been proposed in the past by[5–7]. For example, if the turbulent kinetic energy (TKE) equation is derived on the basis of the compressible Navier-Stokes equations, additional terms appear, i.e. pressure -work and -dilatation, dilatational dissipation, and additional terms related to fluctuations of density, velocity,

pressure, etc. The modification of the TKE in flows with strong heat transfer has been attributed to these terms and according models have been proposed in the past [6–8]. Huang, Bradshaw, and Coakley [5], analyzed the log-layer behaviour of a compressible boundary layer using turbulence models and claimed that the model closure coefficients must be a function of mean density gradients to satisfy the law-of-the-wall obtained with the van Driest velocity transformation [9].

A different approach to sensitize turbulence models for compressible flows with large density variations, was proposed by Catris and Aupoix [10]. They used the formulation developed by Huang *et al.* [5] for the closure coefficients, to modify the diffusion term of the turbulent dissipation transport equation. Additionally, they argued that the diffusion of TKE acts upon the energy per unit volume $[(kg\, m^2/s^2)/m^3]$ of turbulent fluctuations, which can be expressed as the density times the TKE (ρk). The diffusion of TKE is therefore based on ρk, while the diffusion coefficient is divided by the density on the basis of dimensional consistency. Their approach improved eddy viscosity models for supersonic adiabatic boundary layer flows, without including the additional compressibility terms. However, these ad-hoc corrections to the TKE equations need to be assessed for a wide range of flows, including standard low-speed flows [11] and free shear flows [12].

In this chapter, we analytically derive modifications of eddy viscosity models for flows with strong property variations, which are based on the fact that the "leading-order effect" of variable properties on wall bounded turbulence can be characterized by the semi-local Reynolds number only [13,14]. The developed methodology is generic and applicable to a wide range of eddy viscosity models. To demonstrate the improvement, we have applied the modifications to five different Eddy viscosity models (EVM) from literature [15–19] and compared the results to direct numerical simulations of heated fully-developed turbulent channel flows with varying thermo-physical properties [14,20]. Furthermore, the density corrections proposed by Catris and Aupoix [10] has been considered as well. The matlab source code used in this research and the DNS data from Patel *et al.* in 2016 [14] are available on GitHub [21].

2.2   SLS turbulence modelling

The semi-local scaling (SLS) as proposed by Huang *et al.* in 1995 [8], is based on the wall shear stress $\tilde{\tau}_w$ and on local-mean (instead of wall) quantities of density and viscosity to account for changes in viscous scales due to mean variations in the thermo-physical properties. The aim of the SLS was to collapse turbulence statistics for compressible flows at high Mach numbers with those of incompressible flows. In the SLS framework, the friction velocity and viscous length scale are defined as $u_\tau^\star = \sqrt{\tilde{\tau}_w/\langle\tilde{\rho}\rangle}$ and $\delta_v^\star = \langle\tilde{\mu}\rangle/\langle\tilde{\rho}\rangle\,u_\tau^\star$, respectively, where $\langle\cdot\rangle$ indicates Reynolds averaging. Accordingly, the semi-local wall distance can be defined as $y^\star = \tilde{y}/\delta_v^\star$ and the semi-local Reynolds number as,

$$Re_\tau^\star = \frac{u_\tau^\star\,\langle\tilde{\rho}\rangle\,\tilde{h}}{\langle\tilde{\mu}\rangle} = \sqrt{\frac{\langle\tilde{\rho}\rangle}{\tilde{\rho}_w}}\frac{\tilde{\mu}_w}{\langle\tilde{\mu}\rangle}Re_\tau, \tag{2.1}$$

19

where $Re_\tau = u_\tau \tilde{\rho}_w \tilde{h}/\tilde{\mu}_w$ and $u_\tau = \sqrt{\tilde{\tau}_w/\tilde{\rho}_w}$, are the conventional friction Reynolds number and friction velocity based on viscous wall units. In general, any flow variable can be non-dimensionalized using wall-based units and semi-local units. This is outlined in more detail in table 2.1. It is important to note, that the friction velocities of both scaling are related through the wall shear stress by $\tilde{\tau}_w = \tilde{\rho}_w u_\tau^2 = \langle \tilde{\rho} \rangle u_\tau^{\star 2}$. This relation will be used frequently throughout this chapter.

Instead of exclusively using the semi-local scaling to collapse turbulence statistics for compressible flows with different Mach numbers, Pecnik and Patel[13] extended the use of the scaling to derive an alternative form of the TKE equation for wall-bounded flows with a strong wall-normal variations of density and viscosity. Starting from the semi-locally-scaled non-conservative form of the momentum equations, and with the assumption that the wall shear stress $\tilde{\tau}_w$ changes slowly in the stream-wise direction, the SLS TKE equation reads,

$$t_\tau^\star \frac{\partial \{\hat{k}\}}{\partial \tilde{t}} + \frac{\partial \{\hat{k}\}\{\hat{u}_j\}}{\partial \hat{x}_j} = \hat{P}_k - \hat{\varepsilon}_k + \hat{T}_k + \hat{C}_k + \hat{\mathcal{D}}_k, \qquad (2.2)$$

with production $\hat{P}_k = -\{\hat{u}_i''\hat{u}_j''\}\partial\{u_i^{vD}\}/\partial\hat{x}_j$, dissipation per unit volume $\hat{\varepsilon}_k = \langle \hat{\tau}_{ij}' \partial \hat{u}_i'/\partial \hat{x}_j \rangle$, diffusion (containing viscous diffusion, turbulent transport, and pressure diffusion) $\hat{T}_k = \partial(\langle \hat{u}_i' \hat{\tau}_{ij} \rangle - \{\hat{u}_j''\hat{k}\} - \langle \hat{p}' \hat{u}_j' \rangle)/\partial \hat{x}_j$, and compressibility $\hat{C}_k = \langle \hat{p}' \partial \hat{u}_j'/\partial \hat{x}_j \rangle - \langle \hat{u}_j'' \rangle \partial \langle \hat{p} \rangle /\partial \hat{x}_j + \langle \hat{u}_i'' \rangle \partial \langle \hat{\tau}_{ij} \rangle /\partial \hat{x}_j$. $\hat{\tau}_{ij} = \hat{\mu}/Re_\tau^\star \left[\left(\partial \hat{u}_i/\partial \hat{x}_j + \partial \hat{u}_j/\partial \hat{x}_i \right) - 2/3(\partial \hat{u}_k/\partial \hat{x}_k)\delta_{ij} \right]$ is the shear stress tensor.

Due to the semi-local scaling, additional terms appear in equation (2.2), which are lumped in $\hat{\mathcal{D}}_k = (\{\hat{u}_j\}\{\hat{k}\} + \{\hat{u}_j''\hat{k}\})d_j - \langle \hat{u}_i'' \, \partial \hat{D}_{ij}/\partial \hat{x}_j \rangle$, with

$$\hat{D}_{ij} = \frac{\hat{\mu}}{Re_\tau^\star} \left[\left(\hat{u}_i d_j + \hat{u}_j d_i \right) - \frac{2}{3}\hat{u}_k d_k \delta_{ij} \right],$$

$d_i = 1/2 \langle \rho \rangle^{-1} \partial \langle \rho \rangle /\partial \hat{x}_i$, and δ_{ij} the Kronecker delta. The mean density gradient appears since the turbulent kinetic energy (and/or the velocity) within the derivatives is scaled by the semi-local friction velocity $u_\tau^\star$. For example, taking the derivative of $u_\tau^\star$, one can write (assuming that the averaged wall shear stress is constant),

$$\frac{\partial u_\tau^\star}{\partial \hat{x}_i} = \sqrt{\tau_w}\frac{\partial \sqrt{1/\langle \rho \rangle}}{\partial \hat{x}_i} = \sqrt{\tau_w}\frac{\partial \sqrt{1/\langle \rho \rangle}}{\partial \langle \rho \rangle}\frac{\partial \langle \rho \rangle}{\partial \hat{x}_i} = -\frac{1}{2}\frac{u_\tau^\star}{\langle \rho \rangle}\frac{\partial \langle \rho \rangle}{\partial \hat{x}_i} = -u_\tau^\star d_i.$$

In equation 2.2 and across this chapter, the curly brackets $\{\cdot\}$ indicate Favre averaging and $t_\tau^\star = \tilde{h}/u_\tau^\star$. It is important to mention that the Favre-averaged TKE is defined as $\{\hat{k}\} = \langle \rho\hat{k} \rangle / \langle \rho \rangle$, which, with the Reynolds decomposition of the locally-scaled density as $\langle \rho \rangle = \langle \tilde{\rho} \rangle / \langle \tilde{\rho} \rangle + \langle \tilde{\rho}' \rangle / \langle \tilde{\rho} \rangle = 1$, can also be expressed as $\{\hat{k}\} = \langle \rho\hat{k} \rangle = \langle \rho \hat{u}_i'' \hat{u}_i'' \rangle /2$. This relation $\{\phi\} = \langle \rho\phi \rangle$ will be used frequently in this chapter as well. The reader is referred to Pecnik and Patel[13] for more details on eq. (2.2) and its derivation.

The most important findings in Pecnik and Patel[13] are that effects of property variations on turbulence can be characterized by gradients of the semi-local Reynolds number

Table 2.1: Comparison of local, ϕ, and semi-local, $\hat{\phi}$, scaling for the most relevant quantities. The dimensional quantities are expressed as $\tilde{\phi}$. The subscript w indicates the averaged wall value, which is used in the present study as the reference condition for the local scaling. The friction velocity is used for scaling the velocity. The characteristic length, $\tilde{h}$, is the half channel height in our study.

Quantity			Local scaling		Semi-local sc.
Length	$\tilde{x}_i$	$=$	$x_i \tilde{h}$	$=$	$\hat{x}_i \tilde{h}$
Velocity	$\tilde{u}$	$=$	$u u_\tau$	$=$	$\hat{u} u_\tau^\star$
Pressure	$\tilde{p}$	$=$	$p \tilde{\rho}_w u_\tau^2$	$=$	$\hat{p} \langle \tilde{\rho} \rangle u_\tau^{\star 2}$
Density	$\tilde{\rho}$	$=$	$\rho \tilde{\rho}_w$	$=$	$\hat{\rho} \langle \tilde{\rho} \rangle$
Dyn. viscosity	$\tilde{\mu}$	$=$	$\mu \tilde{\mu}_w$	$=$	$\hat{\mu} \langle \tilde{\mu} \rangle$
Eddy viscosity	$\tilde{\mu}_t$	$=$	$\mu_t \tilde{\rho}_w \tilde{h} u_\tau$	$=$	$\hat{\mu}_t \langle \tilde{\rho} \rangle \tilde{h} u_\tau^\star$
TKE	$\tilde{k}$	$=$	$k u_\tau^2$	$=$	$\hat{k} u_\tau^{\star 2}$
Turb. diss.	$\tilde{\varepsilon}$	$=$	$\varepsilon u_\tau^3 / \tilde{h}$	$=$	$\hat{\varepsilon} u_\tau^{\star 3} / \tilde{h}$
Spec. turb. diss.	$\tilde{\omega}$	$=$	$\omega u_\tau / \tilde{h}$	$=$	$\hat{\omega} u_\tau^\star / \tilde{h}$
Wall distance	$\tilde{y}$	$=$	$y^+ \tilde{h} / Re_\tau$	$=$	$y^\star \tilde{h} / Re_\tau^\star$

$Re_\tau^\star$, and that the turbulent production is governed by the gradient of the van Driest velocity increment, defined as $\partial \{u^{vD}\} = \sqrt{\langle \tilde{\rho} \rangle / \tilde{\rho}_w} \partial (\{\tilde{u}\} / u_\tau)$. Moreover, for the cases investigated in [13], it appears that the terms related to compressible effects and mean density gradients, $\hat{C}_k$ and $\hat{D}_k$, respectively, have a minor effect on the evolution of the SLS TKE.

In the present study, we intend to leverage the knowledge gained from the SLS TKE equation to improve turbulence models predictions of wall-bounded turbulent flows with strong gradients in the thermo-physical properties. As such, we first obtain a closed form of the exact SLS TKE equation, eq. (2.2), which is then scaled back to conventional (wall-based) scales.

For the purpose of obtaining a closed form of the SLS TKE equation, the following assumptions are applied. The production of TKE is estimated using the Boussinesq approximation by modelling the turbulent shear stress. Additionally, it is assumed that the total diffusion $\hat{T}_k$ can be modelled using the gradient diffusion hypothesis [22], and that the dynamic viscosity fluctuations are negligible compared to its averaged counterpart ($\tilde{\mu}' \ll \langle \tilde{\mu} \rangle$). As such, the semi-locally-scaled dynamic viscosity is equal to $\langle \hat{\mu} \rangle = \langle \tilde{\mu} / \langle \tilde{\mu} \rangle \rangle = 1$. Finally, neglecting $\hat{C}_k$ and $\hat{D}_k$, as they have a minor effect, the SLS TKE equation can then be written as

$$t_\tau^\star \frac{\partial \{\hat{k}\}}{\partial \tilde{t}} + \frac{\partial \{\hat{k}\} \{\hat{u}_j\}}{\partial \hat{x}_j} = \hat{P}_k - \hat{\varepsilon} + \frac{\partial}{\partial \hat{x}_j} \left[\left(\frac{1}{Re_\tau^\star} + \frac{\hat{\mu}_t}{\sigma_k} \right) \frac{\partial \{\hat{k}\}}{\partial \hat{x}_j} \right]. \tag{2.3}$$

If this form of the TKE equation is used in conjunction with an eddy viscosity turbulence model, the results for turbulent flows with large thermo-physical property variations significantly improve [13]. However, for general industrial applications with complex geometries, it is not feasible to solve the semi-locally-scaled equations. The reason is that all turbulence variables would need to be rescaled every iteration step by quantities

that depend on the wall friction at the closest wall and by local quantities of density and viscosity.

To overcome this, the focus of the derivation in this chapter is to transform equation (2.3) back to conventional scales, in particular viscous wall units. The scaling transformations outlined in table 2.1 will be used for each term in (2.3). Starting with the turbulent kinetic energy,

$$
\{\hat{k}\} = \langle \hat{\rho} \hat{u}_i'' \hat{u}_i'' \rangle /2 = \left\langle \rho \frac{\tilde{\rho}_w}{\langle \tilde{\rho} \rangle} u_i'' \frac{u_\tau}{u_\tau^\star} u_i'' \frac{u_\tau}{u_\tau^\star} \right\rangle /2 = \left\langle \rho \frac{\tilde{\rho}_w}{\langle \tilde{\rho} \rangle} u_i'' \sqrt{\frac{\langle \tilde{\rho} \rangle}{\tilde{\rho}_w}} u_i'' \sqrt{\frac{\langle \tilde{\rho} \rangle}{\tilde{\rho}_w}} \right\rangle /2
$$

$$
= \langle \rho u_i'' u_i'' \rangle /2 = \langle \rho k \rangle = \langle \rho \rangle \{k\}.
$$

Then, we obtain for the time derivative the following:

$$
t_\tau^\star \frac{\partial \{\hat{k}\}}{\partial \tilde{t}} = t_\tau^\star \frac{\partial \langle \rho \rangle \{k\}}{\partial \tilde{t}}.
$$

The convective term transforms into,

$$
\frac{\partial \{\hat{k}\}\{\hat{u}_j\}}{\partial \hat{x}_j} = \frac{\tilde{h}}{\tilde{h}} \frac{\partial}{\partial x_j} \left[\langle \rho \rangle \{k\}\{u_j\} \sqrt{\frac{\langle \tilde{\rho} \rangle}{\tilde{\rho}_w}} \right] = \frac{\partial}{\partial x_j} \left[\langle \rho \rangle^{1.5} \{k\}\{u_j\} \right] = \frac{\partial \sqrt{\langle \rho \rangle} \langle \rho \rangle \{k\}\{u_j\}}{\partial x_j}
$$

$$
= \sqrt{\langle \rho \rangle} \left(\frac{\partial \langle \rho \rangle \{k\}\{u_j\}}{\partial x_j} + \frac{\langle \rho \rangle \{k\}\{u_j\}}{2 \langle \rho \rangle} \frac{\partial \langle \rho \rangle}{\partial x_j} \right).
$$

As it can be seen, the convection now consists of two terms. However, the second term is a mathematical artefact, which can be canceled by one of the terms in $\hat{\mathcal{D}}_k$. The production of TKE transformed back to a scaling based on wall units, results in

$$
\hat{P}_k = -\{\hat{u}_i'' \hat{u}_j''\} \frac{\partial \{u^{\nu D}\}}{\partial \hat{x}_j} = -\langle \hat{\rho} \hat{u}_i'' \hat{u}_j'' \rangle \frac{\partial \{u^{\nu D}\}}{\partial x_j} = -\left\langle \rho \frac{\tilde{\rho}_w}{\langle \tilde{\rho} \rangle} u_i'' \sqrt{\frac{\langle \tilde{\rho} \rangle}{\tilde{\rho}_w}} u_j'' \sqrt{\frac{\langle \tilde{\rho} \rangle}{\tilde{\rho}_w}} \right\rangle \sqrt{\frac{\langle \tilde{\rho} \rangle}{\tilde{\rho}_w}} \frac{\partial \{u\}}{\partial x_j}
$$

$$
= \sqrt{\langle \rho \rangle} \left(-\langle \rho u_i'' u_j'' \rangle \frac{\partial \{u\}}{\partial x_j} \right) = \sqrt{\langle \rho \rangle} P_k.
$$

The transformation applied for the turbulent dissipation gives,

$$
\hat{\varepsilon} = \varepsilon \left(\frac{u_\tau / \tilde{h}}{u_\tau^\star / \tilde{h}} \right)^3 = \varepsilon \left(\frac{\langle \tilde{\rho} \rangle}{\tilde{\rho}_w} \right)^{1.5} = \sqrt{\langle \rho \rangle} \langle \rho \rangle \varepsilon.
$$

The semi-locally-scaled dynamic viscosity and eddy viscosity can also be written as,

$$
\frac{1}{Re_\tau^\star} = \frac{1}{Re_\tau} \sqrt{\frac{\tilde{\rho}_w}{\langle \tilde{\rho} \rangle}} \frac{\langle \tilde{\mu} \rangle}{\tilde{\mu}_w} = \frac{1}{\sqrt{\langle \rho \rangle}} \frac{\langle \mu \rangle}{Re_\tau},
$$

and,

$$
\frac{\hat{\mu}_t}{\sigma_k} = \frac{\mu_t}{\sigma_k} \frac{\tilde{\rho}_w \tilde{h} u_\tau}{\langle \tilde{\rho} \rangle \tilde{h} u_\tau^\star} = \frac{\mu_t}{\sigma_k} \frac{\tilde{\rho}_w}{\langle \tilde{\rho} \rangle} \sqrt{\frac{\langle \tilde{\rho} \rangle}{\tilde{\rho}_w}} = \frac{1}{\sqrt{\langle \rho \rangle}} \frac{\mu_t}{\sigma_k},
$$

respectively, such that the overall diffusion results in,

$$\frac{\partial}{\partial \hat{x}_j}\left[\left(\frac{1}{Re_\tau^\star} + \frac{\hat{\mu}_t}{\sigma_k}\right)\frac{\partial\{\hat{k}\}}{\partial \hat{x}_j}\right] = \frac{\partial}{\partial x_j}\left[\frac{1}{\sqrt{\langle\rho\rangle}}\left(\frac{\langle\mu\rangle}{Re_\tau} + \frac{\mu_t}{\sigma_k}\right)\frac{\partial\langle\rho\rangle\{k\}}{\partial x_j}\right].$$

Substituting the newly obtained terms into (2.3), and dividing them by $\sqrt{\langle\rho\rangle}$ to convert $t_\tau^\star$ into $t_\tau = \tilde{h}/u_\tau$, we end up with,

$$t_\tau\frac{\partial\langle\rho\rangle\{k\}}{\partial \tilde{t}} + \frac{\partial\langle\rho\rangle\{k\}\{u_j\}}{\partial x_j} = P_k - \langle\rho\rangle\,\varepsilon + \frac{1}{\sqrt{\langle\rho\rangle}}\frac{\partial}{\partial x_j}\left[\frac{1}{\sqrt{\langle\rho\rangle}}\left(\frac{\langle\mu\rangle}{Re_\tau} + \frac{\mu_t}{\sigma_k}\right)\frac{\partial\langle\rho\rangle\{k\}}{\partial x_j}\right]. \quad (2.4)$$

If compared to the conventional model for the TKE, the newly derived equation shows only one major difference that lies in the diffusion term. The diffusion term that emerges from the semi-local-scaling methodology is a function of $\langle\rho k\rangle$ (instead of $\langle k\rangle$), while the diffusion coefficient and the overall diffusion term are divided by $\sqrt{\langle\rho\rangle}$. This is similar to the density corrections proposed by [10], except that in [10] only the diffusion coefficient is divided by $\langle\rho\rangle$.

2.3   Compressible / variable density turbulence models

The derivation described in section 2.2, can now be applied to various EVMs. In this work, we chose five different models (the model equations are given in Appendix A.1 for completeness):

- the eddy viscosity correlation of Cess [15],
- the one-equation model of Spalart-Allmaras (SA) [16],
- the k-ε model of Myong and Kasagi (MK) [17],
- Menter's shear stress transport model (SST) [18],
- and the four-equations $v'^2 - f$ model (V2F) [19].

The resulting compressible / variable density modifications from the SLS approach and the density corrections proposed by [10] are indicated in red in table 2.2, which are mainly related to the diffusion term of the respective transport equations; the averaged operators have been omitted for brevity. The full derivation of all modified turbulent transport equations is given in appendix A.2. Interestingly, the proposed diffusion form by [10] and the result from the SLS approach are equivalent for ε and ω, although both derivations follow alternative routes. For the SA variable, $\check{v}$, the only difference between our diffusion formulation and the one derived by [10] is that we include the kinematic viscosity in the density gradient term. However, this distinction is negligible, as it will be seen later. It is important to remark that the density corrections by [10] were developed following a more heuristic method than the one presented in this work. For the additional equations of the V2F model, the auxiliary transport for v'^2 has the same modifications as the modified TKE diffusion term, and the elliptic relaxation equation f does not need any modification, find

Table 2.2: Diffusion term, normalized by viscous wall units, for the turbulent scalar equations: k, ε, ω and $\check{v}$ (Spalart-Allmaras variable). The differences with respect to the original model are highlight in red. σ_k, σ_ε, σ_ω, c_{b2} and c_{b3} are model constants. More details of turbulence models are shown in appendix A.1. [†]Catris and Aupoix[10] actually use the turbulent dissipation per unit volume as the conserved variable: $D\rho\varepsilon/Dt$.

Material derivative	Conventional	Catris & Aupoix (C&A)[10]	Present study
$\rho\frac{Dk}{Dt} = ...$	$\frac{\partial}{\partial x_j}\left[\left(\frac{\mu}{Re_\tau}+\frac{\mu_t}{\sigma_k}\right)\frac{\partial k}{\partial x_j}\right]$	$\frac{\partial}{\partial x_j}\left[\frac{1}{\rho}\left(\frac{\mu}{Re_\tau}+\frac{\mu_t}{\sigma_k}\right)\frac{\partial \rho k}{\partial x_j}\right]$	$\frac{1}{\sqrt{\rho}}\frac{\partial}{\partial x_j}\left[\frac{1}{\sqrt{\rho}}\left(\frac{\mu}{Re_\tau}+\frac{\mu_t}{\sigma_k}\right)\frac{\partial \rho k}{\partial x_j}\right]$
[†]$\rho\frac{D\varepsilon}{Dt} = ...$	$\frac{\partial}{\partial x_j}\left[\left(\frac{\mu}{Re_\tau}+\frac{\mu_t}{\sigma_\varepsilon}\right)\frac{\partial \varepsilon}{\partial x_j}\right]$	$\frac{1}{\rho}\frac{\partial}{\partial x_j}\left[\frac{1}{\sqrt{\rho}}\left(\frac{\mu}{Re_\tau}+\frac{\mu_t}{\sigma_\varepsilon}\right)\frac{\partial \rho^{1.5}\varepsilon}{\partial x_j}\right]$	$\frac{1}{\rho}\frac{\partial}{\partial x_j}\left[\frac{1}{\sqrt{\rho}}\left(\frac{\mu}{Re_\tau}+\frac{\mu_t}{\sigma_\varepsilon}\right)\frac{\partial \rho^{1.5}\varepsilon}{\partial x_j}\right]$
$\rho\frac{D\omega}{Dt} = ...$	$\frac{\partial}{\partial x_j}\left[\left(\frac{\mu}{Re_\tau}+\frac{\mu_t}{\sigma_\omega}\right)\frac{\partial \omega}{\partial x_j}\right]$	$\frac{\partial}{\partial x_j}\left[\frac{1}{\sqrt{\rho}}\left(\frac{\mu}{Re_\tau}+\frac{\mu_t}{\sigma_\omega}\right)\frac{\partial \sqrt{\rho}\omega}{\partial x_j}\right]$	$\frac{\partial}{\partial x_j}\left[\frac{1}{\sqrt{\rho}}\left(\frac{\mu}{Re_\tau}+\frac{\mu_t}{\sigma_\omega}\right)\frac{\partial \sqrt{\rho}\omega}{\partial x_j}\right]$
$\frac{D\check{v}}{Dt} = ...$	$\frac{1}{c_{b3}}\frac{\partial}{\partial x_j}\left[\left(\frac{v}{Re_\tau}+\check{v}\right)\frac{\partial \check{v}}{\partial x_j}\right]$ $+\frac{c_{b2}}{c_{b3}}\left(\frac{\partial \check{v}}{\partial x_j}\right)^2$	$\frac{1}{\rho c_{b3}}\frac{\partial}{\partial x_j}\left[\rho\left(\frac{v}{Re_\tau}+\check{v}\right)\frac{\partial \check{v}}{\partial x_j}\right]$ $+\frac{\check{v}^2}{2}\frac{\partial \rho}{\partial x_j}+\frac{c_{b2}}{\rho c_{b3}}\left(\frac{\partial \sqrt{\rho}\check{v}}{\partial x_j}\right)^2$	$\frac{1}{\rho c_{b3}}\frac{\partial}{\partial x_j}\left[\rho\left(\frac{v}{Re_\tau}+\check{v}\right)\frac{\partial \check{v}}{\partial x_j}\right]$ $+\left(\frac{v}{Re_\tau}+\check{v}\right)\frac{\check{v}}{2}\frac{\partial \rho}{\partial x_j}+\frac{c_{b2}}{\rho c_{b3}}\left(\frac{\partial \sqrt{\rho}\check{v}}{\partial x_j}\right)^2$

both transport equations in appendix A.2. An additional modification we have introduced is to replace y^+ and Re_τ, e.g. within the eddy viscosity correlation of Cess and for the damping function of the MK turbulence model, by their semi-local counterparts, namely $y^\star$ and $Re_\tau^{\star}$ [13]. The compressible / variable density modification can also be applied to wall-modeled LES [23].

2.4   Fully-developed channel flow

In order to test the proposed compressible / variable density modifications of the EVMs, fully-developed turbulent flows in volumetrically heated channels with isothermal walls are investigated, outlined in table 2.3. The results are compared to direct numerical simulations performed by Patel *et al.* [14], and Trettel and Larsson [20]. For the first three cases, the density, the viscosity, and the thermal conductivity are a function of temperature only. Different constitutive relations are used that resemble behaviours of liquids, gases and fluids close to the vapour-critical point, where the case C$Re_\tau^{\star}$ corresponds to a fluid whose density and viscosity decrease with increasing temperature (similar to supercritical fluids), such that the semi-local Reynolds number remains constant. The other cases resemble a liquid-like (LL) and gas-like (GL) behaviour, such that $Re_\tau^{\star}$ increases away from the wall for the liquid-like case, and $Re_\tau^{\star}$ decreases for the gas-like case, respectively. Due to the uniform thermal conductivity chosen in the DNS, the Prandtl number decreases away from the wall for the cases C$Re_\tau^{\star}$ and LL, while it increases for the GL case. The fourth case corresponds to a supersonic air flow at a bulk Mach number of $M_b = 4$ with decreasing $Re_\tau^{\star}$ towards the channel center and with uniform Prandtl number across the channel.

   In order to model these cases, the Favre-averaged Navier-Stokes equations in Cartesian coordinates are solved in convenctional viscous wall units for the stream-wise mo-

mentum and energy equations, for a fully-developed flow given as

$$\frac{\partial}{\partial y}\left[\left(\frac{\langle\mu\rangle}{Re_\tau}+\mu_t\right)\frac{\partial\{u\}}{\partial y}\right]=-\langle\rho f_x\rangle,\tag{2.5}$$

$$\frac{\partial}{\partial y}\left[\left(\frac{\langle\lambda\rangle}{Re_\tau Pr_w}+\frac{c_p\mu_t}{Pr_t}\right)\frac{\partial\{T\}}{\partial y}\right]=-\Phi,\tag{2.6}$$

with T and λ as temperature and thermal conductivity, respectively. The flows are driven by an external body force, $\langle\rho f_x\rangle$, which for all cases is equal to τ_w/h. Moreover, the flow is heated by a volumetric source term Φ, summarized in table 2.3. For the supersonic case, Φ corresponds to the viscous heating, which is scaled by the Eckert number, defined as $Ec_\tau=u_\tau^2/(\tilde{T}_w\tilde{c}_{p,w})$. For an ideal gas, Ec_τ is related to the friction Mach number as $Ec_\tau=(\gamma-1)M_\tau^2$, with γ as the ratio of specific heats (for air $\gamma=1.4$). In the low-Mach number limit, the viscous heating is negligible. Therefore, for the cases $CRe_\tau^\star$, LL, and GL, Φ is chosen as a uniform volumetric heat source, with arbitrary values such that a desired temperature difference between the channel center and the channel walls is achieved, see[14]. The reference Prandtl number is defined as $Pr_w=\tilde{\mu}_w\tilde{c}_{p,w}/\tilde{\lambda}_w$. For the low-Mach number cases, the isobaric heat capacity is taken as $c_p=\tilde{c}_p/\tilde{c}_{p,w}=1$, while for the supersonic case, $c_p=\gamma R/(\gamma-1)$ with $R=\tilde{R}/(u_\tau^2/\tilde{T}_w)$, where $\tilde{R}$ is the specific gas constant of air. In equations (2.5) and (2.6), the Reynolds shear stress and turbulent heat flux were modelled using the Boussinesq approximation and the gradient diffusion hypothesis, respectively. In Patel *et al.* 2017[24], it was seen that the turbulent Prandtl number, Pr_t, varies around unity for the low-Mach number cases, implying that there is a strong analogy between the momentum and scalar transport. Therefore, we have approximated $Pr_t=1$ also for the high-Mach number case.

A no-slip condition for the velocity and equal temperatures at both channel walls are applied as boundary conditions, resulting in symmetric velocity and temperature profiles. A second-order central difference scheme is used to calculate the gradients on a non-uniform mesh using exact analytic metric transformations of a hyperbolic tangent function that clusters the mesh points near the wall to ensure $y^+\le1$. Mesh independent solutions were obtained for all cases on a mesh with 100 grid points. The system of equations is solved in Matlab. For more insights on the numerical solver, please refer to the source code available on Github[21] with the data for the low-Mach number cases from[14].

2.5 Results

The results for all EVMs are now compared with data from DNS. The velocity profiles are reported in figure 2.1 using the universal velocity transformation, defined in Patel *et al.* 2016[14] as $u^\star=\int_0^{\{u^{vD}\}}\left[1+(y/Re_\tau^\star)\,\partial Re_\tau^\star/\partial y\right]\partial\{u^{vD}\}$. A more quantitative comparison with DNS is given by bar graphs in figure 2.2, showing the relative error of the calculated bulk Reynolds number, defined as $Re_b=u_b\rho_bh/\mu_w$, where the subscript b stands for bulk. Note, the simulations are performed by setting the friction Reynolds number. Also the temperature profiles for all cases are compared with DNS in figure 2.3, and the error of

Table 2.3: Channel flows investigated: $CRe_\tau^\star$ - refers to a variable property case, whose density, ρ and dynamic viscosity, μ are proportional to $1/T$ and $\sqrt{1/T}$, respectively, such that $Re_\tau^\star$ maintains constant across the channel; GL - refers to a variable property case with a gas-like density and viscosity distribution; LL - variable property case with a liquid-like viscosity distribution (density is constant); and a supersonic cases with a bulk Mach number equal to 4 from[20]. The data of the low-Mach number test cases were taken from[13]. λ is the thermal conductivity, $Re_{\tau,c}^\star$ the value of the semi-local Reynolds number at the center of the channel, Pr_w is the Prandtl number at the wall, and Φ refers to the volumetric heat source.

Channel flow	ρ/ρ_w	μ/μ_w	λ/λ_w	$Re_{\tau,w}^\star$	$Re_{\tau,c}^\star$	Pr_w	Φ
Constant $Re_\tau^\star$ ($CRe_\tau^\star$)	$(T/T_w)^{-1}$	$(T/T_w)^{-0.5}$	1	395	395	1.0	$95/(Re\,Pr_w)$
Gas-Like (GL)	$(T/T_w)^{-1}$	$(T/T_w)^{0.7}$	1	950	137	1.0	$75/(Re\,Pr_w)$
Liquid-Like (LL)	1	$(T/T_w)^{-1}$	1	150	945	1.0	$62/(Re\,Pr_w)$
Supersonic (SS)	$\propto (T/T_w)^{-1}$	$(T/T_w)^{-3/4}$	$(T/T_w)^{-3/4}$	1017	203	0.7	$Ec_\tau\left(\frac{\langle\mu\rangle}{Re_\tau}+\mu_t\right)\left(\frac{\partial\langle u\rangle}{\partial y}\right)^2$

the Nusselt number is shown in bar graphs in figure 2.4. The Nusselt number is defined as $Nu = (\partial T/\partial y)_w/[(T_w - T_c)/h]$, where T_c is the temperature at the center of the channel.

In general, the compressibility / variable property modifications clearly improve the results for the velocity and temperature profiles that have been obtained by the EVMs for the cases investigated herein. The model modifications also improve the prediction of the Reynolds and Nusselt numbers for most of the cases. The results for the Reynolds and Nusselt number are correlated, since both the Reynolds shear stress and the turbulent heat flux have been approximated by the eddy viscosity. However, the Nusselt number estimation also depends on the choice of the turbulent Prandtl number, which has been assumed constant in this study. Because of this, the error on the Nusselt number is larger than the error on the Reynolds number for almost all investigated configurations. To verify this, closure models for the turbulent heat flux can be used to improve model results for flows with strong heat transfer[25]. As expected, figures 2.2 and 2.4 depict that for the liquid-like case (LL), for which the density is constant, the compressibility / variable property modifications do not influence the results of the SA, V2F, and SST model.

The results of each turbulence model are now analyzed individually.

- **Cess**: This eddy viscosity correlation has originally been developed by fitting experimental data of turbulent flows in pipes and is simply a function of non-dimensional wall distance and friction Reynolds number (see appendix A.1). Therefore, the results obtained with the unmodified Cess eddy viscosity correlation show large errors for the variable property cases. For example, the error on the Reynolds number is approximately 30% for GL, 1200% for LL, and 90% for case SS, see figure 2.2. However, for the variable property case with constant semi-local Reynolds number (case $CRe_\tau^\star$) the errors are only $\approx$2%, which confirms the fact that turbulence statistics are mainly modified by gradients in $Re_\tau^\star$ only[14]. By simply replacing the model parameters Re_τ and y^+, by their semi-local counterparts $Re_\tau^\star$ and $y^\star$, the results for GL, LL and SS can be considerably improved (figures 2.1-2.4),
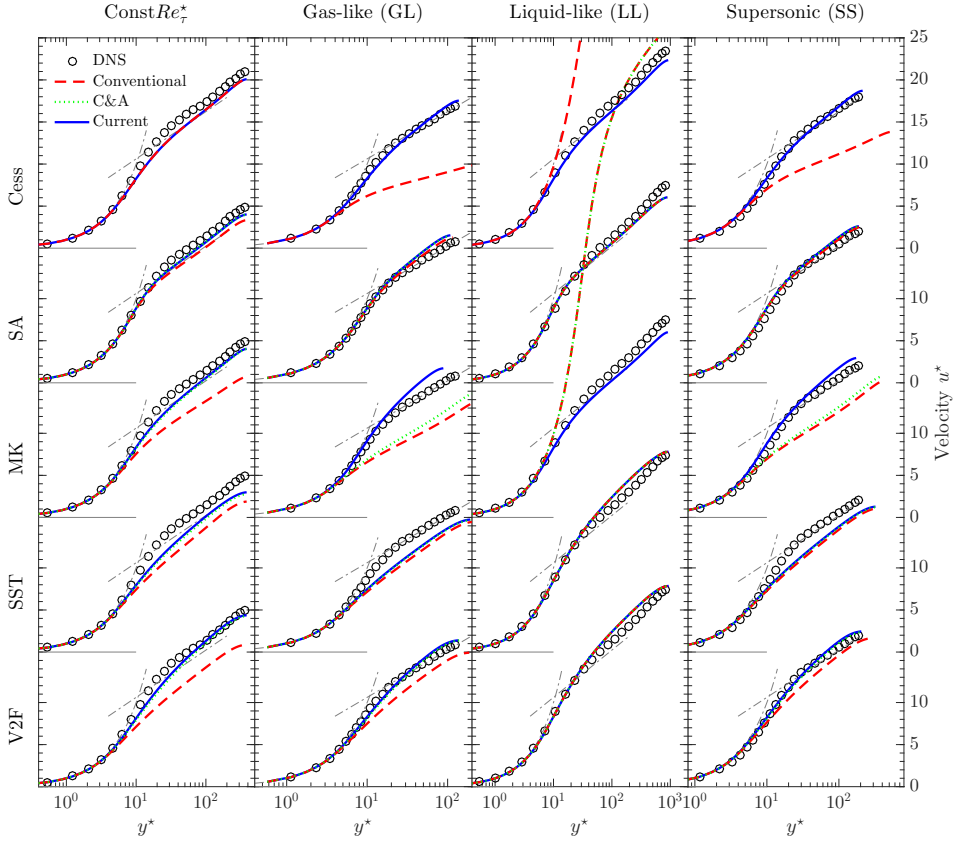
Figure 2.1: Turbulence model and DNS results for the velocity transformation $u^\star$ as a function of $y^\star$ for all channel flows. The grey dashed lines represent $u^\star = y^\star$ and $u^\star = 1/\kappa\, ln(y^\star) + C$, the viscous sublayer and log-law region, respectively, where $C = 5.5$.

again confirming that the turbulence statistics can be characterized by semi-local wall units.

- **SA**: Interestingly, the SA model accurately reproduces the velocity and temperature profiles for all variable property flows without applying any modifications, see figures 2.1 and 2.3. A further improvement, using the compressible / variable property modifications, can only be achieved for the case $CRe_\tau^\star$. For example, our proposed modification slightly improves the results for the Reynolds number (figure 2.2) and considerably improves the result for the Nusselt number, where the error decreases from 4% to below 0.2% (figure 2.4). The reason for this improvement is due to a more accurate approximation of the turbulent heat flux with the modified model. Overall, the two corrections, the one developed by [10] and the
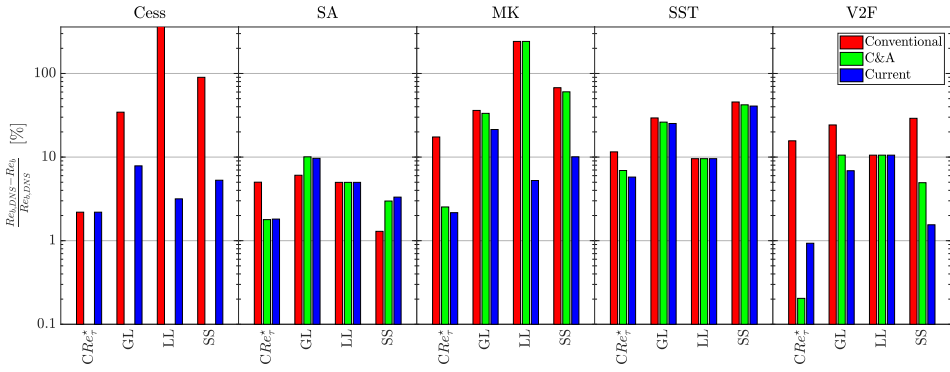
Figure 2.2: Relative error of the bulk Reynolds number (Re_b) calculated by models with respect to DNS data.
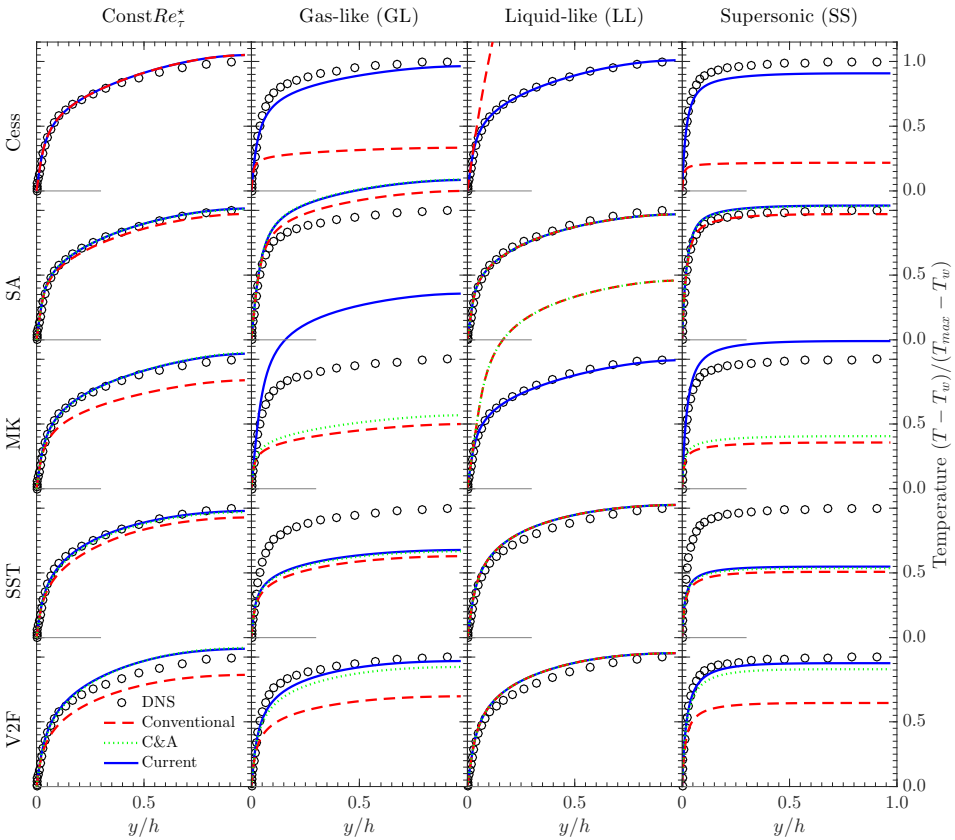
Figure 2.3: Turbulence model and DNS results for the scaled temperature T as a function of y/h for all channel flows.
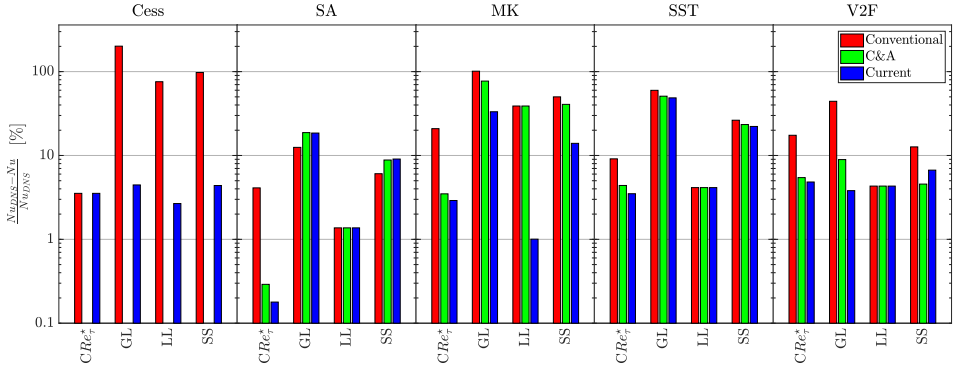
Figure 2.4: Relative error of the Nusselt number calculated by the models with respect to DNS data.

one from the SLS approach, give essentially equivalent results for the cases tested herein, see figures 2.1-2.4.

The reason why the SA model without modifications gives more accurate results than the other models, can be explained as follows. Based on refs.[8,14], it is apparent that the turbulent shear stress profiles collapse for turbulent flows with large variations of density and viscosity, if they are plotted as a function of $y^\star$. Using the stress balance equation, we can then also state that the viscous stresses, $\mu\,du/dy$, must collapse for variable property flows; the universal velocity transformation $u^\star$ has been derived based on this fact. Introducing the Boussinesq approximation to model the Reynolds shear stress, we can further write the stress balance as $(1 + \mu_t/\mu)\mu\,du/dy = (1 - y/h)$, which indicates that also the ratio of μ_t/μ must collapse for flows with variable properties. The SA model makes use of this ratio in $\chi = \check{\nu}/\nu$ (density cancels), which explains why the model performs well for all cases considered herein.

- **MK**: The largest improvements using the compressible / variable property modifications are obtained with the MK model. The effect of modifying the diffusion term and replacing y^+ with $y^\star$ in the damping function can be independently analyzed by inspecting the velocity profiles in figure 2.1. For case $CRe_\tau^\star$, for which $y^+ = y^\star$, the inclusion of the density in the diffusion term clearly improves the model result. On the other hand, the density correction alone does not improve the results for the other cases. For these cases, it is necessary to replace y^+ with $y^\star$ in the damping function, which can be seen by comparing the result from C&A (which still uses y^+ in the damping function) with our approach for the cases GL, LL, and SS.

- **SST**: Contrary to the other models, the SST model results do not improve substantially if used with the compressible / variable property modifications. Except for the case LL, the original model gives unsatisfactory performance with respect

29

to the universal law of the wall, see figure 2.1. The modifications only slightly improve the results for the velocity profiles, as well as, reduce the errors for the Reynolds number and Nusselt number. The only case that shows an improvement is the $CRe_\tau^\star$, see figures 2.1 and 2.3. By further investigating the results, it was seen that the blending function of this model is equal to 1 across the channel height, since the test cases simulated herein have a low Reynolds number. Therefore, the model essentially solves the standard k-ω model[26]. It was also seen by[10], that the density correction of the diffusion term has little effect on the flow field predictions for the k-ω model.

- **V2F**: This model with the compressible / variable property modifications improves the collapse with the DNS data if compared to the conventional form for cases $CRe_\tau^\star$, GL, and SS. These results are consistent with the ones presented in Pecnik and Patel[13], who solved the V2F model in semi-locally-scaled form. In contrast, the present study also solved the energy equation.

2.6   Conclusion

Based on the semi-locally-scaled TKE equation, we have derived a novel methodology to improve eddy viscosity models for predicting wall-bounded turbulent flows with strong variations in thermo-physical properties. The major difference of the new methodology is the formulation of the diffusion term in the turbulence scalar equations. For example, the modified diffusion term of the turbulent kinetic energy equation reads, $\bar{\rho}^{-0.5}\partial_{\tilde{x}}\left[\bar{\rho}^{-0.5}\left(\tilde{\mu}+\tilde{\mu}_t\right)\left(\partial_{\tilde{x}}\bar{\rho}\tilde{k}\right)\right]$ (averaging operators omitted). Common compressibility terms, such as; dilatation diffusion, pressure work, and pressure dilation, are not taken into account in the modified TKE equation. This derived methodology is generic and applicable to several turbulent scalars and it can also be applied to wall-modeled LES. In general, the modified eddy viscosity models result in a better agreement with the DNS data in terms of velocity profiles and heat transfer of fully-developed turbulent channel flows with variable property fluids. Interestingly, the standard Spalart-Allmaras model, originally developed for external flow, gives the most reliable results, with respect to other conventional eddy viscosity models, for the variable property cases investigated herein.

In the following chapter, we apply the compressible / variable property eddy viscosity models to solve a more complex flow configuration: a turbulent pipe flow with a fluid undergoing heat transfer at supercritical pressure.

References

[1] Bradshaw, P., 1977. "Compressible turbulent shear layers". *Annual Review of Fluid Mechanics,* **9**(1), pp. 33–52.

[2] Duan, L., Beekman, I., and Martin, M. P., 2010. "Direct numerical simulation of hypersonic turbulent boundary layers. Part 2. Effect of wall temperature". *Journal of Fluid Mechanics,* **655**(May), pp. 419–445.

[3] Lee, J., Jung, S. Y., Sung, H. J., and Zaki, T. A., 2013. "Effect of wall heating on turbulent boundary layers with temperature-dependent viscosity". pp. 196–225.

[4] Modesti, D., and Pirozzoli, S., 2016. "Reynolds and Mach number effects in compressible turbulent channel flow". *International Journal of Heat and Fluid Flow,* **59**, pp. 33–49.

[5] Huang, P. G., Bradshaw, P., and Coakely, T. J., 1994. "Turbulence models for compressible boundary layers". *AIAA Journal,* **32**(4), pp. 735–740.

[6] Sarkar, S., Erlebacher, G., Hussaini, M., and Kreiss, H., 1991. "The analysis and modelling of dilatational terms in compressible turbulence". *Journal of Fluid Mechanics,* **227**, pp. 473–493.

[7] Zeman, O., 1993. "A new model for super/hypersonic turbulent boundary layers". In 31st Aerospace Sciences Meeting, p. 897.

[8] Huang, P. G., Coleman, G. N., Bradshaw, P., 1995. "Compressible Turbulent channel flows, DNS results and modelling". *JFM*(1995), pp. 185–218.

[9] Van Driest, E., 1951. "Journal of the Aeronautical Sciences". *Journal Of The Aeronautical Sciences,* **40**(6), pp. 145–160.

[10] Catris, S., and Aupoix, B., 2000. "Density corrections for turbulence models". *Aerospace Science and Technology,* **4**(1), pp. 1–11.

[11] Roy, C., Blottner, F., 2007. "Review and assessment of turbulence models for hypersonic flows". pp. 469–530.

[12] Smits, A. J., and Dussauge, J.-P., 2006. *Turbulent shear layers in supersonic flow.* Springer Science & Business Media.

[13] Pecnik, R., and Patel, A., 2017. "Scaling and modelling of turbulence in variable property channel flows". *Journal of Fluid Mechanics,* **823**.

[14] Patel, A., Boersma, B. J., and Pecnik, R., 2016. "The influence of near-wall density and viscosity gradients on turbulence in channel flows". *Journal of Fluid Mechanics,* **809**, pp. 793–820.

[15] Cess, R., 1958. "A survey of the literature on heat transfer in turbulent tube flow". *Res. Rep*, pp. 8–0529.

[16] Spalart, P. R., Allmaras, S. R., et al., 1994. "A one equation turbulence model for aerodynamic flows". *RECHERCHE AEROSPATIALE-FRENCH EDITION-*, pp. 5–5.

[17] Myong, H.K. and Kasagi, N., 1990. "A New Approach to the Improvement of k-e turbulence model for wall-bounded shear flows". *JSME,* **33**(2).

[18] Menter, F. R., 1993. "Zonal Two Equation k-w, Turbulence Models for Aerodynamic Flows". *AIAA paper*, p. 2906.

[19] Durbin, P. A., 1995. "Separated Flow Computations with the k-e-v2 Model". *AIAA Journal,* **33**(4), pp. 659–664.

[20] Trettel, A., and Larsson, J., 2016. "Mean velocity scaling for compressible wall turbulence with heat transfer". *Physics of Fluids,* **28**(2), p. 026102.

[21] Pecnik, R., Otero Rodriguez, G., and Patel, A., 2018. RANS-models for fully developed turbulent channel flow with variable properties solved in Matlab. `https:// github.com/Fluid-Dynamics-Of-Energy-Systems-Team/RANS_Channel`.

[22] Bradshaw, P., and Perot, J. B., 1993. "A note on turbulent energy dissipation in the viscous wall region". *Physics of Fluids A: Fluid Dynamics (1989-1993),* **5**(12), pp. 3305–3306.

[23] Patel, A., Pecnik, R., Peeters, J., Hickel, S., and Moghadam, M., 2016. "Turbulence modulation by variable density and viscosity". In Proceedings of the Summer Program, p. 213.

[24] Patel, A., Boersma, B. J., and Pecnik, R., 2017. "Scalar statistics in variable property turbulent channel flows". *Physical Review Fluids,* **2**(8), p. 084604.

[25] Boutrouche, V., Franquet, E., Serra, S., and Manceau, R., 2018. "Influence of the turbulence model for channel flows with strong transverse temperature gradients". *International Journal of Heat and Fluid Flow,* **70**, pp. 79–103.

[26] Wilcox, D. C., et al., 1998. *Turbulence modeling for CFD*, Vol. 2. DCW industries La Canada, CA.

3

Numerical modelling of heat transfer for supercritical CO$_2$

It is challenging to properly model turbulent heat transfer in a supercritical fluid because of (1) the sharp gradient of thermo-physical properties in the supercritical region, and (2) the heat transfer deterioration. In order to bypass the first issue, we derived in the previous chapter consistent modification for eddy viscosity models, to make them reliable for wall-bounded turbulent flows with variable properties like density and viscosity. To investigate the second problem, we introduced different methods to model the turbulent heat flux, i.e., changing the constant value of the turbulent Prandtl number and using two different algebraic equations. The purpose of this study is to investigate whether the density modification for eddy viscosity models can lead to an improvement in modeling the heat transfer in supercritical fluids when using the turbulent Prandtl number to estimate the turbulent heat flux. The novelty of this work — besides using density-corrected eddy viscosity models — is that we analyse the influence of the turbulent heat flux model on several eddy viscosity models. We gather data from several sources (experimental and direct numerical simulations) to test the accuracy of the Reynolds-Averaged Navier-Stokes (RANS) turbulence model in predicting the heat transfer to supercritical fluids with and without heat transfer deterioration. The results show an improvement of the models with density modification for the force convection test cases. But, when buoyancy starts to influence the flow field and heat transfer deterioration is present, the RANS models with and without density-corrections are not reliable. The value of the turbulent Prandtl number modifies the wall temperature prediction considerably, but the calculation accuracy is case (eddy viscosity model and flow conditions) dependent. To better estimate heat transfer deterioration in an upward flow of a turbulent supercritical fluid flow, further research is needed on the models for turbulent heat flux and buoyancy production of turbulent mixing.

3.1   Introduction

Supercritical fluids — fluids at pressures and temperatures above their liquid-vapour critical point — are being considered for energy conversion systems, in particular in the field of energy generation[1]. For example, the generation IV (GEN-IV) nuclear reactors are supposed to use supercritical fluids as coolants and as working fluids in the power cycle[2,3]. Moreover, renewable energy technologies, such as solar energy and waste heat recovery systems, can benefit from supercritical fluids[4,5]. Other industrial processes with supercritical fluids include pharmaceutical processes or enhanced oil recovery[6]. All these applications require a comprehensive understanding of fluid dynamics and heat transfer of supercritical fluids to correctly model the systems and design their components.

Supercritical fluids exhibit strong deviations from ideal thermodynamic behaviour and do not have a recognizable phase change; the phase transition from a liquid-like to a gas-like occurs in a continuous manner. However, small changes of temperature in the vicinity of the critical point lead to strong gradients of the thermo-physical properties. For example, figure 3.1 illustrates the variation of several thermo-physical properties (density, dynamic viscosity, thermal conductivity, and specific heat capacity) as a function of temperature and pressures above the critical point for carbon dioxide ($\tilde{p}_{cr} = 7.39$ MPa).
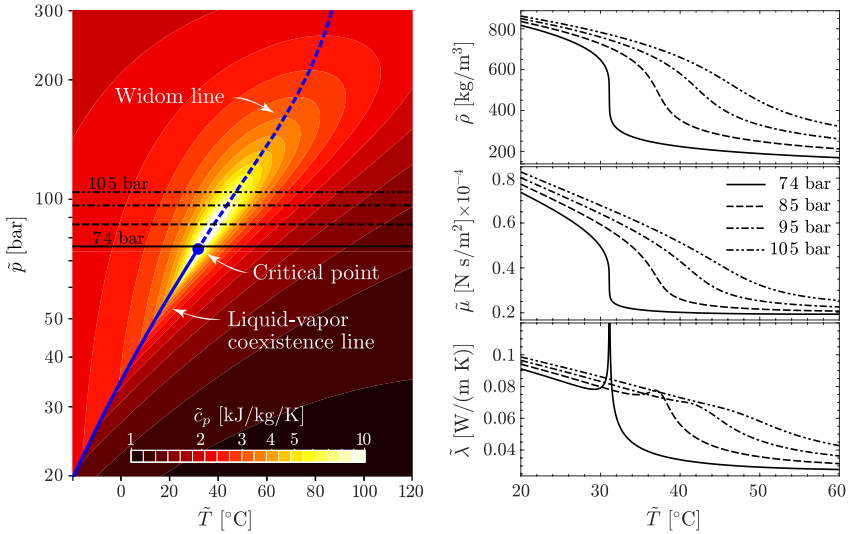
Figure 3.1: Thermo-physical properties variations as a function of the temperature ($\tilde{T}$) at constant pressure ($\tilde{p}$) around the supercritical region.

These abrupt variations of thermo-physical properties result in flow physics and a heat transfer, which are different from flows with ideal gases [7].

The sudden change of thermo-physical properties in heated supercritical fluids in the proximity of the pseudo-critical temperature[1] causes strong non-ideal fluid behaviour and peculiar effects in turbulent heat transfer [7,8]. Flow acceleration due to the thermal expansion of the heated fluid and buoyant forces enhance the variation of density in axial and radial direction, respectively [9]. The varying thermo-physical properties modulate turbulence through several routes, and the additional effect of buoyancy and flow acceleration further complicates energy transfer. Consequently, these effects can cause a localized increase or decrease of wall temperature, which for heated flows is called heat transfer deterioration (HTD) or enhancement, respectively. Namely, a lower wall temperature is associated with increased turbulent mixing and transport of hot fluid away from a heated wall. The conditions at which such an enhancement and degradation of heat transfer may occur are: (1) the wall temperature must be above, while the bulk temperature must be below the pseudo-critical temperature ($\tilde{T}_{wall} > \tilde{T}_{pc} > \tilde{T}_b$), (2) the wall heat flux must be above a particular value, depending on the flow rate and pressure, and (3) strong effects of buoyancy and flow acceleration due to thermal expansion must exist. The abrupt reduction of density, when the pseudo-critical temperature is located in the thermal boundary layer between the heated surface and the bulk fluid, results in a sudden deterioration of the heat transfer coefficient.

---

[1]The pseudo-critical temperature ($\tilde{T}_{pc}$) is the temperature at a constant pressure where the specific heat capacity ($\tilde{c}_p$) has its maximum. The Widom line in figure 3.1 consists of several pseudo-critical points.

Several factors affect the magnitude of the heat transfer enhancement and deterioration, such as the ratio of heat and mass flux [7], the orientation of the flow concerning the gravitational field (vertical upward, vertical downward or, horizontal) [10], the geometry of the flow device [11], and among others. Studies have shown that if the mass flux is large — the flow has a large velocity — the heat transfer may be enhanced due to the sharp gradient of specific heat at the pseudo-critical point [10,12]. For cases of low mass flux, buoyancy always enhances turbulence in vertical downward heated flows, which leads to high values of the heat transfer coefficient [13]. In upwards flows, the buoyancy force causes additional flow acceleration in the near-wall region; the density, and therefore gravity force, is lower close to the heated wall, increasing the velocity in this region. To satisfy mass conservation, this local flow acceleration close to the wall is compensated by a velocity reduction in the core. If the buoyancy effect is large enough, the velocity reduction is the core is such that an M-shape velocity profile can occur [14,15].

Direct numerical simulations (DNS) have been performed to analyze the heat transfer to supercritical fluids in turbulent pipe flows [13,16]. But, these highly accurate simulations are limited to simple geometries and low Reynolds numbers due to the high computational cost needed. To overcome this computational cost, it is possible to solve the RANS equations coupled with eddy viscosity models. However, RANS models rely on limited data, and their development is hampered by the lack of knowledge on supercritical fluid turbulence. Moreover, these models are not fully validated for flows with buoyancy and strong flow acceleration [9]. Hence, there are still several major challenges for modelling turbulent heat transfer to supercritical fluids. In terms of RANS turbulence modelling, the unclosed terms — which appear in the Favre-Reynolds averaged Navier-Stokes equation — are challenging to estimate when solving for supercritical fluids with buoyancy effects. These main unclosed terms are:

1. **Turbulent stresses:** if the Boussinesq assumption for RANS models is used to obtain the turbulent stress tensor, an eddy viscosity turbulence model must account for variable inertia effects on turbulence. Since turbulence models have been developed for incompressible flows, they do not consider variable property effects on turbulence. To overcome this limitation, we recently derived — see Chapter 2 — consistent turbulence model corrections, to make them reliable for wall-bounded turbulent flows with strong gradients of the thermo-physical properties [17].

2. **Turbulent heat flux:** the model for the turbulent heat flux must in addition account for variations of the molecular Prandtl number across the boundary layer. Commonly, the turbulent heat flux is modelled using the analogy between turbulent momentum and heat flux through the turbulent Prandtl number (Pr_t). Normally, Pr_t is modelled as a constant, but several authors have developed algebraic equations to estimate the turbulent Prandtl number for ideal gas flows [18,19].

3. **Buoyancy production of turbulent kinetic energy:** in flows where buoyancy effects are considerable, the turbulence model must account for the production of turbulence kinetic energy due to buoyancy. The buoyancy production term (and models) in the turbulent kinetic energy (TKE) equation was initially derived for

atmospheric and oceanic applications, where it is assumed that the density fluctuations only affect the gravitational force. Additional insight from DNS is required to develop accurate models to account for buoyancy effects in compressible flows.

Already many efforts have been conducted to improve the numerical prediction of supercritical fluids using RANS modelling. He *et al.*[20] evaluate the performance of several eddy viscosity models predicting mixed convection heat transfer to a fluid at supercritical pressure and attributed the lack of accuracy of the simulations to the inability of correctly reproducing the turbulent heat flux in cases with strong buoyancy. Yoo in his review paper[9] reached the same conclusion. Two studies that aimed to improve the approximation of the turbulent heat flux are from Tang *et al.*[21] and Grunloh[22]. The former[21] derived a piecewise function of the turbulent Prandtl number depending on intervals of the ratio of turbulent to molecular viscosity (μ_t/μ). Grunloh[22] recalibrated the closure coefficients of the k-ω SST model[23] and of an algebraic flux model — to estimate the buoyancy production — to better match experimental data of vertical flow in a turbulent heat pipe flow of supercritical CO_2. However, these investigations mainly adjusted turbulence models constants[21,22] to match a certain test case.

In this chapter, we solve the Reynolds/Favre averaged Navier-Stokes equations to model heated turbulent pipe flows with CO_2 at supercritical pressure. To quantify the accuracy of the results, we use data from several sources, DNS and experiments, with and without heat transfer deterioration. The DNS data grant us more detail on turbulent flow statistics; while the experimental data is available for larger Reynolds numbers. Three eddy viscosity models, namely the Myong-Kasagi (MK)[24], Menter's k-ω SST[23], and Spallart-Allmaras (SA)[25] models are used to model the Reynolds stresses. To account for large property variations, we use these models with our recently developed methodology, which properly allows to model variable inertia effects in turbulence[17]. To investigate the accuracy of modelling the turbulent heat flux we use the Reynolds analogy and two different algebraic models for the turbulent Prandtl number[18,19]. A novelty of this work, contrary to other studies[21,26,27], is that we test the influence of the turbulent Prandtl number models in conjunction with several eddy viscosity models which include the modification derived in Chapter 2.

3.2   Test cases

We have selected several test cases to investigate turbulent heat transfer to supercritical fluids in a pipe. We have assembled data from two sources: DNS and experiments, as described in table 3.1. We specify the DNS data cases as DNS1, DNS2, and DNS3, while the two experimental data as EXP1 and EXP2. We selected two and three heat fluxes from EXP1 and EXP2, respectively, distinguished by the wall heat flux: namely Low Heat Flux (LHF), Mid Heat Flux (MHF), and High Heat Flux (HHF). We will use the wall temperature to compare the simulations with the measurements/DNS; figure 3.2 displays the wall temperature from all data sources.

Table 3.1: Test cases investigated in the present study. The bulk Reynolds number, wall Prandtl number, the bulk Froude number and the dimensionaless wall heat flux are defined as $Re_{b,0} = \tilde{u}_b \tilde{\rho}_0 \tilde{D}/\tilde{\mu}_0$, $Pr_{w,0} = \tilde{c}_{p\,0}\tilde{\mu}_0/\tilde{\lambda}_0$, $Fr_{b,0} = \tilde{u}_b/\sqrt{\tilde{g}_z \tilde{D}}$, and $q" = \tilde{q}''_w \tilde{D}/(\tilde{\lambda}_0 \tilde{T}_0)$, respectively, where $\tilde{D}$ is the characteristic length (the pipe diameter), $\tilde{\rho}$ is the density, $\tilde{\mu}$ is the dynamic viscosity, $\tilde{\lambda}$ is the thermal conductivity, $\tilde{c}_p$ is the specific heat capacity, and $\tilde{q}''_w$ is the wall heat flux. Across the whole disseration, the tilde hat ($\tilde{\ }$) denotes dimensional quantities. Moreover, the subscript b and 0 represents bulk quantities and a parameter defined at the inlet of the heated pipe, respectively. $Fr_{b,0}$ quantifies the buoyancy effects with $\tilde{g}_z$ as the gravitational acceleration.

Cases	$\tilde{p}$ [bar]	$\tilde{T}_0$ [°C]	$Re_{b,0}$	$Pr_{w,0}$	$1/Fr_{b,0}^2$	$q"$
DNS1 [13]	8	28	5,300	3.19	0.00	2.4
DNS2 [13]	8	28	5,300	3.19	-0.05	2.4
DNS3 [13]	8	28	5,300	3.19	-0.37	2.4
EXP1 LHF [28]	8.12	5	25,000	2.14	-0.34	5.8
EXP1 HHF [28]	8.12	5	25,000	2.14	-0.34	9.9
EXP2 LHF [29]	8	15	29,000	2.3	-0.31	4.4
EXP2 MHF [29]	8	15	29,000	2.3	-0.31	5.1
EXP2 HHF [29]	8	15	29,000	2.3	-0.31	6.6

3.2.1 DNS data

Direct numerical simulations solve all scales of fluid motion without a turbulence model. As such, DNS data provides an ideal situation to validate (or invalidate) assumptions that have been made in turbulence models. We have chosen DNS data of supercritical CO_2 pipe flow from Nemati *et al.* [13]. Three different conditions have been selected, as depicted in table 3.1: (1) DNS1 is a horizontal flow with no buoyancy effects, (2) DNS2 is a vertical upward flow with low buoyancy effects, and (3) DNS3 is a vertical upward flow with high buoyancy effects. DNS2 and DNS3 consist of mixed convection (pressure and buoyant forces interact), while DNS1 is a purely forced convection pipe flow. Figure 3.2(b) illustrates the averaged wall temperature along the pipe length (non-dimensionalized by the pipe diameter), for the selected cases. DNS2 and DNS3, the upward flows with buoyancy, are affected by HTD. DNS1 and DNS3 both were simulated for a long pipe ($\tilde{z}/D = 60$) if compared to DNS2.

3.2.2 Experimental data

In literature, several experimental data are available for heat transfer to supercritical fluids. For the present study, two experimental data sources [28,29] are chosen to study the heat transfer of flows near the supercritical point. These experiments consist of CO_2 upward flowing in an uniformly heated pipes at various conditions, which are summarized in table 3.1.

The EXP1 experiments, taken from Bae *et al.* [28], are shown in figure 3.2(a). It

(a) Data from EXP1 [28] (b) Data from DNS and EXP2 [29]
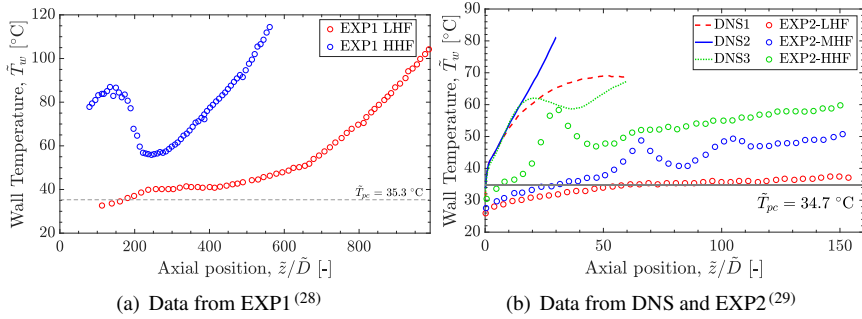
Figure 3.2: Measured wall temperature for experiments and averaged wall temperature for the DNS along the pipe for all data sets of a heated supercritical CO_2 flow. The experimental sources do not include the uncertainties of the measurements.

is important to mention that the measurement results in Bae *et al.* [28] have been reported as a function of bulk enthalpy. For the sake of comparing the cases among each other, we converted the bulk enthalpy to pipe length using the following relation $h_b = 4\,q"/(Re_{\tau,0}\,Pr_{w,0})\,\tilde{z}/\tilde{D}$ [16]. The heat transfer of the lowest heat flux (EXP1 LHF, $q" = 5.8$) is not affected by deterioration, recognized by the monotonic increase of wall temperature. For the experiment with the highest heat flux (EXP1 HHF, $q" = 9.9$), the peak of wall temperature at the beginning of the measurements indicates HTD. These experiments investigate the heat transfer at bulk temperatures from well below to well above the pseudo-critical temperature. For these experiments, the measurements are collected half a meter after the wall heating starts. Consequently, no data is available at the inflow.

The experiments from EXP2, reported by Kim *et al.* [29], show a detailed quantification of the heat transfer deterioration. Figure 3.2(b) depicts the wall temperature along the pipe stream-wise distance. Heat transfer deterioration can be identified for EXP2 MHF and HHF ($q" = 5.1$ and $q" = 6.6$) when the wall temperature crosses the pseudo-critical temperature. The wall temperature shows one or two steep peaks, characteristic of heat transfer deterioration. Compared to the rest of the cases herein, EXP2 has the largest bulk Reynolds number at the inflow ($Re_{b,0} = 29,000$).

3.3 Governing equations

The compressible Navier-Stokes (NS) equations consist of the conservation equations of density, momentum, and total energy. An equation of state (EoS) is used to define the relationship between density, pressure, temperature, and internal energy to close the system of equations. For this, we use the multi-parameter equation of state of Kunz and Wagner [30] to calculate the thermodynamic state of CO_2. Furthermore, we consider the low-Mach number approximation of the NS equation to circumvent the severe time step restriction of the compressible NS equations due to the low speed of sound. By ignoring

the compressible effects, we are capable of determining the whole thermodynamic state independent from the hydrodynamic pressure fluctuations.

The Reynolds/Favre-averaged form of the Navier-Stokes equations, written in cylindrical coordinates, are solved. The governing equations for momentum in stream-wise and radial direction, and energy are expressed in their non-dimensional form (scaled by wall units), assuming a two-dimensional steady-state axis-symmetric flow, as:

$$\frac{\partial \langle\rho\rangle \{u_z\}^2}{\partial z} + \frac{1}{r}\frac{\partial \, r \langle\rho\rangle \{u_z\}\{u_r\}}{\partial r} = -\frac{\partial \langle p\rangle}{\partial z} + \frac{\langle\rho\rangle}{Fr_{\tau,0}{}^2} + \frac{\partial}{\partial z}\left[\frac{\langle\mu\rangle}{Re_{\tau,0}}\left(2\frac{\partial \{u_z\}}{\partial z} - \frac{2}{3}\nabla\cdot\{u\}\right)\right]$$
$$+ \frac{1}{r}\frac{\partial}{\partial r}\left[r\frac{\langle\mu\rangle}{Re_{\tau,0}}\left(\frac{\partial \{u_z\}}{\partial r} + \frac{\partial \{u_r\}}{\partial z}\right)\right] - \left[\frac{1}{r}\frac{\partial \, r\langle\rho u_z'' u_r''\rangle}{\partial r} + \frac{\partial \langle\rho u_z'' u_z''\rangle}{\partial z}\right], \quad (3.1)$$

$$\frac{\partial \langle\rho\rangle \{u_z\}\{u_r\}}{\partial z} + \frac{1}{r}\frac{\partial \, r \langle\rho\rangle \{u_r\}^2}{\partial r} = -\frac{\partial \langle p\rangle}{\partial r} + \frac{1}{r}\frac{\partial}{\partial r}\left[r\frac{\langle\mu\rangle}{Re_{\tau,0}}\left(2\frac{\partial \{u_r\}}{\partial r} - \frac{2}{3}\nabla\cdot\{\mathbf{u}\}\right)\right]$$
$$+ \frac{\partial}{\partial z}\left[\frac{\langle\mu\rangle}{Re_{\tau,0}}\left(\frac{\partial \{u_z\}}{\partial r} + \frac{\partial \{u_r\}}{\partial z}\right)\right] - \frac{1}{r}\frac{\langle\mu\rangle}{Re_{\tau,0}}\left(\frac{\{u_r\}}{r} - \frac{1}{3}\nabla\cdot\{\mathbf{u}\}\right)$$
$$- \left[\frac{1}{r}\frac{\partial \, r\langle\rho u_r'' u_r''\rangle}{\partial r} + \frac{\partial \langle\rho u_r'' u_z''\rangle}{\partial z}\right], \quad (3.2)$$

$$\frac{\partial \langle\rho\rangle \{H\}\{u_z\}}{\partial z} + \frac{1}{r}\frac{\partial \, r \langle\rho\rangle \{H\}\{u_r\}}{\partial r} = \frac{1}{r}\left[\frac{\partial}{\partial r}r\frac{\langle\lambda\rangle/c_p}{Re_{\tau,0}Pr_{w,0}}\frac{\partial \{H\}}{\partial r}\right]$$
$$+ \left[\frac{\partial}{\partial z}\frac{\langle\lambda\rangle/c_p}{Re_{\tau,0}Pr_{w,0}}\frac{\partial \{H\}}{\partial z}\right] - \left[\frac{1}{r}\frac{\partial \, r\langle\rho u_r'' H''\rangle}{\partial r} + \frac{\partial \langle\rho u_z'' H''\rangle}{\partial z}\right], \quad (3.3)$$

where u_z is the stream-wise velocity component, u_r is the radial velocity component, H is the specific enthalpy, and $\nabla\cdot\{\mathbf{u}\}$ is the divergence of the velocity field in cylindrical coordinates. In these equations, we use the Reynolds decomposition for most of the quantities, defined as: $\phi = \langle\phi\rangle + \phi'$ with $\langle\phi'\rangle = 0$, and the Favre decomposition for the velocity and enthalpy, defined as: $\phi = \{\phi\} + \phi''$ with $\langle\rho\rangle\{\phi''\} = 0$, $\langle\rho\rangle\{\phi\} = \langle\rho\phi\rangle$, and $\langle\phi''\rangle \neq 0$. The non-dimensional parameters in the equations above are the friction Reynolds number $Re_{\tau,0} = u_{\tau,0}\tilde{\rho}_{w,0}\tilde{D}/\tilde{\mu}_{w,0}$, the Prandtl number $Pr_{w,0} = \tilde{c}_{p,w,0}\tilde{\mu}_{w,0}/\tilde{\lambda}_{w,0}$, and the Froude number defined with the friction velocity $Fr_{\tau,0} = u_{\tau,0}/\sqrt{\tilde{g}_z\tilde{D}}$. All of these non-dimensional parameters are defined at the inlet of the heated pipe, which in the present chapter is denoted by the subscript 0.

3.4 Turbulence modelling for heated flows with buoyancy

The Reynolds shear stress and turbulent heat flux are modelled using the Boussinesq approximation[31],

$$-\left\langle \rho u_i'' u_j'' \right\rangle \approx \mu_t \left(\frac{\partial \{u_i\}}{\partial x_j} + \frac{\partial \{u_j\}}{\partial x_i} - \frac{2}{3} \delta_{ij} \nabla \cdot \{u\} \right) - \frac{2}{3} \left\langle \rho \right\rangle k \delta_{ij}, \tag{3.4}$$

and the gradient diffusion hypothesis,

$$-\left\langle \rho u_j'' H'' \right\rangle \approx \left\langle \rho \right\rangle \alpha_t \frac{\partial \{H\}}{\partial x_j}, \tag{3.5}$$

respectively. Using these approximations, the number of unknowns has been reduced from 9 (6 for the Reynolds stress tensor plus 3 for the turbulent heat flux) to 3 unknowns. Namely, the eddy viscosity (μ_t), the turbulent kinetic energy k, and the eddy diffusivity (α_t). In the present study, we use the turbulent Prandtl number to estimate the turbulent heat flux as

$$-\left\langle \rho u_j'' H'' \right\rangle \approx \frac{\mu_t}{Pr_t} \frac{\partial \{H\}}{\partial x_j}. \tag{3.6}$$

In this section, we discuss how to model μ_t and Pr_t. Moreover, at the end of this section, we briefly discuss the approximation for the buoyancy production of turbulence (B_k).

3.4.1 Reynolds stress

We have selected three eddy viscosity models, namely the Spalart-Allmaras model[25], the k-ε model of Myong and Kasagi (MK)[24], and Menter's shear stress transport (SST) model[23]. However, these models were developed for constant thermo-physical property flows (incompressible); to overcome this issue, we recently developed a methodology to sensitize them for significant variations of density/viscosity. The modifications are general, unlike extending model constants, and can be applied to arbitrary eddy viscosity models. These modifications are based on the semi-local scaling methodology developed in Pecnik and Patel[32], which leads to the conclusion that the diffusion of turbulent kinetic energy acts upon energy per unit volume (ρk), rather than unit mass (k). We report the derivation of the density modification in Chapter 2 and in our published paper[17]. For the sake of completeness, in Appendix A.1, we give a brief description of the eddy viscosity models. Across this chapter, we refer to the eddy viscosity models with the density modifications as SA$-\rho$, MK$-\rho$, and SST$-\rho$.

3.4.2 Turbulent heat flux

The turbulent Prandtl number is defined as the ratio between the turbulent momentum and turbulent heat transfer diffusivity, and it can be written as

$$Pr_t = \frac{\left\langle \rho u_z'' u_r'' \right\rangle}{\left\langle \rho T'' u_r'' \right\rangle} \frac{\partial \{T\}/\partial r}{\partial \{u\}/\partial r}. \tag{3.7}$$

For this study, we use three approximations of the turbulent Prandtl number, discussed below. More equations to estimate Pr_t have been developed and tested by other authors, see for example [21,27,33].

- The Reynolds analogy is the simplest model for the turbulent heat flux, in which the turbulent Prandtl number is assumed constant and near to unity. It assumes a strong analogy between momentum and scalar transport; the thermal eddy diffusivity (α_t) is approximately equal (or almost equal) to the momentum eddy diffusivity ($\nu_t = \mu_t/\langle\rho\rangle$). In general, the turbulent Prandtl number has been considered constant as $Pr_t = 0.9$. However, it has also been approximated as 1.0, see Ref. [34]. Although the Reynolds analogy holds for many boundary layers flows, this assumption may not hold for flows with a strong variation of the thermo-physical properties [9,20].

- Kays and Crawford in 1993 [18] proposed an approximation of the turbulent Prandtl number based on numerous experimental data from a zero pressure gradient flat-plate turbulent boundary layer of air. The algebraic expression — similar to a mixing length model for the eddy viscosity — is given as:

$$Pr_t = \frac{1}{C_1 + C_2\mu_\gamma - C_3\mu_\gamma^2\left(1 - exp(-C_4/\mu_\gamma)\right)}, \tag{3.8}$$

where $\mu_\gamma = \mu_t/\langle\mu\rangle$ and the model constants are defined as $C_1 = 0.5882$, $C_2 = 0.228$, $C_3 = 0.0441$ and $C_4 = 5.165$. Equation (3.8) provides large value of Pr_t near the wall and approaches to 0.85 when the ratio of turbulent to molecular viscosity (μ_γ) increases [34].

- Irrenfried and Steiner [19] modified the purely experimentally-based model of the turbulent Prandtl number from Kays *et al.* [18] to account for variations on the molecular Prandtl number in the near-wall region. The modified formulation introduces an additional model parameter $\gamma_{IS} = 1/\left[Pr_{t,b} + 0.1Pr^{0.83}\right]$) which depends on the molecular Prandtl number. Irrenfriend and Steiner formulation accurately reproduces DNS solutions of flows with large molecular Prandtl numbers in the near-wall region. This correlation of the turbulent Prandtl number reads

$$Pr_t = \left[\gamma_{IS} + C\,Pe_t\sqrt{2\left(\frac{1}{Pr_{t,b}} - \gamma_{IS}\right)} - (C\,Pe_t)^2\left[1 - exp\left(-\frac{1}{C\,Pe_t}\sqrt{2\left(\frac{1}{Pr_{t,b}} - \gamma_{IS}\right)}\right)\right]\right]^{-1}, \tag{3.9}$$

where $C = 3.0$, and $Pe_t = (\mu_t/\langle\mu\rangle)\,Pr$ is the turbulent Peclet number. In this study, we consider the bulk turbulent Prandtl number as $Pr_{t,b} = 1.0$.

3.4.3 Buoyancy production

Because buoyancy can either weaken or amplify turbulence, depending on stably or unstably stratified configurations, eddy viscosity models must consider an additional source

of turbulent kinetic energy production, namely buoyant TKE production. Compared to the standard production of TKE (P_k), this buoyant production (B_k) is usually one order of magnitude lower[2]; however, in regions of heat transfer enhancement/deterioration $B_k \sim P_k$ [13,16].

The study of turbulent flows with buoyant force is of paramount importance for atmospheric and oceanographic applications, where such force is not negligible[35]. It was in this field were several models of TKE buoyant production were developed, e.g., Launder[36]. To derive the buoyancy production of TKE for such flows, first, the Boussinesq approximation for buoyant flows — density fluctuations only affect the gravitational force — is applied to the Navier-Stokes equations. The resulting momentum equation is used to derive the TKE equation by multiplying it by the velocity fluctuation (u_i') and later taking the Reynolds-averaged of the whole equation. The transport equation for ρk from this derivation has a term depending on the gravitational force (the buoyancy production) as

$$B_k = \frac{1}{Fr_0{}^2} \left\langle \rho' u_z' \right\rangle. \tag{3.10}$$

Note that the other gravitational term that depends on $\langle \rho \rangle \left\langle u_z' \right\rangle$ drops out due to Reynolds-averaging. We include B_k into the turbulent model by adding it to the production of turbulent kinetic energy (P_k) in the transport equations of k, ε, and ω in Appendix A.1.

In our particular case, we would need to derive the TKE equation from the fully compressible Navier-Stokes equations, which does not considers the Boussinesq approximation for buoyant flows. Wilcox[31] gives a detailed description of this procedure without body force. The resulting transport equation of TKE consists of the material derivative of TKE at the left hand side while at the right hand side the terms that appear are the production, dissipation, transport of TKE plus two extra terms: pressure work $\left(- \left\langle u_i'' \right\rangle \partial \langle p \rangle / \partial x_i \right)$ and pressure dilation $\left(\left\langle p' \partial u_i'' / \partial x_i \right\rangle \right)$; the body force term due to gravitational force times the fluctuating velocity drops due to Favre-averaging $\left(\left\langle \rho u_z'' \right\rangle / Fr_0^2 = 0 \right)$. Therefore, to have a buoyant production term, the Reynolds-averaged pressure gradient from the pressure work needs to be substituted with the equation of conservation of momentum, equation (3.1); this procedure is describe in more detail by Bae $et.al$[16]. Then, the pressure work term — in stream-wise direction — results in

$$
\begin{aligned}
- \left\langle u_z'' \right\rangle \frac{\partial \langle p \rangle}{\partial z} &= - \left\langle u_z'' \right\rangle \left(\frac{\partial \langle \rho \rangle \{u_z\}^2}{\partial z} + \frac{1}{r} \frac{\partial r \langle \rho \rangle \{u_z\}\{u_r\}}{\partial r} + \cdots - \frac{\langle \rho \rangle}{Fr_0^2} \right) \\
&= \cdots + \frac{\langle \rho \rangle}{Fr_0^2} \left\langle u_z'' \right\rangle \\
&= \cdots - \frac{1}{Fr_0^2} \left\langle \rho' u_z' \right\rangle,
\end{aligned}
\tag{3.11}
$$

which now includes the buoyant production of TKE. In the final step of equation(3.11), we used the fact that $\left\langle u_z'' \right\rangle = - \left\langle \rho' u_z' \right\rangle / \langle \rho \rangle$. To the knowledge of the authors, this deriva-

---

[2]There are test cases with only buoyancy production, e.g., Rayleigh-Bernard convection.

tion of the buoyant production term for compressible flows is not mentioned by any other RANS study in the field, see [20,27,37,38].

To model B_k, we first need to relate the density fluctuation with the temperature fluctuations ($d\rho \approx \rho'$, $dT \approx T'$) as

$$\rho' \approx d\rho = \left.\frac{\partial\rho}{\partial T}\right|_p dT + \left.\frac{\partial\rho}{\partial p}\right|_T dp \overset{0}{=} \left.\frac{\partial\rho}{\partial T}\right|_p dT = -\beta_T \langle\rho\rangle dT \qquad (3.12)$$
$$\rho' \approx -\beta_T \langle\rho\rangle T',$$

resulting in

$$B_k = -\frac{1}{Fr_0{}^2}\beta_T \left\langle \rho u_z' T' \right\rangle, \qquad (3.13)$$

where the thermal expansion coefficient is defined as $\beta_T = -1/\langle\rho\rangle\,(\partial\rho/\partial T)$. It is important to note that the thermal expansion, as other thermo-physical properties, undergoes a sharp gradient in the supercritical region. The closure of the $\left\langle \rho u_z' T' \right\rangle$ term is generally accomplished using the gradient-diffusion hypothesis models. In the present study, we use the Generalized Gradient Diffusion Hypothesis (GGDH), as applied in [39]. The GGDH is a more sophisticated approach than the simple gradient diffusion hypothesis as it accounts for the anisotropic turbulent diffusivity using the Reynolds shear stress as:

$$\left\langle \rho u_z' T' \right\rangle = -C_t T_\tau \left(\left\langle \rho u_z'' u_r'' \right\rangle \frac{\partial \{T\}}{\partial r} + \left\langle \rho u_z'' u_z'' \right\rangle \frac{\partial \{T\}}{\partial z} \right), \qquad (3.14)$$

where C_t is a positive constant equal to 0.333. This model requires a turbulent time scale T_τ, which for a k-ϵ and a k-ω model is given by $T_\tau = k/\varepsilon$ and $T_\tau = 1/\omega$, respectively. It is possible to estimate a turbulent time scale for the SA model; however, deriving the buoyancy production term for this particular model is not straightforward. Therefore, we do not consider buoyancy production for the SA model. Recently, Zhang *et al.* [37] and Grunloh [22] used algebraic flux models (AFM) to approximate B_k. However, to apply AFM, two extra transport equations need to be solved — increasing the computational cost — for the temperature fluctuation and its dissipation to model the eddy diffusivity (α_t).

Figure 3.3 depicts the inter-relation between the different closure models. The eddy viscosity (μ_t) is crucial in the overall procedure because it determines all three non-linear terms. The eddy viscosity determines (1) the Reynolds stresses using the Boussinesq approximation for RANS modeling, (2) the turbulent heat flux (by applying the gradient diffusion hypothesis) and the turbulent Prandtl number (via the algebraic models), and (3) the buoyancy production through the Reynolds stresses. The primary purpose of this chapter is to investigate whether the density modification for eddy viscosity models can lead to an improvement in modeling the heat transfer to supercritical fluids even if we apply simplified models for the turbulent heat flux and buoyancy production.
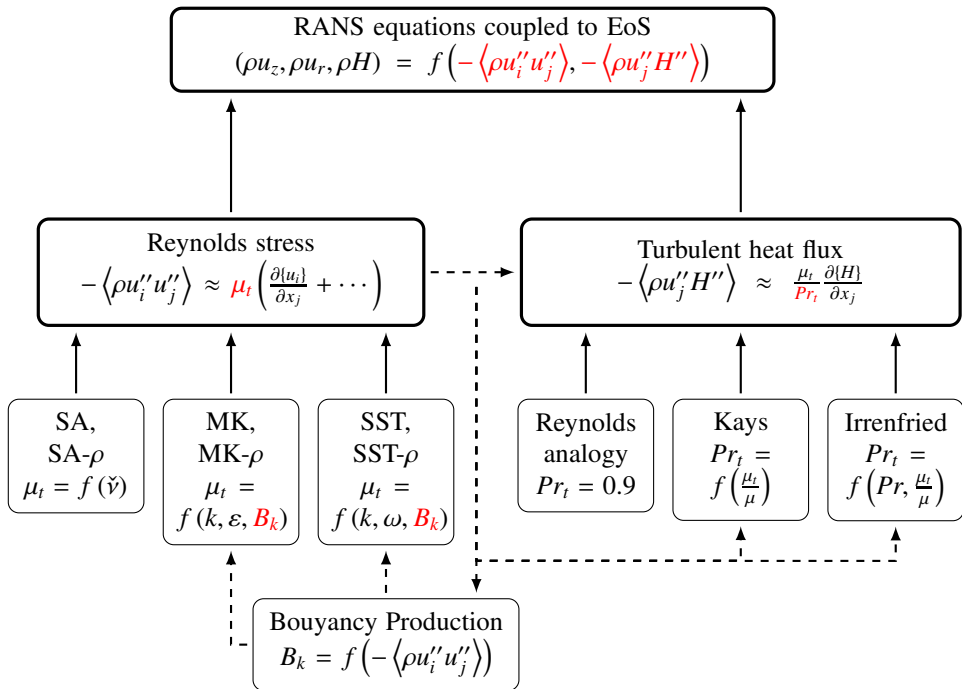
Figure 3.3: Inter-relation between turbulence models in the RANS solver.
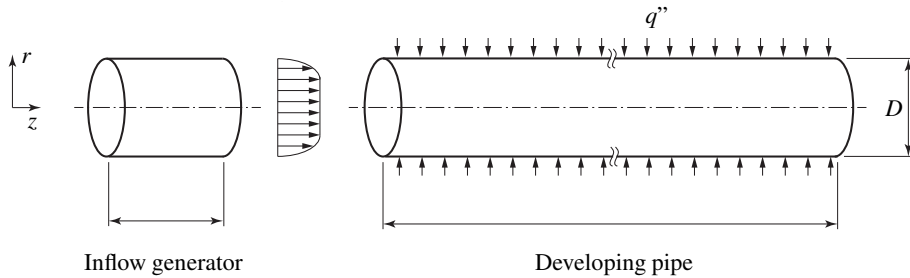
Figure 3.4: Numerical set-up for the computational fluid dynamic (CFD) simulations

3.5 Numerical set-up

An in-house RANS code solves the governing equations — with a Poisson solver for the pressure — for momentum in radial and axial direction, enthalpy and turbulent scalars; the number of turbulent scalars is dependent on the eddy viscosity model. These equations are solved using a staggered arrangement of the variables: the scalar equations ($\{H\}$, k, etc.) are discretized at the cell center, whereas the momentum equations ($\langle\rho\rangle\{u_z\}$, $\langle\rho\rangle\{u_r\}$) are discretized at the cell face. A second-order central-difference scheme is used for the discretization in space. An iterative procedure — using an Euler time integration scheme — is solve for the conserved variables; the diffusion terms in the radial direction are treated implicitly, while the rest are discretized explicitly.

The simulation set-up consists of two parts, as depicted by figure 3.4. First, an in-flow generator is used to achieve a fully developed turbulent pipe flow. Periodic inlet and outlet boundaries and an isothermal flow are enforced to generate the inflow for the developing simulation. Afterward, the fully developed profile is provided as the inlet boundary condition for the developing pipe flow simulation, which is uniformly heated at the wall.

The numerical domain of the pipe is axis-symmetric with a uniform discretization in the stream-wise direction and a non-uniform discretization in the wall-normal direction. A hyperbolic tangent function is used to cluster the mesh points near the wall to ensure mesh cells at the wall with $y^+ < 1$. Mesh independent results were obtained for all simulated cases.

3.6 Result

This section of the chapter reports the results of the RANS simulations for several turbulent pipe flow cases with CO_2 undergoing heat transfer at supercritical pressure. As mentioned in section 4.2, the RANS equations are coupled to three eddy viscosity models — the MK, the SST, and the SA models. For these three models we will also assess the impact of the density modification on predicting the heat transfer. First, we solve the RANS equations for three DNS cases[13]; we compare the wall temperature and the

stream-wise profiles concerning the DNS data. This comparison allows to determine the weaknesses of the turbulence models when estimating turbulent heat transfer to supercritical fluids. Later, we compare the RANS results with the experimental data with are at a larger Reynolds number. We then analyse the influence of the turbulent heat flux model on the different eddy viscosity models when estimating an upward flow of supercritical CO_2.

3.6.1 Impact of the eddy viscosity model

In this section of the results, we analyze the impact of the eddy viscosity model — with and without density modifications — on the estimation of the test cases of table 3.1. We assume in this section a constant turbulent Prandtl number of 0.9.

3.6.1.1 Comparison with the DNS data

Figure 3.5 depicts the comparison between the DNS data[13] and the RANS solver: the temperature along the pipe wall as a function of the stream-wise distance. Moreover, we investigate the radial profiles of the velocity and temperature at certain axial position in figures 3.6 and 3.7.

The RANS models are capable of estimating the heat transfer to the supercritical fluid for the forced convection case (DNS1). The conventional SST model shows the best agreement with the DNS data, see figure 3.5. The worst results are obtained using the conventional MK model, which significantly overestimates the wall temperature. However, using the density modification for the MK model, clearly improves the result. In figure 3.6, we display the stream-wise velocity and temperature profile at an axial distance of $\tilde{z}/\tilde{D} = 25$ for all RANS models and DNS data. The RANS models can predict fairly accurately the velocity profile, except for the MK and SST-ρ. In terms of the temperature profile, the RANS model collapses the temperature distribution far away from the wall, but a large variation can be observed among the models close to the wall. The density modifications have a small influence over the SA model, a significant improvement over the MK model, and no improvement (even detrimental) for the SST model. This observation is in accordance with our conclusions of Chapter 2.

For the low-buoyancy case (DNS2), the RANS models can quantitatively estimate the heat transfer. DNS2 suffers from HTD; the buoyancy in an upward flow configuration causes a local flow acceleration. The flow does not experience heat transfer recovery within the simulated domain. Similar to DNS1, the conventional SST model predicts the wall temperature reasonably well. However, the SST-ρ model shows the worst performance for all simulated models. The SA-ρ model shows a small improvement if compared to the standard SA. On the one hand, the MK-ρ model accurately predicts the wall temperature at the beginning of the pipe ($\tilde{z}/\tilde{D} < 10$) but deviates from the DNS further down the pipe. On the other hand, the standard MK qualitatively predicts the increasing behaviour of the wall temperature along the stream-wise direction.

For the case with high buoyancy, shown in figure 3.5 as DNS3, the flow experiences both heat transfer deterioration and enhancement. The increase of wall temperature at the
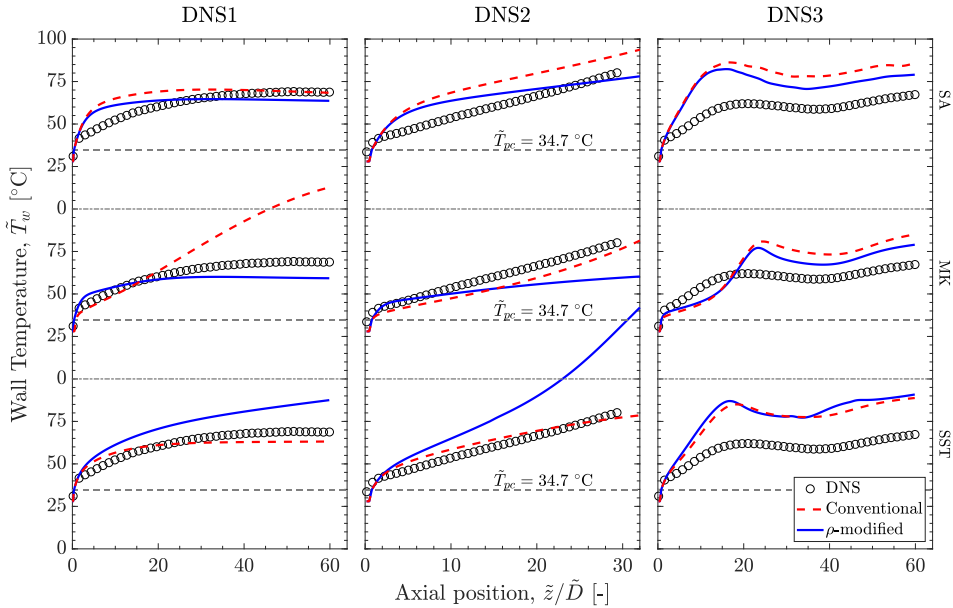
Figure 3.5: Wall temperature distribution as a function of the pipe stream-wise distance. Comparison between the three DNS cases and the RANS models.
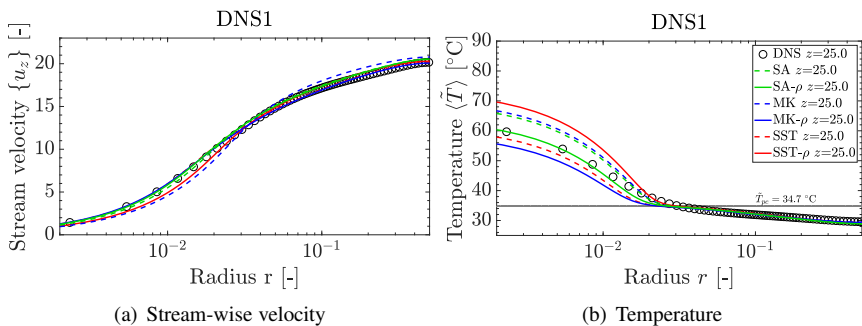

(a) Stream-wise velocity

(b) Temperature

Figure 3.6: Profile of stream-wise velocity and temperature — where the highest predicted wall temperature occurs — as a function of the radius solving for DNS1 with different eddy viscosity models.

beginning of the heated pipe ($\tilde{z}/\tilde{D} < 20$) implies HTD, while afterward, the wall temperature decreases, indicating a better heat transfer and thus a heat transfer enhancement. The RANS models estimate the deterioration and enhancement using their conventional and density-modify forms. The SST and SA model in standard and modified form both estimate the peak of wall temperature at approximately the same locations as the DNS. However, all RANS models over-predict the wall temperature. For this specific case, the ρ-versions of SA and MK estimate the $\tilde{T}_w$ closer to the DNS data after the HTD.

The density modification, derived in the previous chapter, improves the accuracy of the RANS models for estimating the heat transfer to a supercritical fluid with forced convection because of the property variations are account by the eddy viscosity model. For the cases with mixed convection, an extra level of complexity is added — considerable buoyancy effects — which is not correctly account for by the turbulence model. Therefore, the inability of the density-corrected models to estimate the mixed convection flow field is not related to the sharp variation of the properties in the supercritical region but rather the flow acceleration due to buoyancy, which may result in heat transfer deterioration.

To understand in more detail the difficulties of estimating heat transfer deterioration and enhancement transition, figure 3.7 depicts the stream-wise velocity and temperature profiles as a function of the dimensionless radius for DNS3 at the location of the maximum wall temperature for all eddy viscosity models and the DNS data. The RANS models incorrectly predict the overshoot of the stream-wise velocity in the near-wall region (see figure 3.7(a)); all models overpredict the amplitude of the overshoot. Moreover, the RANS models can collapse the temperature far away from the wall; however, when $\tilde{T} > \tilde{T}_{pc}$ in near-wall region, the estimated temperature is off. Even though the eddy viscosity models estimate the peak of wall temperature at different stream-wise locations, the profiles of both velocity and temperature have similar features; the velocities calculated by the RANS models collapse with each other close to the wall. In terms of the density modifications, there is no influence away from the wall; however, in the near-wall region, the wall temperature deviation can be as high as 4 °C with and without the modifications.

In figure 3.7(a), u_z has an M-shape profile which identifies the onset of heat transfer recovery[20,40]. This unique velocity profile is related to the flow acceleration and the variation of temperature; there is a kink in the temperature profile around $\tilde{T}_{pc}$, as seen by figure 3.7(b). The eddy viscosity models are incapable of estimating this velocity distribution correctly. Moreover, the M-shape velocity profile implies that along the wall-normal direction there is a location in the flow field where $\partial u_z/\partial r = 0$. According to the definition of the turbulent Prandtl number, see equation (3.8), Pr_t is inversely proportional to the stream-wise velocity gradient in the wall-normal direction. Therefore at the location of maximum stream-wise velocity in the wall-normal direction, the turbulent Prandtl number is undetermined.
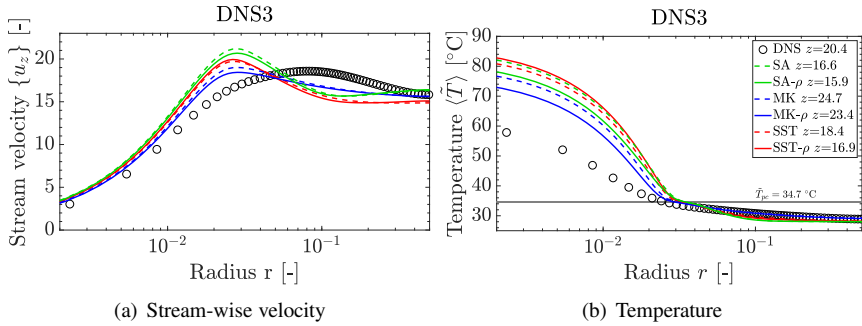
Figure 3.7: Profile of stream-wise velocity and temperature — where the highest predicted wall temperature occurs — as a function of the radius solving for DNS3 with different eddy viscosity models.

3.6.1.2 Comparison with the experimental data

Experimental case 1

Most of the turbulence models accurately estimate the wall temperature for EXP1 LHF, see figure 3.8. One exception is the SST-ρ model, but as already mentioned, the density modifications have detrimental effects on this specific model. The standard MK model is another model that lacks accuracy when compared to the experiments. With the density modifications, the MK-ρ model improves considerably, resulting in a close match with the experimental data. The SA and SA-ρ both have a similar prediction; these models slightly overestimate the wall temperature below the pseudo-critical enthalpy. The SST model accurately matches the experimental values. For this particular experiment, the RANS calculations have sufficient accuracy, except for the MK and SST-ρ models. Therefore, we do not include these two models in the remainder of this chapter. In terms of the bulk temperature, not shown in the figure, all eddy viscosity models can closely follow the experimental data.

For the EXP1 HHF, the results with all the RANS models agree qualitatively with the experiments; we do not include the SST-ρ and MK models. At the inlet section of the pipe, the wall temperature increase to 80 °C and then drops below 60 °C at around the pseudo-critical enthalpy. None of the models can reproduce these wall temperature distribution quantitatively (see figure 3.8). The SST model does not estimate any HTD, estimating a wall temperature below the measured values. The MK-ρ model overestimates the wall temperature until an axial position of $\approx$ 160, where the RANS solver predicts a substantial heat transfer enhancement. The SA models with and without density modifications qualitative predict the heat transfer deterioration but underestimating the wall temperature at $\tilde{z}/\tilde{D} < 220 kJ/kg$. Downstream of $\tilde{z}/\tilde{D} = 200$, where a monotonic increase of wall temperature is measured, all models are close to the experimental data, except the MK-ρ model.

Figure 3.8: Wall temperature distribution as a function of the pipe stream-wise distance. Comparison between the experimental data from Bae *et al.* [28] (EXP1) and the RANS models.

Experimental case 2

Despite not having any buoyancy production term, SA and SA-ρ are the only turbulence model able to reproduce heat transfer deterioration and recovery for the EXP2 MHF, see figure 3.9. These models estimate the two peaks of wall temperature qualitatively, but not at the correct location. The rest of the models cannot predict heat transfer deterioration for this case; MK-ρ and SST predict a smooth increase of wall temperature. For EXP2, q" $= 5.1$ is the value of heat flux where heat transfer deterioration starts to occur; for example, for EXP2 LHF (q" $= 4.4$), no deterioration is observed in the experiments (see figure 3.2(b)).

All the turbulence models can qualitatively reproduce heat transfer deterioration for EXP2 HHF (see figure 3.9). Consistent with the results of EXP MHF, the SA models are capable of predicting the sudden increase of wall temperature but again at the wrong location. The most prominent wall temperature peak of the SST and MK-ρ models occurs upstream from the measured data. Moreover, the SA, SA-ρ, and MK-ρ overestimate the maximum of wall temperature; the SST model underestimates it. The wall temperature trends after this point differ among the models. The SA and SST models predict a prolong heat transfer enhancement; the heat transfer coefficient increases, lowering wall temperature. Although overestimating the wall temperature, the MK-ρ model predicts the wall temperature tendency with a steady increase of wall temperature at the outlet section of the pipe ($\tilde{z}/\tilde{D} > 80$) qualitatively.

We depict the stream-wise velocity and temperature profiles at several stream-wise locations in figure 3.10 for EXP2 HHF, estimated with the SA-ρ model. The stream-wise velocity has an M-shape profile at the peak of wall temperature ($z = 19.4$); this is
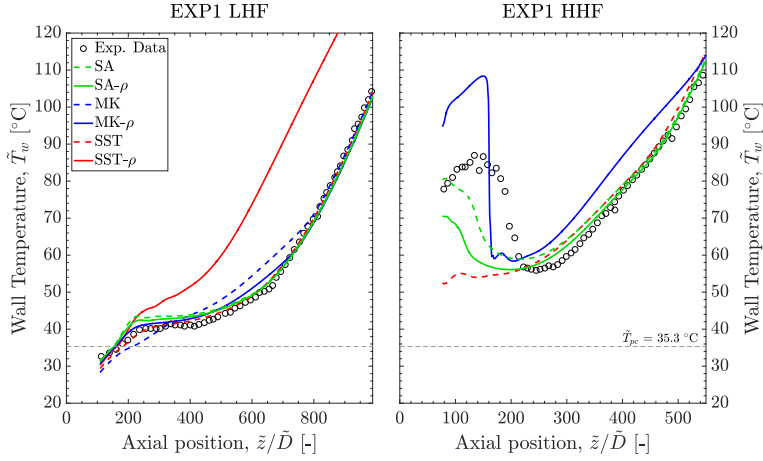
Figure 3.9: Wall temperature distribution as a function of the pipe stream-wise distance. Comparison between experimental data from Kim *et al.* [29] (EXP2) and the RANS models.

also the location where the sharpest temperature gradient in the wall-normal direction is estimated. At this axial location, the velocity and temperature profiles are comparable to the ones from DNS3 (figure 3.7). But, it is clear from these plots that the profiles are being modified along the pipe length. On the one hand, during HTD ($z = 10$), the stream-wise velocity has a regular turbulent boundary layer profile with a visible log law. Further down the pipe, the velocity profile does not follow the log-law of the wall. Downstream, where the recovery of heat transfer occurs ($z > 20$), the velocity profile continues to exhibit an overshoot; additionally, the velocity peak enlarged in the radial direction from the region close to the viscous-layer to the log-layer. Consequently, downstream from the HTD, the stream-wise velocity profile has an inflection point concerning the wall-normal distance ($\partial u_z / \partial r = 0$).

The RANS simulation results for EXP2 for all four eddy viscosity models — including our modified models — are comparable to the inlet section of EXP1 HHF [28] (figure 3.8). First, the SST model barely predicts heat transfer deterioration. Second, the SA and SA-ρ models predict the HTD earlier than observed by the experiments. Finally, the MK-ρ model overestimates $\tilde{T}_w$ but follows the trend of the experiments qualitatively. However, the performance of the turbulence models is not satisfactory. Therefore, in the following section, we test different approximations of the turbulent Prandtl number with the expectation of a better approximation of the turbulent heat flux.

3.6.2 Impact of the turbulent heat flux model

DNS studies of supercritical fluids have demonstrated that Pr_t is by no means constant in the near-wall region where heat transfer deterioration and enhancement occur [13]. Hence,

(a) Stream-wise velocity
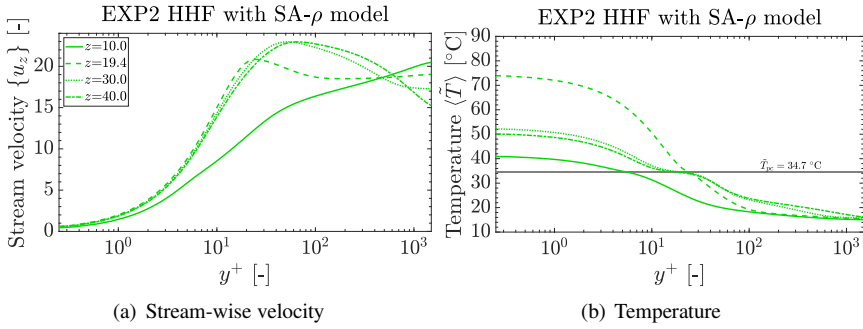
(b) Temperature

Figure 3.10: Profile of stream-wise velocity and temperature along the pipe as a function of the dimensionless radial wall distance solving for EXP2 HHF with the SA-ρ model; the highest predicted wall temperature appears at $z = 19.4$.
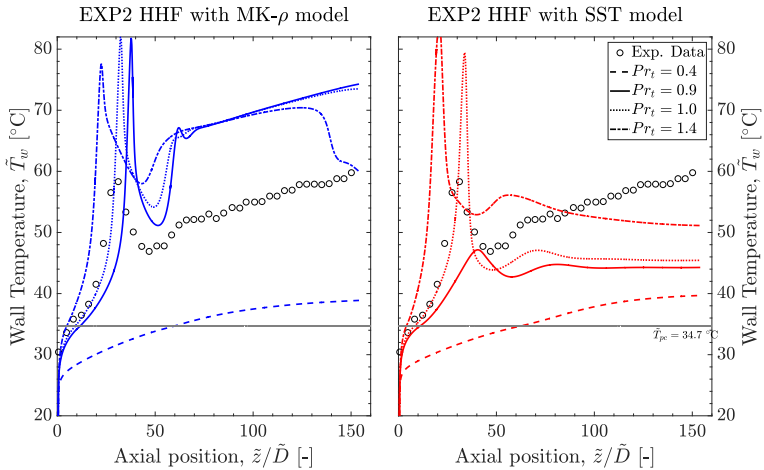
Figure 3.11: Wall temperature distribution as a function of the pipe stream-wise distance. Comparison between the experimental data from EXP2 HHF and two eddy viscosity models (MK-ρ and SST) with various constant values of Pr_t.
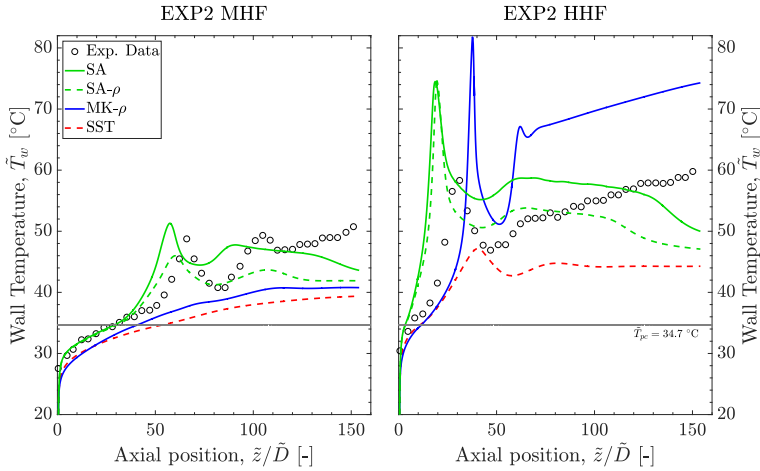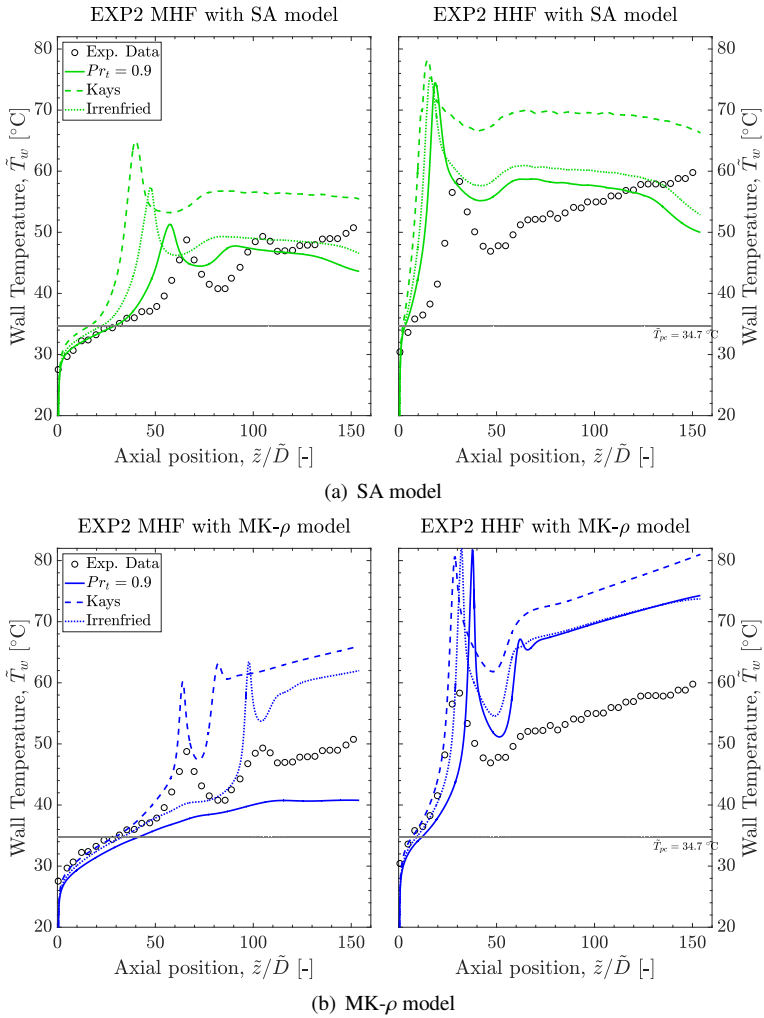
Figure 3.12: Wall temperature distribution as a function of the pipe stream-wise distance. Comparison between the experimental data from EXP2 and two eddy viscosity models (SA and MK-ρ) with algebraic equations of Pr_t.

we investigate different methods to model the turbulent Prandtl number. First, we investigate the overall impact of setting Pr_t to different constant values. And second, model Pr_t using two algebraic expressions[18,19]. We consider Kim *et al.*[29] experiments (EXP2) as, for this test case, the RANS models were considerably unreliable. The goal is to evaluate the influence of the turbulent Prandtl model on the RANS calculations.

The turbulent heat flux is inversely proportional to Pr_t; the lower the Pr_t value is, the higher the turbulent heat flux. Figure 3.11 illustrates the results obtained with the MK-ρ and SST model with four different constant values of turbulent Prandtl number: 0.4, 0.9, 1.0, and 1.4. There is a correlation between the value of the turbulent Prandtl number and the wall temperature peak (location and maximum value). The calculations with the lowest turbulent Prandtl number shows no trace of HTD. By increasing the constant value of Pr_t, the maximum wall temperature increases (except for the MK-ρ model with $Pr_t = 1.4$), the heat transfer deterioration occurs earlier, and the region of wall temperature overshooting shortens. The value that better matches the measured data for both eddy viscosity models is $Pr_t = 1$; the estimated wall temperature and the measurement data collapse for $\tilde{z}/\tilde{D} < 25$, and the RANS models estimate the wall temperature peak at the correct location. However, this outcome is test-case and eddy viscosity model dependant. For an eddy viscosity model that already overestimates the wall temperature — e.g., SA models for EXP2 HHF — increasing Pr_t would result in a more significant overestimation. As expected, the turbulent Prandtl number considerably influences the prediction of heat transfer deterioration. However, there is hardly any qualitative difference downstream from the deteriorated heat region, except for the MK-ρ model with $Pr_t = 1.4$.

The algebraic equations increase the value of the turbulent Prandtl number in the near-wall region, which decreases the turbulent heat flux. Figure 3.12 shows the resulting wall temperature along the stream-wise direction for the SA and MK-ρ using the Reynolds analogy ($Pr_t = 0.9$) and two algebraic equations[18,19] to model the turbulent Prandtl number. The algebraic equations provide a larger Pr_t between the wall and where $\partial u_z / \partial r = 0$ as depicted by figures 3.13 and 3.14 for EXP2 MHF and HHF, respectively. Kays'[18] and Irrefriend's[19] model in the near wall-region estimate a Pr_t of ≈ 1.7 and ≈ 1.1, respectively, which results in a higher wall temperature peak; this follows the results with a higher constant value of Pr_t of figure 3.11. The resulting Pr_t profile for the algebraic equations is almost independent of the eddy viscosity model and flow conditions, even though the thermodynamic state in the near-wall region crosses the pseudo-critical point.

The interaction between the Reynolds stress and the turbulent Prandtl models influence the RANS calculations of supercritical fluids with strong buoyancy effects. The algebraic models have detrimental effects over the SA model, as depicted by figure 3.12. The SA model with $Pr_t = 0.9$ overestimates the measured wall temperature; the overestimation is even more significant with the two algebraic models. The only case where the algebraic equations improve the prediction of the wall temperature is with the MK-ρ model for EXP2 MHF, see figure 3.12. Compared to the constant Prandtl number approach, the MK-ρ model coupled to algebraic equations is capable of predicting heat transfer deterioration and later enhancement for this particular test case. Even when the algebraic equations improve the performance of RANS modelling, the calculated wall temperature is still not accurate compared to the measured data.

For the results shown in this section, it is clear the importance of the turbulent heat flux model when performing a RANS simulation of a supercritical fluid with heat transfer deterioration. As discussed when comparing the RANS models to the DNS data, the turbulent Prandtl number approximation is flawed for a supercritical fluid flow with significant buoyancy effects. Due to the influence of buoyancy and the development of heat transfer deterioration, an inflection point develops in the stream-wise velocity profile, but not in the temperature field; for such a case, Pr_t is undetermined. Moreover, the interplay between μ_t and Pr_t makes the turbulent heat flux model susceptible to the eddy viscosity model and the test case conditions. And, even though the density modifications account for variable thermo-physical properties, the modify eddy viscosity models can not cope with buoyancy effects. Therefore, for a better approximation of the heat transfer in a supercritical fluid with heat transfer deterioration, eddy viscosity models need to account for gravitational effects accurately, making the RANS model able to predict the M-shape velocity profile correctly. Moreover, the turbulent heat flux should be modelled with an alternative method, for example, with the turbulent thermal diffusivity (α_t) to bypass the pitfall of Pr_t [22,37,41].

3.7   Conclusions

In this chapter, we analyzed different turbulence models to predict the heat transfer of supercritical CO_2 flowing upwards in a pipe at conditions with and without buoyancy effects. The severe property variation in the supercritical region and the heat transfer deterioration in vertical flows makes the estimation of heat transfer of such a flow rather challenging. Three eddy viscosity models with and without density correction — as proposed in Chapter 2 — are analyzed, namely the Spalart-Allmaras (SA), Myong and Kasagi (MK), and Menter's $k - \omega$ SST model. Moreover, we test different models for the turbulent heat flux model: the Reynolds analogy (Pr_t=constant) and two algebraic equations by Kays and Crawford [18], and Irrenfried and Steiner [19].

Utilizing the standard model for the turbulent heat flux $Pr_t = 0.9$, most of the turbulence models accurately predict heat transfer in the absence of heat transfer deterioration; the standard MK, and the modified SST models are the exceptions. On the one hand, the SST model gives the best results overall for the standard turbulence models when there is no heat transfer deterioration; this model has shown adequate performance for other authors in the past [21,22,42]. On the other hand, when buoyancy effects become dominant, the accuracy of the SST model drops, barely predicting any heat transfer deterioration/enhancement. The comparison between different values of Pr_t demonstrated that the reason why the SST model is not predicting heat transfer deterioration is due to the approximation of the turbulent heat flux rather than the eddy viscosity modelling. The SA model, even though being the simplest model tested, which does not include any buoyancy production term, is the only eddy viscosity model capable of always predicting qualitatively heat transfer deterioration and enhancement with $Pr_t = 0.9$. In Chapter 2, we concluded that the SA model is the most robust eddy viscosity model — for the ones tested herein — for variable property flows. Compared to other eddy viscosity models, the MK model ob-

(a) Stream-wise velocity

(b) Turbulent Prandtl number

(c) Stream-wise velocity

(d) Turbulent Prandtl number
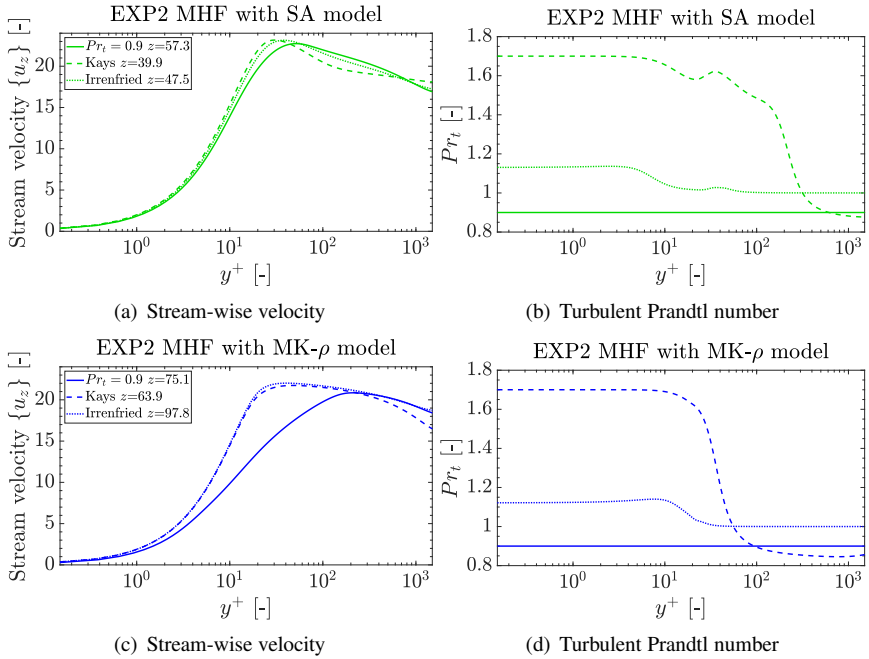
Figure 3.13: Profile of stream-wise velocity and turbulent Prandtl number — where the highest predicted wall temperature appears — as a function of the dimensionless radial wall distance solving for EXP2 MHF with SA and MK-ρ models coupled to the algebraic equations for Pr_t.
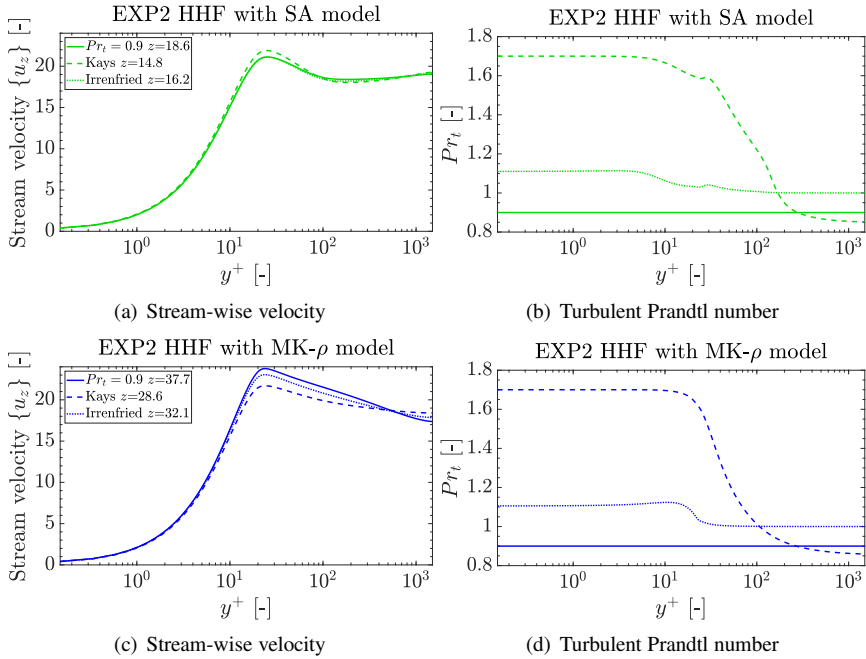
Figure 3.14: Profile of stream-wise velocity and turbulent Prandtl number — where the highest predicted wall temperature appears — as a function of the dimensionless radial wall distance solving for EXP2 HHF with SA and MK-ρ models coupled to the algebraic equations for Pr_t.

tained the most substantial improvement using density modifications; for large wall heat flux, this model with $Pr_t = 0.9$ can qualitatively estimate heat transfer deterioration and recovery. Still, the density modification to the eddy viscosity models do not give a quantitative improvement when estimating heat transfer to supercritical fluids with gravitational effect.

The scientific community attributes the lack of accuracy of the RANS simulations to the inability to accurately predicting the turbulent heat flux of supercritical fluids with buoyancy effects. For this reason, we investigated the influence of the turbulent Prandtl number on supercritical fluid flows estimations for conditions when heat transfer deterioration occurs. We coupled two different algebraic models for the turbulent Prandtl number with the RANS models. The coupling of the eddy viscosity model and algebraic model gave mix results. On the one hand, the MK model with density modification improved; this RANS model was able to estimate heat transfer deterioration qualitatively. On the other hand, coupling the algebraic models to the SA model gave a significant overestimation of the wall temperature, highlighting the importance of testing new turbulent heat flux models with several eddy viscosity models and at different flow conditions to check for validity.

If the buoyancy force is dominant and the wall heat flux is large enough, the streamwise velocity has an M-shaped profile downstream from the heat transfer deterioration. Two problems arise: (1) eddy viscosity models — derived for incompressible flow with negligible gravitational effect — are incapable of predicting such a velocity distribution in the near-wall region, and (2) the derivative of this velocity is zero along the wall-normal direction. According to its definition, Pr_t is undetermined for an M-shape velocity profile; therefore, approximating the turbulent heat flux with the turbulent Prandtl number is flawed. Alternative methods need to be research to solved these issues; for instance, derive eddy diffusivity (α_t) models capable of estimating turbulent heat transfer for flows with strong gradients of the thermo-physical properties.

References

[1] Dyreby, J., 2014. "Modeling the Supercritical Carbon Dioxide Brayton Cycle with Recompression, PhD Thesis". PhD thesis, The University of Wisconsin, Madison.

[2] Locatelli, G., Mancini, M., and Todeschini, N., 2013. "Generation IV nuclear reactors: Current status and future prospects". *Energy Policy,* **61**, pp. 1503–1520.

[3] Neises, T., and Turchi, C., 2014. "A comparison of supercritical carbon dioxide power cycle configurations with an emphasis on CSP applications". *Energy Procedia,* **49**, pp. 1187–1196.

[4] Pioro, I., and Mokry, S., 2011. "Thermophysical properties at critical and supercritical pressures". In *Heat Transfer-Theoretical Analysis, Experimental Investigations and Industrial Systems*. IntechOpen.

[5] González-Portillo, L. F., Muñoz-Antón, J., and Martínez-Val, J. M., 2019. "Thermodynamic mapping of power cycles working around the critical point". *Energy Conversion and Management,* **192**, pp. 359–373.

[6] Fages, J., Lochard, H., Letourneau, J.-J., Sauceau, M., and Rodier, E., 2004. "Particle generation for pharmaceutical applications using supercritical fluid technology". *Powder Technology,* **141**(3), pp. 219–226.

[7] Jackson, J. D., 1997. "SUPERCRITICAL HEAT TRANSFER". In *A-to-Z Guide to Thermodynamics, Heat and Mass Transfer, and Fluids Engineering*, Vol. v. Begellhouse.

[8] Pioro, I., and Mokry, S., 2011. "Heat Transfer To Fluids At Supercritical Pressure". In *Theoretical Analysis, Experimental Investigations and Industrial Systems*, A. Belmiloudi, ed. IntechOpen, pp. 481–504.

[9] Yoo, J. Y., 2013. "The Turbulent Flows of Supercritical Fluids with Heat Transfer". *Annual Review of Fluid Mechanics,* **45**(1), jan, pp. 495–525.

[10] Pizzarelli, M., 2018. "The status of the research on the heat transfer deterioration in supercritical fluids: A review". *International Communications in Heat and Mass Transfer,* **95**, pp. 132–138.

[11] Lei, X., Li, H., Zhang, W., Dinh, N. T., Guo, Y., and Yu, S., 2017. "Experimental study on the difference of heat transfer characteristics between vertical and horizontal flows of supercritical pressure water". *Applied Thermal Engineering,* **113**, feb, pp. 609–620.

[12] Wang, Y., Li, S., and Dong, M., 2014. "Numerical study on heat transfer deterioration of supercritical n-decane in horizontal circular tubes". *Energies,* **7**(11), pp. 7535–7554.

[13] Nemati, H., Patel, A., Boersma, B. J., and Pecnik, R., 2015. "Mean statistics of a heated turbulent pipe flow at supercritical pressure". *International Journal of Heat and Mass Transfer,* **83**, pp. 741–752.

[14] Wood, R. D., and Smith, J., 1964. "Heat transfer in the critical region—temperature and velocity profiles in turbulent flow". *AIChE Journal,* **10**(2), pp. 180–186.

[15] Kurganov, V., and Kaptil'Ny, A., 1992. "Velocity and enthalpy fields and eddy diffusivities in a heated supercritical fluid flow". *Experimental thermal and fluid science,* **5**(4), pp. 465–478.

[16] Bae, J. H., Yoo, J. Y., and Choi, H., 2005. "Direct numerical simulation of turbulent supercritical flows with heat transfer". *Physics of fluids,* **17**(10), p. 105104.

[17] Patel, A., Diez, R., Pecnik, R., et al., 2018. "Turbulence modelling for flows with strong variations in thermo-physical properties". *International Journal of Heat and Fluid Flow,* **73**, pp. 114–123.

[18] Kays, W. M., Crawford, M. E., and Weigand, B., 2005. "Convective heat and mass transfer".

[19] Irrenfried, C., and Steiner, H., 2017. "Dns based analytical p-function model for rans with heat transfer at high prandtl numbers". *International journal of heat and fluid flow,* **66**, pp. 217–225.

[20] He, S., Kim, W., and Bae, J., 2008. "Assessment of performance of turbulence models in predicting supercritical pressure heat transfer in a vertical tube". *International Journal of Heat and Mass Transfer,* **51**(19-20), pp. 4659–4675.

[21] Tang, G., Shi, H., Wu, Y., Lu, J., Li, Z., Liu, Q., and Zhang, H., 2016. "A variable turbulent prandtl number model for simulating supercritical pressure co2 heat transfer". *International Journal of Heat and Mass Transfer,* **102**, pp. 1082–1092.

[22] Grunloh, T. P., 2019. "Four equation k-omega based turbulence model with algebraic flux for supercritical flows". *Annals of Nuclear Energy,* **123**, pp. 210–221.

[23] Menter, F. R., 1993. "Zonal Two Equation k-w, Turbulence Models for Aerodynamic Flows". *AIAA paper*, p. 2906.

[24] Myong, H.K. and Kasagi, N., 1990. "A New Approach to the Improvement of k-e turbulence model for wall-bounded shear flows". *JSME,* **33**(2).

[25] Spalart, P. R., Allmaras, S. R., et al., 1994. "A one equation turbulence model for aerodynamic flows". *RECHERCHE AEROSPATIALE-FRENCH EDITION-*, pp. 5–5.

[26] Bazargan, M., Fraser, D., and Chatoorgan, V., 2005. "Effect of Buoyancy on Heat Transfer in Supercritical Water Flow in a Horizontal Round Tube". *Journal of Heat Transfer,* **127**(8), p. 897.

[27] Bae, Y. Y., 2016. "A new formulation of variable turbulent prandtl number for heat transfer to supercritical fluids". *International Journal of Heat and Mass Transfer,* **92**, pp. 792–806.

[28] Bae, Y.-Y., Kim, H.-Y., and Kang, D.-J., 2010. "Forced and mixed convection heat transfer to supercritical CO2 vertically flowing in a uniformly-heated circular tube". *Experimental Thermal and Fluid Science,* **34**(8), nov, pp. 1295–1308.

[29] Kim, J. K., Jeon, H. K., Yoo, J. Y., and Lee, J. S., 2005. "Experimental Study on Heat Transfer Characteristics of Turbulent Supercritical Flow in Vertical Circular / Non-Circular Tubes". In The 11th International Topical Meeting on Nuclear Reactor Thermal-Hydraulics (NURETH-11).

[30] Kunz, O., and Wagner, W., 2012. "The gerg-2008 wide-range equation of state for natural gases and other mixtures: an expansion of gerg-2004". *Journal of chemical & engineering data,* **57**(11), pp. 3032–3091.

[31] Wilcox, D. C., 1993. "Turbulence modeling". *DCW Industries*.

[32] Pecnik, R., and Patel, A., 2017. "Scaling and modelling of turbulence in variable property channel flows". *Journal of Fluid Mechanics,* **823**.

[33] Bazargan, M., and Mohseni, M., 2009. "Effect of turbulent prandtl number on convective heat transfer to turbulent upflow of supercritical carbon dioxide". In ASME 2009 Heat Transfer Summer Conference collocated with the InterPACK09 and 3rd Energy Sustainability Conferences, American Society of Mechanical Engineers, pp. 295–302.

[34] Kays, W. M., 1994. "Turbulent prandtl number—where are we?". *Journal of Heat Transfer,* **116**(2), pp. 284–295.

[35] Lazeroms, W., 2015. "Turbulence modelling applied to the atmospheric boundary layer". PhD thesis, KTH Royal Institute of Technology.

[36] Launder, B., 1975. "On the effects of a gravitational field on the turbulent transport of heat and momentum". *Journal of Fluid Mechanics,* **67**(3), pp. 569–581.

[37] Zhang, G., Zhang, H., Gu, H., Yang, Y., and Cheng, X., 2012. "Experimental and numerical investigation of turbulent convective heat transfer deterioration of super-critical water in vertical tube". *Nuclear Engineering and Design,* **248**, pp. 226–237.

[38] Pucciarelli, A., Borroni, I., Sharabi, M., and Ambrosini, W., 2015. "Results of 4-equation turbulence models in the prediction of heat transfer to supercritical pressure fluids". *Nuclear Engineering and Design,* **281**, pp. 5–14.

[39] Ince, N., and Launder, B., 1989. "On the computation of buoyancy-driven turbulent flows in rectangular enclosures". *International Journal of Heat and Fluid Flow,* **10**(2), pp. 110–117.

[40] Bellmore, C., and Reid, R., 1983. "Numerical prediction of wall temperatures for near-critical para-hydrogen in turbulent upflow inside vertical tubes". *Journal of heat transfer,* **105**(3), pp. 536–541.

[41] Kenjereš, S., Gunarjo, S., and Hanjalić, K., 2005. "Contribution to elliptic relaxation modelling of turbulent natural and mixed convection". *International Journal of Heat and Fluid Flow,* **26**(4), pp. 569–586.

[42] Li, Z., Wu, Y., Tang, G., Zhang, D., and Lu, J., 2015. "Comparison between heat transfer to supercritical water in a smooth tube and in an internally ribbed tube". *International Journal of Heat and Mass Transfer,* **84**, pp. 529–541.

Part II

High-expansion ORC turbine simulations

As discussed in Chapter 1, organic Rankine cycle (ORC) turbogenerators are a practical solution to convert low-temperature heat sources into electricity. The expander is particularly crucial because of its direct impact on the overall system performance. But, to achieve an efficient high-expansion turbine is challenging because of the intrinsic unsteady flow and the real-gas effects; the working fluid expands in the dense-vapour region, where the ideal gas law is no longer valid. Moreover, the small enthalpy drop of the organic fluid results in a large pressure ratio per stage and a highly supersonic flow in the stator exit. Currently, steady-state and quasi-three-dimensional computational fluid dynamics (CFD) simulations are used to design and to analyze the performance of ORC turbines. However, these calculations ignore several loss mechanisms — e.g., secondary flow, shock-shock, and shock-boundary layer interactions — that reduce the performance of the expander. In this part of the dissertation, we present a detailed unsteady numerical simulation of a high-expansion ORC turbine via three-dimensional calculations, including the real-gas effects. First, in Chapter 4, we describe the numerical set-up for the ORC turbine simulations; this includes the governing equations, numerical schemes, equation of state, and a conservative flux-assembling technique for non-matching meshes. Later in Chapter 5, we apply the numerical set-up to simulate the turbine geometry from an ORC manufacturer. We analyze the expander in terms of unsteady and three-dimensional effects. In Chapter 6, we propose a design methodology for high-expansion ORC turbines, which includes the three-dimensional effects and the intrinsic unsteady flow inside the expander. We apply this methodology to the expansion process discussed in Chapter 5 to produce a new ORC turbine design.

4

Numerical set-up for the turbomachinery simulations

In this chapter, we discuss the numerical infrastructure used for the computational fluid dynamic simulations of the organic Rankine cycle (ORC) turbines in Chapters 5 and 6. The expansion process in an ORC takes place close to the working fluid's critical point, in the dense-vapour region, where the ideal gas assumption is invalid. Moreover, an organic fluid features a small specific enthalpy drop that results in a few expansion stages with a large pressure ratio; consequently, the turbine has a highly supersonic flow at the stator exit. We describe the numerical schemes used to capture the flow complexities inside a high-expansion ORC turbine. First, the compressible Navier-Stokes equations are presented. Afterward, numerical details such as spatial and temporal discretization are given, including an approximate Riemann solver to accurately estimate shock waves in the flow field. Utilizing the knowledge from Chapter 2, we select the most robust turbulence model for a flow field with variable properties. The use of look-up table interpolation of fluid properties is presented as an alternative to the direct solution of the multi-parameter equation-of-state model to estimate the real-gas effects. Finally, to account for the unsteady stator-rotor interaction, a conservative flux-assembling technique for non-matching three-dimensional meshes is described.

4.1   Introduction

Internal turbomachinery flow are among the most complex flow fields in any fluid dynamics applications[1]. The number of possible fluid dynamics mechanisms and flow regimens is considerable. Viscous/turbulent flow is common in turbomachinery, with flow transition from laminar to turbulent within a blade passage[2,3]. Complex vortical structures can dominate the flow field in a specific section of the machine; turbomachinery often suffers from flow separation in the blade channel and vortex shedding from the blade trailing edge[4,5]. The flow regimen inside turbomachinery can be incompressible, or transition from a subsonic regimen passing through Mach equals to 1 (sonic conditions) until the flow becomes supersonic[6,7]; the latter of which may result in shock waves[8]. The near-wall region (viscous or turbulent) can encounter sharp pressure gradients, flow rotation, surface curvature, or shock wave/boundary-layer interaction[9]. Three-dimensional effects can disturb the flow in turbomachinery, for example, secondary flows and tip leakage[5,10–12]. Depending on the thermodynamic state of the flow, the turbomachine may experience from multiphase flow or real-gas effects[13,14]. Moreover, the flow field in the rotor is unsteady by nature[8,15]. All of these physical phenomena may be present in turbomachinery, influencing the machine's performance.

An organic Rankine cycle (ORC) turbine is what is called an unconventional turbomachinery[16,17]; the expansion process takes place close to the working fluid's critical point, in the dense-vapor region, where the ideal gas assumption is invalid. Moreover, an ORC expander features a small specific enthalpy drop due to the molecular complexity of the organic fluid. Therefore, the designer can choose a few numbers of stages (one or two) without the expander suffering from efficiency drop or high rotational speed problems. As a consequence, the expander has a large pressure ratio per stage. The high-expansion ratio and the low speed of sound of organic fluids — relative to air or steam — lead to a

highly supersonic flow at the stator exit. Therefore, the flow field inside an ORC turbine is highly complex, featuring phenomena like real-gas effects, turbulent boundary layer and shock waves interaction, and strong coupling between the stator and the rotor resulting in unsteady effects. Recently, several authors conducted numerical simulations of ORC turbomachinery for a better physical understanding of its fluid dynamic operation[8,18,19].

Computational fluid dynamics (CFD) plays an instrumental part in the aerodynamic evaluation, design, and optimization of any turbomachinery. Nowadays, it is common practice — after the preliminary seizing — to make the detailed aerodynamic design of turbomachinery with a CFD tool[20]. In the past decades, the increase of computing power promoted the use of optimization routines to design the aerodynamic features of a turbomachinery[21–23]. Still, it is essential to acknowledge the limitation and underlying assumptions of CFD.

Numerical errors exist in CFD due to assumptions/approximations that are unavoidable in any numerical method[24]. The approximation that flow properties vary linearly between two grid points is one of the most common numerical errors generally called numerical dissipation; this issue is relevant at flow regions with sharp property gradients, e.g., ORC turbines. Therefore, a high-quality mesh and a correct selection of the numerical method is of paramount importance to achieve a fully resolve CFD simulation.

Creating a high-quality mesh of turbomachinery is a challenging task that often requires unstructured or multi-block grids[25]. Unstructured grids are often used to efficiently quantify features on a variety of length scales, including boundary layers, shock waves, and vortices[26]. In terms of multi-block grids, there are instances in turbomachinery simulation where a non-matching interface between elements is necessary, e.g., to estimate the flow features due to the relative motion between the static and rotating domain[8]. However, standard numerical schemes require a node-to-node connectivity between the mesh elements. The CHIMERA interpolation technique on overlapping grids is the most widely used solution for multi-block grids[27]; but this method is intrinsically not conservative and has uncertainty in capturing shock waves. Rinaldi *et al.*[28] describe a flux treatment for non-conformal mesh block interfaces that is fully conservative of the numerical solution; the authors applied this methodology to simulate a high-expansion ORC turbine[8].

The quality of the mesh is particularly crucial for flows with a high Reynolds number. Most turbomachinery flows are turbulent; this phenomenon influences the aerodynamic and thermodynamic performance of turbomachinery[1]. Turbulence is associated with losses in the system because of its diffusive (mixing) and dissipative (transform kinetic energy into internal energy) nature. For complex geometries, e.g., turbomachinery, it is impossible to resolve all the turbulent scales of the flow field. The highest-order CFD simulation of turbomachinery achieved to date is Large Eddy Simulations (LES)[29,30]. The statistical approach commonly used to estimate the small scales of turbulence — Reynolds/Favre decomposition — adds more unknowns to the system, which are estimate with turbulence models. However, these models were developed for incompressible flows, an invalid assumption for ORC expanders with a highly compressible flow.

Compressible flows in the dense-gas region exhibit qualitatively different features concerning ideal gases. Therefore, complex equations of state (EoS) are necessary to describe

organic fluids accurately. Hoffren *et al.* [31] were one of the first to consider the real-gas effects during the development of an ORC turbine design. More recently, Colonna *et al.* [32] proved the importance of implementing real-gas effects on an expansion near the critical point of a complex fluid. Moreover, Guardone [33] adapted the Method of Characteristic (MOC) for real gases to design the divergent portion of nozzles operating in the dense-gas regime for fluids of different molecular complexity. Therefore, when dealing with a molecularly complex fluid near its thermodynamic critical point ORC turbine, it is of paramount importance to include the real-gas effects.

In this chapter, we introduce the numerical infrastructure used for unsteady calculations of high-expansion ORC turbines employing three-dimensional computational fluid dynamics simulations; we apply this numerical set-up in Chapters 5 and 6. We first present the fully compressible Navier-Stokes equations, which are the governing equations of our system. Next, the details of the numerical implementation are discussed with the numerical schemes applied to discretized — in space and in time — and to model the eddy viscosity and the thermodynamic representation of the fluid. Finally, we describe a conservative flux-assembling technique for non-matching three-dimensional meshes.

4.2 Governing equations

The fluid dynamics community considers the fully compressible Navier-Stokes equations as the complete mathematical representation of fluid motion; these equations are the conservation of mass, momentum, and energy, which in conservative form reads (Pecnik *et al.* [34]):

$$\frac{\partial \langle \tilde{\rho} \rangle}{\partial \tilde{t}} + \frac{\partial \langle \tilde{\rho} \rangle \{ \tilde{u}_j \}}{\partial \tilde{x}_j} = 0 \tag{4.1}$$

$$\frac{\partial \langle \tilde{\rho} \rangle \{ \tilde{u}_i \}}{\partial \tilde{t}} + \frac{\partial \langle \tilde{\rho} \rangle \{ \tilde{u}_i \} \{ \tilde{u}_j \}}{\partial \tilde{x}_j} = -\frac{\partial \langle \tilde{p} \rangle}{\partial \tilde{x}_i} + \frac{\partial \left(\langle \tilde{\tau}_{ij} \rangle + \langle \tilde{\tau}_{ij}^R \rangle \right)}{\partial \tilde{x}_j} \tag{4.2}$$

$$\frac{\partial \langle \tilde{\rho} \rangle \{ \tilde{E} \}}{\partial \tilde{t}} + \frac{\partial \langle \tilde{\rho} \rangle \{ \tilde{u}_j \} \{ \tilde{E} \}}{\partial \tilde{x}_j} = \frac{\partial}{\partial \tilde{x}_j} \left[-\langle \tilde{p} \rangle \{ \tilde{u}_j \} + \left(\langle \tilde{\tau}_{ij} \rangle + \langle \tilde{\tau}_{ij}^R \rangle \right) \{ \tilde{u}_j \} \right]$$
$$- \frac{\partial}{\partial \tilde{x}_j} \left[\left(\frac{\tilde{\lambda}}{\tilde{c}_p} + \frac{\mu_t}{Pr_t} \right) \frac{\partial \{ \tilde{H} \}}{\partial \tilde{x}_j} \right] \tag{4.3}$$

with the stress tensor defined as

$$\langle \tilde{\tau}_{ij} \rangle = \langle \tilde{\mu} \rangle \langle \tilde{S}_{ij} \rangle = \langle \tilde{\mu} \rangle \left[\frac{\partial \langle \tilde{u}_i \rangle}{\partial \tilde{x}_j} + \frac{\partial \langle \tilde{u}_j \rangle}{\partial \tilde{x}_i} - \frac{2}{3} \frac{\partial \langle \tilde{u}_k \rangle}{\partial \tilde{x}_k} \delta_{ij} \right], \tag{4.4}$$

and the Reynolds stresses — modelled with Boussineq approximation — as:

$$\langle \tilde{\tau}_{ij}^R \rangle = \mu_t \langle \tilde{S}_{ij} \rangle = \mu_t \left[\frac{\partial \langle \tilde{u}_i \rangle}{\partial \tilde{x}_j} + \frac{\partial \langle \tilde{u}_j \rangle}{\partial \tilde{x}_i} - \frac{2}{3} \frac{\partial \langle \tilde{u}_k \rangle}{\partial \tilde{x}_k} \delta_{ij} \right], \tag{4.5}$$

In these equations and across the whole dissertation, the tilde hat (˜) denotes dimensional quantities. The variables $\tilde{t}$, $\tilde{\rho}$, $\tilde{x}_j$, $\tilde{u}_j$, $\tilde{p}$, $\tilde{\mu}$, μ_t, $\tilde{E}$, $\tilde{\lambda}$, $\tilde{c}_p$, Pr_t, and $\tilde{H}$ are the time, density, coordinate, velocity component, pressure, dynamic viscosity, eddy viscosity, total internal energy ($\tilde{E} = \tilde{\rho}(\tilde{e} + \frac{1}{2}|\tilde{u}_{ij}|^2)$), thermal conductivity, isobaric heat capacity, turbulent Prandtl number, and the specific enthalpy, respectively. δ_{ij} is the Kronecker delta. Moreover, we use the Reynolds decomposition for most of the quantities, defined as: $\phi = \langle\phi\rangle + \phi'$ with $\langle\phi'\rangle = 0$, and the Favre decomposition for the velocity and total energy, defined as: $\phi = \{\phi\} + \phi''$ with $\langle\rho\rangle\{\phi''\} = 0$, $\langle\rho\rangle\{\phi\} = \langle\rho\phi\rangle$, and $\langle\phi''\rangle \neq 0$. Notice that in equation (4.3), we approximated $d\tilde{H} = \tilde{c}_p d\tilde{T}$ and the turbulent heat flux with the Reynolds analogy; we model the turbulent Prandtl number as a constant ($Pr_t = 0.9$). An EoS is used to define the relationship between density, pressure, temperature, and internal energy; more details of the EoS is given in section 4.3.3.

4.3 Numerical schemes

4.3.1 Numerical discretization

We use an in-house CFD parallel solver for the solution of the compressible Navier-Stokes equations[34], which has been already validated for turbomachinery flows in previous studies[8,14,34,35]. The spatial discretization scheme is based on a finite-volume formulation on arbitrary polyhedral mesh elements. The code is entirely written in C++; it employs a subdomain decomposition through the freely available package PARMETIS[36] and the Message Passing Interface (MPI) as the parallel infrastructure.

The equations are discretized in the conservative form as

$$\frac{\partial}{\partial \tilde{t}} \int_{\tilde{\Omega}} \mathbf{U} d\tilde{\Omega} = - \int_{\partial\tilde{\Omega}} (\mathbf{F}_c(\mathbf{U}) - \mathbf{F}_d(\mathbf{U})) \, d\tilde{A}, \tag{4.6}$$

where $\mathbf{U} = (\tilde{\rho}, \tilde{\rho}\tilde{u}_{ij}, \tilde{E})^{\mathrm{T}}$ represents the conserved variables vector; $\mathbf{F}_c$ and $\mathbf{F}_d$ are the Euler (convection and pressure) and diffusive flux vectors, respectively. The physical domain of interest is denoted by $\tilde{\Omega}$ and its external boundary by $d\tilde{\Omega}$. On the right-hand side (RHS), Gauss' divergence theorem was applied. In the finite-volume formulation, $\tilde{\Omega}$ is discretized numerically as control volume. We re-write equation (4.6) in a semi-discrete form at the cell center of each control volume (cv) as

$$\frac{\partial \mathbf{U}_{cv}}{\partial \tilde{t}} = -\mathbf{RHS(U)}, \tag{4.7}$$

with

$$\mathbf{RHS(U)} = \frac{1}{\tilde{V}_{cv}} \sum_{f=1}^{N_f} [\mathbf{F}_c(\mathbf{U}) - \mathbf{F}_d(\mathbf{U})] \tilde{A}_f. \tag{4.8}$$

We approximate the surface integral as the sum of the fluxes over all faces of the control volume, where N_f and $\tilde{A}_f$ are the number of faces and face's surface area, respectively. In section 4.4.2, we describe about the flux assembly over a control volume in more detailed.

For supersonic CFD simulations, an approximate Riemann solver (ARS) is the most common approach to evaluate the Euler flux. ARS approximates the wave speeds from an arithmetic or a square-root average of the left and right states of the Riemann problem[37]. An ARS aims to accurately capture shock waves and contact discontinuities with minimal numerical dissipation and oscillation. In the present numerical infrastructure, we use the improved advection upstream splitting method (AUSM$^+$) ARS proposed by Liou[38] to discretized the Euler term; AUSM schemes split the Euler flux into a convective and acoustic wave contribution.

The Euler flux evaluation discussed above leads to a first-order-accurate approximation. We achieve a second-order-accurate by computing the states at each side of a given face using second-order interpolation. The state reconstruction at the face is given as:

$$\phi_f = \phi_{CV} + \psi_{CV} \, \nabla\phi|_{cv} \cdot \mathbf{r}_f, \tag{4.9}$$

where ϕ is a generic variable and $\nabla\phi|_f$ is an approximation of the gradient at the cell center of the control volume, estimated using a standard least-squares approximation. ψ_{CV} is a slope-limiter function, and $\mathbf{r}_f$ is the vector connecting the control volume's cell center and the center of the face f. We include ψ_{CV} to reduce the discrete gradient in regions where the solution changes rapidly, e.g., a discontinuity, and to guarantee the monotonicity of the reconstructed variable at the face center. For more details in the slope-limiter, refer to[34,39]. Finally, to ensure the thermodynamic consistency of the reconstructed state, the EoS is evaluated at the faces using the interpolated density and pressure.

The discretization of diffusive fluxes needs an accurate and efficient evaluation of the velocity and temperature gradient at the control volume's faces. We estimate the gradient normal to the face as

$$\nabla\phi|_f \cdot \mathbf{n}_f = \frac{\phi_{nbr} - \phi_{cv}}{|\mathbf{x}_{nbr} - \mathbf{x}_{cv}|}\alpha_f + \frac{1}{2}\left(\nabla\phi|_{cv} + \nabla\phi|_{nbr}\right)\cdot\left(\mathbf{n}_f - \alpha_f\mathbf{s}_f\right), \tag{4.10}$$

where cv and nbr (neighbour) are the control volumes that share the face f; $\mathbf{x}$ is the position vector of the control volume centroid. The variables $\mathbf{n}_f$ and $\mathbf{s}_f$ are the vector normal to the face and the normalized vector connecting the cell centroid across the face f, respectively. α_f is the dot product between $\mathbf{s}_f$ and $\mathbf{n}_f$.

For the temporal discretization, we use an implicit two-step Backward differentiation scheme to advance the simulation in time. Moreover, we solve the sparse system resulting from the fluxes ($\mathbf{F}_c, \mathbf{F}_d$) linearization with a Biconjugate Gradient Stabilized Method (BCGSTAB)[40].

4.3.2   Turbulence modelling

In equations (4.2)-(4.3), we modelled the Reynolds shear stress and turbulent heat flux using the Boussinesq approximation and the gradient diffusion hypothesis, respectively. The one-equation turbulence model of Spalart-Allmaras (SA)[41] is used to model the eddy viscosity and close the system of equations; for this reason, we did not include the turbulent kinetic energy term ($-2/3k\delta_{ij}$) in equation (4.5). The SA model equations are

given in Appendix A.1 for completeness. Other authors have also used this eddy viscosity model for ORC turbomachinery [7,8,42]. Moreover, in Chapters 2 and 3, the SA model gave the most robust results (five eddy viscosity were tested in total) when solving turbulent flows with a strong variation on the thermo-physical properties.

4.3.3   Equation of state

We can not represent the thermodynamic state with the ideal gas law to calculate the expansion of an ORC turbine due to the proximity of the inlet state to the fluid's critical point. Therefore, we model the thermodynamic state of the organic fluid with a multi-parameter equation of state based on Helmholtz energy function derived by Lemmon and Span [43]. We use the thermodynamic property library Fluidprop [44], which also compiles constitutive relations for transport properties and secondary thermodynamic properties.

The main challenge of using a complex equation of state is the computational cost required for the thermodynamic state evaluation. Instead of performing a direct evaluation of the properties via real-gas EoS, we apply a look-up table (LUT) interpolation, which provides simplicity and flexibility. We generate a LUT for a range of two independent thermodynamic variables and store all thermophysical properties of interest. During the CFD simulation, the code can access the table by specifying any two thermodynamic properties. Rinaldi *et al.* [45] makes a thorough review of this look-up table method.

For our particular case, we generate a LUT for toluene — the working medium of the ORC turbine — for a range of $\rho = [0.005, 145.0] \, kg/m^3$ and $T = [310, 690] \, K$ using 400 nodes for each axis. A uniform and a logarithmic spacing, for the temperature and the density, respectively, are used to discretize the thermodynamic table; figure 4.1 illustrates the thermodynamic table of toluene. The LUT tabulates pressure, entropy, enthalpy, viscosity, thermal conductivity, the speed of sound, and secondary thermodynamics properties. When neither density nor temperature is available as input for the interpolation function, a Newton–Raphson iterative procedure is used to evaluate the corresponding ρ and T inversely. The iteration is stopped with a relative tolerance of 10^{-10} on the calculated ρ and T. The computational cost of the properties evaluation is drastically reduced, more than 20 times, by the use of the LUT interpolation, measuring a maximum interpolation error below 0.01% [8].

4.4   Non-matching mesh interface treatment

In the field of ORC turbomachinery, it is common practice to perform CFD simulation under the assumption of steady-state with the implementation of the mixing plane boundary condition at the interface between the stator and the rotor, e.g., see references [18,19]. Because of the averaging of the numerical solution at the interface and the assumption of periodicity in the tangential direction, only one blade passage is simulated per rotor — independent of the number of blades of the turbine stage — making the simulation computationally less expensive. However, because of the mixing plane assumption, the unsteady information between the stator and the rotor is lost. An alternative method is
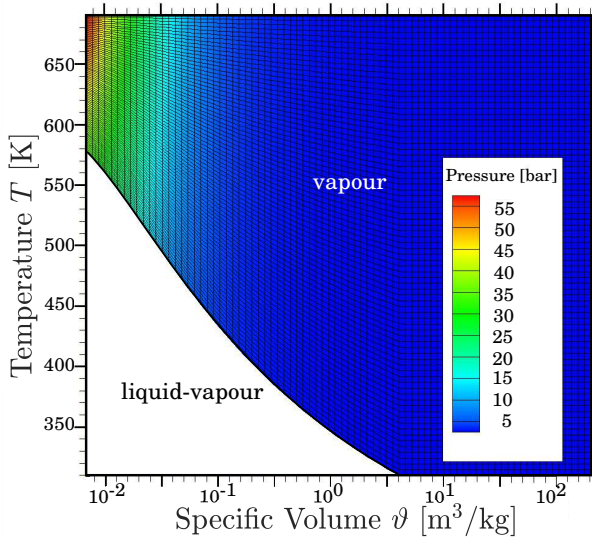
Figure 4.1: Illustration of the thermodynamic table for toluene. The discretization was coarsened by five times (80 nodes per axis) to visualize the grid of the thermodynamic table.

to use the frozen rotor approximation[46], but it is still physically inconsistent due to the absence of inertia in the transition from the static to the rotating frame. These type of simulations are unable to accurately estimate unsteady effects that bring insights on otherwise unmeasured loss mechanisms[8].

4.4.1 Supermesh construction

For our simulations of ORC turbines, we use a fully-conservative flux assembling technique for the treatment of non-matching mesh interfaces to model the unsteady stator-rotor interaction[28]. An auxiliary grid or "supermesh" is created at the shared boundary surface of the two non-conformal grids. Connectivity in the supermesh is established by the intersection of the elements from the two parent meshes; we display an example in figure 4.2.

The authors from the references[47,48] describe the essential features of the auxiliary grid as: (1) all the nodes from the parent meshes must be contained in the supermesh, and (2) the intersection area of each element of the supermesh with any face element of the parent mesh must be either null or measure the whole supermesh element area. Therefore, the construction of the supermesh is an intersection problem. As depicted by figure 4.2(a), for a two-dimensional (2D) meshes, the supermesh consists of one-dimensional segments demarcated by the supermesh nodes; these nodes coincide with the nodes of the parent meshes non-matching faces (boundary nodes of mesh A and mesh B in figure 4.2(a)).
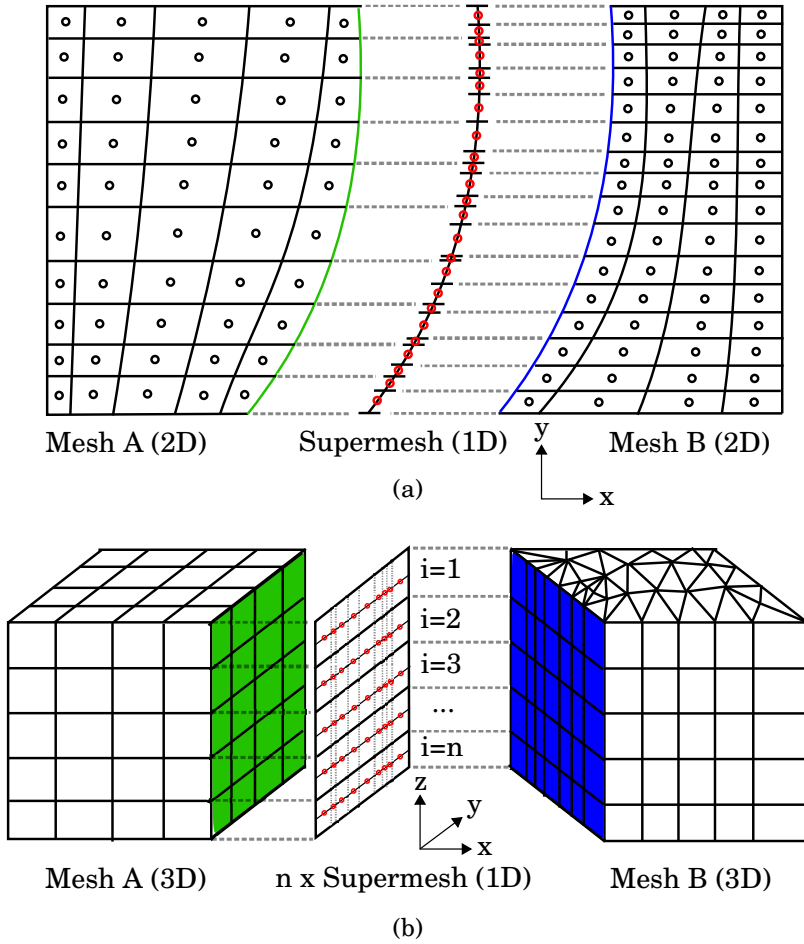
Figure 4.2: Interface supermesh definition for (a) 2D and (b) 3D parent grids. In both cases the mesh blocks are displaced for the sake of clarity and the interface supermesh is displayed in the middle. n is the number of discretization cells minus 1 in the z-direction of b.
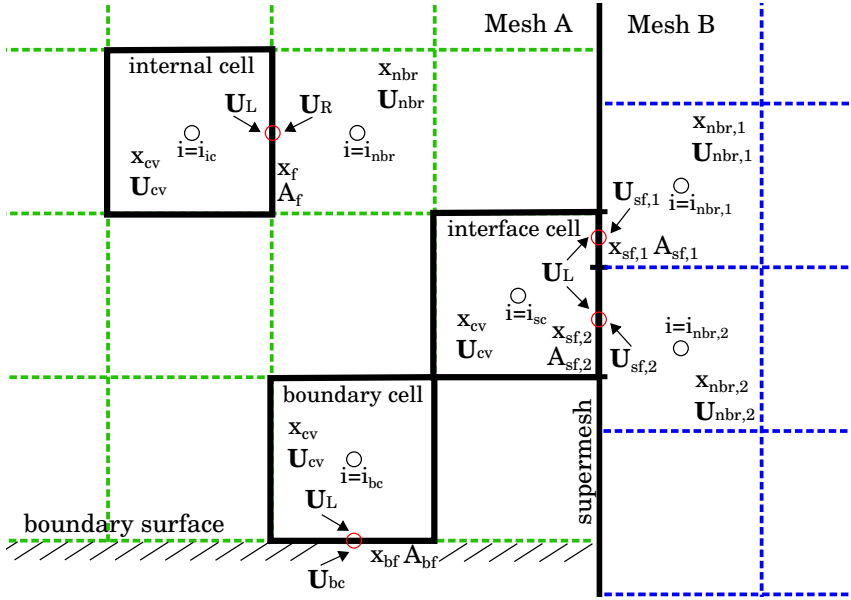
Figure 4.3: Schematic of the finite volume discretization. The i is the grid index. In this particular case, the *internal cell* has $N_{if} = 4$ and $N_{bf} = N_{sf} = 0$; the *boundary cell* has $N_{if} = 3$, $N_{bf} = 1$, and $N_{sf} = 0$; and the *interface cell* has $N_{if} = 3$, $N_{bf} = 0$, and $N_{sf} = 2$.

When solving an unsteady simulation, where one of the parent meshes has a relative motion with respect to the other mesh, the auxiliary grid updates itself at each time step to establish new connectivity.

For three-dimensional (3D) geometries, the construction of the supermesh elements is more complex; the supermesh definition consists of a two-dimensional face intersection problem between two interface surface meshes. Rinaldi *et .al*[28] create a stable algorithm capable of generating such a 2D supermesh from quadrilateral and/or triangular cells. Still, this method is computationally expensive; even more so if we consider that for an unsteady simulation, the supermesh connectivity needs to be remade at each time step.

In the current study, we implemented a different approach for 3D geometries: employing an array of one-dimensional supermesh to intersect two 2D surface meshes as depicted in figure 4.2(b). This procedure is faster than the one presented in Rinaldi *et .al*[28] as the generation of the n-supermesh (n is the size of the array) is done only in one direction; the drawback of this procedure is that the discretization of the two parent mesh must be equivalent along one-direction, for example, z-direction in figure 4.2(b). Still, the array of one-dimensional supermesh does not need to be equidistant.

4.4.2 Conservative flux assembly

We ensure conservation of the numerical solution by calculating the fluxes at the elements of the auxiliary mesh and adding their contribution to the respective control volumes of the parent meshes. The flux treatment does not involve any interpolation; therefore, conservation is guaranteed by construction, without enforcing additional constrains.

To explain the flux assembly, we can re-write equation (4.8) in terms of internal (subscript if), boundary (subscript bf), and supermesh (subscript sf) faces considering the flux ($\mathbf{F} = \mathbf{F}_c - \mathbf{F}_d$) at the face as a function of the left and right side conserved variables:

$$\mathbf{RHS}(\mathbf{U}_{cv}) = \frac{1}{\tilde{V}_{cv}} \left[\sum_{f=1}^{N_{if}} \mathbf{F}\left(\mathbf{U}_L, \mathbf{U}_R\right) \tilde{A}_f + \sum_{bf=1}^{N_{bf}} \mathbf{F}\left(\mathbf{U}_L, \mathbf{U}_{bc}\right) \tilde{A}_{bf} + \sum_{sf=1}^{N_{sf}} \mathbf{F}\left(\mathbf{U}_L, \mathbf{U}_{sf}\right) \tilde{A}_{sf} \right].$$

(4.11)

We display three examples of a control volume — internal cell, boundary cell, and interface cell — in figure 4.3 with the same nomenclature as equation (4.11). N_{if}, N_{bf}, and N_{sf} are the number of internal, boundary, and supermesh faces defining the control volume; the total number of faces is defined as $N_f = N_{if} + N_{bf} + N_{sf}$. The solver calculates the value of the flux with the conservative variables on the left and the right side of the face ($\mathbf{U}_L, \mathbf{U}_R$). A first-order-accurate scheme is obtained if $\mathbf{U}_L$ and $\mathbf{U}_R$ are assumed equal to the values in the cell center of the respective control volumes, e.g., for the internal control volume in figure 4.3: $\mathbf{U}_L = \mathbf{U}_{cv}$ and $\mathbf{U}_R = \mathbf{U}_{nbr}$. For a second-order-accurate approximation, we use equations (4.9) and (4.10) to estimate the value at the face. For a boundary face, the boundary condition is used for the flux estimation ($\mathbf{U}_R = \mathbf{U}_{bc}$).

In our interface treatment, for interface control volumes, we replace the non-matching faces of the parent meshes with the supermesh elements in the flux balance. At each supermesh element, $\mathbf{U}_L$ and $\mathbf{U}_R$ are taken from the corresponding control volume. Therefore, the supermesh is mapped concerning the parent meshes; for every element of the supermesh, the grid index "i" of the parent meshes control volume mush be known. For example for the interface cell of figure 4.3, the two supermesh elements (sf_1, sf_2) are mapped as follows: sf_1 is the supermesh element shared by control volumes with indices i_{sc} and $i_{nbr,1}$, while sf_2 is shared by i_{sc} and $i_{nbr,2}$. The supermesh construction guarantees the conservation of the flux integral over the whole interface.

References

[1] Lakshminarayana, B., 1991. "An assessment of computational fluid dynamic techniques in the analysis and design of turbomachinery—the 1990 freeman scholar lecture". *Journal of fluids engineering,* **113**(3), pp. 315–352.

[2] Akin, M. B., and Sanz, W., 2014. "The influence of transition on cfd calculations of a two-stage counter-rotating turbine". In ASME Turbo Expo 2014: Turbine Technical Conference and Exposition, American Society of Mechanical Engineers Digital Collection.

[3] Bode, C., Aufderheide, T., Kožulović, D., and Friedrichs, J., 2014. "The effects of turbulence length scale on turbulence and transition prediction in turbomachinery flows". In ASME Turbo Expo 2014: Turbine Technical Conference and Exposition, American Society of Mechanical Engineers Digital Collection.

[4] Walraevens, R., and Cumpsty, N., 1995. "Leading edge separation bubbles on turbomachine blades". *Journal of Turbomachinery,* **117**(1), pp. 115–125.

[5] You, D., Wang, M., Moin, P., and Mittal, R., 2007. "Large-eddy simulation analysis of mechanisms for viscous losses in a turbomachinery tip-clearance flow". *Journal of Fluid Mechanics,* **586**, pp. 177–204.

[6] Schmidt, E., 1980. "Computation of supercritical compressor and turbine cascades with a design method for transonic flows". *Journal of Engineering for Power,* **102**(1), pp. 68–74.

[7] Anand, N., Vitale, S., Pini, M., Otero, G. J., and Pecnik, R., 2019. "Design methodology for supersonic radial vanes operating in nonideal flow conditions". *Journal of Engineering for Gas Turbines and Power,* **141**(2), p. 022601.

[8] Rinaldi, E., Pecnik, R., and Colonna, P., 2016. "Unsteady operation of a highly supersonic organic rankine cycle turbine". *Journal of turbomachinery,* **138**(12), p. 121010.

[9] Schreiber, H., and Starken, H., 1992. "An investigation of a strong shock-wave turbulent boundary layer interaction in a supersonic compressor cascade". *Journal of Turbomachinery,* **114**(3), pp. 494–503.

[10] Sharma, O., and Butler, T., 1987. "Predictions of endwall losses and secondary flows in axial flow turbine cascades". *Journal of turbomachinery,* **109**(2), pp. 229–236.

[11] Lakshminarayana, B., 1970. "Methods of predicting the tip clearance effects in axial flow turbomachinery". *Journal of Basic Engineering,* **92**(3), pp. 467–480.

[12] Gbadebo, S. A., Cumpsty, N. A., and Hynes, T. P., 2005. "Three-dimensional separations in axial compressors". *Journal of turbomachinery,* **127**(2), pp. 331–339.

[13] Baltadjiev, N. D., Lettieri, C., and Spakovszky, Z. S., 2015. "An investigation of real gas effects in supercritical co2 centrifugal compressors". *Journal of Turbomachinery,* **137**(9), p. 091003.

[14] Rinaldi, E., Pecnik, R., and Colonna, P., 2015. "Computational fluid dynamic simulation of a supercritical CO2 compressor performance map". *Journal of Engineering for Gas Turbines and Power,* **137**(7), p. 072602.

[15] Bader, P., and Sanz, W., 2015. "Steady and unsteady cfd calculation of the laminar-to-turbulent transition in a turning mid turbine frame with embedded design". In ASME Turbo Expo 2015: turbine technical conference and exposition, American Society of Mechanical Engineers Digital Collection.

[16] Pini, M., Persico, G., Casati, E., and Dossena, V., 2013. "Preliminary design of a centrifugal turbine for organic rankine cycle applications". *Journal of Engineering for Gas turbines and power,* **135**(4), p. 042312.

[17] Bahamonde, S., Pini, M., De Servi, C., Rubino, A., and Colonna, P., 2017. "Method for the preliminary fluid dynamic design of high-temperature mini-organic rankine cycle turbines". *Journal of Engineering for Gas Turbines and Power,* **139**(8), p. 082606.

[18] Bülten, B., Althaus, W., Weidner, E., and Stoff, H., 2015. "Experimental and numerical flow investigation of a centripetal supersonic turbine for organic rankine cycle applications". In 11th European Conference on Turbomachinery Fluid Dynamics & Thermodynamics, Madrid, Spain, Mar, pp. 23–27.

[19] Harinck, J., Pasquale, D., Pecnik, R., van Buijtenen, J., and Colonna, P., 2013. "Performance improvement of a radial organic Rankine cycle turbine by means of automated computational fluid dynamic design". *Proceedings of the Institution of Mechanical Engineers, Part A: Journal of Power and Energy,* **227**(6), pp. 637–645.

[20] Denton, J., and Dawes, W., 1998. "Computational fluid dynamics for turbomachinery design". *Proceedings of the Institution of Mechanical Engineers, Part C: Journal of Mechanical Engineering Science,* **213**(2), pp. 107–124.

[21] Wang, D., and He, L., 2010. "Adjoint aerodynamic design optimization for blades in multistage turbomachines—part i: Methodology and verification". *Journal of Turbomachinery,* **132**(2), p. 021011.

[22] Pini, M., Persico, G., Pasquale, D., and Rebay, S., 2015. "Adjoint method for shape optimization in real-gas flow applications". *Journal of Engineering for Gas Turbines and Power,* **137**(3), p. 032604.

[23] Li, Z., and Zheng, X., 2017. "Review of design optimization methods for turbomachinery aerodynamics". *Progress in Aerospace Sciences,* **93**, pp. 1–23.

[24] Denton, J. D., 2010. "Some limitations of turbomachinery cfd". In ASME Turbo Expo 2010: Power for Land, Sea, and Air, American Society of Mechanical Engineers, pp. 735–745.

[25] Khawaja, A., and Kallinderis, Y., 2000. "Hybrid grid generation for turbomachinery and aerospace applications". *International Journal for Numerical Methods in Engineering,* **49**(1-2), pp. 145–166.

[26] Katz, A., and Sankaran, V., 2012. "High aspect ratio grid effects on the accuracy of navier–stokes solutions on unstructured meshes". *Computers & Fluids,* **65**, pp. 66–79.

[27] Benek, J., Steger, J., Dougherty, F., and Buning, P., 1986. Chimera. a grid-embedding technique. Tech. rep., ARNOLD ENGINEERING DEVELOPMENT CENTER ARNOLD AFB TN.

[28] Rinaldi, E., Colonna, P., and Pecnik, R., 2015. "Flux-conserving treatment of non-conformal interfaces for finite-volume discretization of conservation laws". *Computers & Fluids,* **120**, pp. 126–139.

[29] de Wiart, C. C., Hillewaert, K., Lorriaux, E., and Verheylewegen, G., 2015. "Development of a discontinuous galerkin solver for high quality wall-resolved/modelled dns and les of practical turbomachinery flows on fully unstructured meshes". In ASME Turbo Expo 2015: Turbine Technical Conference and Exposition, American Society of Mechanical Engineers, pp. V02BT39A035–V02BT39A035.

[30] Krank, B., Fehn, N., Wall, W. A., and Kronbichler, M., 2017. "A high-order semi-explicit discontinuous galerkin solver for 3d incompressible flow with application to dns and les of turbulent channel flow". *Journal of Computational Physics,* **348**, pp. 634–659.

[31] Hoffren, J., Talonpoika, T., Larjola, J., and Siikonen, T., 2002. "Numerical simulation of real-gas flow in a supersonic turbine nozzle ring". *Journal of engineering for gas turbines and power,* **124**(2), pp. 395–403.

[32] Colonna, P., Harinck, J., Rebay, S., and Guardone, A., 2008. "Real-gas effects in organic Rankine cycle turbine nozzles". *Journal of Propulsion and Power,* **24**(2), pp. 282–294.

[33] Guardone, A., Spinelli, A., and Dossena, V., 2013. "Influence of molecular complexity on nozzle design for an organic vapor wind tunnel". *Journal of engineering for gas turbines and power,* **135**(4), p. 042307.

[34] Pecnik, R., Terrapon, V. E., Ham, F., Iaccarino, G., and Pitsch, H., 2012. "Reynolds-averaged navier-stokes simulations of the Hyshot II scramjet". *AIAA journal,* **50**(8), pp. 1717–1732.

[35] Pecnik, R., Witteveen, J. A., and Iaccarino, G., 2013. "Assessment of uncertainties in modeling of laminar to turbulent transition for transonic flows". *Flow, turbulence and combustion,* **91**(1), pp. 41–61.

[36] Karypis, G., Schloegel, K., and Kumar, V., 1997. "Parmetis: Parallel graph partitioning and sparse matrix ordering library". *Version 1.0, Dept. of Computer Science, University of Minnesota*, p. 22.

[37] Roe, P. L., 1981. "Approximate riemann solvers, parameter vectors, and difference schemes". *Journal of computational physics,* **43**(2), pp. 357–372.

[38] Liou, M.-S., 1996. "A sequel to ausm: Ausm+". *Journal of computational Physics,* **129**(2), pp. 364–382.

[39] Venkatakrishnan, V., 1995. "Convergence to steady state solutions of the euler equations on unstructured grids with limiters". *Journal of computational physics,* **118**(1), pp. 120–130.

[40] Van der Vorst, H. A., 1992. "Bi-CGSTAB: A fast and smoothly converging variant of Bi-CG for the solution of nonsymmetric linear systems". *SIAM Journal on scientific and Statistical Computing,* **13**(2), pp. 631–644.

[41] Spalart, P., and Allmaras, S., 1992. "A one-equation turbulence model for aerodynamic flows". In 30th aerospace sciences meeting and exhibit, p. 439.

[42] Wheeler, A. P., and Ong, J., 2014. "A study of the three-dimensional unsteady real-gas flows within a transonic ORC turbine". In ASME Turbo Expo 2014: Turbine Technical Conference and Exposition, American Society of Mechanical Engineers, pp. V03BT26A003–V03BT26A003.

[43] Lemmon, E. W., and Span, R., 2006. "Short fundamental equations of state for 20 industrial fluids". *Journal of Chemical & Engineering Data,* **51**(3), pp. 785–850.

[44] Colonna, P., and Van der Stelt, T., 2004. "Fluidprop: a program for the estimation of thermo physical properties of fluids". *Energy Technology Section, Delft University of Technology, Delft, The Netherlands, http://www. FluidProp. com*.

[45] Rinaldi, E., Pecnik, R., and Colonna, P., 2014. "Exact jacobians for implicit navier–stokes simulations of equilibrium real gas flows". *Journal of Computational Physics,* **270**, pp. 459–477.

[46] Kunte, H. S., and Seume, J. R., 2013. "Design of a partial admission impulse turbine for an automotive orc-application". In 2nd International Seminar on ORC Power Systems.

[47] Farrell, P., Piggott, M., Pain, C., Gorman, G., and Wilson, C., 2009. "Conservative interpolation between unstructured meshes via supermesh construction". *Computer Methods in Applied Mechanics and Engineering,* **198**(33-36), pp. 2632–2642.

[48] Menon, S., and Schmidt, D. P., 2011. "Conservative interpolation on unstructured polyhedral meshes: An extension of the supermesh approach to cell-centered finite-volume variables". *Computer Methods in Applied Mechanics and Engineering,* **200**(41-44), pp. 2797–2804.

5

Three-dimensional unsteady stator-rotor interactions in a high-expansion ORC turbine

Currently, steady-state and quasi-three-dimensional computational fluid dynamics (CFD) simulations are used to analyze the performance of organic Rankine cycle (ORC) turbines. However, these calculations ignore several loss mechanisms — e.g. secondary flow, shock-shock, and shock-boundary layer interactions — that reduce the performance of the expander. Moreover, little is known about how the three-dimensional effect impacts the performance of a high-expansion ORC turbine. In this chapter, we present a detailed unsteady numerical simulation of a high-expansion ORC turbine via three-dimensional calculations, including the real-gas effects utilizing the numerical infrastructure discussed in Chapter 4. The simulations indicate strong three-dimensional and unsteady effects, especially in the rotor blade passage. Because of the highly supersonic flow at the stator exit, unsteady shock waves emanate from the trailing edge of the stator and interact downstream with a bow shock at the rotor leading edge and a separation bubble in the suction side of the blade. The three-dimensional effects indicate that the blade's height distribution and/or the blade profile (at different span-wise locations) needs to be adjusted to reduce losses — generated by flow separation, secondary flow, and shock waves — and to increase the power output of the simulated high-expansion cantilever ORC turbine. The turbine researcher needs to consider these loss mechanisms, the unsteady and three-dimensional effects, when predicting the stage performance of a high-expansion ORC turbine.

5.1   Introduction

ORC power systems are a viable alternative to convert low-to-medium grade heat sources at temperatures between 120 to 500 °C[1] to electrical power. The thermal energy available from biomass combustion, solar radiation, geothermal reservoirs, or waste heat from industrial processes, is arguably immense. Still, the low temperature of these heat sources is the main drawback for their conversion into electricity. While the operating principle of a steam Rankine cycle is comparable, the working fluid of an ORC is an organic compound with a high molecular-weight. As a result, the fluid can be selected to best match the temperature of the heat source, adding a degree of freedom to the system design, yielding a higher thermal efficiency compared to a steam Rankine cycle for the same conditions[1]. In terms of overall efficiency, the expander is the most critical component because of its direct impact on the overall system performance[2].

The expansion process of an ORC is distinct from its Rankine or Brayton cycle counterpart. First, the expansion takes place close to the working fluid's critical point, in the dense-vapour region, where the ideal gas assumption is invalid. Consequently, complex equations of state (EoS) are necessary to accurately describe organic fluids[3–6]. Second, an ORC expander features a small specific enthalpy drop due to the molecular complexity of the organic fluid. Therefore, the designer can choose a few numbers of stages (one or two) without the expander experiencing from efficiency drop or high rotational speed[1]. As a consequence, large pressure ratios per stage are achieved, as large as 200 in a number of applications. However, the large expansion ratio and the low speed of sound of organic fluids — relative to air or steam — lead to supersonic flows with inevitable shock waves

Table 5.1: Literature on numerical simulations of ORC rotors/turbines with information related to the working fluid, the expander type, the pressure ratio (PR), the simulation approach, and the flow regimen between the stator and rotor.

Reference	Fluid	Expander	PR	Simulation	Flow regime S/R
Pini et al. [8]	MDM	Cantilever	4	Flow through method	Subsonic
Sauret and Yuantong [9]	R143a	Radial inflow	2.7	3D steady	Transonic
Vitale et al. [10]	D4	Radial outflow	5	3D steady	Transonic
Fiaschi et al. [11]	R134a	Radial inflow	5	3D steady	Subsonic
Jubori et al. [12]	Several	Axial	6	3D steady	Subsonic
Harinck et al. [13]	Toluene	Cantilever	> 100	3D steady	Supersonic
White and Sayma [14]	R245fa	Radial inflow	3	3D steady & unsteady	Transonic
Wheeler and Ong [15]	Pentane	Radial inflow	11	3D steady & unsteady	Transonic
Bülten et al. [16]	Methylcyclohexane	Cantilever	60	quasi-3D steady	Supersonic
Rinaldi et al. [17]	Toluene	Cantilever	> 100	quasi-3D unsteady	Supersonic
Persico et al. [18]	MDM	6 stages centrifugal	58	quasi 3D unsteady	Transonic
Marconcini et al. [19]	Cyclopentane	Radial inflow	20	3D steady & unsteady	Transonic
Rubechini et al. [20]	Not specified	Radial inflow	≈ 10	3D steady & unsteady	Transonic

and complex flow features. For these two reasons, mean-line flow models and diagrams derived from experimental data (e.g., Balje diagram), which are commonly used for steam and gas turbines, are not highly reliable for designing ORC turbines[7].

Several efforts in improving the predictive capability and understanding the flow features have been conducted, which are summarized in table 5.1. This literature survey is expanded in the following paragraphs, structured in terms of simulation type, for instance, time-independent / dependent simulations or estimations considering three-dimensional numerical domains.

Most CFD studies of ORC turbomachinery are under the assumption of steady-state with a mixing plane boundary condition at the interface between the stator and the rotor[9–13,16]. Because of the averaging at the interface and the assumption of periodicity in the tangential direction, only one blade passage is simulated per rotor — independent of the number of blades of the turbine stage — making the simulation computationally less expensive. However, because of the mixing plane assumption, the unsteady information between the stator and the rotor is lost. For instance, the impact of the viscous wake emanating from the trailing edge of the stator over the rotor blade can not be quantified[21]. An alternative is to use the frozen rotor approximation. Still, these simulations are physically inconsistent due to the absence of unsteadiness. These types of simulations are unable to accurately estimate unsteady effects that bring insights on otherwise unmeasured loss mechanisms[14,15,17].

To evaluate large expansion ratio ORC turbines (PR> 10) operating with an organic compound with a relatively low speed of sound, it is of paramount importance to consider time-resolved unsteady simulations. Such machines have a transonic/supersonic flow at the exit of the stator. This flow regime enhances the already inherently unsteady flow between the stator and rotor due to the formation of shock waves, which interact with the boundary layer and enhance flow mixing. Several studies that compared both steady and unsteady simulations of an ORC turbine stage with a pressure ratio in the order of 15 are[14,15,19,20]. All these studies reported a significant performance drop in the unsteady

simulation if compared to the steady computation. In particular, Rubechini *et al.*[20] recognized a nearly linear relationship of the relative error between the two computations (steady and unsteady) with the nozzle discharge Mach number. To the authors' knowledge, Rinaldi *et al.*[17] is the first available open literature, which modelled the stator/rotor interaction of an ORC turbine with a PR greater than 100. From this study, the unsteady losses resulted in a 1.4% drop in efficiency. It is obvious from these studies that unsteady effects influence the predicted performance of an ORC turbine with a large pressure ratio.

Three-dimensional (3D) effects are another flow feature in ORC turbines that are frequently overlooked, as only a few studies have accounted for them in their CFD simulations[10,12,13,15]. Most papers consider a two-dimensional (2D) or a quasi-three-dimensional (Q3D) flow, see[16,17]. An article that does consider the full 3D geometry of a high-expansion ORC turbine is Harinck *et al.*[13]. This scientific paper utilized a commercial software, ANSYS CFX, to perform a steady-state simulation of a cantilever ORC turbine. Marconcini *et al.*[19] investigated the unsteady interaction of a radial inflow ORC turbine (PR=20) by performing a full annulus simulation. More recently, Vitale *et al.*[10] performed a 3D simulation of an optimized rotor blade of a radial outflow ORC turbine. Other authors have also performed 3D simulations of ORC turbines but mainly consider standard radial inflow turbines with an expansion ratio of less than 11, see for example[11,12,15].

To the authors' knowledge, the present study is the first CFD investigation of a ORC turbine stage with a pressure ratio larger than 100 which accounts for the combination of real gas effects, unsteady stator/rotor interaction, and three-dimensional effects. The three-dimensional, supersonic (Mach $\approx$ 2.5), and highly unsteady flow of a cantilever single-stage ORC turbine (expansion ratio $\approx$ 100) operating with toluene ($C_6H_5 - CH_3$) as the working fluid, is investigated in the present work. The unsteady Reynolds-averaged Navier-Stokes (RANS) equations[22] are solved with a multi-parameter equation of state[23], to capture the unsteady shock wave interactions and to account for the strong non-linearity of the thermodynamic properties close to the critical point of the organic fluid, respectively. A fully-conservative flux-assembling technique for the treatment of non-matching mesh interfaces[24] is used to model the unsteady interaction between the stator and the rotor. The novelty of this work is that it shows for the first time a detailed analysis of the three-dimensional unsteady phenomena (shock waves, viscous wakes, and shockwave-boundary layer interaction) in high-expansion ORC turbines.

The structured of this chapter is as follows: the computational domain with an overview of the ORC turbine 3D geometry is described in section 5.2. An summary of the numerical infrastructure and the methods — discussed in detailed in chapter 4 — used for the CFD simulations are given in section 5.3. The simulation results are discussed in section 5.4. This includes the flow field at different rotor rotational speeds and the comparison between the quasi-3D and the 3D unsteady simulations of a high-expansion ORC turbine. Finally, the conclusions are presented in section 5.5.

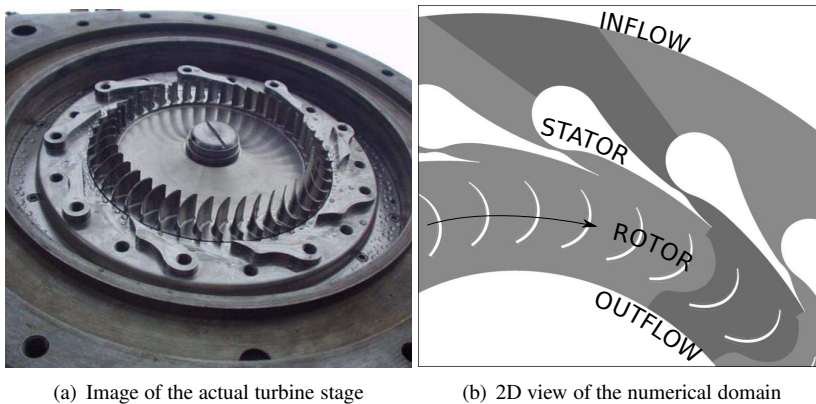(a) Image of the actual turbine stage   (b) 2D view of the numerical domain

Figure 5.1: Geometry and numerical domain of a cantilever ORC turbine: a) Image of the actual turbine stage, b) 2D view of the numerical domain, where we distinguish the domain with dark grey.

5.2 Geometry and computational domain

In the present study, a cantilever turbine (radial inflow-radial outflow turbine) is studied for thermodynamic conditions representative of a commercial ORC unit. The electrical power output of the ORC turbogenerator, manufactured by Tri-O-Gen BV in the Netherlands, is in the range of 150-200 kW. Figure 5.1(a) shows a photograph of Tri-O-Gen's turboexpander which consists of 18 stator nozzles and 43 rotor blades. The simulated numerical domain is illustrated in figure 5.1(b). The expander has a PR> 100 and operates with toluene as working fluid with inlet conditions close to the critical point. The reduced temperature and pressure are in the range of $T_{red} = [0.9, 1.0]$ and $p_{red} = [0.75, 0.85]$, respectively. Moreover, the rotational speed of this ORC turbine is in the range of $\omega = [400, 500]$ Hz. For more detailed information on the ORC turbine please refer to [25].

5.2.1 Turbine stage geometry

We developed our own parametrization to design the stator nozzle and rotor blade, instead of using Tri-O-Gen's turbine geometry. A summary of the thermodynamic and geometrical inputs, used to generate the turbine stage, are depicted in table 5.2.

A innovative in-house methodology to design radial inflow supersonic vanes operating with non-ideal flows was used to generate the supersonic stator, as described in our previous research [26]. For the nozzle design, the flow is assumed to be steady, uniform and isentropic (no viscous losses). Initially, the diverging section of stator vane is designed using the Method of Characteristics (MOC) for an axial configuration. MOC was already extended for fluids near the critical point by Guardone *et al.* 2013 [5]. This super-

Table 5.2: Input parameters for the design of a radial-inflow turbine

	Design parameter	
	Total turbine inlet temperature	$T_{o,in}$
Conditions	Total turbine inlet pressure	$p_{o,in}$
	Static pressure between stator and rotor	p_{sr}
	Static turbine outlet pressure	p_{out}
	Inlet radius	$R_{s,in}$
	Outlet radius	$R_{s,out}$
Stator	Outlet angle	ϕ
	Vane construction parameters	$c_{1,2,3},\, n_{a1,a2},\, n_{b1,b2,b3}$
	Trailing edge thickness	dx
	Leading edge radius	R_{rle}
	Trailing edge radius	R_{rte}
	Leading edge angle	β_{rle}
	Trailing edge angle	β_{rte}
	Leading edge thickness	r_{rle}
Rotor	Trailing edge thickness	r_{rte}
	Stagger angle	δ
	Blade thickness	th
	Blade thickness location	s_{th}
	Blade height distribution	$h_r = f(R_r)$

sonic axial nozzle is then converted into a radial configuration using conformal mapping to conserve the area ratio and the outflow angle. Figure 5.2 illustrates the resulting stator vane with the construction parameters for the converging section of the nozzle. The reader is referred to [26] for more details on the stator vane design methodology.

The geometry of the rotor blade is determined by ten geometrical parameters, as summarized by table 5.2. From Tri-O-Gen's expander, the blade design methodology and the general geometry size of the rotor section are conserved, including the inlet and outlet radii, the blade angles, stagger angle, and the blade height distribution. However, other geometrical inputs, such as the blade thickness and the edges' thickness, are slightly changed.

The procedure to create the blade profile is as follows: first, the leading and trailing points of the blade are created using the rotor radii (R_{rle}, R_{rte}) and the stagger angle (δ). The camber line of the blade is constructed using a Bezier curve, utilizing the leading and trailing location, and the direction given by the blade angles (β_{rle}, β_{rte}). The suction side (SS) and pressure side (PS) of the blade are generated with the blade thickness (th) at a known position (s_{th}) normal to the camber line. The leading and trailing edges are constructed using semi-circles with a given radii (r_{rle}, r_{rte}) to finalize the blade profile. An illustration of the rotor blade parametrization is depicted in figure 5.2.

Cantilever turbines, which are usually of low reaction [27], require an increase of the cross-sectional area due to the expansion of the medium. However, an increase of the
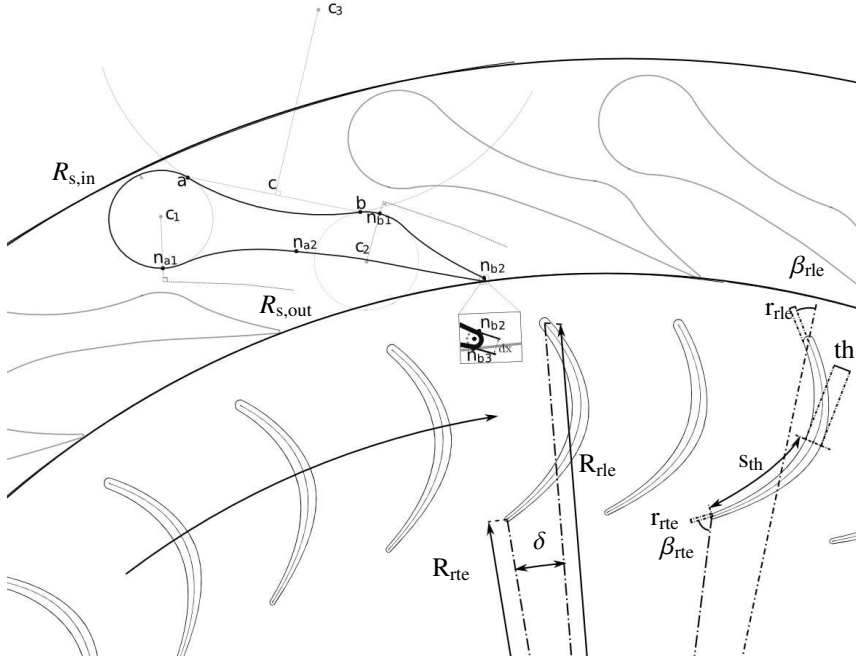
Figure 5.2: Geometrical construction of the radial inflow-radial outflow turbine.

cross-sectional area in the blade passage is difficult to accommodate due to the high volume flow ratio of organic fluids and due to the radial inflow configuration. The blade height distribution (h_r), depicted in figure 5.3, can hence be used as a free parameter to control the cross-sectional area distribution in the rotor passage.

In terms of the construction of the blade in the third direction, the thickness of the blade varies from hub to shroud because of strength and vibrational limitations in the existent machine. Hence the rotor blade is thicker at the root and thinner at the shroud. To account for this mechanical constrain, five blade profiles are generated using the blade parametrization at equally spaced span level surfaces. We interpolate in the span-wise direction to fill the whole three-dimensional structure and create the full 3D blade.

5.2.2 Discretization of the numerical domain

Several approximations are available in the literature to alleviate the computational demand of a 3D unsteady simulation. The most common are the phase-lagged boundary conditions[28], harmonic balance[29], and changing the blade count. While phase lagged can take a long time to converge, the harmonic balance has drawbacks in handling discontinuities at boundaries. We chose to scale the rotor blade count as it represents a trade-off between accuracy and computational cost. The number of rotor blades was decreased to

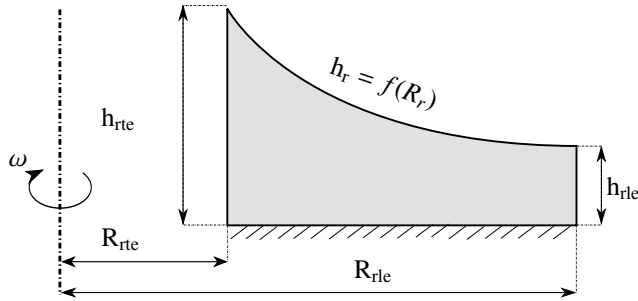Figure 5.3: Geometrical construction of the z-direction of the rotor blade

36, such that the numerical domain consists of two rotor blades per one stator nozzle, see figure 5.1(b). The blade count reduction changes the solidity, which leads to inaccuracies in the blade loading and loss mechanism.

Since this study aims to investigate three-dimensional unsteady effects in a high-expansion ORC turbine, we perform two types of simulations: Q3D and fully 3D simulations. Note, to have a reasonable comparison, the grid topology and number of mesh cells from the Q3D mesh is also used for the 3D mesh at mid-span and then projected towards the respective end walls. This 2D plane grid with a total of 45,000 cells (60% of which are quadrilateral and 40% triangles) is depicted in figure 5.4(a). The nozzle and blade boundary layers are discretized with O-type structured meshes. Their elements are also clustered at the wall, controlled by a hyperbolic tangent function, to achieve a $y^+ \approx 1$.

A Q3D domain corresponds to the meridional plane utilizing a single cell in the span-wise direction. Therefore, it is not possible to observe 3D effects in this type of numerical domain. The cross-sectional area varies with the distance from the axis of rotation to allow the fluid to expand as in the 3D geometry.

A 3D simulation accounts for the whole blade passage in span-wise direction, using 50 cells in this direction, see figure 5.4(b), making it possible to estimate the flow behaviour in the direction normal to the meridional plane. The 3D geometry is discretized into five span-wise level surface, as previously discussed. A 2D grid is only generated at the mid-span location to have an equal number of nodes and therefore correct element connectivity in span-wise direction. Because the blade thickness changes in the span-wise direction, the 2D mesh is smoothed in the other span-wise levels to have a high-quality computational grid. Afterwards, the smoothed 2D grids are projected to their corresponding span-wise level. Finally, a node interpolation in the span-wise direction is performed to fill the three-dimensional domain. The 3D domain is discretized in the span-wise direction by 50 cells, clustered near the walls at the hub and the shroud, achieving a $y^+ < 1$ for most of the hub and shroud; however, close to the rotor leading edge at the shroud the simulations achieved a $y^+_{max} < 10$. Even though a shroud leakage is present in the real machine, the tip-clearance is out of the scope in this research; therefore, we simulate shrouded blades. The computational mesh of the 3D domain consists of over 2.2 million cells.

(a) 2D mesh, constant for all cases

(b) Full 3D
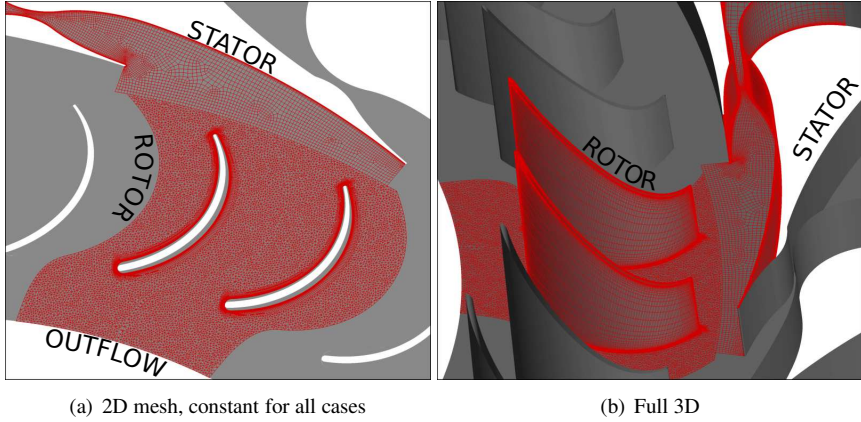
Figure 5.4: Numerical discretization of the computational domain

5.3 Numerical infrastructure and methods

Solver

As discussed in chapter 4, an in-house CFD code is used, which discretizes the compressible Navier-Stokes equation using the finite volume formulation. This in-house code has been extensively validated for turbomachinery flows in previous studies[17,30–32] and more details about the implemented numerical methods and models can be found in[22]. In this work, all simulations are performed with a second-order accurate spatial and temporal discretization scheme.

Thermophysical model

The fluid properties for toluene are obtained with the multi-parameter EoS of Lemmon and Span[23] and tabulated using a look-up table (LUT) approach as discussed in Rinaldi et al.[17]. The ranges for temperature and density are ($T = [310, 390]$ K) and ($\rho = [0.005, 145.0]$ kg/m^3), respectively, using 400 points in each direction. The LUT tabulates pressure, entropy, enthalpy, viscosity, thermal conductivity, and the speed of sound. The computational time with the LUT is drastically reduced, more than 20 times, and the maximum interpolation error is below 0.01%[17].

Turbulence modelling

Turbulence has been modelled with the one-equation turbulence model of Spalart-Allmaras (SA)[33], in accordance to previous authors[15–17]. The SA model equations can be found in Appendix A.1. Moreover, in Chapter 2, the SA model gave accurate results in fully-developed channels with non-ideal gases if compared to direct numerical simulations.

Table 5.3: CFD boundary conditions. [†] To initialize the flow field, a static pressure is prescribed at the outflow.

Numerical domain	Inflow	Outflow[†]	Walls	S/R Interface	Top & bottom	ω [Hz]
Q3D	T_0, p_0, α	$\nabla p = 0$	Adiabatic	Conservative flux assembling technique	$\nabla u_n = 0$	430, 470, 525
3D					Adiabatic wall	

Boundary conditions

The boundary conditions are set as follows: at the turbine inlet constant total conditions, a constant value of the SA scalar ($\tilde{\nu}_{in}$), and velocity angle are given. In the 3D simulation, we impose a zero angle in the span-wise direction of the inflow velocity. Static pressure was prescribed at the outflow to initialize the flow field. Neumann boundary condition is applied later at the outflow because the radial direction of the relative velocity is supersonic; therefore, the outflow is not influenced by the pressure at the outlet. At all walls, a no-slip, a SA scalar equal to zero and adiabatic boundary condition are applied, this includes the stator vane, the rotor blades, and the turbine's hub and shroud of the 3D simulations. On the other hand, for the Q3D simulation, a symmetry boundary is set at the top and bottom of the domain. In table 5.3, a summary is given of the boundary conditions.

A fully-conservative flux-assembling technique for the treatment of non-matching mesh interfaces is used to model the unsteady stator-rotor interaction. An auxiliary mesh is generated at the interface between the stator and rotor by the intersection of the elements of the two non-conformal grids to establish connectivity between the two meshes. When solving an unsteady simulation, where the rotor mesh has a relative motion concerning the stator mesh, the auxiliary mesh updates itself at each time step to establish new connectivity. The conservation of the variables is ensured by calculating the fluxes in the elements of the auxiliary mesh and adding their contribution to the respective control volumes of the original meshes. The reader is referred to Chapter 4 for more details on the flux-conserving technique.

5.4 Results

This section reports the outcome from all unsteady simulations of the high-expansion ORC turbine. We have conducted six simulations, three per domain (Q3D and 3D) which correspond to different rotational speeds, namely 430 Hz ($\approx$ 26 krpm), 470 Hz ($\approx$ 28 krpm), and 530 Hz ($\approx$ 32 krpm). The structure of the results is as follows: first, the convergence of the unsteady simulations and the grid independence of the results are verified. Subsequently, to examine the unsteadiness of the flow field, time-evolution contour plots are employed. Afterwards, the influence of the rotational speed over the flow field, blade loading, and overall performance, is investigated. Finally, the three-dimensional effects are analyzed by visualizing the flow field at different span-wise and by quantitatively comparing the Q3D and 3D simulations.
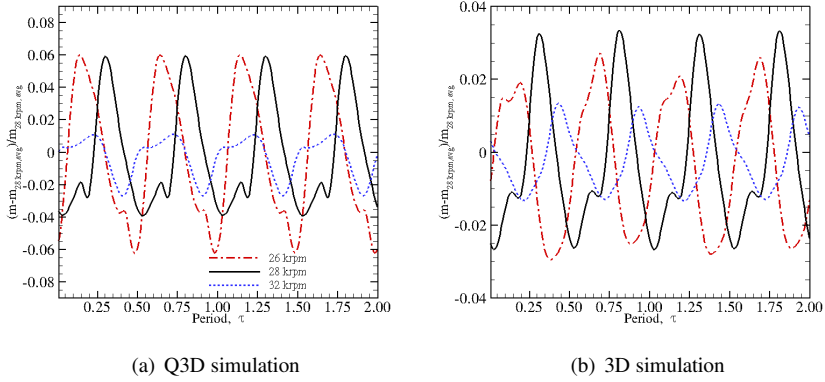
(a) Q3D simulation   (b) 3D simulation

Figure 5.5: Unsteady convergence.

Table 5.4: The quantities' relative differences were calculated for a Q3D simulation with a rotational speed of 28 krpm in a coarse (45,000 elements) and a fine (68,000 elements) grid.

$\Delta\eta_{is}(\%)$	$\Delta\eta_{ts}(\%)$	$\Delta\dot{m}_{S/R}(\%)$	$\Delta H_{o,out}(\%)$	$\Delta p_{o,out}(\%)$	$\Delta s_{out}(\%)$
0.083	0.129	0.144	0.045	0.001	0.032

5.4.1 Simulation and grid convergence

An unsteady simulation is converged when a characteristic quantity of the calculation becomes periodic in time. For all simulations, we have verified the convergence with the transient statistics of the mass flow rate, see figure 5.5. The frequency of the mass flow signal in figure 5.5 is related to the passing of a rotor blade (two blade passing per period).

To ensure mesh-independent results, we performed a Q3D simulation on a fine grid, which was determined using a grid refinement strategy to the grid depicted in figure 5.4(a). We evaluate grid convergence in terms of the turbine stage performance, mass flow rate between stator and rotor ($\tilde{\dot{m}}_{S/R}$), and outflow averaged (in space and in time) conditions (total enthalpy $\tilde{H}_{o,out}$, total pressure $\tilde{p}_{o,out}$, and entropy $\tilde{s}_{out}$), see table 5.4. Throughout Chapters 5 and 6, turbine performance is measured by isentropic efficiency $\eta_{is} = \left(\tilde{H}_{in} - \tilde{H}_{out}\right) / \left(\tilde{H}_{in} - \tilde{H}_{out,is}\right)$ and the total-to-static efficiency $\eta_{ts} = \left(\tilde{H}_{in,0} - \tilde{H}_{out,0}\right) / \left(\tilde{H}_{in,0} - \tilde{H}_{out,is}\right)$. The relative difference between the fine and coarse grid is of $< 0.2\%$ for all reported quantities in table 5.4. It is therefore justified to use the mesh described in section 5.2.2.
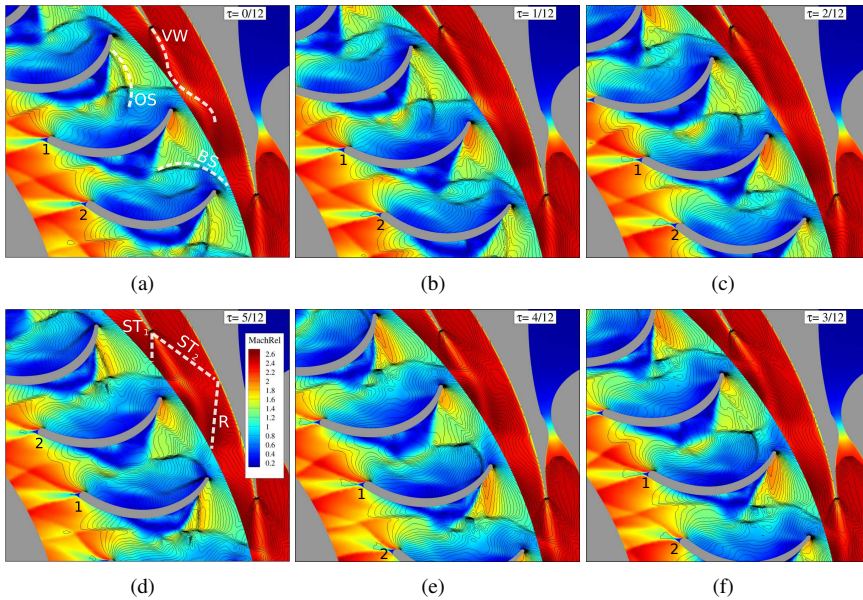
Figure 5.6: Time evolution of the relative Mach number contour with isobaric lines for the Q3D numerical domain with a rotational speed of 28 krpm.

5.4.2 Unsteady flow interaction

In figures 5.6 and 5.7, we present the time evolution of the relative Mach number contour with isobaric lines of the Q3D and 3D simulations, respectively, for a speed of 28 krpm. We have limited our analysis to half the angular period — the rotation of one rotor blade — given the periodic nature of the flow field. In these plots, and all contour plots in Chapter 5 and 6, the isobars — depicted as continuous black lines — illustrate a pressure ratio of 100. A cluster of pressure lines represent a strong pressure gradient, which indicates a shock wave. Therefore, the unsteady interaction of shock waves and viscous wakes can be visualized using theses plots.

The flow features in the static passage are typical of a radial inflow supersonic stator vane. Because of the high-expansion of the turbine, the flow is accelerated to sonic conditions at the throat of the stator and later becomes supersonic in the divergent section. A highly supersonic flow is reached at the end of the nozzle, with a Mach number of around 2.7. As the flow enters in the free expansion region between the stator and the rotor, the supersonic flow can not maintain its direction due to the flow coming from the adjacent nozzle. Therefore, two oblique shock waves, ST_1 and ST_2 in figure 5.6(d), emanate from the stator trailing edge (STE). The shock wave ST_1 directly enters the rotor passage, while ST_2 hits the neighboring stator wall. This shock wave is then reflected (R) towards the rotor as well, as can be seen in the pressure gradient contour in figure 5.8(a). Both shock waves disturb the flow field downstream. However, these are weak oblique shocks and do
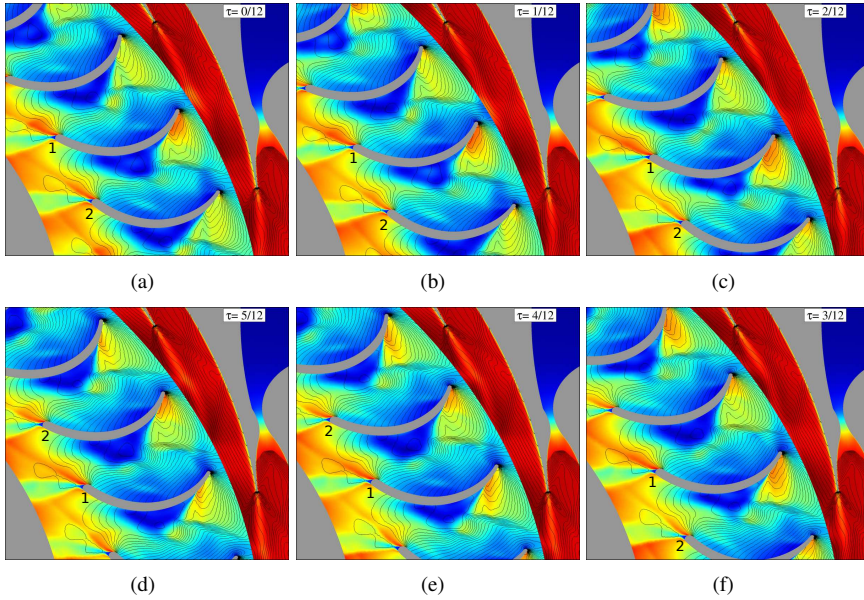
Figure 5.7: Time evolution of the relative Mach number contour at mid-span (50%) with isobaric lines for the 3D numerical domain with a rotational speed of 28 krpm. Contour scale is same as figure 5.6.

not generate strong recompression in the semi-bladed region between the stator and rotor. Thus the design of the stator blade achieves the desired expansion ratio.

The rotor blade suffers from several flow phenomena that increase losses. A bow shock is formed at the rotor leading edge (RLE) because the flow is supersonic in the relative frame of reference (relative Mach number is approximately 1.25). Moreover, the flow becomes detached at the suction side (SS) of the blade inducing a recirculation bubble and another oblique shock wave. The flow detachment is likely produced by the strong curvature of the suction side and an excessive incidence angle at the RLE. Because of the increase of the cross-sectional area in the blade passage, the flow continues to accelerate; therefore, two oblique shocks emanate from the rotor trailing edge (RTE). Two obvious solutions to reduce losses in the rotor passage are (1) a thicker blade that would reduce the flow recirculation on the SS, and (2) a higher rotational speed to have a subsonic flow in the relative frame of reference at the inlet of the rotor. The latter solution is discussed in the next section, where the flow field of a higher rotational speed is analyzed while the former solution is considered in Chapter 6.

In terms of the type of domain, the contours of the Q3D and 3D (at mid-span) simulations, see figures 5.6-5.7, have similar flow field structures with disparities on key features especially in the rotor. The agreement is satisfactory in the stator nozzle between both simulation. Therefore, we infer that the flow field structures in the stator nozzle are
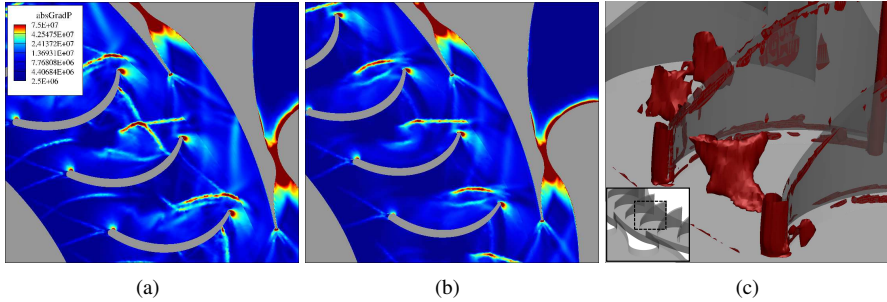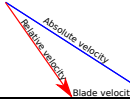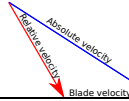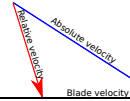
Figure 5.8: Snapshot of the magnitude of the pressure gradient field for 28 krpm: (a) Q3D simulation; (b) XY view, 3D simulations; and (c) Iso-surfaces of the pressure gradient (= 3 10^7).

not influenced by the three-dimensional effects. In the rotating domain, we can see that the shock waves are weaker in the 3D simulation at mid-span, confirmed by the snapshot of the pressure gradient in figure 5.8(a)-(b). However, the bow shock in the 3D simulation is part of a larger 3D shock as seen in figure 5.8(c). In terms of viscous induced structures, the flow separation at the SS of the blade is present in both simulations. From these results, we can already identify differences between a Q3D and 3D simulations of a high-expansion ORC turbine, e.g., the shock waves structures in the rotor section.

Figures 5.6 and 5.7 also reveal unsteady nature of the flow between the stator and the rotor, and in the rotor blade passage. To avoid redundancy, we will only discuss the unsteady shock wake interaction for the Q3D simulation. Following three unsteady structures within the old rotor blade passage one can observe the viscous wake (VW) of the STE, the bow shock (BS) at the RLE, and the oblique shock (OS) emanating from the flow separation of the SS of the blade; all named in figure 5.6(a). The blade rotation influences the shock waves (ST$_1$ and ST$_2$) and VW from the STE, generating a highly unsteady flow between stator and rotor. From $\tau = 3/12$ to $\tau = 5/12$, the BS at the RTE of blade 2 interacts with the VW emanating from the STE. This interaction continues until the wake enters the rotating domain, seen at $\tau = 1/12$ and $\tau = 2/12$ for the BS of the RTE of blade 1. From $\tau = 0/12$ we observe — between the PS of blade 1 and SS of blade 2 — how the BS and OS interact with each other, thereby unfolding a complex flow field in this area. This shock-shock interaction is rotating with the flow, as illustrated at $\tau = 1/12 - 3/12$ until it impinges at blade 1 PS at $\tau = 4/12$. At $\tau = 5/12$ the three unsteady structures (BS, OS, and VW) interact with each other near the RLE of blade 1. The detached flow at the SS of the blade is also unsteady, e.g., at $\tau = 3/12$ and $\tau = 4/12$, we observe shock waves induced by the separation bubble of the SS of blade 1. These shock waves are created by the interaction of the VW with the flow separation; this is observed by following the VW that impinges in blade 2 RLE at $\tau = 0/12$ and continues to disturb the flow until $\tau = 3/12$. Between $\tau = 4/12$ and $\tau = 5/12$, the OS at the SS of blade 1 is formed as a consequence of the flow detachment. This OS interacts with

Table 5.5: Averaged Mach numbers — absolute and relative— and representative velocity triangles at the RTE for the Q3D simulations at all rotational speeds.

	26 krpm	28 krpm	32 krpm
Ma_{abs}	2.60	2.57	2.56
Ma_{rel}	1.25	1.15	0.94
Velocity Triangle			

the shock wave induced by the separation and the BS at the RLE of blade 2 ($\tau = 5/12$); this is how the complex shock-shock interaction, already discussed above, is formed. It is important to note that this highly non-uniform flow field and these unsteady interactions can only be captured with unsteady simulations. Accordingly, unsteady simulations are necessary to account for their associated loss mechanism in the stage performance.

5.4.3 Influence of the rotational speed

In low-reaction turbines, the relative Mach number at the inlet of the rotor is inversely proportional to the blade velocity and therefore to the rotational speed of the turbine. This can be easily deduced by evaluating the velocity triangles at the RLE for the simulated conditions, see table 5.5. Therefore, the operator can choose a higher speed, if possible, to reduce shock wave losses in the rotor passage.

A higher rotational speed can prevent several loss mechanisms in the rotor section of the simulated high-expansion ORC turbine. We chose a speed of 32 krpm because at this blade velocity the flow is no longer supersonic in the relative frame of reference, see table 5.5, eradicating the bow shock wave at RLE. This can be visualized in figure 5.9 where the time-averaged entropy contours of the Q3D simulation for all shaft speeds are depicted. From these plots, the increase of thermodynamic entropy is visible at the stator boundary layer due to viscous dissipation, a phenomenon which is rotational speed independent. The bow shock at RLE and the oblique shock wave at the SS of the blade are stronger for lower speed, compare figures 5.9(a)-5.9(b). Another benefit in terms of a higher rotational speed is the decrease in size of the separation bubble at the SS of the blade. If compared to the simulations with lower speeds, namely 26 krpm and 28 krpm, the 32 krpm simulation has less losses related to irreversibilities and shock waves.

The time-averaged, maximum, and minimum values of the pressure distribution at the rotor blade are displayed in figure 5.10 to quantitatively analyse the rotational speed effect on the rotor blade surface. Ideally, the blade loading along the surfaces should be as high and uniform as possible. However, we interpret large oscillations of the blade loading from these figures as the minimum and maximum pressure largely deviate from the time-averaged values, especially at lower shaft speed. For example, the maximum pressure differs from the time-averaged value by around 1 bar at the RLE pressure side for the 26 krpm simulation, see figure 5.10(a). This pressure oscillations are directly related to
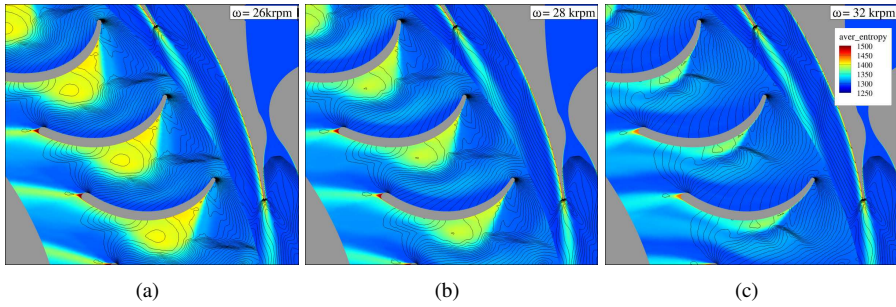
Figure 5.9: Time-averaged entropy contour with time-averaged isobars for the Q3D numerical domain.
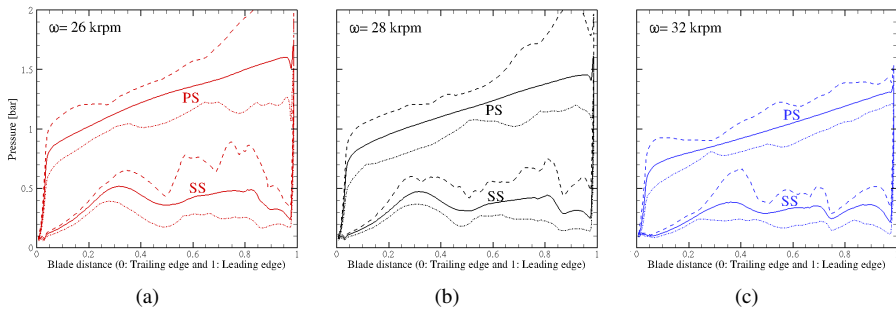

Figure 5.10: Time-averaged (solid lines), maximum (dashed lines), and minimum (dotted lines) values of the blade loading at the suction (SS) and pressure (PS) side of the rotor for a Q3D numerical domain.
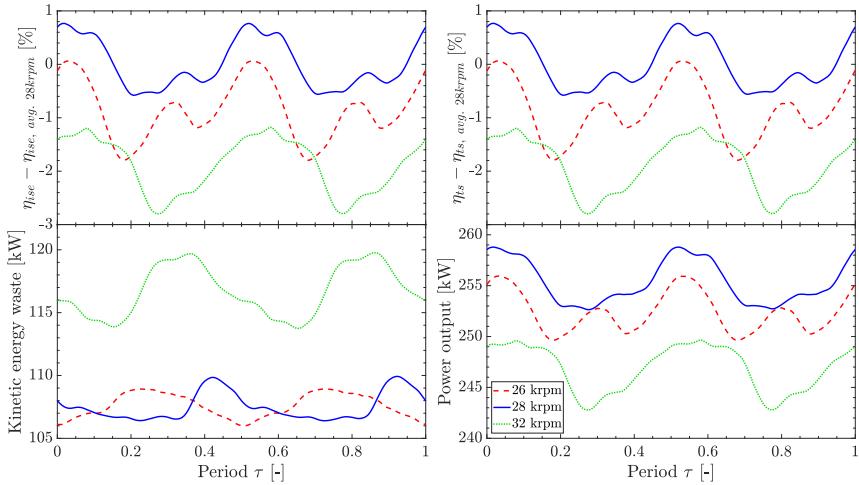
Figure 5.11: Unsteady behaviour of several quantities of interest for a Q3D numerical domain.

the bow shock at the RLE. In these plots, the flow detachment of the rotor blade is visible for the low rotational speed between a blade chord distance of 0.5 and 0.9; a significant variation is seen at this location between the maximum and minimum pressure loading. As such, the forces acting on the blade are highly unsteady (especially for the rotational speeds where the rotor inflow is supersonic in the relative frame of reference) and can be included in the mechanical and vibrational analysis of the rotor blade loading.

If we use the previous results as a reference, we would expect that the performance of the ORC turbine is best at a higher rotational speed. The turbine achieves higher isentropic efficiency at a greater shaft speed, see figure 5.11, a consequence of the already discussed irreversibilities and shock losses. As expected, the amplitude of the η_{is} is greater for lower speeds because the flow field is more unsteady as seen in the blade loading analysis. However, if we measure performance with the total-to-static efficiency the conclusion is the opposite. The turbine performs worst at a higher speed, while at 28 krpm η_{ts} is the highest. This same conclusion is drawn from the power output ($P = \dot{m} \, \Delta H_0$) as depicted in figure 5.11. At a speed of 32 krpm, the rotor blade is not able to turn the fluid to the intended angle; the relative velocity at the rotor exit does not match the metal blade angle as shown by the viscous wake emanating from the RTE in figure 5.9(c). The rotor at the highest simulated rotational speed converts less kinetic energy into mechanical power; more kinetic energy is wasted at the outflow, see figure 5.11. The losses related to kinetic energy at the outflow for 32 krpm exceed the entropy and shock losses for the lower speeds. These results support the importance of a diffuser in high-expansion ORC turbines to recover static pressure from the outflow kinetic energy.

5.4.4   Span-wise flow field analysis

A 3D simulation provides the possibility to investigate the flow of the turbine at all span-wise locations. In this regard, figure 5.12 describes the time-averaged entropy contours for the 3D simulations for all rotational speeds and at three span-wise levels: 10% (near the hub), 50% (at mid-span), and 90% (near the shroud). A more quantitative description of the flow field is shown in figure 5.13, where the accumulative rate of entropy generation per unit volume across the turbine stage is plotted along the radius for the hub (mass averaging between 0% − 35% span), mid-span (35% − 65% span), and shroud (65% − 100% span) sections of the domain. The rate of entropy generation per unit volume[34] is calculated as:

$$\tilde{s}_{gen} = \frac{\tilde{\lambda}}{\tilde{T}^2}\left(\frac{\partial \tilde{T}}{\partial \tilde{x}_i}\right)^2 + \frac{\tilde{\tau}_{ij}}{\tilde{T}} \cdot \frac{\partial \tilde{u}_i}{\partial \tilde{x}_j}, \tag{5.1}$$

where $\tilde{\lambda}$ and $\tilde{\tau}_{ij}$ are the thermal conductivity and the shear stress, respectively.

In terms of the flow field in the stator domain, figure 5.12, there is no change in the span-wise direction. This was already discussed when we compared the unsteady flow contour at mid-span of the 3D and Q3D simulations, see section 5.4.2. However, clear differences are seen in the rate of entropy generated for different span-wise locations, as shown by figure 5.13. There is more entropy generated after the stator throat near the hub and the shroud, as a consequence of the boundary layer formation at the top and bottom stator walls. Still, these losses are not a result of three-dimensional effects. Therefore, the nozzle vane can be designed at mid-span without any consequence in the third direction.

Large differences in the flow field are observed in the span-wise direction in the rotor passage, see figure 5.12. Three important flow features change along the span-wise direction: (1) the size and location of the recirculation at the SS of the blade, (2) the strength of the bow shock at the RLE, and (3) the viscous wake of the RTE. All these differences are a consequence of the three-dimensional effects that are modifying the flow field in the rotor passage.

Contrary to the mid-span, the entropy increase along the rotor passage at the hub are not restricted to the recirculation bubble, compare for example the rotor section in figures 5.12(a) and 5.12(b). All the simulations with different rotational speeds have similar behaviour, check figures 5.12(d) and 5.12(g). The rate of entropy generated in the hub increases faster than at the mid-span section as seen in figure 5.13. These discrepancies between the mid-span and hub are a consequence of the boundary layer at the hub wall.

The flow field near the blade shroud has the highest difference if compared to the mid-span. The flow detachment is at a different location relative to the chord distance of the blade; the separation bubble at the shroud is closer to the RLE, see figures 5.12(c), 5.12(f), and 5.12(i). Moreover, the shape of the flow separation at the shroud is distinct. Figure 5.14 depicts the reason for these differences; a secondary flow caused by the strong flow detachment at the suction side and the high flaring angle of the blade height distribution. The high flaring angle of the height distribution is a consequence of (1) the radial inflow configuration, and (2) the high volume flow ratio. Therefore, the height distribution needs to increase rapidly in the rotor passage to compensate for these two
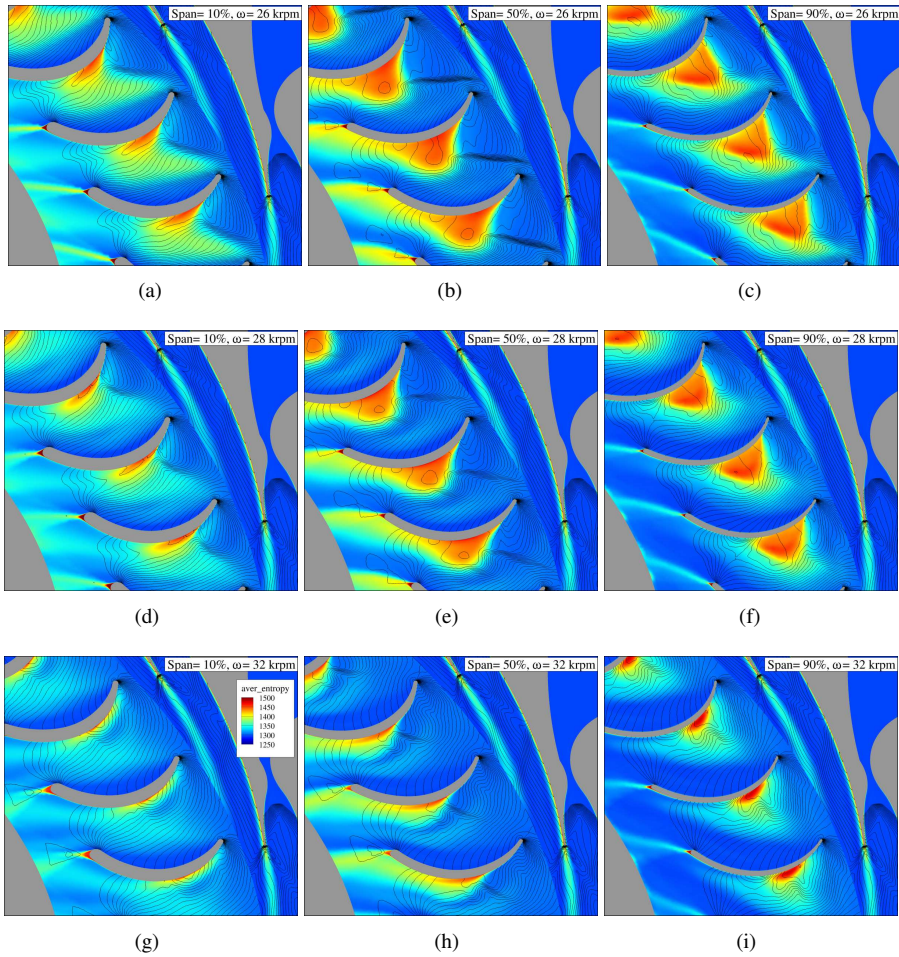
Figure 5.12: Time-averaged entropy contour with time-averaged isobars for the 3D numerical domain for the three rotational speeds and at three span-wise locations.

Figure 5.13: Accumulative rate of entropy generation per unit volume along the radius of the turbine stage at three span-wise sections and at the three rotational speeds.

factors. In this particular case, the high flaring angle in the radial-to-axial bend drives low momentum fluid towards the shroud because of flow recirculation and the meridional stream-wise curvature in the span-wise direction[15]. The flow separation intensifies the secondary flow; at a speed of 32 krpm, the secondary flow is less severe. We discuss the quantitative implication of the secondary flow in the following section. Regarding figure 5.13, the entropy generation increase at the shroud is equivalent to the hub — due to the already discuss near-wall effects — until the location where the height distribution starts to change in the rotor passage. An increase in the rate of entropy generation due to the secondary flow is seen at the inlet of the rotor passage for the shroud section, take for example at a speed of 28 krpm in figure 5.13. The 3D effects are actively modifying the flow field inside the high-expansion ORC turbine; therefore, the designer needs to consider these span-wise effects during the design phase by adapting both the blade profile and height distribution.

The time-averaged contours of the entropy of the Q3D and 3D simulation have similarities and difference, as shown by figures 5.9 and 5.12. In terms of rotational speed, the conclusions fromthe 3D simulation follow the ones discussed for the Q3D in section 6.3.2.2; a higher shaft speed results in no bow shock at the RTE and a smaller recirculation at the SS of the rotor passage. Moreover, the results from figure 5.13 correspond with the isentropic efficiency of figure 5.11(a); the lower speed has the greatest rate of entropy generated while for high rotational speed this is less. In terms of the entropy contour, the 3D flow field has a higher rate of entropy generated for all shaft speeds. The difference between performing Q3D and 3D simulations are apparent by qualitative inspecting the flow field. In the following, a more quantitative approach is applied to study the difference between these two types of simulations.
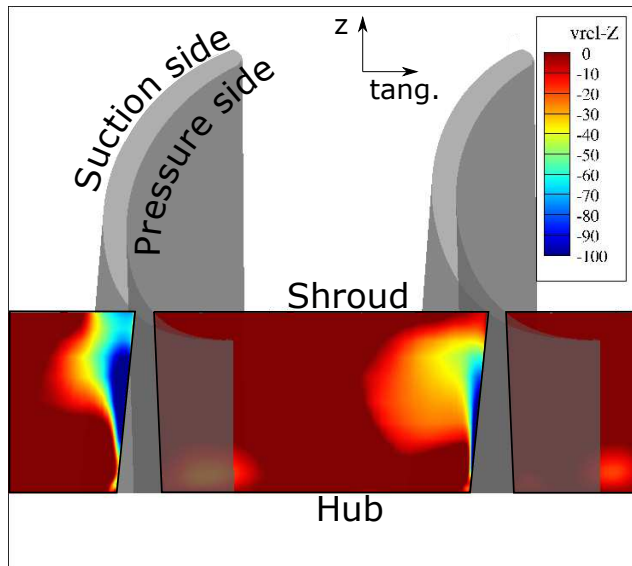
Figure 5.14: Radius iso-surface snapshot with a contour of the relative velocity in the z-direction at $\tau = 5/12$.

5.4.5 Quantitative comparison between 3D and Q3D simulations

The rate of entropy generation of the 3D simulation, including the whole span, is always higher than for the Q3D simulation for the same rotational speed. Figure 5.15 gives a quantitative representation of the rate of entropy generation increase relative to the turbine stage radius in the Q3D and 3D simulations; the latter considers the entropy generation increase for the whole numerical domain and only for the mid-span section (35% to 70% span). The rate of entropy generation in the stator is negligible until the throat. In the diverging part of the stator nozzle, there is a large increase in the rate of entropy generation for all simulations. The blade passage has a substantial increase in the cumulative rate of entropy generation, which is directly proportional to the flow detachment at the suction side of the blade.

The accumulated rate of the entropy generated across the turbine stage is comparable between the two simulations — Q3D and 3D — at mid-span. In the stator nozzle and until the RLE, both simulation types have equivalent accumulated rate of entropy generation. However, for the 26 krpm and 28 krpm, the parity between both type of simulations ends at the rotor passage; the secondary flow on the 3D simulations increases the accumulated rate of entropy generation. For high rotational speed — where the secondary flow is less dominant — this parity between the two simulations type is partially maintained across the rotor passage, see 32 krpm in figure 5.15. Consequently, the 3D effects, i.e., the secondary flow, have a substantial impact in terms of entropy generation across the rotor of the simulated high-expansion ORC turbine.
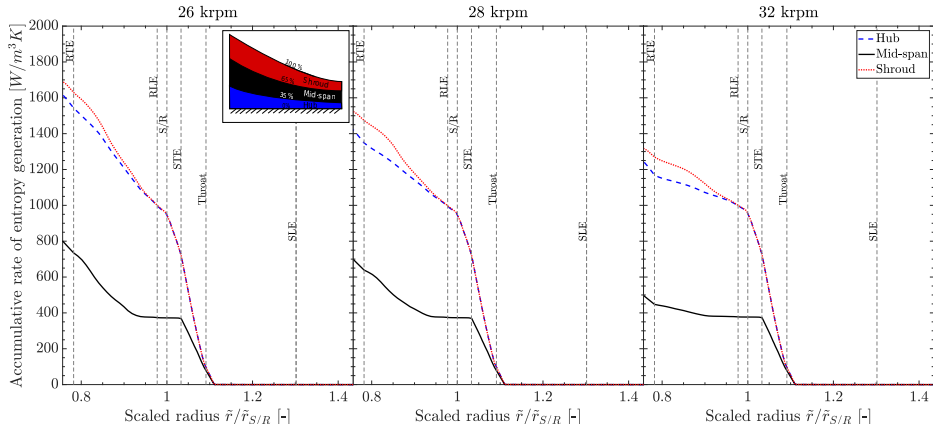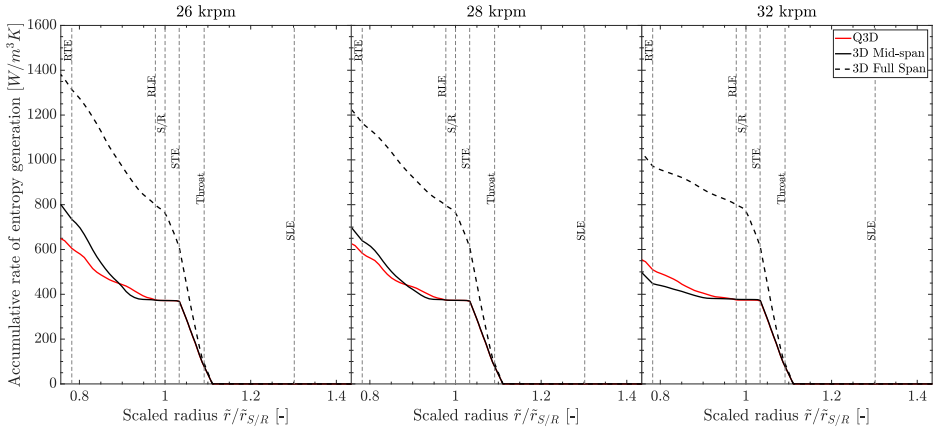
Figure 5.15: Accumulative rate of entropy generation per unit volume along the radius of the turbine stage for the Q3D and 3D simulations at the three rotational speeds.

Table 5.6: Deviation of the time-averaged performance between the Q3D and 3D simulations for the three rotational speeds. The deviations are defined as $\Delta\phi = \phi_{Q3D} - \phi_{3D}$.

	26 krpm	28 krpm	32 krpm
$\Delta\eta_{is}$ [$\Delta\%$]	3.12	3.15	3.54
$\Delta\eta_{ts}$ [$\Delta\%$]	0.98	1.19	0.96
Δ kinetic energy wasted [ΔkW]	12.9	12.0	14.7
ΔP [ΔkW]	15.0	15.3	14.0

The 3D calculations show a worse performance of the high-expansion ORC turbine compared to the Q3D counterpart for all simulated rotational speeds. Table 5.6 reports the deviation between the Q3D and 3D simulations relative to the isentropic efficiency, the total-to-static efficiency, the kinetic energy wasted, and the power output. There is a $\approx 3\Delta\%$ and $\approx 1\Delta\%$ drop on the 3D simulation relative to isentropic and total-to-static efficiency, respectively, for all shaft speeds. However, the kinetic energy wasted is lower in the 3D simulations, between 12 and 15 kW. Still, the energy wasted because of entropy and shock losses is much greater in the 3D, resulting in less power output: $\approx 15\Delta$kW for all rotational speeds. The additional loss mechanisms, quantifiable by a 3D simulation, decrease the performance of the simulated high-expansion ORC turbine stage.

5.5   Conclusion

Utilizing detailed RANS simulations, we investigated the three-dimensional, supersonic, and highly unsteady flow of a high-expansion ORC turbine operating with toluene as the working fluid. We performed two types of numerical simulations, namely a quasi-three-dimensional and a fully three-dimensional calculations, for three rotational speeds (430 Hz, 467 Hz, and 525 Hz). The fluid expansion takes place close in the dense-vapour region; therefore the fluid's thermodynamic properties were evaluated with a multi-parameter equation of state. The originality of this work is that for the first time the unsteady phenomena of a high-expansion ORC turbine is analyzed via three-dimensional calculations. In a broader sense, our detailed simulation results are valuable for designers in (1) ORC applications with different working fluids under similar thermodynamic conditions (reduced pressure and temperature) and (2) supersonic turbomachinery where there is a strong unsteady shock-wave interaction between the stator and the rotor.

The high-expansion cantilever turbine has an unsteady fluid dynamics. Between the stator and the rotor, there is a strong coupling between the rotation of the blades, and the shock waves and viscous wake emanating from the stator trailing edge. Moreover, these unsteady phenomena emerging from the stator modified the flow field downstream in the rotor passage. As a consequence, the blade loading and stage performance are highly fluctuating. The pressure fluctuation at the leading edge of the blade can be higher than 1 bar. Regarding all the cases simulated, we observed that the unsteady mechanisms are dependent on both the rotational speed and the span-wise location of the turbine.

The three-dimensional simulations resulted in a drop in performance if compared to the quasi-three-dimensional simulations. The performance drop is a consequence of the loss mechanisms quantifiable only with a three-dimensional simulation: the hub and shroud boundary layer, and a secondary flow in the blade passage. As a consequence, the ORC turbine in the three-dimensional simulation had a lower isentropic and total-to-static efficiency, a drop of $\approx 3\Delta\%$ and $\approx 1\Delta\%$, respectively, for all rotational speeds. Moreover, the turbine produced less power, around 15 ΔkW less, in the three-dimensional configuration. On the one hand, regarding the stator section, there are no three-dimensional effects; therefore, the nozzle vane can be designed at mid-span without any consequence in the span-wise direction. The rotor, on the other hand, is influenced by the three-dimensional

effects, especially a high-expansion ORC turbine at low rotational speed. The flow structures and the entropy increase differ at distinct span-wise locations. Hence, the overall flow field of the simulated turbine can benefit from a variable rotor blade profile in the span-wise direction.

The outcome of our analysis illustrates which are the most relevant aerodynamic features that need to be addressed to increase the performance of the simulated high-expansion ORC turbine. An increase in rotational speed makes the flow at the inlet of the rotor subsonic, partially eliminating shock wave losses. However, the downside of higher rotational speed for the simulated turbine is the decrease in power because the turbine converts less fluid flow energy into torque; the ORC turbine is wasting kinetic energy at the rotor outflow. Therefore, we advise having a diffuser after the turbine stage capable of converting this energy into pressure. In all simulated cases, we observed flow detachment at the suction side of the blade. A thicker blade profile can reduce the viscous losses and limit the entropy increase in the rotor passage. Finally, the designer of the high-expansion ORC turbine needs to analyze the effect of the height distribution — more specifically the flaring angle — relative to secondary flow at the rotor passage.

In the following chapter, we propose a design procedure for high-expansion ORC turbines that includes an extra step: an assessment of the turbine design employing three-dimensional unsteady simulations. We apply this procedure to the expansion process discussed in this chapter and generate a new high-expansion ORC turbine geometry.

References

[1] Colonna, P., Casati, E., Trapp, C., Mathijssen, T., Larjola, J., Turunen-Saaresti, T., and Uusitalo, A., 2015. "Organic Rankine cycle power systems: from the concept to current technology, applications, and an outlook to the future". *Journal of Engineering for Gas Turbines and Power,* **137**(10), p. 100801.

[2] Macchi, E., 2013. "The choice of working fluid: the most important step for a successful organic rankine cycle (and an efficient turbine)". In Second International Seminar on ORC Power Systems, Rotterdam, The Netherlands, Oct, pp. 7–8.

[3] Hoffren, J., Talonpoika, T., Larjola, J., and Siikonen, T., 2002. "Numerical simulation of real-gas flow in a supersonic turbine nozzle ring". *Journal of engineering for gas turbines and power,* **124**(2), pp. 395–403.

[4] Colonna, P., Harinck, J., Rebay, S., and Guardone, A., 2008. "Real-gas effects in organic Rankine cycle turbine nozzles". *Journal of Propulsion and Power,* **24**(2), pp. 282–294.

[5] Guardone, A., Spinelli, A., and Dossena, V., 2013. "Influence of molecular complexity on nozzle design for an organic vapor wind tunnel". *Journal of engineering for gas turbines and power,* **135**(4), p. 042307.

[6] Wheeler, A. P., and Ong, J., 2013. "The role of dense gas dynamics on organic Rankine cycle turbine performance". *Journal of Engineering for Gas Turbines and Power,* **135**(10), p. 102603.

[7] Persico, G., and Pini, M., 2017. "Fluid dynamic design of organic rankine cycle turbines". In *Organic Rankine Cycle (ORC) Power Systems*. Elsevier, pp. 253–297.

[8] Pini, M., Persico, G., Pasquale, D., and Rebay, S., 2015. "Adjoint method for shape optimization in real-gas flow applications". *Journal of Engineering for Gas Turbines and Power,* **137**(3), p. 032604.

[9] Sauret, E., and Gu, Y., 2014. "Three-dimensional off-design numerical analysis of an organic Rankine cycle radial-inflow turbine". *Applied Energy,* **135**, pp. 202–211.

[10] Vitale, S., Pini, M., Ghidoni, A., and Colonna di Paliano, P., 2015. "Fluid dynamic design and analysis of a highly loaded centrifugal rotor for mini ORC power systems". In 3rd International Seminar on ORC Power Systems, Brussels, Belgium, 12-14 October 2015, ASME.

[11] Fiaschi, D., Innocenti, G., Manfrida, G., and Maraschiello, F., 2016. "Design of micro radial turboexpanders for ORC power cycles: From 0d to 3d". *Applied Thermal Engineering,* **99**, pp. 402–410.

[12] Al Jubori, A., Al-Dadah, R. K., Mahmoud, S., Ennil, A. B., and Rahbar, K., 2017. "Three dimensional optimization of small-scale axial turbine for low temperature heat source driven organic Rankine cycle". *Energy conversion and management,* **133**, pp. 411–426.

[13] Harinck, J., Pasquale, D., Pecnik, R., van Buijtenen, J., and Colonna, P., 2013. "Performance improvement of a radial organic Rankine cycle turbine by means of automated computational fluid dynamic design". *Proceedings of the Institution of Mechanical Engineers, Part A: Journal of Power and Energy,* **227**(6), pp. 637–645.

[14] White, M., and Sayma, A., 2016. "Investigating the effect of changing the working fluid on the three-dimensional flow within organic Rankine cycle turbines". In ASME Turbo Expo 2016: Turbomachinery Technical Conference and Exposition, American Society of Mechanical Engineers, pp. V003T25A002–V003T25A002.

[15] Wheeler, A. P., and Ong, J., 2014. "A study of the three-dimensional unsteady real-gas flows within a transonic ORC turbine". In ASME Turbo Expo 2014: Turbine Technical Conference and Exposition, American Society of Mechanical Engineers, pp. V03BT26A003–V03BT26A003.

[16] Bülten, B., Althaus, W., Weidner, E., and Stoff, H., 2015. "Experimental and numerical flow investigation of a centripetal supersonic turbine for organic rankine cycle applications". In 11th European Conference on Turbomachinery Fluid Dynamics & Thermodynamics, Madrid, Spain, Mar, pp. 23–27.

[17] Rinaldi, E., Pecnik, R., and Colonna, P., 2016. "Unsteady operation of a highly supersonic organic rankine cycle turbine". *Journal of turbomachinery,* **138**(12), p. 121010.

[18] Persico, G., Romei, A., Dossena, V., and Gaetani, P., 2018. "Impact of shape-optimization on the unsteady aerodynamics and performance of a centrifugal turbine for orc applications". *Energy,* **165**, pp. 2–11.

[19] Marconcini, M., Rubechini, F., Arnone, A., Del Greco, A. S., and Biagi, R., 2012. "Aerodynamic investigation of a high pressure ratio turbo-expander for organic rankine cycle applications". In Turbo Expo: Power for Land, Sea, and Air, Vol. 44748, American Society of Mechanical Engineers, pp. 847–856.

[20] Rubechini, F., Marconcini, M., Arnone, A., Del Greco, A. S., and Biagi, R., 2013. "Special challenges in the computational fluid dynamics modeling of transonic turbo-expanders". *Journal of Engineering for Gas Turbines and Power,* **135**(10), p. 102701.

[21] Mailach, R., and Vogeler, K., 2004. "Rotor-stator interactions in a four-stage low-speed axial compressor—part i: Unsteady profile pressures and the effect of clocking". *Journal of Turbomachinery,* **126**(4), pp. 507–518.

[22] Pecnik, R., Terrapon, V. E., Ham, F., Iaccarino, G., and Pitsch, H., 2012. "Reynolds-averaged navier-stokes simulations of the Hyshot II scramjet". *AIAA journal,* **50**(8), pp. 1717–1732.

[23] Lemmon, E. W., and Span, R., 2006. "Short fundamental equations of state for 20 industrial fluids". *Journal of Chemical & Engineering Data,* **51**(3), pp. 785–850.

[24] Rinaldi, E., Colonna, P., and Pecnik, R., 2015. "Flux-conserving treatment of non-conformal interfaces for finite-volume discretization of conservation laws". *Computers & Fluids,* **120**, pp. 126–139.

[25] van Buijtenen, J., Larjola, J., Turunen-Saaresti, T., Honkatukia, J., Esa, H., Backman, J., and Reunanen, A., 2003. "Design and validation of a new high expansion ratio radial turbine for ORC application". In Proceedings of the Fifth European Conference on Turbomachinery, pp. 1–14.

[26] Anand, N., Vitale, S., Pini, M., Otero, G. J., and Pecnik, R., 2019. "Design methodology for supersonic radial vanes operating in nonideal flow conditions". *Journal of Engineering for Gas Turbines and Power,* **141**(2), p. 022601.

[27] Weiß, A. P., 2015. "Volumetric expander versus turbine–which is the better choice for small ORC plants". In 3rd International Seminar on ORC Power Systems, October, pp. 12–14.

[28] Schennach, O., Pecnik, R., Paradiso, B., Göttlich, E., Marn, A., and Woisetschläger, J., 2008. "The effect of vane clocking on the unsteady flow field in a one-and-a-half stage transonic turbine". *Journal of turbomachinery,* **130**(3).

[29] Rubino, A., Pini, M., Colonna, P., Albring, T., Nimmagadda, S., Economon, T., and Alonso, J., 2018. "Adjoint-based fluid dynamic design optimization in quasi-periodic unsteady flow problems using a harmonic balance method". *Journal of Computational Physics,* **372**, pp. 220–235.

[30] Pecnik, R., Rinaldi, E., and Colonna, P., 2012. "Computational fluid dynamics of a radial compressor operating with supercritical CO_2". *Journal of Engineering for Gas Turbines and Power,* **134**(12), p. 122301.

[31] Pecnik, R., Witteveen, J. A., and Iaccarino, G., 2013. "Assessment of uncertainties in modeling of laminar to turbulent transition for transonic flows". *Flow, turbulence and combustion,* **91**(1), pp. 41–61.

[32] Rinaldi, E., Pecnik, R., and Colonna, P., 2015. "Computational fluid dynamic simulation of a supercritical CO2 compressor performance map". *Journal of Engineering for Gas Turbines and Power,* **137**(7), p. 072602.

[33] Spalart, P., and Allmaras, S., 1992. "A one-equation turbulence model for aerodynamic flows". In 30th aerospace sciences meeting and exhibit, p. 439.

[34] Sciacovelli, A., Verda, V., and Sciubba, E., 2015. "Entropy generation analysis as a design tool—a review". *Renewable and Sustainable Energy Reviews,* **43**, pp. 1167–1181.

6

Detailed design assessment of a high-expansion ORC turbine

The design of an organic Rankine cycle (ORC) turboexpander is a challenging procedure due to the non-ideal thermo-physical behavior of organic fluids and the large expansion ratio per stage, which can lead to a real-gas transonic/supersonic flow inside the machine. Moreover, the lack of experimental data of organic vapors at the conditions of interest complicates the process even further. In this context, ORC turbine designers apply standard design tools based on empirical loss models and shape optimization using computational fluid dynamics (CFD) to achieve an aerodynamic design. These methodologies concentrate on delivering a turbine design at the meridional plane, neglecting the span-wise direction. Another loss mechanism commonly overlooked by designers is the unsteadiness flow features between the stator and rotor and in the rotor passage, e.g., shock-shock, and shock-boundary layer interactions. In this chapter, we proposed a design procedure for high-expansion ORC turbines, which includes an extra step: a detail design assessment utilizing high-fidelity CFD models that consider the full three-dimensional geometry and the unsteady features of the flow. We apply our innovative procedure to design a new high-expansion cantilever ORC turbine with an equivalent expansion process as the one discussed in Chapter 5. The detailed blade design consist of an inverse approach which is purely geometrical; the new rotor blade has a smooth flow turning and a steady increase of cross-sectional area. The detail design assessment indicates strong three-dimensional and unsteady effects, especially between the stator and rotor and within the rotor blade passage. The high-expansion of the turbine generates a highly supersonic flow at the end of the stator nozzle; unsteady shock waves and a viscous wake emanate from the stator trailing edge and interact with the mixing zone between the stator and the rotor, and disturb the flow in the rotor passage. The former — the free expansion between stator and rotor — is influenced by the rotor expansion. The three-dimensional effects in the blade passage indicate that radial-to-axial bend can be improved, e.g., by including the span-wise flow direction when estimating the cross-sectional area during the detail design. If compared to the rotor blade design from Chapter 5, the new blade enhances the performance of the turbine stage — higher power output and total-to-static efficiency — by extracting more kinetic energy from the fluid.

6.1   Introduction

Organic Rankine cycle (ORC) power systems are currently a profitable technology for the efficient conversion of low-to-medium grade energy sources to the electricity[1]. Concerning a steam cycle, an ORC takes advantage of the molecularly complex and heavy organic fluid to harness energy from heat sources with temperature levels below 500 °C, while having a simple system configuration and reducing the design complexity. This technology is mature enough to have commercial products; it is competitive in terms of capital/operative cost and reliability. The most crucial component is the expander as it profoundly influences the performance, the cost, and the control of the overall ORC power system[2].

An ORC expansion features a small specific enthalpy drop due to the molecular weight of the organic fluid. The specific work required by the turboexpander is relatively small

if compared to the steam counterpart. Therefore, the designer can choose few number of stages which leads to a compact turbomachinery (less moving parts and lower cost); still, the expansion ratio remains large. The high-expansion ratio per stage and the low speed of sound of organic fluids — compared to steam or air — lead to a transonic or supersonic ORC turbines. Consequently, the flow inside the expander is chocked and shock waves may influence the turbomachinery aerodynamics.

Furthermore, the complexity of ORC expansion is intensified by the non-ideal thermodynamic behaviour of organic fluids in the state conditions of interest; part of the expansion process takes place in closed proximity to the thermodynamic critical point. The ideal gas assumption is invalid for ORC turbines due to severe real-gas effect[3]; complex multi-parameter equation of state are necessary to properly described the thermodynamic state of the fluid[4].

The aerodynamic design of ORC turbines is particularly challenging because of the transonic/supersonic flow and non-ideal thermodynamic behavior (discussed above). There is limited experimental data regarding the expansion of organic fluids. Moreover, state-of-the-art design methodologies based on empirical loss models used for steam and gas turbine are not highly reliable for ORC turbines. Still, this simplified design tools are used for the preliminary design phase and are later combined with more advance design techniques based in high-fidelity flow models[5].

Several degrees of complexity can be included in the design of ORC turboexpanders. Many studies have gone into detail on this topic in terms of preliminary design methodologies[6–9], shape optimization using computational fluid dynamics (CFD)[10–13], and detail blade design applying the two-dimensional method of characteristics (MOC)[14,15]. All of these studies have concentrated on delivering a turbine design at the meridional plane, neglecting the span-wise direction. This may be an acceptable approximation for the stator nozzle, but for the rotor — and more specifically for a radial inflow turbine — the three-dimensional (3D) effects can become significant depending on the conditions, fluid, and expander architecture[16]. Recently, Jubori *et al.*[17] performed a 3D multi-objective optimization of a small-scale axial turbine for ORC applications, but the authors did not examine the 3D flow features.

Another flow feature commonly ignored at the design phase is the intrinsic unsteady flow between the stator and the rotor. Most studies apply a steady-state assumption for the design of ORC turbines. Most of the high-fidelity design model does not consider the unsteadiness in the turbomachine[5]1; these CFD simulations use the mixing plane assumption at the interface between the stator and rotor[18,19]. The flow in high-expansion ORC turbines can be supersonic causing shock waves to occur that interact with boundary layers and generate losses. These interactions required unsteady time-resolved simulations to capture complex phenomena otherwise overlooked[16,20,21]. Unlike research for conventional gas turbines, there is limited studies on the unsteady three-dimensional supersonic flows inside ORC turboexpanders.

There is a high computational cost involved in time-accurate design problems. To

---

1There are several studies that do consider the unsteady and/or the 3D geometry during the aerodynamic design, see for example[6,13,17]
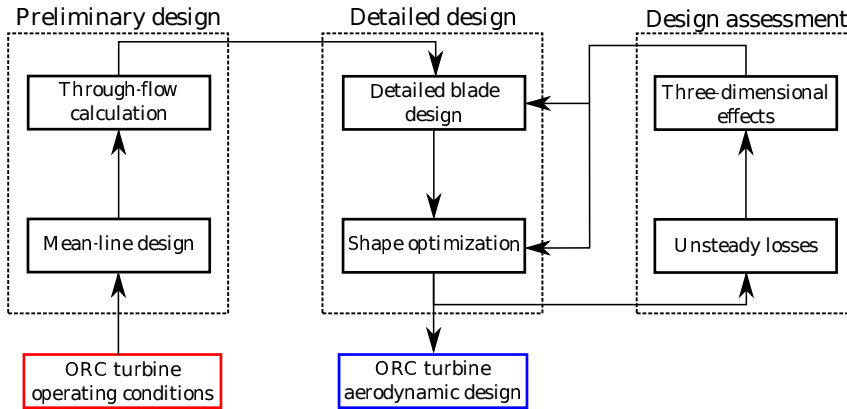
Figure 6.1: Adapted schematic of the fluid-dynamic design process for an ORC turbine [5].

bypass the computational cost of an unsteady CFD simulation, several authors have used reduced-order models [22,23]. For example, Rubino *et al.* [24] performed a shape optimization using the harmonic balance method to characterize the unsteady flow of a turbine cascade. A different approach is to perform a steady-state optimization and asses later the unsteady phenomena. Persico *et al.* [13] performed a shape-optimization of a six-stage ORC centrifugal turbine with a total pressure ratio of 58 (expansion ratio of around 2 per stage) and MDM as working fluid; they indicate that the optimal blades reduce the unsteady stator-rotor interaction.

There is currently no design methodology of an ORC turbine that considers the whole flow field complexity. Persico and Pini described the different phases in an ORC turbine design [5]. First, the preliminary design is made with mean-line design tools and through flow calculations that depend on the operating condition from the cycle; the general seizing of the radii, metal angle, among others, is done at this stage. Later, the detailed blade design is made with CFD, which can include a shape optimization procedure, to finally generate the ORC turbine aerodynamic design. In this study, we add an extra step to this design procedure: a detailed design assessment, as shown by figure 6.1. High-fidelity CFD models are used to solve the whole complexity of the machine: the real-gas effects, the unsteady stator/rotor interaction, and the full 3D geometry. The conclusions from the design assessment can be feedback to the detailed design to create an ORC turbine with higher performance and/or more robustness.

In this chapter, we apply the design path, as depicted in figure 6.1, to a high-expansion cantilever single-stage ORC turbines using toluene ($C_6H_5 - CH_3$) as the working fluid. We consider the same expansion process thoroughly discussed in Chapter 5; therefore, we skip the preliminary design and the detailed stator nozzle design, and only consider the aerodynamic design of the rotor blade. We briefly explain, in section 6.2, the detailed rotor blade design procedure, which includes a shape optimization via a genetic algorithm. The main focus of this chapter is in the detailed design assessment of the new ORC turbine

Table 6.1: Input parameters for the new design of a radial-inflow rotor

Inlet: radius, height	$R_{r,in}$, $h_{r,in}$
Outlet: radius	$R_{r,out}$, $h_{r,out}$
Leading edge: radius, angle, height	R_{rle}, β_{rle}, h_{rle}
Trailing edge: radius, angle, height	R_{rte}, β_{rte}, h_{rte}
Stagger angle	δ
Passage width distribution	$W_r = f(\text{Chord})$

design considering the unsteady and 3D phenomena, including the stator/rotor interaction employing 3D CFD simulations. We analyze the flow field inside the turboexpander in section 6.3, including 3D flow structures, viscous and shock wave losses, and the unsteady stator-rotor interaction.

6.2 Detailed design

We design a radial inflow-radial outflow, also called cantilever turbine, for the expansion conditions of Tri-O-Gen B.V. ORC unit. This ORC turbogenerator has an electrical power output in the range of 150-200 kW. The expander of such a machine has a pressure ratio > 100 and operates with toluene as working fluid with inlet conditions close to the critical point; the reduced temperature and pressure are in the range of T_{red} = [0.9, 1.0] and p_{red} = [0.75, 0.85], respectively. Moreover, the rotational speed of the ORC turbine is in the range of ω = [400, 500] Hz. The expansion process is equivalent to the one discussed in Chapter 5, see[6] for more details.

The turbine blade (hereafter will be named as old blade) from Tri-O-Gen's ORC expander has several aerodynamic flow features that the designer needs to address to increase the power output of the turbine, as discussed in Chapter 5. We observed flow detachment in the suction side of the blade; this mechanism increases the losses, e.g., large entropy generation. In the previous chapter, we managed to reduce the recirculation by increasing the rotational speed, but the power output did not increase due to the significant kinetic energy losses at the outlet of the turbine. In terms of span-wise effects, we discovered a secondary flow in the leading edge of the rotor blade near the shroud, a consequence of the large flow detachment and the height distribution. We aim with the new rotor blade design to reduce these aerodynamic features that hamper the performance of the turbine and, therefore, the overall ORC unit. In terms of the stator, we maintain the stator blade[15] discussed in Chapter 5.

6.2.1 Rotor blade design

We use an inverse design approach to generate a new rotor blade geometry. The methodology to generate the cantilever-type rotor blade is purely geometrical; the idea is to create a rotor blade that has a smooth turning flow and a steady increase in the cross-sectional

(a) Flow line

(b) Blade thickness

(c) Height distribution
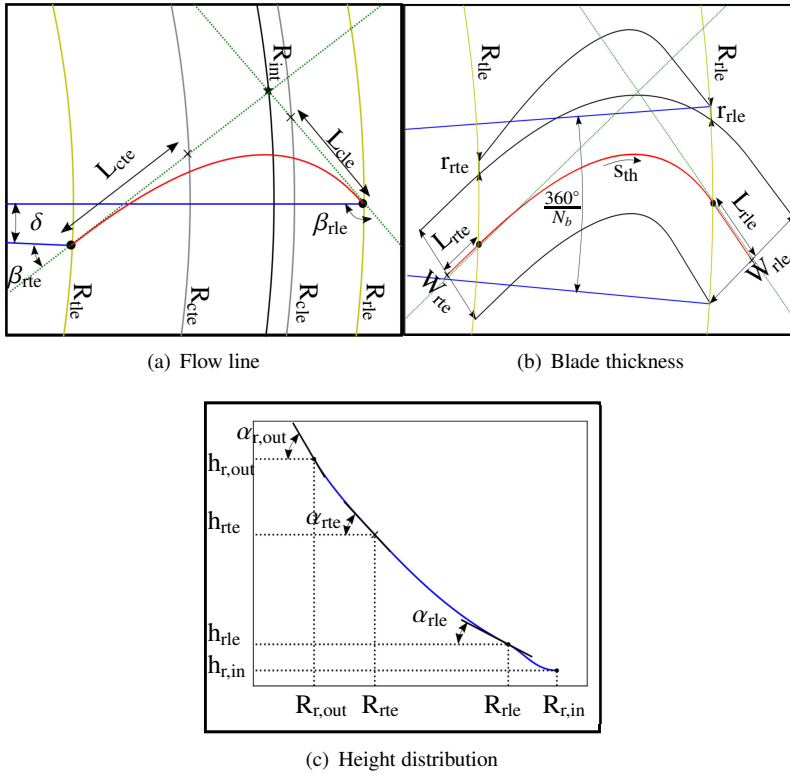
Figure 6.2: Parametrization of the new ORC turbine blade

area. The design of the rotor blade is a function of 18 parameters, as summarized by table 6.1. The procedure to generate a blade geometry — which includes three uncoupled optimization routines — is as follows:

1. **Flow line:** The flow line is constructed using a Bezier curve, as depicted by figure 6.2(a). The inputs for the flow line are the leading and trailing radius (R_{rle}, R_{rte}) and flow angles (β_{rle}, β_{rte}), the stagger angle (δ), and two free parameters (R_{cle}, R_{cte}) to control the Bezier curve. We derive the desire flow line by an optimization routine, which minimizes the curve's second derivative by modifying the free parameters (L_{cte}, L_{cle}, R_{cte}, and R_{cle}).

2. **Blade passage:** The rotor passage is constructed using the flow line — used as the center of the passage — and the width distribution along the passage ($W = f(s_{th})$), see figure 6.2(b). The width of the passage is a linear distribution with respect to the blade chord (s_{th}). To achieve the desire leading and trailing edge thickness (r_{rle}, r_{rte}), the width of the passage undergoes a minimization procedure given the

number of blades (N_b).

3. **Height distribution:** The height of the blade (h_r) is the free parameter we use to achieve the desired cross-sectional area distribution in the blade passage. The cross-sectional area (A_i) is calculated along the flow line by multiplying the width (blade-to-blade distance) normal to the flow field and the height of the blade. Because of the height changes with the radius (R) and consequently along the passage width, we perform a summation across several discretized elements (N_d) as

$$A_i = \sum_{j=1}^{N_d} \left[\frac{W_i}{N_d} h_r \left(R_{i,j} \right) \right]. \tag{6.1}$$

The height distribution is define as a spline of 4 points in the r-z plane (see figure 6.2(c)): rotor inlet, rotor leading edge (RLE), rotor trailing edge (RTE), and rotor outlet. The inputs of the height distribution are the radius of the inlet, RLE, RTE, and outlet ($R_{r,in}$, R_{rle}, R_{rte}, $R_{r,out}$) and the height at the inlet, RLE, and RTE ($h_{r,in}$, h_{rle}, h_{rte}). The 4 free parameters (the height and shroud angle at the rotor outflow, and the shroud angle at the RLE and RTE) are determined by minimizing the second derivative of the cross-sectional area distribution of the rotor passage. Therefore, the rotor passage has a steady increasing of the cross-sectional area distribution.

4. **Blade tips:** The blade profile is closed by constructing the leading and trailing tips. Splines are fitted between the blade camber line, the suction side (SS), and the pressure side (PS). The camber line is approximated as half-way between the SS and the PS.

6.2.2 Shape optimization

To achieve the blade geometry with the best performance, we use a genetic algorithm to find the optimal profile and height distribution as a function of: β_{rle}, β_{rte}, δ, N_b, h_{rle}, and h_{rte}. The objective of the optimization is to minimize the outlet total enthalpy, which essentially results in an increased power output of the turbine stage. We did not aim to maximize the turbine's total-to-static efficiency because the outflow of the domain is supersonic: the outlet boundary static pressure is not fixed. Therefore, the algorithm could inadvertently decrease the pressure ratio of the turboexpander by optimizing the efficiency. The fitness of each blade is estimated by means of Q3D simulations using SU2 (CFD solver)[25] with a mixing plane approximation between the stator and rotor; the mixing plane surface includes a non-reflecting boundary condition as presented by Giles[26]. For further information on the new blade design methodology, the reader is referred to[27].

In figure 6.3, we depicted the resulting blade profile and height distribution from the detailed design methodology including a shape optimization. This figure compares the new blade with the old one from Chapter 5. The blade thickness and the number of blades
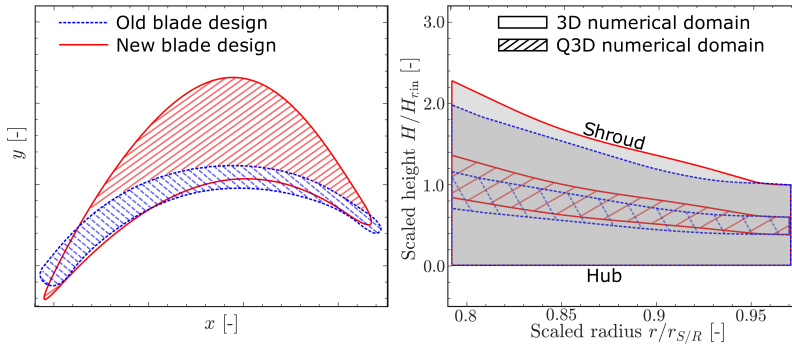
Figure 6.3: Comparison between the old and new blades in terms of profile (left) and height distribution (right).

have increased for the new design. However, to achieve a steady increase in the cross-sectional area, the blade height distribution has also increased, such that the trailing edge height of the new blade is almost 15% larger than the one of the old blade. The flow field of the new blade is analyzed in detail in the following section with unsteady 3D CFD simulations.

The new rotor blade design is planned to be constructed and tested by Tri-O-Gen B.V. The blade profile will remain constant along the span-wise direction; a mechanical analysis performed by the ORC manufacturer prove that no vibrational or strength related issues would arise. Therefore, we consider a prismatic blade for the ORC turbine design assessment.

We do not describe in more detail the rotor design and optimization routine because the focus of this chapter is the design assessment concerning the unsteady and three-dimensional effects of the high-expansion ORC turbine. For more details on our design blade methodology, the reader is referred to Smit *et al.*[27].

6.3 Design assessment

6.3.1 Numerical infrastructure

We use an in-house CFD code that solves the compressible Reynolds-Averaged Navier-Stokes (RANS) equations, developed by Pecnik *et al.*[28], to simulate the ORC turbine. This in-house solver has been already validated for turbomachinery flows in previous studies[21,29–31]. In Chapter 4, we discussed in detail the discretization methods —in time (two-step Backward differentiation scheme) and space (finite volume formulation and second-order accurate) — and the numerical models. The Euler fluxes are calculated using Liou's ASUM$^+$[32] approximate Riemann solver. We model the Reynolds stress with the one-equation Spalart-Allmaras (SA) eddy viscosity model[33] to close the RANS equations. A multi-parameter equation of state[34] is used to represent the fluid properties;
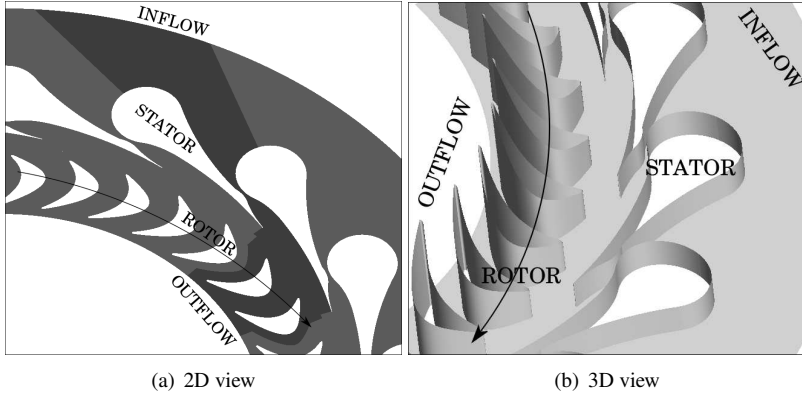
(a) 2D view   (b) 3D view

Figure 6.4: Numerical domain of the new design ORC turbine design. In the 2D view,we distinguish the domain with dark grey.

the computational cost of the properties evaluation is drastically reduced, more than 20 times, by the use of the look-up table interpolation. For more details in the numerical infrastructure and methods, please refer to Chapter 4.

We approximate the new high-expansion ORC turbine design with the numerical domain depicted in figure 6.4; the number of rotating blades was decreased to 36 to reduce the computational domain, which is less than the number of blades (47) derived from the genetic algorithm. Therefore, we model only a section of the turbine — 20° of the whole circumference — including one stator blade per two rotor blades, see figure 6.4(a). We assume periodicity in the azimuthal direction.

We employ two different computational meshes: a Q3D and a 3D, as depicted in the right plot of figure 6.3. Following the discretization methodology described in section 5.2.2, we generate a 2D plane grid at mid-span (see figure 6.5(a)) with a total of 70,000 quadrilateral cells, which is constant for both computational meshes. We generate all boundary layers using an O-mesh, and cells are cluster at the wall in order to have a $y^+ \approx 1$. For the Q3D mesh, the 2D plane grid is generated at mid-span only using one cell in the span-wise direction; the height of this cell changes as a function of the distance from the axis of rotation to include the actual cross-sectional area distribution. For the 3D mesh, we maintained the blade profile constant (it is a prismatic geometry) and prescribed 50 discretization cells in the span-wise direction; the numerical mesh consists of over 3.4 million cells, see figure 6.5(b).

The boundary conditions are specified as follows. Uniform distributions of total pressure, total temperature, eddy viscosity and velocity angle are prescribed at the inlet of the computational domain. At the outflow of the rotor domain the static pressure is prescribed, as long as the radial outflow velocity is subsonic, otherwise, Neumann boundary conditions are specified for all quantities. At all walls no-slip boundary conditions are specified for the velocity and the eddy viscosity is set to zero. Adiabatic boundary con-
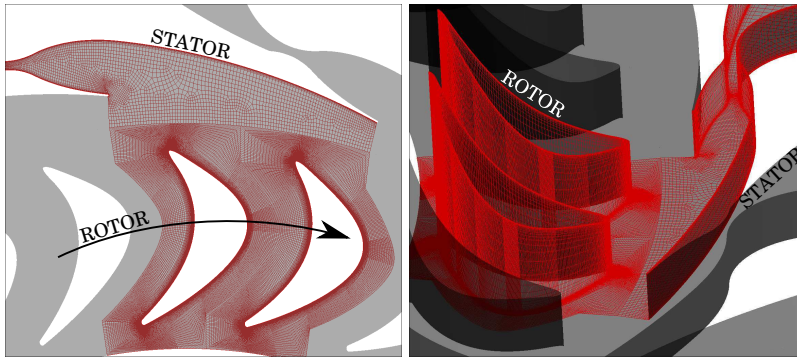
Figure 6.5: Numerical discretization of the computational domain: a) XY view of the mesh, constant for all cases and b) three-dimensional view of the mesh

ditions are applied for the wall temperature, which includes the stator vane, the rotor blades, and the turbine's hub and shroud of the 3D simulations. For the Q3D simulation, a symmetry boundary is set at the top and bottom of the domain. A fully-conservative flux-assembling technique for the treatment of non-matching mesh interfaces is used to model the unsteady stator-rotor interaction, as described in section 4.4.

6.3.2 Simulations results

In this section, we describe the results from the CFD simulations of the new high-expansion ORC turbine design, including the unsteady and 3D effects. First, we analyze the flow features of the ORC turbine, taking a particular focus on the unsteadiness between the stator and rotor, and in the rotor passage. Later, we performed an off-design analysis on the new turbine by presenting simulation results at different rotational speeds. The design speed is 426 Hz ($\approx$ 26 krpm), but in section 6.3.2.2, we increase the speed to 467 Hz ($\approx$ 28 krpm) and 525 Hz ($\approx$ 32 krpm). At the end of this section, we analyze the three-dimensional effects and quantify the performance of the new design; we compare all the results in this section with the old design (discussed in detail in Chapter 5).

6.3.2.1 Unsteady flow interaction

The time evolution of the relative Mach number contour for the Q3D simulations are depicted in figure 6.6; the isobars — depicted as continuous black lines — illustrate a pressure ratio of 100. To avoid any redundancy, we only discuss the unsteady interaction for the Q3D simulation with a rotational speed of 426 Hz. Given the periodic nature of the flow field, we limited our analysis to one rotor blade passage, which is half an angular period.

The flow field in the stator nozzle is typical from a radial inflow supersonic vane. As a consequence of the large pressure ratio, the flow passing through the stator blades
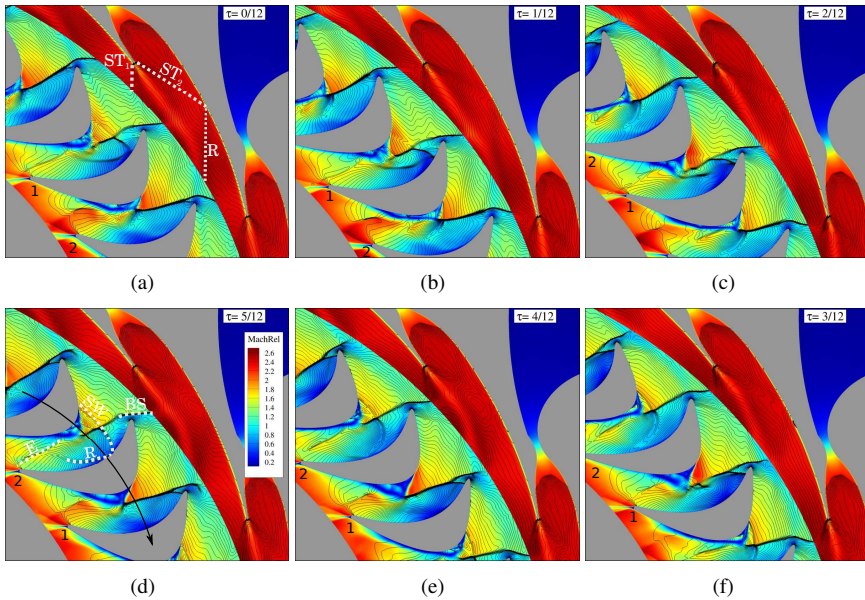
Figure 6.6: Time evolution of the relative Mach number contour with isobaric lines for the Q3D numerical domain with a rotational speed of 26 krpm.

expands to sonic conditions at the throat and later becomes supersonic in the divergent section of the nozzle; the flow achieves a Mach number of around 2.7 at this location. Due to the supersonic nature of the flow in this region and the fact at two streams — one from the suction and one from the pressure side of the stator blade — with different directions collide at the stator trailing edge (STE), two oblique shock waves emanate from the STE, named ST_1 and ST_2 in figure 6.6(a). ST_1 enters directly towards the rotating domain while ST_2 impinges in the boundary layer in the long stator blade wall; the latter is reflected (R) and enters into the rotor passage. Both shock waves (ST_1 and R) disturb the flow field downstream in the rotor passage. ST_1 and ST_2 are weak oblique shocks and do not generate strong recompression between stator and rotor. However, the free expansion area — flow downstream of ST2 — is affected by the rotor as it will be seen later; the rotor further expands the flow because we designed a low-reaction turbine.

The flow field is highly unsteady between the stator and the rotor, and in the rotor passage, consequence of the highly supersonic flow in the nozzle exit, and the rotation of the rotor blades. The oblique shock waves stemming from the STE (ST_1 and ST_2) and its reflection (R) intensifies the non-uniformity of the flow in the region between stator and rotor and in the rotor passage. Because the rotor inlet flow is still supersonic in the relative frame of reference, shock waves are produced in the rotor blade passage. Three shock waves in the rotor blade passage are named in figure 6.6(d): (1) a bow shock (BS) produced at the RLE because the flow is supersonic in the relative frame of reference
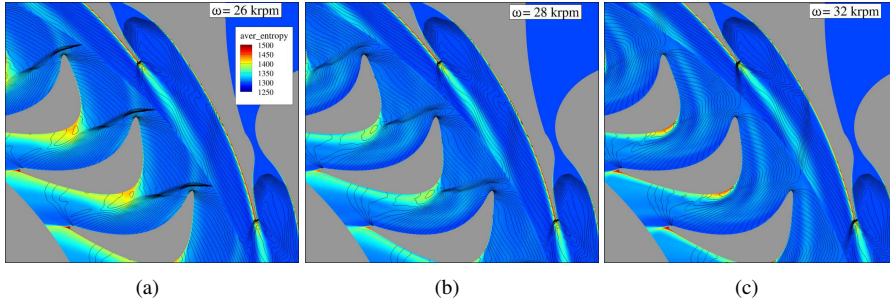
Figure 6.7: Time-averaged entropy contour with time-averaged isobars for the Q3D numerical domain.

($Ma_{rel} \approx 1.3$), (2) a separation shock wave (SW) generated by the flow detachment at the suction side of the blade, and (3) the reflected shock (R) from the tail of SW impinging at the PS of the rotor blade. These three shock waves rotate with the blade developing a complex shock structure at the PS of blade 1, which is highly unsteady, see from $\tau = 0/12$ to $\tau = 2/12$. Subsequently, at $\tau = 3/12$, R and the tail of SW interact with the BS until this shock-shock interaction merges into a single shock at $\tau = 4/12$. Near the reattachment region at the SS of blade 1, an expansion fan (E) is being generated, see figure 6.6(d); the flow recompresses in this region. The flow continues to accelerate after the separation bubble achieving supersonic conditions again. Therefore, a fish-tail shock waves emanate from the RTE.

Compared to the old rotor, the new blade prevents several loss mechanisms in the rotor passage, compare figures 5.6 and 6.6. The new blade reduces the separation bubble at the SS of the blade. However, the new blade still shows a flow detachment at the suction side, which might be the result of assuming less rotor blades. To assess this, a simulation with the actual number of rotor blades has been performed by Smit *et al.*[27], which also still shows flow separation. The flow detachment is likely to be produced by the strong curvature of the SS of the blade. Moreover, the new blade has a more uniform expansion, if compared to the old blade, along the rotor passage, as depicted by the isobars in figure 6.6. Qualitatively, the new blade considerably improves the flow field inside the high-expansion ORC turbine; even though the flow field is highly supersonic downstream of the nozzle.

6.3.2.2 Rotational speed influence

In this section, we analyze the impact of the rotational speed on the new turbine blade by using three Q3D simulations. In Chapter 5 for the old blade profile, we concluded that an increase in shaft speed would reduce the entropy losses and shock waves. Still, it does not imply additional power output due to the waste of kinetic energy at the exit of the
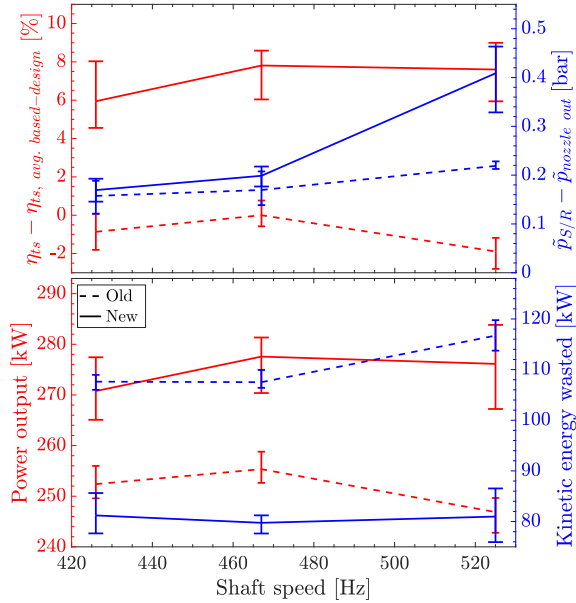
Figure 6.8: Turbine characteristic values as a function of the rotational speed for the old (dashed lines) and new (solid lines) rotor blade. We calculate the time-averaged total-to-static efficiency, static pressure difference between the stator/rotor interface and the nozzle outlet ($\tilde{p}_{nozzle\ out}$), power output, and kinetic energy wasted at the outlet; the bars represent the difference between the average quantity with the maximum and minimum value for a rotation period. The solid and dashed lines represented the new and old blade, respectively.

rotor.

Figure 6.7 depicts the time-averaged entropy contour with isobaric lines for the three rotational speed — (a) 26 krpm, (b) 28 krpm, and (c) 32 krpm — for a Q3D numerical domain; these plots illustrate the primary sources of entropy losses in the turbine stage: the viscous wake from the STE and flow recirculation at the SS of the rotor blade. In terms of entropy losses and shock waves, the rotor blade can benefit from an increase in rotational speed. First, the pressure gradient across the BS at the RLE is inversely proportional to the shaft speed; at a speed of 32 krpm, the flow is no longer supersonic at the inlet of the rotor, eradicating the BS at the RLE. And second, the flow separation at the SS of the blade is reduced at higher rotational speeds. The old rotor blade (Chapter 5) had a similar behavior — attenuation of the BS and separation bubble — at a higher shaft speed. The flow field from the simulation with the highest speed (32 krpm) has less losses related to entropy and shock waves if compared to lower speeds, including the design speed (26 krpm).

According to our Q3D simulations, there is the potential to increase the performance

of the new turbine stage by increasing the rotational speed. Figure 6.8 depicts the turbine performance as a function of the rotational speed: the solid red lines represent the total-to-static efficiency $\left[\eta_{ts} = \left(\tilde{H}_{in,0} - \tilde{H}_{out,0}\right) / \left(\tilde{H}_{in,0} - \tilde{H}_{out,is}\right)\right]$ and the power output $\left[P = \tilde{m}\left(\tilde{H}_{in,0} - \tilde{H}_{out,0}\right)\right]$ in the top and bottom figure, respectively. Moreover, this figure also illustrates — the blue solid lines — the pressure between stator and rotor ($\tilde{p}_{S/R}$) and the kinetic energy waste at the outlet of the turbine. Even though the design speed for the new turbine is 426 Hz (26 krpm), both the total-to-static efficiency and the power output increase for a speed of 467 Hz (28 krpm) by $\approx 2\Delta\%$ and $\approx 7\Delta$kW, respectively. For an even higher rotational speed (525 Hz), the turbine performance does not increase any further. Unlike the old turbine design, it is not due to the kinetic energy wasted at the outlet, which is almost rotational speed independent. The reason for the drop in performance for the higher speed is a larger pressure between the stator and rotor. The performance of the new turbine design increases with the rotational speed, but it reaches a maximum before 32 kprm.

The pressure at the interface between the stator and rotor changes dramatically at a speed of 525 Hz for the new turbine design. The expansion in the rotor — and the degree of reaction — depends on the rotational speed. As shown by the top plot of figure 6.8, the static pressure difference between the stator/rotor interface and the nozzle outlet[2] is more significant at 525 Hz compared to lower rotational speeds even though the total pressure ratio of the turbine stage is maintained constant. There is larger recompression (almost double) at 525 Hz in the free expansion region between the stator and rotor. Therefore, stronger oblique shocks emanate from the STE, which results in more unsteadiness and a less uniform flow at the inlet of the rotor.

For the simulations shown herein, the unsteadiness between stator and rotor is due to waves generated by the blade rotation that travel upstream to the stator. The strength of these waves depends on the rotational speed and the blade thickness. For 525 Hz, a large pressure wave influences the flow in the free expansion region of the stator, making the stream at the inlet of the rotor less uniform and adding an extra time fluctuating mode. We can corroborate this result with the difference between the maximal and minimal power output, which for a period is 12.3, 13.0, and 16.6 ΔkW for 26 krpm, 28 krpm, and 32 krpm, respectively. However, this phenomenon did not occur in the old turbine design as showcased by the dashed line in the top plot of figure 6.8, where the pressure between stator and rotor is almost independent of the rotational speed; the thicker blade of the new turbine design is the most probable cause for this discrepancy. These flow features are not quantifiable without the coupling between the stator and rotor and using an unsteady simulation with the proper method to account for the non-matching domains.

The new turbine design has a better performance — according to the Q3D simulation – than the old one at design and off-design rotational speed; figure 6.8 depicts several characteristic values of the turbine stage as a function of the rotational speed for the old (dashed lines) and new (solid lines) design. There is a significant increase in power

---

[2]The nozzle outlet is upstream from the oblique shock wave (ST$_2$); ST$_2$ is reflected (R) in the long stator blade wall, see figure 6.6(a). The pressure at this location is the design parameter used for the stator nozzle design, which is a fixed pressure for all simulations.
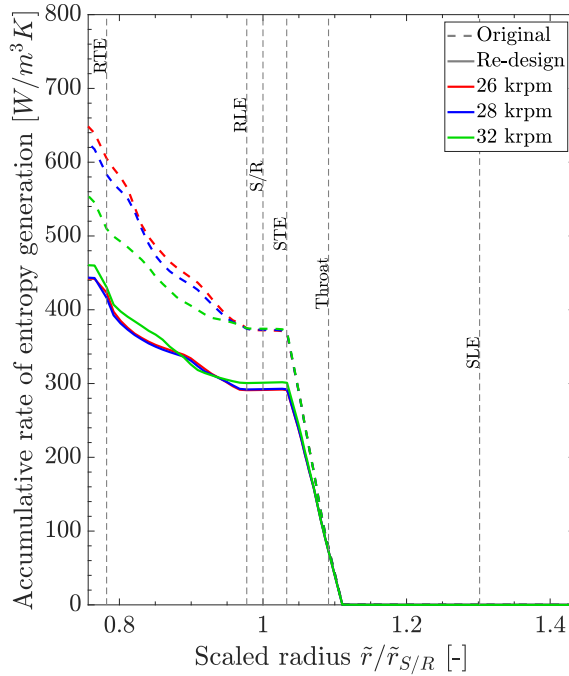
Figure 6.9: Accumulative rate of entropy generation per unit volume along the radius of the turbine stage at the three rotational speeds for the old (dashed lines) and new (solid lines) turbine design.

output for the new geometry if compared to the old one: +18.3, +22.2, and +29.3 ΔkW for 26 krpm, 28 krpm, and 32 krpm, respectively. The reason for such an improvement is because the new blade is capable of extracting more kinetic energy from the flow; the new turbine stage is wasting less kinetic energy: -26.4, -27.8, and -35.7 ΔkW for 26 krpm, 28 krpm, and 32 krpm, respectively. In terms of entropy losses, the accumulative rate of entropy generation[3], depicted in figure 6.9, in the rotor passage is less for the new design; this is a consequence of the reduction of the separation bubble at the suction side of the blade. The entropy accumulation difference between the two turbines in the stator is attributed to the free expansion region. For the new geometry, there is a slight increase in entropy generation in the stator for the high rotational speed simulation (32 krpm): a more substantial entropy accumulation due to the already discussed recompression between the stator and rotor. At a sub-sonic speed at the rotor inlet (32 krpm), the losses attributed to the bow shock at the RLE are no longer there, but the separation bubble for this case results in a more intense entropy increase, see figure 6.7(c). The new turbine design not only results in higher power output at design conditions, but it is also more robust at off-design rotational speed.

---

[3]We calculate the rate of entropy generation per unit volume[(35)] using equation (5.1).
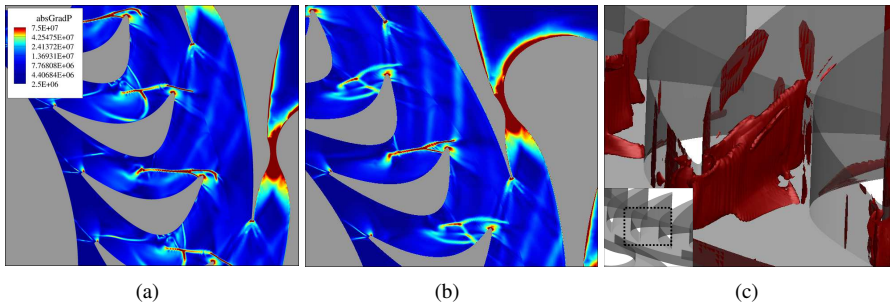
Figure 6.10: Snapshot of the magnitude of the pressure gradient field at 28 krpm: (a) Q3D simulation; (b) XY view, 3D simulations; and (c) Iso-surfaces of the pressure gradient (= $3 \cdot 10^7$).
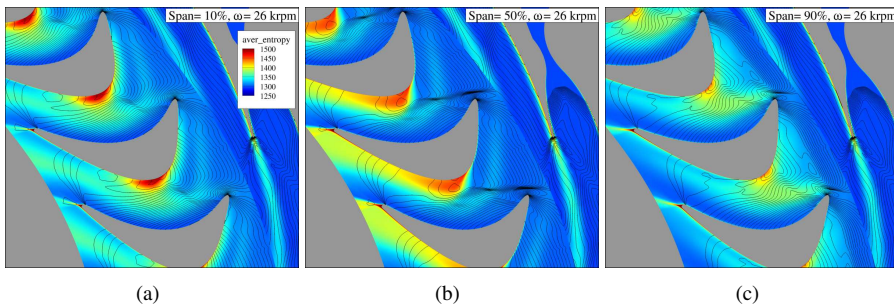
Figure 6.11: Time-averaged entropy contour with time-averaged isobars for the 3D numerical domain at three span-wise locations: a) 10%, a) 50%, and a) 90% span for a rotational speed of 26 krpm.

6.3.2.3 Three-dimensional flow analysis analysis

Qualitative comparison between the Q3D and 3D simulations

There are distinct similarities and differences between the flow field of the Q3D and 3D (at mid-span) simulations for the new ORC turbine, which we will highlight by plotting the instantaneous pressure gradient (figure 6.10) and the time-averaged entropy contours of the Q3D and 3D simulations at mid-span for a shaft speed of 26 krpm (figures 6.7(a) and 6.11(b), respectively).

Concerning the similarities, both simulations (Q3D and 3D) depict equivalent phenomena, e.g., the viscous wake from the STE, the flow separation at the SS of the blade (compare figures 6.7(a) and 6.11(b)), and complex shock-shock interaction at the rotor passage (see figures 6.10(a-b)). No qualitative differences are seen in the stator flow field between the two simulation types.
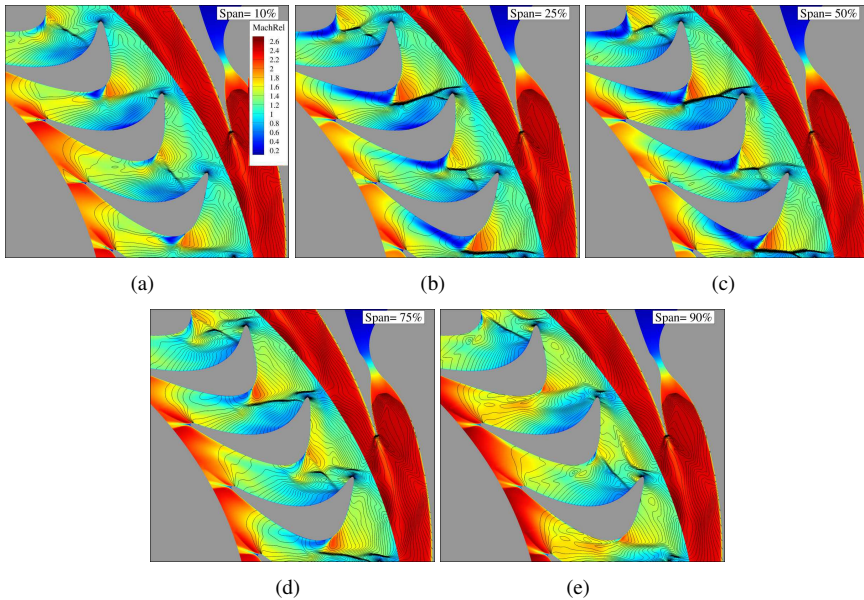
Figure 6.12: Snapshot of the relative Mach number contour with isobars at five span-wise locations (10%, 25%, 50%, 75%, and 90%) for the 3D simulation for a rotational speed of 26 krpm.

Concerning the differences, the 3D simulation at mid-span shows a thicker wake and larger thermodynamic entropy increase within the recirculation bubble, a consequence of the span-wise effects, and a change in the strength of the bow shock at the RLE. The rotor passage suffer from span-wise effects, which we will investigate in more detail in the following sub-section.

Span-wise effects

The three-dimensional effects become apparent in the rotor passage as shown by the time-averaged entropy contour of figures 6.11 and the instantaneous relative Mach number contour in figure 6.12 at different span-wise locations. There is a sudden expansion at the inlet of the rotor passage near the shroud, check the rotor inlet of figure 6.11(a) and 6.12(e). This pressure change is related to the height distribution, see right plot of figure 6.3, which has an abrupt blade height increase at this radius.

The bow shock at the RLE is a three-dimensional structure as depicted in figure 6.10(c). The shock wave structures within the rotor passage are stronger at mid-span, given the absence of near-wall effects. Compared to the 25% span-wise location, there is barely any difference in the relative Mach number contour, compare figures 6.12 (b) and (c). However, there is a significant disparity with the rest of span-wise locations, see fig-
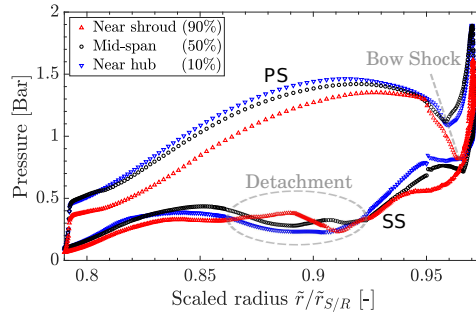
Figure 6.13: Time-averaged values of the blade loading at the suction (SS) and pressure (PS) side of the rotor at different span-wise location

ures 6.12(a), (d) and (e). For the flow near the hub (10%) and the shroud (90%), the bow shock at the RLE is much weaker, which can be attributed to near-wall effects. Furthermore, this 3D bow shock wave affects the blade loading; there is a sharp decrease in pressure at the PS in figure 6.13 near the inlet of the rotor.

There is flow separation in all span-wise contours in the rotor passage, but differ due to the 3D effects close to the casing and shroud:

- At 90% span, the flow detachment is barely present. The entropy increase due to near-wall effects from the shroud have a larger influence in the flow field at this region. As mentioned already, the pressure at the inlet of the rotor passage is less ($\approx 0.3 \Delta bar$) at the shroud than at other span-wise locations. This phenomenon is also clearly seen in the blade loading near the shroud at a scaled radius of 0.97 (figure 6.13).

- Near the hub (10%), the separation creates a sharp increase in thermodynamic entropy and has a distinct shape, different from the mid-span and near the shroud, see figure 6.11(c); a secondary flow — illustrated by figure 6.14 — causes this sharp entropy increase at the hub.

The flow in the rotor passage suffers from a secondary flow because of a significant increase in shroud height. The sharp expansion at the shroud of the rotor inlet drives fluid to bend from radial to the axial direction; still, not all the fluid manages to turn, especially near the hub, as depicted by figure 6.14. If compared to the old blade, the new design leads to reduce viscous losses by decreasing the separation bubble at the SS of the blade; still, strong span-wise effects are generated in the rotor passage.

The three-dimensional effects generate losses in the new turbine design, e.g., secondary flow, 3D shock waves. For a better 3D construction of the rotor blade, we advise the following:

1. Estimate the cross-sectional area correctly. In our blade design methodology, we calculate the height distribution with an optimization routine of the cross-sectional
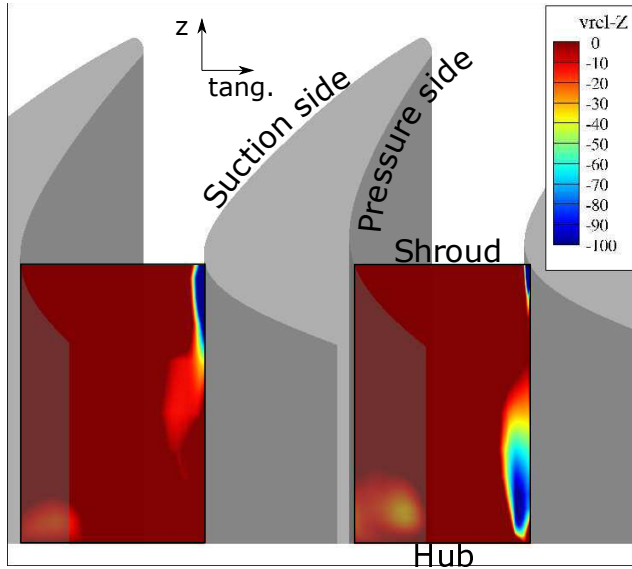
Figure 6.14: Radius iso-surface snapshot with a contour of the relative velocity in the z-direction.

area distribution in the rotor passage; the optimization routine minimizes the second derivative of this area distribution. To calculate this cross-sectional area, we use two distances: the blade-to-blade distance and the height of the blade, see equation (6.1). The blade-to-blade distance (or width of the passage) is the distance normal to the flow line (figure 6.2); this distance is not at a constant height. However, what we did not consider is that the cross-sectional area also needs to be normal to the mid-span plane. Figure 6.15 depicts a schematic of the current and corrected method in red and blue, respectively. The drawback of calculating the cross-sectional area with this new procedure is the extra complexity needed: the blade-to-blade distance changes in the direction perpendicular to the mid-span plane.

2. Improve the radial-to-axial bend by changing the hub surface. The method to generate the new blade shape is purely geometrical. Therefore, it is the designer's responsibility to include fluid dynamics understanding into the procedure. For example, to overcome the secondary flow, we recommended the designer to have a hub surface which is not for a constant height, but that considers a radial-to-axial bend; this is the case for typical radial inflow turbines which the hub surface has a complete radial-to-axial bend. The main drawback of this suggestion is that the shroud blade height would increase to maintain the same cross-sectional area distribution.
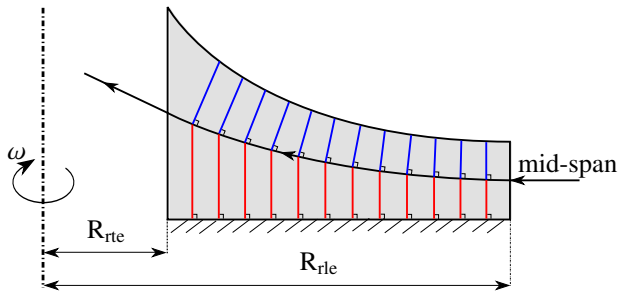
Figure 6.15: Visualization of the cross-sectional area calculation in the span-wise direction, in red the current method and in blue the corrected method.

6.3.2.4 Quantitative analysis

We now quantitatively compare the new rotor blade with the old one (analyzed in detail in Chapter 5), utilizing both numerical domains: Q3D and 3D, by analyzing the accumulative rate of entropy generation (figure 6.16) and the time-averaged performance (table 6.2).

Accumulative rate of entropy generation

The accumulative entropy generation analysis of the ORC turboexpander can help us to clearly identify the sources of losses. Furthermore, by comparing the mid-span simulation with its 3D counterpart, we can also discover which potential losses are concealed by a mid-span design approach.

Q3D simulations: By examining the accumulative entropy generation for the Q3D simulation of the two blades in the right plot of figure 6.16, we arrive at two conclusions. (1) The strong bow shock of the old blade disturbs the flow field upstream, as depicted in figure 5.8(a), resulting in a significant increase of the entropy generation between the throat and STE as compared to the new blade; this demonstrates the importance of taking into account unsteady effects, as steady-state simulations can not capture this phenomenon. (2) Reducing the flow detachment lowers the entropy generation in the rotor passage as the slope of the accumulative entropy generation line between the RLE and RTE has decreased significantly for the new blade if compared to the old one.

Q3D/3D Stator: In terms of the stator nozzle, there is no significant qualitative or quantitative difference between the Q3D and 3D simulations. The flow field and the accumulative entropy generation from the Q3D simulations agree well with the ones from the 3D simulations for the stator nozzle. Therefore, we conclude that the nozzle can be designed using a mid-span approach because there are no additional 3D effects (apart from the boundary layers at hub and shroud) that affect the stator performance. Furthermore, entropy generation before the throat is negligible due to the low velocity.

Q3D/3D Rotor: For the rotor, the comparison between the Q3D and 3D simulations prove that designing a rotor blade using a mid-span approach can potentially conceal ad-
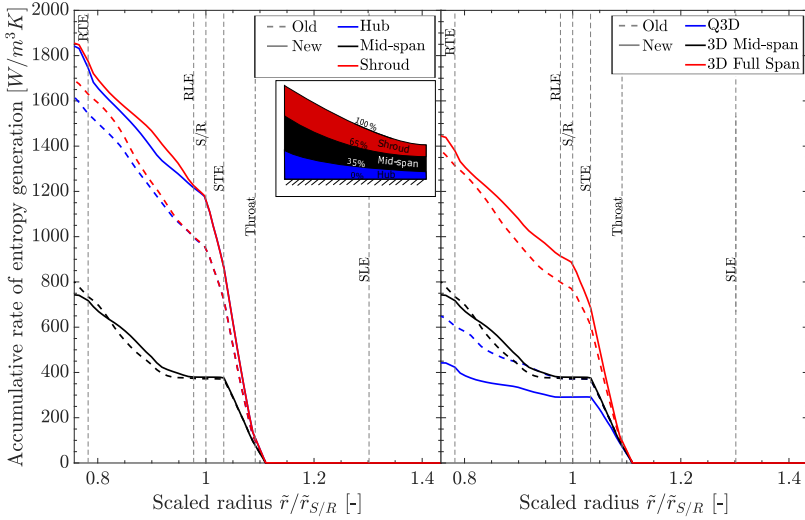
Figure 6.16: Accumulative rate of entropy generation.

ditional losses. Both of rotor designs have substantial entropy generation due to secondary span-wise flow effects that cannot be captured by Q3D simulations. The 3D simulations exhibit two different span-wise mechanisms that can introduce additional losses:

1. Span-wise effects close to the rotor inlet can significantly alter the pressure ratio over the free expansion region between the stator and rotor. In the case of the new blade, the sharp expansion at the rotor inlet is modifying the pressure between the stator and rotor (see table 6.2), leading to an increase in entropy generation in that region; this is not captured by the Q3D simulation (see Q3D concerning the 3D at mid-span for the new blade in figure 6.16). Concerning the old blade, however, a 3D effect (the secondary flow) occurs further downstream of the rotor passage because of the more conservative increase of the shroud height. It, therefore, does not affect the free expansion region between the stator and the rotor.

2. 3D flow effects can increase the entropy generation locally. In the rotor blade passage, the accumulation of entropy generation is higher for the 3D simulation; this is observed in the right plot of figure 6.16, where for both simulation types (Q3D and 3D), the accumulative entropy generation of the old blade is equivalent until the rotor passage where the secondary flow is located.

3D simulations: Figure 6.16 shows that the turbine with the new blade has a higher entropy generation, than the one with the old blade, at the exit of the stage. This can be explained using the mechanisms described above. First, due to the first span-wise mechanism, the PR over the free expansion region increases for the new rotor blade. Extra entropy is generated near the hub and shroud compared to the old blade (see left figure 6.16), leading to a larger entropy accumulation at the inlet of the rotor. Second, due

Table 6.2: Time-averaged performance comparison between the old and new blade for the high-expansion ORC turbine for a Q3D and 3D simulation.

	Old blade		New blade	
	Q3D	3D	Q3D	3D
Power output [kW]	252.4	237.9	270.8	249.9
Kinetic energy waste [kW]	107.6	95.12	81.21	79.81
$\eta_{ts} - \eta_{ts,\ old-design\ 3D}\ [\Delta\%]$	0.98	0.00	7.79	4.22
$\eta_{isen} - \eta_{isen,\ old-design\ 3D}\ [\Delta\%]$	3.12	0.00	3.66	0.36
$\tilde{p}_{S/R} - \tilde{p}_{nozzle\ out}\ [\Delta bar]$	0.158	0.100	0.169	0.267

to the second span-wise mechanism, there is a steep increase in entropy production in the rotor passage near the shroud of the old blade, a loss mechanism that is considerably less for the new rotor. Furthermore, because the entropy production at mid-span is almost similar for both blade geometries, we can conclude that the reduction of entropy generation near the shroud of the new geometry is the leading cause for a larger entropy generation in the rotor passage compared to the old blade.

The entropy generation analysis demonstrates the importance of considering the span-wise and unsteady flow effects, and in particular, its influence over the pressure between the rotor and stator ($\tilde{p}_{S/R}$). The unsteady stator-rotor interaction strongly modifies the free expansion region, e.g., there is a quantitative difference in entropy generation between both rotor blades for the Q3D simulations. In the 3D simulation of the new blade, $\tilde{p}_{S/R}$ changes significantly from its Q3D counterpart ($\approx 0.16\Delta bar$) due to the sharp expansion at the shroud of the RLE. This pressure is of paramount importance because it affects the flow field in the free expansion region (oblique shock waves and viscous wake from the STE) and, therefore, the uniformity of the flow entering the rotor blade passage. Moreover, the region between the stator and rotor can be the source of additional (mixing) losses that are not accounted for in a steady-state Q3D simulation, as seen in the right plot of figure 6.16. Even though the rotor performance does not directly influence the stator nozzle design, special care must be taken with the pressure between the stator and rotor as it affects the oblique shock wave from the STE and the flow uniformity at the rotor inlet.

Turbine performance

The 3D calculations give a worse performance of the high-expansion ORC turbines compared to the Q3D counterpart. We have measured the performance of the ORC turbine employing the power output, and the isentropic and total-to-static efficiency, as displayed by table 6.2. The new turbine stage has a drop in performance, similarly to the old turbine, for the 3D simulation: -3.57$\Delta\%$, -3.30$\Delta\%$, and -20.9ΔkW for the total-to-static, isentropic efficiency and power output, respectively. The additional loss mechanisms, quantifiable by a 3D simulation, decrease the performance of the high-expansion cantilever ORC turbine stage, proving the importance of the span-wise effects in such a machine.

The steady-state optimization that produced the new rotor blade improves the perfor-

mance of the cantilever ORC turbine. There is an increment on the power output — if compared to the old blade — for both types of simulations: 18.38ΔkW and 11.97ΔkW for Q3D and 3D, respectively. In terms of total-to-static efficiency, the improvement of the new rotor blade is of +6.81Δ% and +4.22Δ% for Q3D and 3D, respectively. The ORC turbine does not have such an improvement in terms of isentropic efficiency (<+0.55Δ%), a result that matches the entropy generation analysis of the 3D simulation for both geometries (right plot of figure 6.16). The reason for such an improvement of power output and total-to-static efficiency of the high-expansion ORC turbine is because the new blade is capable of extracting more kinetic energy from the flow, as illustrated by table 6.2.

6.4   Conclusions

We presented in this chapter the application of the design process for a high-expansion cantilever organic Rankine cycle turbine using toluene as working fluid. The originality of this work is that we propose an additional step in the design process of such a turbomachine: a detailed design assessment. Utilizing detailed three-dimensional and unsteady simulations, we are capable of investigating and accounting for phenomena otherwise neglected by common steady-state quasi-three-dimensional simulation or by standard design methodologies.

For the detailed blade design, we have considered an inverse design approach which is purely geometrical; a rotor blade is generated with an smooth turning flow and a steady increase of cross-sectional area. The blade geometry design considers three uncoupled optimizations for the flow line curvature, the blade thickness distribution, and the cross-sectional area increase. Moreover, we applied a genetic algorithm for the blade shape optimization. We assessed the blade geometry resulting from the genetic algorithm using two types of numerical domains: a quasi-three-dimensional where the cross-sectional area distribution is accounted for with one cell in the span-wise direction, and a three-dimensional where the whole span-wise geometry is considered.

The design assessment of the high-expansion cantilever organic Rankine cycle turbine via unsteady 3D simulations gave valuable insights into the flow field. We have several recommendations that will be feedback to the design procedure. (1) The cross-sectional area calculation needs to be adjusted to account for the radial-to-axial bend that the fluid suffers. The cross-sectional area distribution needs to calculate normal to the mid-span direction of the flow. The extra complexity of the optimization routine of the height distribution is the main drawback. (2) The hub casing of the rotor needs to include a radial-to-axial bend. Adding this extra parameter to the blade design will make it easier to bend the overall flow field, eradicating the secondary flow near the hub of the rotor passage. (3) There is the potential to increase the performance of the turbine stage by increasing the rotational speed. The off-design analysis using Q3D simulations revealed an increase of power output of +7ΔkW if the speed increased to 467 Hz.

During the detailed assessment, the free expansion region between the stator and rotor is modified by the rotor blade's profile, rotational speed, and height distribution. The three-dimensional and unsteady effects do not directly influence the stator nozzle; how-

ever, the conditions between the stator and rotor do modify the mixing region between the long stator wall and the rotor inlet. We advise to use the insights from this study to alter the stator blade design by changing the nozzle's back-pressure; therefore, less mixing losses and weaker oblique shock waves will result between stator and rotor.

According to the simulations herein, the blade designed in the present chapter results in a better ORC turbine performance than the original blade design (discussed in detail in Chapter 5). The new blade design has a better flow field qualitatively; the large separation bubble at the suction side of the original blade has been reduced considerably and there is a more even expansion. However, the main improvement of the new turbine design over the original geometry (of Chapter 5) is its capacity of extracting more kinetic energy from the fluid; this results into a higher power output ($>10\Delta$kW), a higher total-to-static efficiency ($>4\Delta\%$), and less kinetic energy wasted at the outlet ($<15\Delta$kW).

The investigation presented in this chapter has shown that in non-conventional turbomachinery — like a high-expansion cantilever ORC turbine, current design methodologies neglect several loss mechanisms that greatly influence the performance. First, the standard design method concentrates on delivering a turbine design on the meridional plane, ignoring the span-wise effect. Moreover, loss mechanisms related to the unsteadiness of the flow that reduces the performance are not accounted for, e.g., shock-shock, and shock-boundary layer losses. A detailed assessment of the turbine design is a viable alternative to include these complex phenomena into the design procedure.

References

[1] Colonna, P., Casati, E., Trapp, C., Mathijssen, T., Larjola, J., Turunen-Saaresti, T., and Uusitalo, A., 2015. "Organic Rankine cycle power systems: from the concept to current technology, applications, and an outlook to the future". *Journal of Engineering for Gas Turbines and Power,* **137**(10), p. 100801.

[2] Macchi, E., 2013. "The choice of working fluid: the most important step for a successful organic rankine cycle (and an efficient turbine)". In Second International Seminar on ORC Power Systems, Rotterdam, The Netherlands, Oct, pp. 7–8.

[3] Colonna, P., Harinck, J., Rebay, S., and Guardone, A., 2008. "Real-gas effects in organic Rankine cycle turbine nozzles". *Journal of Propulsion and Power,* **24**(2), pp. 282–294.

[4] Hoffren, J., Talonpoika, T., Larjola, J., and Siikonen, T., 2002. "Numerical simulation of real-gas flow in a supersonic turbine nozzle ring". *Journal of engineering for gas turbines and power,* **124**(2), pp. 395–403.

[5] Persico, G., and Pini, M., 2017. "Fluid dynamic design of organic rankine cycle turbines". In *Organic Rankine Cycle (ORC) Power Systems*. Elsevier, pp. 253–297.

[6] van Buijtenen, J., Larjola, J., Turunen-Saaresti, T., Honkatukia, J., Esa, H., Backman, J., and Reunanen, A., 2003. "Design and validation of a new high expansion ratio radial turbine for ORC application". In Proceedings of the Fifth European Conference on Turbomachinery, pp. 1–14.

[7] Pini, M., Persico, G., Casati, E., and Dossena, V., 2013. "Preliminary design of a centrifugal turbine for organic Rankine cycle applications". *Journal of Engineering for Gas turbines and power,* **135**(4), p. 042312.

[8] Casati, E., Vitale, S., Pini, M., Persico, G., and Colonna, P., 2014. "Centrifugal turbines for mini-organic Rankine cycle power systems". *Journal of Engineering for Gas Turbines and Power,* **136**(12), p. 122607.

[9] Uusitalo, A., Turunen-Saaresti, T., Gronman, A., Honkatukia, J., and Backman, J., 2015. "Combined thermodynamic and turbine design analysis of small capacity waste heat recovery ORC". *Proceedings of the ASME ORC*.

[10] Pasquale, D., Ghidoni, A., and Rebay, S., 2013. "Shape optimization of an organic Rankine cycle radial turbine nozzle". *Journal of Engineering for Gas Turbines and Power,* **135**(4), p. 042308.

[11] Rodriguez-Fernandez, P., and Persico, G., 2015. "Automatic design of orc turbine profiles using evolutionary algorithms". In 3rd International Seminar on ORC Power Systems, Vol. 133.

[12] Pini, M., Persico, G., Pasquale, D., and Rebay, S., 2015. "Adjoint method for shape optimization in real-gas flow applications". *Journal of Engineering for Gas Turbines and Power,* **137**(3), p. 032604.

[13] Persico, G., Romei, A., Dossena, V., and Gaetani, P., 2018. "Impact of shape-optimization on the unsteady aerodynamics and performance of a centrifugal turbine for orc applications". *Energy,* **165**, pp. 2–11.

[14] Bufi, E. A., and Cinnella, P., 2018. "Preliminary design method for dense-gas supersonic axial turbine stages". *Journal of Engineering for Gas Turbines and Power,* **140**(11), p. 112605.

[15] Anand, N., Vitale, S., Pini, M., Otero, G. J., and Pecnik, R., 2019. "Design methodology for supersonic radial vanes operating in nonideal flow conditions". *Journal of Engineering for Gas Turbines and Power,* **141**(2), p. 022601.

[16] Wheeler, A. P., and Ong, J., 2014. "A study of the three-dimensional unsteady real-gas flows within a transonic ORC turbine". In ASME Turbo Expo 2014: Turbine Technical Conference and Exposition, American Society of Mechanical Engineers, pp. V03BT26A003–V03BT26A003.

[17] Al Jubori, A., Al-Dadah, R. K., Mahmoud, S., Ennil, A. B., and Rahbar, K., 2017. "Three dimensional optimization of small-scale axial turbine for low temperature heat source driven organic Rankine cycle". *Energy conversion and management,* **133**, pp. 411–426.

[18] Bülten, B., Althaus, W., Weidner, E., and Stoff, H., 2015. "Experimental and numerical flow investigation of a centripetal supersonic turbine for organic rankine cycle applications". In 11th European Conference on Turbomachinery Fluid Dynamics & Thermodynamics, Madrid, Spain, Mar, pp. 23–27.

[19] Bufi, E. A., Obert, B., Cinnella, P., and ENERTIME, C. F., 2015. "Fast design methodology for supersonic rotor blades with dense gas effects". In 3 International Seminar on ORC Power Systems, October 12-14, 2015, Brussels, Belgium.(Paper accepted, under revision).

[20] White, M., and Sayma, A., 2016. "Investigating the effect of changing the working fluid on the three-dimensional flow within organic Rankine cycle turbines". In ASME Turbo Expo 2016: Turbomachinery Technical Conference and Exposition, American Society of Mechanical Engineers, pp. V003T25A002–V003T25A002.

[21] Rinaldi, E., Pecnik, R., and Colonna, P., 2016. "Unsteady operation of a highly supersonic organic rankine cycle turbine". *Journal of turbomachinery,* **138**(12), p. 121010.

[22] Wang, Z., Zhang, W., Wu, X., and Chen, K., 2018. "A novel unsteady aerodynamic reduced-order modeling method for transonic aeroelastic optimization". *Journal of Fluids and Structures,* **82**, pp. 308–328.

[23] Li, K., Kou, J., and Zhang, W., 2019. "Deep neural network for unsteady aerodynamic and aeroelastic modeling across multiple mach numbers". *Nonlinear Dynamics,* **96**(3), pp. 2157–2177.

[24] Rubino, A., Pini, M., Colonna, P., Albring, T., Nimmagadda, S., Economon, T., and Alonso, J., 2018. "Adjoint-based fluid dynamic design optimization in quasi-periodic unsteady flow problems using a harmonic balance method". *Journal of Computational Physics,* **372**, pp. 220–235.

[25] Pini, M., Vitale, S., Colonna, P., Gori, G., Guardone, A., Economon, T., Alonso, J., and Palacios, F., 2017. "Su2: the open-source software for non-ideal compressible flows". In Journal of Physics: Conference Series, Vol. 821, IOP Publishing, p. 012013.

[26] Giles, M. B., 1990. "Nonreflecting boundary conditions for euler equation calculations". *AIAA journal,* **28**(12), pp. 2050–2058.

[27] Smit, S., Eppinga, Q., Otero Rodriguez, G., and Pecnik, R., 2019. "Optimization of a high expansion ORC turbine using a genetic algorithm". In 5th International Seminar on ORC Power Systems, September 9-11, 2019, Athens, Greece.(Paper accepted, under revision).

[28] Pecnik, R., Terrapon, V. E., Ham, F., Iaccarino, G., and Pitsch, H., 2012. "Reynolds-averaged navier-stokes simulations of the Hyshot II scramjet". *AIAA journal,* **50**(8), pp. 1717–1732.

[29] Pecnik, R., Rinaldi, E., and Colonna, P., 2012. "Computational fluid dynamics of a radial compressor operating with supercritical CO_2". *Journal of Engineering for Gas Turbines and Power,* **134**(12), p. 122301.

[30] Pecnik, R., Witteveen, J. A., and Iaccarino, G., 2013. "Assessment of uncertainties in modeling of laminar to turbulent transition for transonic flows". *Flow, turbulence and combustion,* **91**(1), pp. 41–61.

[31] Rinaldi, E., Pecnik, R., and Colonna, P., 2015. "Computational fluid dynamic simulation of a supercritical CO2 compressor performance map". *Journal of Engineering for Gas Turbines and Power,* **137**(7), p. 072602.

[32] Liou, M.-S., 1996. "A sequel to AUSM: AUSM$^+$". *Journal of computational Physics,* **129**(2), pp. 364–382.

[33] Spalart, P., and Allmaras, S., 1992. "A one-equation turbulence model for aerodynamic flows". In 30th aerospace sciences meeting and exhibit, p. 439.

[34] Lemmon, E. W., and Span, R., 2006. "Short fundamental equations of state for 20 industrial fluids". *Journal of Chemical & Engineering Data,* **51**(3), pp. 785–850.

[35] Sciacovelli, A., Verda, V., and Sciubba, E., 2015. "Entropy generation analysis as a design tool—a review". *Renewable and Sustainable Energy Reviews,* **43**, pp. 1167–1181.

7

Conclusions

In this final chapter, we summarize the conclusions of the dissertation and we high-light the main contributions to the respective fields of research. Moreover, we provide recommendations for future research on related topics.

7.1 Conclusions

This dissertation presents a crucial step towards accurate numerical modeling of non-ideal fluids for non-conventional power cycles, i.e., the supercritical carbon dioxide (s-CO$_2$) power cycle and the organic Rankine cycle (ORC). We focus on the most relevant components of the s-CO$_2$ power and ORC that operate closest to the critical point — where the flow experiences the most significant non-ideal behavior: the heat exchanger and the expander, respectively. Therefore, we divide this thesis into two parts, the first addressing turbulence modeling of supercritical fluids (Chapters 2 and 3) and the second covering computational fluid dynamic simulation of organic Rankine cycle turbines (Chapters 4, 5, and 6). Below, the main conclusions of each part are summarized and discussed.

Part I: Turbulence modeling of supercritical fluids

The two most important phenomena a heat exchanger designer needs to balance are the heat transfer between two (or more) fluids and the pressure drop due to frictional forces, both of which, at high Reynolds numbers, are influenced by turbulence. However, re-searchers know little about how turbulence is affected by the non-ideality of supercritical fluids. Moreover, standard eddy viscosity models (EVMs), used to estimate the Reynolds stresses, were developed for incompressible flows and are not able to provide accurate results for s-CO$_2$ applications with considerable heat transfer. Therefore, this part of the dissertation introduces improvements for modeling the eddy viscosity of supercritical flu-ids and analyze their performance — coupled to several turbulent heat flux models — for supercritical fluids with heat transfer.

Chapter 2 presents a novel methodology to improve EVMs for predicting wall-bounded turbulent flows with strong variations of the thermo-physical properties. The central distinguishing feature of our method lies in the formulation of the diffusion term in the turbulence scalar equations; the modified diffusion term of the turbulent scalar transport depends on the density. This derived methodology is generic in terms of EVMs, and it can also be applied to wall-modeled Large-Eddy simulations. Moreover, the de-rived modifications are easy to implement and can be used for estimating (i) cooling and heating of a liquid or gas, and (ii) compressible flows (e.g. ORC expander), among oth-ers. We tested the eddy viscosity models in conventional and modified form in a fully developed turbulent channel flow with sharp variations of the thermo-physical proper-ties. The conventional EVMs were not reliable with the exception of the one-equation Spalart-Allmaras model. In general, the modified eddy viscosity models resulted in a bet-ter agreement — in terms of velocity profile and heat transfer — with direct numerical simulations.

In **Chapter 3**, we analyze different turbulence models — including our density-corrected EVMs and several models for the turbulent Prandtl number (Pr_t) — to model an upward heated turbulent pipe flow with CO_2 at supercritical pressure with and without buoyancy effects. For forced convection, there is an improvement in the prediction using the modified eddy viscosity models; however, when buoyancy effects are not negligible and heat transfer deterioration is present, all turbulence models lack accuracy when compared to the direct numerical simulations and experimental data. We analyzed several turbulent Prandtl number approximations (different constant values and two algebraic models) to model the turbulent heat flux, and there is a qualitative improvement, depending on the combination of eddy viscosity model and turbulent Prandtl number model; still, quantitatively all turbulence models are imprecise with respect to the experimental data. According to its definition, Pr_t is undetermined for an M-shape velocity profile produced by the heat transfer deterioration.

Part II: High-expansion ORC turbine simulations

It is challenging to develop an efficient high-expansion ORC expander because of the flow's inherent unsteadiness and the real-gas effects. The organic working fluid expands in the dense-gas region, where the ideal gas law is not valid. The current design procedures for such an expander concentrate on delivering the turbine geometry at the meridional plane; this includes a shape optimization that applies steady-state and quasi-three dimensional computational fluid dynamics (CFD) simulation to estimate the performance. However, these simulations neglect several loss mechanisms, such as secondary flows and shock-shock interactions, that can hamper the expander performance. For this reason, Part II of this dissertation aims to estimate these losses through CFD simulation in order to use these flow insights during the design phase of a high-expansion ORC turbine. We investigate the expansion process of a commercially available ORC unit, whose pressure ratio is of more than 100. The working fluid is toluene, and the electrical power output is in the range of 150-200 kW. The expander consists of a single-stage radial inflow - radial outflow turbine.

In **Chapter 4**, we describe the numerical infrastructure needed to simulate a high-expansion ORC turbine employing unsteady three-dimensional (3D) calculations. We apply these numerical schemes in Chapters 5 and 6. We introduce the fully compressible Navier-Stokes equations and the numerical discretization of the solver using a finite volume approximation. The discretization schemes, in both time and space, are of second-order accuracy. The use of look-up table interpolation of fluid properties is presented as an alternative to the direct evaluation of a multi-parameter equation-of-state model to estimate the real gas effects. Utilizing the findings of Part I, we select the Spalart-Allmaras model to represent the Reynolds stress and close the system of equations. To account for the unsteady stator-rotor interaction of the high-expansion ORC turbine, we implement a conservative flux-assembling technique for non-matching three-dimensional meshes.

Chapter 5 presents the first of its kind numerical simulation of a high-expansion ORC turbine with an unsteady three-dimensional CFD simulation. The three-dimensional effects have an impact on the performance of the high-expansion ORC turbines in terms

of the power output (-15 ΔkW), isentropic-efficiency (-3Δ%), total-to-static efficiency (-1Δ%), and accumulative rate of entropy generation. Regarding the impact of the 3D effects on the design of the machine, the stator blade can be designed at mid-span without any consequence in the third direction; this section of the ORC turbine has no three-dimensional effects. However, the rotor blade should account for the three-dimensional effects during the design phase either by changing the blade shape in the span-wise direction or through the height distribution. In terms of the flow field in the ORC turbine, the main entropy losses are caused by the viscous wake emanating from the stator trailing edge, the substantial flow detachment at the suction side of the rotor blade, and a secondary flow near the shroud at the rotor leading edge. The machine operates with less entropy generation at higher rotational speed due to a decrease of the relative Mach number at the inlet of the rotor (weaker or no shock-waves in the rotor channel) and the smaller recirculation bubble at the suction side of the blade. Nonetheless, this does not lead to a higher power output because less fluid energy is converted into torque; namely, the kinetic energy loss at the turbine outlet is higher. Moreover, the rotor blade loading features sharp fluctuations (as high as 1 bar) as a consequence of the unsteady shock-wave interactions. Shape optimization for blade design can benefit from the unsteady data aiming to minimize the fluctuations of the blade loading.

Standard design methodologies of non-conventional turbomachinery neglect several loss mechanics that greatly influence the performance of the expander. In **Chapter 6**, we propose a novel design procedure for high-expansion ORC turbines, which considers the three-dimensional effects and unsteadiness of the flow. We achieve this by adding an extra step to the standard design procedure (i.e. preliminary and detailed design). We use our numerical infrastructure from Chapter 4 to assess the geometry a posteriori — with high-fidelity CFD models that consider the full three-dimensional geometry and the unsteady features of the flow — and feedback the observations and conclusions to modify the expander. We apply the proposed design methodology to the flow expansion as discussed in Chapter 5 and generate a new turbine design. From the detailed assessment, several suggestions emerged for a better turbine design: (1) The axial-to-radial bend the fluid suffers in the third direction (span-wise direction) must be accounted for during the blade height definition; therefore, the blade channel's cross-sectional area needs to be calculated normal to the mid-span plane during the blade height design. (2) The hub of the rotor needs to include a radial-to-axial bend, giving the designer more control over the flow bending and eradicating the secondary flow estimated by our simulation. (3) A higher rotational speed can improve the performance of the turbine stage as the relative Mach number at the inlet of the rotor decreases, and therefore the shock-wave interaction becomes weaker in the rotor channel. Even though the stator nozzle design is independent of the unsteady and three-dimensional effects, the free expansion area between the stator and rotor is being modified by the rotor blade's profile, shaft speed, and height distribution. The designer can use these findings on the mixing region between stator and rotor during a (possible) stator re-design by changing the nozzle's back-pressure. If compared to the rotor blade design from Chapter 5, the new blade enhances the performance of the turbine stage — higher power output (+10 ΔkW) and total-to-static efficiency (+4Δ%) — by extracting more kinetic energy from the fluid.

7.2 Recommendations

This dissertation addressed several research questions related to turbulence modeling of supercritical fluids, and we have carefully analyzed high-expansion ORC radial inflow radial - outflow turbines; still, there are additional questions that should be addressed in future studies.

Part I: Turbulence modeling of supercritical fluids

- To increase confidence of our modified eddy viscosity models, a more extensive validation campaign needs be performed; we tested for two specific systems with variable properties. Our research group plans to test the modified models for zero-pressure-gradient fully developed flat-plate turbulent boundary layers with heated and unheated isothermal walls at supercritical pressures. We envision that other researchers will further test these improved EVMs for flows at different conditions and geometries.

- Several turbulence models currently used to predict supercritical fluid flows were developed for idealized conditions:

  1. The original buoyant production of the turbulent kinetic energy (TKE) term was derived from the assumption that density fluctuations affect the gravitational force only; this is invalid for a compressible flow. Without this assumption, we manage to derive the same buoyant production term. But by doing so we inadvertently add extra terms — that need closing — to the TKE equation. Further investigations need to be made related to the buoyant production of TKE for compressible flows.

  2. Eddy diffusivity models (EDMs) for the turbulent heat flux are a practical way to circumvent the pitfall of the turbulent Prandtl number for flows with heat transfer deterioration. Still, the available EDMs were developed for an incompressible flow, taking the temperature field as a passive scalar. Following a similar methodology as shown in Chapter 2, we can include the variation of density (and/or thermal conductivity) to EDMs.

- We limit our studies to heated flows with strong variations of thermo-physical properties (e.g. a supercritical fluid being heated); however, from an application point of view, heat rejection is also important in supercritical power cycles. The flow device of the s-CO$_2$ power cycle closest to the supercritical region is a heat exchanger that cools the s-CO$_2$. The questions is: can current turbulence models approximate heat rejection (cooling) correctly at supercritical pressures?

Part II: High-expansion ORC turbine simulations

- The ORC manufacturer is currently instrumenting both high-expansion turbine designs investigated in this dissertation, which will provide a unique opportunity to

validate our detailed three-dimensional unsteady simulations and to quantify the impact of the reduced blade count approximation — a limitation of our methodology.

- Follow-up research should investigate the impact of the tip clearance on the free-expansion region between the stator and the rotor, as well as on the secondary flow in the rotor channel for a high-expansion ORC turbine.

- As discussed in Chapters 5 and 6 during the off-design analysis with different rotational speeds, there is significant potential to recover the kinetic energy at the exit of the turbine. A diffuser at the exit of the rotor needs to be investigated; the goal of this component is to recover static pressure by gradually decelerating — and turning from radial-to-axial direction — a supersonic flow, in order to avoid flow detachment. Still, this is a challenging task in the turbine of the ORC manufacturer due to space restrictions.

- High-expansion ORC turbines are subject to blade loads of high amplitude and frequency induced by the inherent flow unsteadiness. How can the unsteady structural loads be accounted for in the design process?

7.3   Perspectives

The contribution of this dissertation is twofold. It involves (1) the development of a novel methodology to improve eddy viscosity models for predicting turbulent flows with substantial property variations, and (2) the study of the complex fluid dynamic behavior of a high-expansion ORC expander operating near the vapor-liquid critical point including the unsteady and three-dimensional effects. The documented investigation succeeded in improving the numerical modeling capabilities and fluid dynamics comprehension of non-ideal fluids, which will help to overcome the technical and economic challenges of non-conventional power cycles. The long-term goal is to apply the s-CO2 power cycle and ORC to improve the existing industrial process (e.g., in power plants) and to aid in the transition to renewable energy sources in order to decrease greenhouse gas emissions.

Appendix

A.1 Eddy viscosity models

A.1.1 Cess' eddy viscosity correlation

In 1958, Cess[1] developed a correlation for the effective viscosity $(\mu + \mu_t)$ in fully developed turbulent pipe flows. It combines a van Driest[2] type damping function for the laminar sublayer with the outer layer solution proposed by Reichardt[3]. The correlation was later extended for channel flows by Hussain and Reynolds[4], which reads for a channel whose walls are located at $y = 0$ and $y = 2$, as

$$\frac{\mu_t}{\langle\mu\rangle} = \frac{1}{2}\left[1 + \frac{\kappa^2 Re_\tau^2}{9}\left(2y_w - y_w^2\right)^2 \left(3 - 4y_w - y_w^2\right)^2 \left(1 + e^{-y^+/A^+}\right)^2\right]^{1/2} - \frac{1}{2},$$

with the normalized wall distance $y_w = \tilde{y}_w/\tilde{h}$, $A^+ = 25.4$, $\kappa = 0.41$ the von Karman constant, and $\tilde{h}$ is the characteristic length of the system.

A.1.2 Spalart-Allmaras turbulence model

The Spalart-Allmaras (SA) model is a one-equation turbulence model, derived on the basis of dimensional analysis, Galilean invariance and empiricism[5]. The standard form of the SA model reads

$$\frac{\partial\check{\nu}}{\partial t} + \{u_j\}\frac{\partial\check{\nu}}{\partial x_j} = c_{b1}\check{S}\check{\nu} - c_{w1}f_w\left(\frac{\check{\nu}}{y_w}\right)^2 + \frac{c_{b2}}{c_{b3}}\left(\frac{\partial\check{\nu}}{\partial x_j}\right)^2 + \frac{1}{c_{b3}}\frac{\partial}{\partial x_j}\left[\left(\frac{\langle\nu\rangle}{Re_\tau} + \check{\nu}\right)\frac{\partial\check{\nu}}{\partial x_j}\right].$$

The model functions are:

$$\check{S} = S + \frac{\check{\nu}}{\kappa^2 y_w^2}f_{v2}, \quad f_{v2} = 1 - \frac{\chi}{1 + \chi f_{v1}}, \quad f_{v1} = \frac{\chi^3}{\chi^3 + c_{v1}^3},$$

$$\chi = \frac{\check{\nu}}{\langle\nu\rangle}, \quad f_w = g\left[\frac{1 + c_{w3}^6}{g^6 + c_{w3}^6}\right]^{1/6}, \quad g = r + c_{w2}(r^6 - r),$$

$$r = \frac{\check{\nu}}{\check{S}\kappa^2 y_w^2}.$$

where the modulus of the strain rate tensor is $S = \sqrt{2S_{ij}S_{ij}}$, with $S_{ij} = \frac{1}{2}\left(\partial\{u_i\}/\partial x_j + \partial\{u_j\}/\partial x_i\right)$. The eddy viscosity is modelled as

$$\mu_t = \langle\rho\rangle\,\breve{v}f_{v1}.$$

The model coefficient are: $c_{b1} = 0.1355$, $c_{b2} = 0.622$, $c_{b3} = 2/3$, $c_{v1} = 7.1$, $c_{w1} = c_{b1}/\kappa^2 + (1 + c_{b2})/c_{b3}$, $c_{w2} = 0.3$, $c_{w3} = 2$ and the von Karman constant $\kappa = 0.41$. The wall boundary condition is $\breve{v}_w = 0$.

A.1.3   Myong and Kasagi model

Myong and Kasagi (MK) model[6] is a low-Reynolds k-ϵ model, given as

$$\frac{\partial\langle\rho\rangle k}{\partial t} + \frac{\partial\langle\rho\rangle k\{u_j\}}{\partial x_j} = P_k - \langle\rho\rangle\varepsilon + \frac{\partial}{\partial x_j}\left[\left(\frac{\langle\mu\rangle}{Re_\tau} + \frac{\mu_t}{\sigma_k}\right)\frac{\partial k}{\partial x_j}\right],$$

$$\frac{\partial\langle\rho\rangle\varepsilon}{\partial t} + \frac{\partial\langle\rho\rangle\varepsilon\{u_j\}}{\partial x_j} = C_{\varepsilon1}P_k\frac{\varepsilon}{k} - C_{\varepsilon2}f_\varepsilon\langle\rho\rangle\frac{\varepsilon^2}{k} + \frac{\partial}{\partial x_j}\left[\left(\frac{\langle\mu\rangle}{Re_\tau} + \frac{\mu_t}{\sigma_\varepsilon}\right)\frac{\partial\varepsilon}{\partial x_j}\right],$$

where, P_k is the production of TKE using the Boussinesq approximation. The functions and the eddy viscosity are given as:

$$f_\varepsilon = \left[1 - \frac{2}{9}e^{[-(\frac{Re_t}{6})^2]}\right]\left[1 - e^{(-\frac{y^+}{5})}\right]^2, \quad f_\mu = \left[1 - e^{(-\frac{y^+}{70})}\right]\left[1 + \frac{3.45}{\sqrt{Re_t}}\right], \quad \mu_t = C_\mu f_\mu\langle\rho\rangle\frac{k^2}{\varepsilon},$$

with $Re_t = \langle\rho\rangle k^2/\langle\mu\rangle\varepsilon$ and $y^+ = yRe_\tau$. The model constants are: $C_{\varepsilon1} = 1.4$, $C_{\varepsilon2} = 1.8$, $C_\mu = 1.4$, $\sigma_k = 1.4$, and $\sigma_\varepsilon = 1.3$. Finally, the wall boundary conditions for the scalars are

$$k_w = 0, \quad \varepsilon_w = \frac{\mu_w}{\rho_w}\frac{\partial^2 k}{\partial y^2}\bigg|_w \approx \frac{2\mu_w k_1}{\rho_w y_1^2}.$$

A.1.4   Menter Shear Stress Transport (SST) model

Menter's SST model[7] is given as

$$\frac{\partial\langle\rho\rangle k}{\partial t} + \frac{\partial\langle\rho\rangle k\{u_j\}}{\partial x_j} = P_k^{\text{lim}} - \beta^\star\langle\rho\rangle k\omega + \frac{\partial}{\partial x_j}\left[\left(\frac{\langle\mu\rangle}{Re_\tau} + \sigma_k\mu_t\right)\frac{\partial k}{\partial x_j}\right],$$

$$\frac{\partial\langle\rho\rangle\omega}{\partial t} + \frac{\partial\langle\rho\rangle\omega\{u_j\}}{\partial x_j} = \frac{\alpha\langle\rho\rangle}{\mu_t}P_k - \beta\langle\rho\rangle\omega^2 + (1 - F_1)CD_{k\omega} + \frac{\partial}{\partial x_j}\left[\left(\frac{\langle\mu\rangle}{Re_\tau} + \sigma_\omega\mu_t\right)\frac{\partial\omega}{\partial x_j}\right],$$

with $P_k^{\text{lim}} = min\,(P_k, 20\beta^\star\langle\rho\rangle\omega k)$, and

$$CD_{k\omega} = 2\frac{\langle\rho\rangle\sigma_{\omega2}}{\omega}\frac{\partial k}{\partial x_j}\frac{\partial\omega}{\partial x_j}.$$

The blending functions and the eddy viscosity are given by:

$$F_1 = tanh\left[\left(min\left[max\left(\gamma_1, \gamma_2\right), \gamma_3\right]\right)^4\right], \quad F_2 = tanh\left[\left(max\left(2\,\gamma_1, \gamma_2\right)\right)^2\right],$$

$$\gamma_1 = \frac{\sqrt{k}}{\beta^\star \omega y}, \quad \gamma_2 = \frac{500\,\langle\mu\rangle}{\langle\rho\rangle\, y_w^2\,\omega}, \quad \gamma_3 = \frac{4\,\langle\rho\rangle\,\sigma_{\phi 2}k}{y_w^2\,max\left(CD_{k\omega}, 10^{-20}\right)},$$

$$\mu_t = \frac{\langle\rho\rangle\,C_\mu k}{max\left(C_\mu\omega, \Omega F_2\right)},$$

with Ω as the vorticity magnitude. The model coefficient are $\beta^\star = 0.09$ and $C_\mu = 0.31$. The other model coefficient are calculated with the blending function F_1 using the relation $C = F_1 C_1 + (1 - F_1)C_2$, with $\beta_1 = 0.075, \beta_2 = 0.0828, \sigma_{k1} = 0.85, \sigma_{k2} = 0.5, \sigma_{\omega 1} = 1.0, \sigma_{\omega 2} = 0.856, \alpha_1 = \beta_1/\beta^\star - \sigma_{\omega 1}\kappa^2/\sqrt{\beta^\star}$, and $\alpha_2 = \beta_2/\beta^\star - \sigma_{\omega 2}\kappa^2/\sqrt{\beta^\star}$. Finally, the wall boundary condition are:

$$k_w = 0, \quad \omega_w = \frac{60\mu_w}{\rho_w \beta_1 y_w^2}.$$

A.1.5 Durbin's v'^2-f model

Durbin's v'^2-f model[(8)] is a k-ϵ model with an additional transport equation for the wall-normal velocity fluctuation v'^2, and an elliptic relaxation equation f that models the pressure strain correlation for v'^2. The model equations are given as:

$$\frac{\partial\langle\rho\rangle\,k}{\partial t} + \frac{\partial\langle\rho\rangle\,k\{u_j\}}{\partial x_j} = P_k - \langle\rho\rangle\,\varepsilon + \frac{\partial}{\partial x_j}\left[\left(\frac{\langle\mu\rangle}{Re_\tau} + \frac{\mu_t}{\sigma_k}\right)\frac{\partial k}{\partial x_j}\right],$$

$$\frac{\partial\langle\rho\rangle\,\varepsilon}{\partial t} + \frac{\partial\langle\rho\rangle\,\varepsilon\{u_j\}}{\partial x_j} = \frac{1}{T_t}\left[C_{\varepsilon 1}\left(1 + 0.045\sqrt{\frac{k}{v'^2}}\right)P_k - C_{\varepsilon 2}\langle\rho\rangle\,\varepsilon\right] + \frac{\partial}{\partial x_j}\left[\left(\frac{\langle\mu\rangle}{Re_\tau} + \frac{\mu_t}{\sigma_\varepsilon}\right)\frac{\partial\varepsilon}{\partial x_j}\right],$$

$$\frac{\partial\langle\rho\rangle\,v'^2}{\partial t} + \frac{\partial\langle\rho\rangle\,v'^2\{u_j\}}{\partial x_j} = \langle\rho\rangle\,kf - N\frac{\langle\rho\rangle\,v'^2}{k}\varepsilon + \frac{\partial}{\partial x_j}\left[\left(\frac{\langle\mu\rangle}{Re_\tau} + \mu_t\right)\frac{\partial v'^2}{\partial x_j}\right],$$

$$f - L_t^2\nabla^2 f = \left(C_{f1} - 1\right)\frac{2/3 - v'^2/k}{T_t} - C_{f2}\frac{P_k}{\langle\rho\rangle\,k} + (N - 1)\frac{v'^2}{kT_t}.$$

The turbulent time and length scale, and the eddy viscosity are modelled as,

$$T_t = max\left(\frac{k}{\varepsilon}, 6\sqrt{\frac{\langle\mu\rangle}{\langle\rho\rangle\,\varepsilon}}\right), \quad L_t = 0.23\,max\left(\frac{k^{3/2}}{\varepsilon}, 70\left(\frac{\langle\mu\rangle^3}{\langle\rho\rangle^3\,\varepsilon}\right)^{1/4}\right), \quad \mu_t = C_\mu\langle\rho\rangle\,v'^2 T_t.$$

The model closure coefficient are $C_{\varepsilon 1} = 1.4, C_{\varepsilon 2} = 1.9, C_\mu = 0.22, C_{f1} = 1.4, C_{f2} = 0.3$ and $N = 6$. Finally, the wall boundary conditions are:

$$k_w = 0, \quad \varepsilon_w = \frac{\mu_w}{\rho_w}\frac{\partial^2 k}{\partial y^2}\bigg|_w, \quad v_w'^2 = 0, \quad f_w = 0.$$

A.2 Density modifications to Eddy viscosity transport equations

The aim of these derivations is to convert the semi-local transport equation of the turbulent scalars back to conventional scales, in particular viscous wall units. The scaling transformation outlined in table 2.1 of Chapter 2 is used.

A.2.1 Turbulent dissipation rate ε

The semi-locally-scaled turbulent dissipation rate transport equation — as defined in Pecnik et al.[9] — is given as:

$$t_\tau^\star \frac{\partial \hat{\epsilon}}{\partial \tilde{t}} + \frac{\partial \hat{\epsilon}\{\hat{u}_j\}}{\partial \hat{x}_j} = \frac{C_{\epsilon 1}\hat{P}_k - C_{\epsilon 2}\hat{\epsilon}}{\hat{T}_t} + \frac{\partial}{\partial \hat{x}_j}\left[\left(\frac{1}{Re_\tau^*} + \frac{\mu_t}{\sigma_\epsilon}\right)\frac{\partial \hat{\epsilon}}{\partial \hat{x}_j}\right].$$

We start the transformation from semi-local to local wall scaling with the turbulent dissipation rate:

$$\hat{\epsilon} = \varepsilon\left(\frac{u_\tau/\tilde{h}}{u_\tau^\star/\tilde{h}}\right)^3 = \varepsilon\left(\frac{\langle\tilde{\rho}\rangle}{\tilde{\rho}_w}\right)^{1.5} = \sqrt{\langle\rho\rangle}\,\langle\rho\rangle\,\varepsilon.$$

Then, we obtain for the time derivative the following:

$$t_\tau^\star \frac{\partial \hat{\epsilon}}{\partial \tilde{t}} = t_\tau^\star \frac{\partial \langle\rho\rangle^{1.5}\,\epsilon}{\partial \tilde{t}} = t_\tau^\star\left[\sqrt{\langle\rho\rangle}\frac{\partial \langle\rho\rangle\,\epsilon}{\partial \tilde{t}} + \frac{\langle\rho\rangle\,\epsilon}{2\sqrt{\langle\rho\rangle}}\frac{\partial \langle\rho\rangle}{\partial \tilde{t}}\right]$$

$$= t_\tau^\star \sqrt{\langle\rho\rangle}\left[\frac{\partial \langle\rho\rangle\,\epsilon}{\partial \tilde{t}} + \frac{\epsilon}{2}\frac{\partial \langle\rho\rangle}{\partial \tilde{t}}\right].$$

The convecting term transforms into:

$$\frac{\partial \hat{\epsilon}\{\hat{u}_j\}}{\partial \hat{x}_j} = \frac{\tilde{h}}{\tilde{h}}\frac{\partial}{\partial x_j}\left[\langle\rho\rangle^{1.5}\,\varepsilon\sqrt{\langle\rho\rangle}\{u_j\}\right] = \frac{\partial \langle\rho\rangle\,\langle\rho\rangle\,\epsilon\{u_j\}}{\partial x_j} = \langle\rho\rangle\left(\frac{\partial \langle\rho\rangle\,\epsilon\{u_j\}}{\partial x_j} + \epsilon\{u_j\}\frac{\partial \langle\rho\rangle}{\partial x_j}\right).$$

The time and convective terms now consist of two parts. However, the second part of these terms is a mathematical artifact; this is a parallel from the derivation of the modified TKE equation. The turbulent production of turbulent kinetic energy and the turbulent time scale are transformed to local scale as:

$$\hat{P}_k = -\{\hat{u}_i''\hat{u}_j''\}\frac{\partial \{u^{vD}\}}{\partial \hat{x}_j} = -\langle\hat{\rho}\hat{u}_i''\hat{u}_j''\rangle\frac{\partial \{u^{vD}\}}{\partial x_j} = -\left\langle\rho\frac{\tilde{\rho}_w}{\langle\tilde{\rho}\rangle}u_i''\sqrt{\frac{\langle\tilde{\rho}\rangle}{\tilde{\rho}_w}}u_j''\sqrt{\frac{\langle\tilde{\rho}\rangle}{\tilde{\rho}_w}}\right\rangle\sqrt{\frac{\langle\tilde{\rho}\rangle}{\tilde{\rho}_w}}\frac{\partial \{u\}}{\partial x_j}$$

$$= \sqrt{\langle\rho\rangle}\left(-\langle\rho u_i''u_j''\rangle\frac{\partial \{u\}}{\partial x_j}\right) = \sqrt{\langle\rho\rangle}P_k.$$

and

$$\hat{T}_t = max \left[\frac{\{\hat{k}\}}{\hat{\varepsilon}}, \sqrt{\frac{1}{Re_\tau^\star \hat{\varepsilon}}} \right] = max \left[\frac{\langle\rho\rangle \{k\}}{\sqrt{\langle\rho\rangle} \langle\rho\rangle \varepsilon}, \sqrt{\frac{\langle\mu\rangle}{\sqrt{\langle\rho\rangle}Re_\tau\langle\rho\rangle^{1.5}\varepsilon}} \right]$$

$$= max \left[\frac{\{k\}}{\sqrt{\langle\rho\rangle}\varepsilon}, \frac{1}{\sqrt{\langle\rho\rangle}} \sqrt{\frac{\langle\mu\rangle}{Re_\tau\langle\rho\rangle\varepsilon}} \right] = \frac{T_t}{\sqrt{\langle\rho\rangle}}.$$

respectively. Then, the production and diffusion transforms into,

$$\frac{C_{\epsilon1}\hat{P}_k - C_{\epsilon2}\hat{\varepsilon}}{\hat{T}_t} = \frac{C_{\epsilon1}\sqrt{\langle\rho\rangle}P_k - C_{\epsilon2}\sqrt{\langle\rho\rangle}\langle\rho\rangle\epsilon}{T_t/\sqrt{\langle\rho\rangle}} = \langle\rho\rangle \frac{C_{\epsilon1}P_k - C_{\epsilon2}\langle\rho\rangle\epsilon}{T_t}.$$

The semi-locally-scaled dynamic viscosity and eddy viscosity can also be written as,

$$\frac{1}{Re_\tau^\star} + \frac{\hat{\mu}_t}{\sigma_\varepsilon} = \frac{1}{\sqrt{\langle\rho\rangle}} \frac{\langle\mu\rangle}{Re_\tau} + \frac{1}{\sqrt{\langle\rho\rangle}} \frac{\mu_t}{\sigma_\varepsilon},$$

such that the overall diffusion results in,

$$\frac{\partial}{\partial \hat{x}_j} \left[\left(\frac{1}{Re_\tau^\star} + \frac{\hat{\mu}_t}{\sigma_\varepsilon} \right) \frac{\partial \hat{\varepsilon}}{\partial \hat{x}_j} \right] = \frac{\partial}{\partial x_j} \left[\frac{1}{\sqrt{\langle\rho\rangle}} \left(\frac{\langle\mu\rangle}{Re_\tau} + \frac{\mu_t}{\sigma_\varepsilon} \right) \frac{\partial \langle\rho\rangle^{1.5}\varepsilon}{\partial x_j} \right].$$

Substituting the newly obtained terms into semi-locally-scaled ε, dividing them by $\langle\rho\rangle$ and converting $t_\tau^\star$ into $t_\tau = \tilde{h}/u_\tau$ with the remaining $1/\sqrt{\langle\rho\rangle}$, we end up with,

$$t_\tau \frac{\partial \langle\rho\rangle \epsilon}{\partial \tilde{t}} + \frac{\partial \langle\rho\rangle \epsilon\{u_j\}}{\partial x_j} = \frac{C_{\epsilon1}P_k - C_{\epsilon2}\langle\rho\rangle\epsilon}{T_t} + \frac{1}{\langle\rho\rangle} \frac{\partial}{\partial x_j} \left[\frac{1}{\sqrt{\langle\rho\rangle}} \left(\frac{\langle\mu\rangle}{Re_\tau} + \frac{\mu_t}{\sigma_\varepsilon} \right) \frac{\partial \langle\rho\rangle^{1.5}\varepsilon}{\partial x_j} \right].$$

A.2.2 Turbulent specific dissipation rate ω

The semi-locally-scaled turbulent specific dissipation rate transport equation — as defined in Pecnik et al.[9] — is given as:

$$t_\tau^\star \frac{\partial \hat{\omega}}{\partial \tilde{t}} + \frac{\partial \hat{\omega}\{\hat{u}_j\}}{\partial \hat{x}_j} = C_{\omega1}\hat{P}_k \frac{\hat{\omega}}{\{\hat{k}\}} - C_{\omega2}\hat{\omega}^2 + \frac{\partial}{\partial \hat{x}_j} \left[\left(\frac{1}{Re_\tau^*} + \frac{\mu_t}{\sigma_\omega} \right) \frac{\partial \hat{\omega}}{\partial \hat{x}_j} \right].$$

We start the transformation from semi-local to local scaling with the specific turbulent dissipation rate:

$$\hat{\omega} = \omega \left(\frac{u_\tau/\tilde{h}}{u_\tau^\star/\tilde{h}} \right) = \omega \sqrt{\frac{\langle\tilde{\rho}\rangle}{\tilde{\rho}_w}} = \sqrt{\langle\rho\rangle}\omega.$$

Then, we obtain for the time derivative the following:

$$t_\tau^\star \frac{\partial \hat{\omega}}{\partial \tilde{t}} = t_\tau^\star \frac{\partial \sqrt{\langle\rho\rangle}\omega}{\partial \tilde{t}} = t_\tau^\star \left[\frac{1}{\sqrt{\langle\rho\rangle}} \frac{\partial \langle\rho\rangle \omega}{\partial \tilde{t}} - \frac{\langle\rho\rangle \omega}{2\langle\rho\rangle^{1.5}} \frac{\partial\langle\rho\rangle}{\partial \tilde{t}} \right]$$

$$= \frac{t_\tau^\star}{\sqrt{\langle\rho\rangle}} \left[\frac{\partial \langle\rho\rangle \omega}{\partial \tilde{t}} - \frac{\omega}{2} \frac{\partial\langle\rho\rangle}{\partial \tilde{t}} \right].$$

The time term now consists of two parts. We can substitute the second term with continuity resulting a convective term two. However, this extra term is a mathematical artifact; this is a parallel from the derivation of the modified TKE equation. The convecting term transforms into:

$$\frac{\partial \hat{\omega}\{\hat{u}_j\}}{\partial \hat{x}_j} = \frac{\tilde{h}}{\tilde{h}} \frac{\partial}{\partial x_j} \left[\sqrt{\langle\rho\rangle}\omega \sqrt{\langle\rho\rangle}\{u_j\} \right] = \frac{\partial \langle\rho\rangle \omega\{u_j\}}{\partial x_j}.$$

The production and diffusion transforms into,

$$C_{\omega 1}\hat{P}_k \frac{\hat{\omega}}{\{\hat{k}\}} - C_{\omega 2}\hat{\omega}^2 = C_{\omega 1} \sqrt{\langle\rho\rangle}P_k \frac{\sqrt{\langle\rho\rangle}\omega}{\langle\rho\rangle\{k\}} - C_{\omega 2} \langle\rho\rangle \omega^2 = C_{\omega 1} P_k \frac{\omega}{\{k\}} - C_{\omega 2} \langle\rho\rangle \omega^2.$$

The overall diffusion results in,

$$\frac{\partial}{\partial \hat{x}_j} \left[\left(\frac{1}{Re_\tau^\star} + \frac{\hat{\mu}_t}{\sigma_\omega} \right) \frac{\partial \hat{\omega}}{\partial \hat{x}_j} \right] = \frac{\partial}{\partial x_j} \left[\frac{1}{\sqrt{\langle\rho\rangle}} \left(\frac{\langle\mu\rangle}{Re_\tau} + \frac{\mu_t}{\sigma_\omega} \right) \frac{\partial \sqrt{\langle\rho\rangle}\omega}{\partial x_j} \right].$$

Substituting the newly obtained terms into semi-locally-scaled ω and converting $t_\tau^\star$ into $t_\tau = \tilde{h}/u_\tau$ with the remaining $1/\sqrt{\langle\rho\rangle}$, we end up with,

$$t_\tau \frac{\partial \langle\rho\rangle \omega}{\partial \tilde{t}} + \frac{\partial \langle\rho\rangle \omega\{u_j\}}{\partial x_j} = C_{\omega 1}P_k \frac{\omega}{\{k\}} - C_{\omega 2} \langle\rho\rangle \omega^2 + \frac{\partial}{\partial x_j} \left[\frac{1}{\sqrt{\langle\rho\rangle}} \left(\frac{\langle\mu\rangle}{Re_\tau} + \frac{\mu_t}{\sigma_\omega} \right) \frac{\partial \sqrt{\langle\rho\rangle}\omega}{\partial x_j} \right].$$

A.2.3 Turbulent scalar from the Spalart-Allmaras model $\check{\nu}$

The semi-locally-scaled Spalart-Allmaras turbulent scalar transport equation is given as:

$$t_\tau^\star \frac{\partial \hat{\check{\nu}}}{\partial \tilde{t}} + \hat{u}_j \frac{\partial \hat{\check{\nu}}}{\partial \hat{x}_j} = c_{b1}\hat{\check{S}}\hat{\check{\nu}} - c_{w1}f_w \left(\frac{\hat{\check{\nu}}}{\hat{y}_w} \right)^2 + \frac{c_{b2}}{c_{b3}} \left(\frac{\partial \hat{\check{\nu}}}{\partial \hat{x}_j} \right)^2 + \frac{1}{c_{b3}} \frac{\partial}{\partial \hat{x}_j} \left[\left(\frac{\hat{\nu}}{Re_\tau^\star} + \hat{\check{\nu}} \right) \frac{\partial \hat{\check{\nu}}}{\partial \hat{x}_j} \right].$$

We start by defining the local and semi-local scaling for the turbulent scalar of Spalart-Allmaras model:

$$\tilde{\check{\nu}} = \hat{\check{\nu}}u_\tau^*\tilde{h} = \check{\nu}u_\tau\tilde{h} \implies \hat{\check{\nu}} = \sqrt{\langle\rho\rangle}\check{\nu}.$$

Then, we obtain for the time derivative the following:

$$t_\tau^\star \frac{\partial \hat{\check{\nu}}}{\partial \tilde{t}} = t_\tau^\star \frac{\partial \sqrt{\langle\rho\rangle}\check{\nu}}{\partial \tilde{t}} = t_\tau^\star \left[\sqrt{\langle\rho\rangle}\frac{\partial \check{\nu}}{\partial \tilde{t}} + \frac{\check{\nu}}{2\sqrt{\langle\rho\rangle}}\frac{\partial \langle\rho\rangle}{\partial \tilde{t}} \right] = \frac{t_\tau^\star}{\sqrt{\langle\rho\rangle}} \left[\langle\rho\rangle\frac{\partial \check{\nu}}{\partial \tilde{t}} + \frac{\check{\nu}}{2}\frac{\partial \langle\rho\rangle}{\partial \tilde{t}} \right].$$

The convecting term transforms into:

$$\{\hat{u}_j\}\frac{\partial \hat{\check{\nu}}}{\partial \hat{x}_j} = \sqrt{\langle\rho\rangle}\{u_j\}\frac{\tilde{h}}{\tilde{h}}\frac{\partial \sqrt{\langle\rho\rangle}\check{\nu}}{\partial x_j} = \sqrt{\langle\rho\rangle}\{u_j\} \left[\sqrt{\langle\rho\rangle}\frac{\partial \check{\nu}}{\partial x_j} + \frac{\check{\nu}}{2\sqrt{\langle\rho\rangle}}\frac{\partial \langle\rho\rangle}{\partial x_j} \right]$$

$$= \langle\rho\rangle\{u_j\}\frac{\partial \check{\nu}}{\partial x_j} + \frac{\{u_j\}\check{\nu}}{2}\frac{\partial \langle\rho\rangle}{\partial x_j}.$$

The time and convective terms now consist of two parts. However, the second part of these terms is a mathematical artifact; this is a parallel from the derivation of the modified TKE equation. The strain function of the Spalart-Allmaras model is transformed to local scale as:

$$\hat{S} = \sqrt{\langle\rho\rangle}S + \frac{\sqrt{\langle\rho\rangle}\check{v}}{\kappa^2 y_w}f_{v2} = \sqrt{\langle\rho\rangle}\check{S}.$$

This makes the production term into

$$c_{b1}\hat{\check{S}}\hat{\check{v}} = c_{b1}\sqrt{\langle\rho\rangle}\check{S}\sqrt{\langle\rho\rangle}\check{v} = c_{b1}\check{S}\langle\rho\rangle\check{v} \tag{1}$$

Note that the model function scale as:

$$\hat{S} = \sqrt{\langle\rho\rangle}S, \quad \hat{\chi} = \chi, \quad \hat{y}_w = y_w, \quad \hat{g} = g, \quad \hat{r} = r.$$

The destruction term transforms into:

$$c_{w1}f_w\left(\frac{\hat{\check{v}}}{\hat{y}_w}\right)^2 = c_{w1}f_w\left(\frac{\sqrt{\langle\rho\rangle}\check{v}}{y_w}\right)^2 = c_{w1}f_w\langle\rho\rangle\left(\frac{\check{v}}{y_w}\right)^2.$$

The first term of the dissipation transforms into:

$$\frac{c_{b2}}{c_{b3}}\left(\frac{\partial\hat{\check{v}}}{\partial\hat{x}_j}\right)^2 = \frac{c_{b2}}{c_{b3}}\left(\frac{\tilde{h}}{\tilde{h}}\frac{\partial\sqrt{\langle\rho\rangle}\check{v}}{\partial x_j}\right)^2 = \frac{c_{b2}}{c_{b3}}\left(\frac{\partial\sqrt{\langle\rho\rangle}\check{v}}{\partial x_j}\right)^2.$$

Finally the dissipation of $\check{v}$ converts into:

$$\begin{aligned}
\frac{1}{c_{b3}}\frac{\partial}{\partial\hat{x}_j}\left[\left(\frac{\hat{v}}{Re_\tau^\star}+\hat{\check{v}}\right)\frac{\partial\hat{\check{v}}}{\partial\hat{x}_j}\right] &= \frac{1}{c_{b3}}\frac{\partial}{\partial x_j}\left[\sqrt{\langle\rho\rangle}\left(\frac{v}{Re_\tau}+\check{v}\right)\frac{\partial\sqrt{\langle\rho\rangle}\check{v}}{\partial x_j}\right] \\
&= \frac{1}{c_{b3}}\frac{\partial}{\partial x_j}\left[\sqrt{\langle\rho\rangle}\left(\frac{v}{Re_\tau}+\check{v}\right)\left(\sqrt{\langle\rho\rangle}\frac{\partial\check{v}}{\partial x_j}+\frac{\check{v}}{2\sqrt{\langle\rho\rangle}}\frac{\partial\langle\rho\rangle}{\partial x_j}\right)\right] \\
&= \frac{1}{c_{b3}}\frac{\partial}{\partial x_j}\left[\langle\rho\rangle\left(\frac{v}{Re_\tau}+\check{v}\right)\frac{\partial\check{v}}{\partial x_j}+\left(\frac{v}{Re_\tau}+\check{v}\right)\frac{\check{v}}{2}\frac{\partial\langle\rho\rangle}{\partial x_j}\right].
\end{aligned}$$

Substituting the newly obtained terms into semi-locally-scaled ε, dividing them by $\langle\rho\rangle$ and converting $t_\tau^\star$ into $t_\tau = \tilde{h}/u_\tau$ with the remaining $1/\sqrt{\langle\rho\rangle}$, we end up with,

$$\begin{aligned}
t_\tau\frac{\partial\check{v}}{\partial\tilde{t}} + \{u_j\}\frac{\partial\check{v}}{\partial x_j} &= c_{b1}\check{S}\check{v} - c_{w1}f_w\left(\frac{\check{v}}{y_w}\right)^2 + \frac{c_{b2}}{\langle\rho\rangle c_{b3}}\left(\frac{\partial\sqrt{\langle\rho\rangle}\check{v}}{\partial x_j}\right)^2 \\
&\quad + \frac{1}{\langle\rho\rangle c_{b3}}\frac{\partial}{\partial x_j}\left[\langle\rho\rangle\left(\frac{v}{Re_\tau}+\check{v}\right)\frac{\partial\check{v}}{\partial x_j}+\left(\frac{v}{Re_\tau}+\check{v}\right)\frac{\check{v}}{2}\frac{\partial\langle\rho\rangle}{\partial x_j}\right].
\end{aligned}$$

A.2.4   Fluctuating wall normal velocity v''^2

The semi-locally-scaled fluctuating wall normal velocity transport equation — as defined in Pecnik et al. [9] — is given as:

$$t_\tau^\star \frac{\partial \hat{v'^2}}{\partial \tilde{t}} + \frac{\partial \hat{v'^2}\{\hat{u}_j\}}{\partial \hat{x}_j} = \{\hat{k}\}\hat{f} - N\frac{\hat{v'^2}}{\{\hat{k}\}}\hat{\varepsilon} + \frac{\partial}{\partial \hat{x}_j}\left[\left(\frac{1}{Re_\tau^*} + \mu_t\right)\frac{\partial \hat{v'^2}}{\partial \hat{x}_j}\right].$$

We start the transformation from semi-local to local scaling with the turbulent dissipation rate:

$$\hat{v'^2} = v'^2\left(\frac{u_\tau}{u_\tau^\star}\right)^2 = v'^2\frac{\langle\tilde{\rho}\rangle}{\tilde{\rho}_w} = \langle\rho\rangle v'^2.$$

Then, we obtain for the time derivative the following:

$$t_\tau^\star \frac{\partial \hat{v'^2}}{\partial \tilde{t}} = t_\tau^\star \frac{\partial \langle\rho\rangle v'^2}{\partial \tilde{t}}.$$

The convecting term transforms into:

$$\frac{\partial \hat{v'^2}\{\hat{u}_j\}}{\partial \hat{x}_j} = \frac{\tilde{h}}{\tilde{h}}\frac{\partial}{\partial x_j}\left[\langle\rho\rangle v'^2\sqrt{\langle\rho\rangle}\{u_j\}\right] = \frac{\partial}{\partial x_j}\left[\langle\rho\rangle^{1.5}v'^2\{u_j\}\right] = \frac{\partial\sqrt{\langle\rho\rangle}\langle\rho\rangle v'^2\{u_j\}}{\partial x_j}$$

$$= \sqrt{\langle\rho\rangle}\left(\frac{\partial\langle\rho\rangle v'^2\{u_j\}}{\partial x_j} + \frac{v'^2\{u_j\}}{2}\frac{\partial\langle\rho\rangle}{\partial x_j}\right).$$

The convective terms now consists of two parts. However, the second part of this term is a mathematical artifact; this is a parallel from the derivation of the modified TKE equation. The scaling of the ellipctic relaxation function is as follows:

$$\tilde{f} = \hat{f}u_\tau^*\tilde{h} = fu_\tau\tilde{h} \implies \hat{f} = \sqrt{\langle\rho\rangle}f.$$

Then, the production and diffusion transforms into,

$$\{\hat{k}\}\hat{f} - N\frac{\hat{v'^2}}{\{\hat{k}\}}\hat{\varepsilon} = \langle\rho\rangle\{k\}\sqrt{\langle\rho\rangle}f - N\frac{\langle\rho\rangle v'^2}{\langle\rho\rangle\{k\}}\langle\rho\rangle^{1.5}\varepsilon = \sqrt{\langle\rho\rangle}\left(\langle\rho\rangle\{k\}f - N\frac{\langle\rho\rangle v'^2}{\{k\}}\varepsilon\right).$$

The overall diffusion results in,

$$\frac{\partial}{\partial \hat{x}_j}\left[\left(\frac{1}{Re_\tau^\star} + \hat{\mu}_t\right)\frac{\partial \hat{v'^2}}{\partial \hat{x}_j}\right] = \frac{\partial}{\partial x_j}\left[\frac{1}{\sqrt{\langle\rho\rangle}}\left(\frac{\langle\mu\rangle}{Re_\tau} + \mu_t\right)\frac{\partial\langle\rho\rangle v'^2}{\partial x_j}\right].$$

Substituting the newly obtained terms into (2.3), and dividing them by $\sqrt{\langle\rho\rangle}$ to convert $t_\tau^\star$ into $t_\tau = \tilde{h}/u_\tau$, we end up with,

$$t_\tau\frac{\partial\langle\rho\rangle v'^2}{\partial \tilde{t}} + \frac{\partial\langle\rho\rangle v'^2\{u_j\}}{\partial x_j} = \langle\rho\rangle\{k\}f - N\frac{\langle\rho\rangle v'^2}{\{k\}}\varepsilon + \frac{1}{\sqrt{\langle\rho\rangle}}\frac{\partial}{\partial x_j}\left[\frac{1}{\sqrt{\langle\rho\rangle}}\left(\frac{\langle\mu\rangle}{Re_\tau} + \mu_t\right)\frac{\partial\langle\rho\rangle v'^2}{\partial x_j}\right].$$

A.2.5 Elliptic relaxation function f

The semi-locally-scaled elliptic relaxation function — as defined in Pecnik et al. [9] — is given as:

$$\hat{f} - \hat{L}_t^2 \nabla^2 \hat{f} = \left(C_{f1} - 1\right) \frac{2/3 - \hat{v'^2}/\{\hat{k}\}}{\hat{T}_t} - C_{f2} \frac{\hat{P}_k}{\{\hat{k}\}} + (N - 1) \frac{\hat{v'^2}}{\{\hat{k}\}\hat{T}_t}.$$

We start the transformation from semi-local to local scaling with the turbulent length scale:

$$\hat{L}_t = 0.23 \, max \left[\frac{\{\hat{k}\}^{3/2}}{\hat{\varepsilon}}, 70 \left(\frac{(1/Re_\tau^*)^3}{\hat{\varepsilon}} \right)^{1/4} \right]$$

$$= 0.23 \, max \left[\frac{\langle\rho\rangle^{3/2} \{k\}^{3/2}}{\langle\rho\rangle^{3/2} \, \varepsilon}, 70 \left(\frac{\langle\mu\rangle^3 / \left(\langle\rho\rangle^{3/2} Re_\tau^3\right)}{\langle\rho\rangle^{3/2} \, \varepsilon} \right)^{1/4} \right]$$

$$= 0.23 \, max \left[\frac{\{k\}^{3/2}}{\varepsilon}, 70 \left(\frac{\langle\mu\rangle^3 / Re_\tau^3}{\langle\rho\rangle^3 \, \varepsilon} \right)^{1/4} \right] = L_t.$$

Then, the left hand side of the semi-local elliptic relaxation equation transforms into

$$\hat{f} - \hat{L}_t^2 \nabla^2 \hat{f} = \sqrt{\langle\rho\rangle} f - L_t^2 \sqrt{\langle\rho\rangle} \Delta f = \sqrt{\langle\rho\rangle} \left(f - L_t^2 \Delta f \right).$$

The first term of the right hand side converts into:

$$\left(C_{f1} - 1\right) \frac{2/3 - \hat{v'^2}/\{\hat{k}\}}{\hat{T}_t} = \left(C_{f1} - 1\right) \frac{2/3 - \langle\rho\rangle \, v'^2 / \left(\langle\rho\rangle \{k\}\right)}{T_t / \sqrt{\langle\rho\rangle}}$$

$$= \sqrt{\langle\rho\rangle} \left(C_{f1} - 1\right) \frac{2/3 - v'^2/\{k\}}{T_t}.$$

The second term of the right hand side converts into:

$$C_{f2} \frac{\hat{P}_k}{\{\hat{k}\}} = C_{f2} \frac{\sqrt{\langle\rho\rangle} P_k}{\langle\rho\rangle \{k\}}$$

$$= \sqrt{\langle\rho\rangle} C_{f2} \frac{P_k}{\langle\rho\rangle \{k\}}.$$

And the final term of the right hand side converts into:

$$(N - 1) \frac{\hat{v'^2}}{\{\hat{k}\}\hat{T}_t} = (N - 1) \frac{\langle\rho\rangle \, v'^2}{\langle\rho\rangle \{k\}\hat{T}_t / \sqrt{\langle\rho\rangle}}$$

$$= \sqrt{\langle\rho\rangle} (N - 1) \frac{v'^2}{\{k\}T_t}.$$

Substituting the newly obtained terms into (2.3), and dividing them by $\sqrt{\langle\rho\rangle}$, we end up with,

$$f - L_t^2 \nabla^2 f = \left(C_{f1} - 1\right) \frac{2/3 - v'^2/\{k\}}{T_t} - C_{f2} \frac{P_k}{\langle\rho\rangle\{k\}} + (N-1) \frac{v'^2}{\{k\}T_t}.$$

A.2.6 Extra modifications for the SST model

In section A.2.2, we have transform the generic semi-locally-scaled specific turbulent dissipation rate; however the SST model's transport equation of $\hat{\omega}$ has some differences, see A.1.4. For example the production term in the ω equation scales as:

$$\frac{\alpha}{\hat{\mu}_t}\hat{P}_k = \frac{\alpha\sqrt{\langle\rho\rangle}}{\mu_t}\sqrt{\langle\rho\rangle}P_k = \frac{\alpha\langle\rho\rangle}{\mu_t}P_k,$$

which does not add any difference with respect to the derived modified transport equation of ω in local scales. However, the cross derivative develops extra terms:

$$
\begin{aligned}
\hat{CD}_{k\omega} &= 2\frac{\sigma_{\omega2}}{\hat{\omega}}\frac{\partial\{\hat{k}\}}{\partial\hat{x}_j}\frac{\partial\hat{\omega}}{\partial\hat{x}_j} = 2\frac{\sigma_{\omega2}}{\sqrt{\langle\rho\rangle}\omega}\frac{\partial\langle\rho\rangle\{k\}}{\partial x_j}\frac{\partial\sqrt{\langle\rho\rangle}\omega}{\partial x_j} \\
&= 2\frac{\sigma_{\omega2}}{\sqrt{\langle\rho\rangle}\omega}\left[\left(\langle\rho\rangle\frac{\partial\{k\}}{\partial x_j} + \{k\}\frac{\partial\langle\rho\rangle}{\partial x_j}\right)\left(\sqrt{\langle\rho\rangle}\frac{\partial\omega}{\partial x_j} + \frac{\omega}{2\sqrt{\langle\rho\rangle}}\frac{\partial\langle\rho\rangle}{\partial x_j}\right)\right] \\
&= 2\frac{\sigma_{\omega2}\langle\rho\rangle}{\omega}\left[\frac{\partial\{k\}}{\partial x_j}\frac{\partial\omega}{\partial x_j} + \frac{\omega}{2\langle\rho\rangle}\frac{\partial\{k\}}{\partial x_j}\frac{\partial\langle\rho\rangle}{\partial x_j} + \frac{\{k\}}{\langle\rho\rangle}\frac{\partial\langle\rho\rangle}{\partial x_j}\frac{\partial\omega}{\partial x_j} + \frac{\{k\}\omega}{2\langle\rho\rangle^2}\left(\frac{\partial\langle\rho\rangle}{\partial x_j}\right)^2\right].
\end{aligned}
$$

References

[1] Cess, R., 1958. "A survey of the literature on heat transfer in turbulent tube flow". *Res. Rep*, pp. 8–0529.

[2] Van Driest, E. R., 1956. "On turbulent flow near a wall". *J. Aeronaut. Sci,* **23**(11), pp. 1007–1011.

[3] Reichardt, H., 1951. "Vollständige darstellung der turbulenten geschwindigkeitsverteilung in glatten leitungen". *ZAMM-Journal of Applied Mathematics and Mechanics/Zeitschrift für Angewandte Mathematik und Mechanik,* **31**(7), pp. 208–219.

[4] Hussain, A. K. M. F., and Reynolds, W. C. "Measurements in Fully Developed Turbulent Channel Flow". *Journal of Fluids Eng.*(7).

[5] Spalart, P. R., Allmaras, S. R., et al., 1994. "A one equation turbulence model for aerodynamic flows". *RECHERCHE AEROSPATIALE-FRENCH EDITION-*, pp. 5–5.

[6] Myong, H.K. and Kasagi, N., 1990. "A New Approach to the Improvement of k-e turbulence model for wall-bounded shear flows". *JSME,* **33**(2).

[7] Menter, F. R., 1993. "Zonal Two Equation k-w, Turbulence Models for Aerodynamic Flows". *AIAA paper*, p. 2906.

[8] Durbin, P. A., 1995. "Separated Flow Computations with the k-e-v2 Model". *AIAA Journal,* **33**(4), pp. 659–664.

[9] Pecnik, R., and Patel, A., 2017. "Scaling and modelling of turbulence in variable property channel flows". *Journal of Fluid Mechanics,* **823**.

List of publications

Journal papers

Otero, G.J., Gonzalez Portillo, L.F., Smit, S.H.H.J., and Pecnik, R., "Numerical modelling of heat transfer for supercritical CO2 in a vertical tube". In preparation.

Otero, G.J., Smit, S.H.H.J., and Pecnik, R., 2020. "Three-dimensional unsteady stator-rotor interactions in a high-expansion ORC turbine". *Energy*, **217**.

Otero, G.J., Patel, A., Diez, R., and Pecnik, R., 2018. "Turbulence modelling for flows with strong variations in thermo-physical properties". *International Journal of Heat and Fluid flow*, **73**, pp. 114-123.

Anand, N., Vitale, S., Pini, M., **Otero, G.J.**, and Pecnik, R., 2018. "Design Methodology for Supersonic Radial Vanes Operating in Nonideal Flow Conditions". *Journal of Engineering for Gas Turbines and Power*, **141**(2), pp. 022601.

Otero, G.J., Polanco, G. and Asuaje, M., 2016. "Analysis of a pneumatic system for a two-phase flow sugar". *The International Journal of Multiphysics*, **7**(4). (Not included in this thesis)

Conference proceedings

Otero, G.J., Smit, S.H.H.J., and Pecnik, R., 2019. "Three-dimensional unsteady stator-rotor interactions in a high-expansion ORC turbine". *Proceedings of the 5th International Seminar on ORC Power Systems*, Athens, Greece.

Smit, S.H.H.J.,Eppinga, Q., **Otero, G.J.**, and Pecnik, R., 2019. "Optimization of a high-expansion ORC turbine using genetic algorithm". *Proceedings of the 5th International Seminar on ORC Power Systems*, Athens, Greece.

Otero, G.J., Gonzalez Portillo, L.F., and Pecnik, R., 2019. "Turbulence modelling for supercritical CO2 flows in vertical tube". *Proceedings of the 3rd European supercritical CO2 conference –2019-sCO2*, Paris - France.

Gonzalez Portillo, L.F., Marys, S., **Otero, G.J.**, Fernandez-Cosials, K., and Pecnik, R., 2019. "Analysis of RANS turbulence models for supercritical carbon dioxide simulation with heat transfer". *Proceedings of the XI Congreso Nacional y II Internacional de Ingenieria Termodinamica–11CNIT*, Madrid - Spain.

Otero, G.J., Patel, A., and Pecnik, R., 2018. "Turbulence modelling for flows with strong variations in thermo-physical properties". *Proceedings of the 12th International ERCOF-TAC Symposium on Engineering Turbulence Modelling and Measurements –ETMM12*, Montpellier - France.

Otero, G.J., Patel, A., and Pecnik, R., 2018. "A novel approach to accurately model heat transfer to supercritical fluids". *Proceedings of the 2nd European supercritical CO2 conference –2018-sCO2*, Essen - Germany.

Otero, G.J., Patel, A., and Pecnik, R., 2018. "A novel approach to accurately model heat transfer to supercritical fluids". *Proceedings of the 6th International Symposium on supercritical CO2 power cycles*, Pittsburgh - United State of America.

Acknowledgements

This dissertation encompasses 4 years (and more) of my life. The challenges of a Ph.D. are technical (as expected) but also related to time management, staying focus, keep motivated, and maintain self-confidence. Across these pages, I presented the results of equations, models, and simulations but also the result of hard work, commitment, and failures (lots of them). I have only managed to overcome these challenges because of the people I have surrounded myself professionally, academically, and personally. I want to express my sincere gratitude to everyone that has helped me along the way to achieve what is documented in these pages.

First and foremost, I would like to thank the people that trusted me — even when there was no funding — to carry out this project: Prof. dr. ir. B.J. Boersma, Prof. ir. Jos van Buijtenen, Dr. R. Pecnik, Prof. dr. ir. S. Klein, and Dr. Matteo Pini. Looking back, I hope that your trust in me was not misplaced.

I am genuinely grateful for my supervising team: Dr. R. Pecnik and Prof. dr. ir. S. Klein. I not only see you as my mentors but also as friends, which I hope we stay for long in the future. I hope you do not miss me so much during the teaching periods. I can not stress how thankful I am for having Rene as my daily supervisor; your inputs and feedback not only have had a massive impact on my research (e.g., this dissertation) but also on myself as a person.

I would also like to thank my dissertation committee: Prof. dr. ir. H.C. de Lange, Prof. T. Turunen-Saaresti, Prof. dr. S. Hickel, Prof. P. Cinnella, Prof. dr. D.J.E.M. Roekaerts, and Prof. dr. ir. B.J. Boersma, for taking the time to evaluate this work and for their remarks that helped improve this thesis. Similarly, I am grateful to all my anonymous reviewers from journals and conferences during the past years.

My experience during this project wouldn't have been the same without my peers and co-authors: Enrico, Hassan, Jurriaan, Ashish, Uttiya, Jie, Mohammad, Simone, Stephan, Luis (Spanish import), and Nitish. I was fortunate to work among the brightest individuals I have ever met. Moreover, I would also like to thank all the Power and propulsion group at Aerospace (Dr. Matteo Pini and Prof. dr. Piero Colonna) for our collaboration and continuous discussions on non-conventional turbomachinery with non-ideal fluids.

None of this would have been possible without the funding from NWO Applied and Engineering Sciences and the project approval from the user's committee. Our TTW meetings gave me a different perspective towards my research, thank you: Dr. Leo Korstanje, Rogier Lammers, Dr. Bambang Soemarwoto, Dr. Damian Vogt, Dr. Lars Axelsson, Willy Ahout, and Mark Rankenberg. Also, I am very grateful to Tri-O-Gen B.V., especially to Prof. ir. Jos van Buijtenen and Ir. Quirijn Eppinga, who were a vital driving

force of my career; I will remember fondly the last six years I spend working with you.

I would also like to thank other staff members of the university that have helped me, in anyway, to make this possible: P&E staff members (i.e., Eveline, Leslie, Helma, Carlos, and Rob), Can Ayas (my Ph.D. mentor), and the graduate school related staff (i.e., Marscha, Nadia, Kees Lemmons, Sandra, and Enne).

I am grateful for the master students I supervised during their thesis: Nitish, Lucrezia, Pulkit, Stella, Girish, Marco, and Patrick. It was a pleasure working with you and thank you for the valuable inputs you gave towards this thesis.

I would also like to thank Stephan Smit and Simon Spoelstra for translating the summary of this dissertation.

Probably, people thought I was crazy for coming from Amsterdam to Delft (almost) every day. Yes, for four years, I woke up at 6:45, ate breakfast, left home (with my super carpooling buddy Saman), arrived at the TU at around 8:30-9:00, and then back home at around 18:00. I only achieved this because of how much I enjoyed my colleagues (Simone, Stephan, Carla, Samira, Johan, Fatma, Hassan, Hakan, Elyas, Jelle, Andrea, Marloes, Ali, Sergio, Luis, Meng Meng, Meng, Tim, Juan Pablo, Guillermo, Jack, Nayara, ...). Besides, I was part of what came to be known as the most awesome office of the whole faculty (Rishabh, Nikolakis, Vilborg, Queen Noura, Uttiya, Mohammad, Seyed, Reza the traitor, Selva, Meng Meng, Mat, Vincent, Karsten BAUMGARTEN, Martijn). Some may say it was impossible to focus in our office (both Vilborg and I were there, so they have a point), but I am proof that you can "successfully" finish a Ph.D. (or at least write a dissertation) at 34-K-1-290 coming everyday from Amsterdam. Thank you all for helping me maintaining sanity during the Ph.D. I will always remember our intellectual discussions during lunch and coffee breaks (about international politics, economics, social inequality, among others), our yoga and ping pong sessions (to relax our body and mind), and our extremely fun social gatherings (including trips and weddings). I also will never forget our significant sports achievements, i.e., defeating the P&E master students, after 30 years, with the help from Stephan, Ivan, Mate, Lindert, Xu, Xuang, Rezeb, Eric, Marian, and Tabish. This brings me to another group of people with whom I enjoyed playing football: my Tutor FC team-mates (Chris, Elyas, Abdula, Neils, Marijn, Martijn, Lars, Kees, Samir, Kenny, Ken, Nino, Brian, Wouter, Tom, and Kunal). To my TU Delft colleagues, office-mates, team-mates but more precisely to my dear friends: thank you for all the laughs, drinks, and experiences in general; I will carry these memories (and bruises from my bachelor party) for the rest of my life.

Since I moved to the Netherlands I have had the opportunity to meet a people that since have become of paramount importance in my life. Starting with my adoptive Dutch family (Han, Lisbeth, Hans, and Maria), my friends from the M.Sc. (Koen and Anshuman), and my futsal friends (Maarten, Ramon, Mark, Matt, Hector, Enrique, Dan, ...); I am grateful of having you on my side these last 8 years, you have made my adaptation to the Netherlands extremely easy: "dankjewel Sinterklaas".

Finalmente, me gustaria dar las gracias a todos los que hayan aportado algo en mi vida desde mi inicios en Venezuela. Gran parte de la culpa que he llegado aqui es por ustedes, empezando por mis profesores (Luis Tabares, Pedro, Migual Asuaje, Luis Rojas) y mis amigos (Pipe, Trucu, Carlos, Colladito, Daniela. Universidad: Rafa, Monika, Gaba,

Tharek, Carlos, Luis), pero especialemente a mi familia y a mi esposa Daniela. El que haya llegado a terminar el doctorado es consecuencia de su apoyo incondicional. Ustedes me han inculcado a siempre conquistar mis objetivos. Gracias totales!

Gustavo J. Otero Rodriguez
Amsterdam, January, 2021

About the author

Gustavo Jose Otero Rodriguez was born in Caracas, Venezuela, on December 22nd, 1987. He decided to enroll for a five-year Bachelor program at Universidad Simon Bolivar in his home city of Caracas, Venezuela. He completed his undergraduate program in Mechanical Engineering and successfully graduated in 2012 with a cumulative GPA of 4/5. During his Bachelor period, Gustavo participated in a 6-month exchange program with the Abo Akademi University in Turku, Finland. This experience changed Gustavo's perspective about the world and stimulated him to continue his studies abroad: more specifically in the Netherlands. Gustavo was admitted for a master program on Mechanical Engineering — the Sustainable Process and Energy Technology (SPET) track — at the faculty of Mechanical, Maritime and Materials Engineering (3mE) at the Technical University of Delft. He carried out a Master project in the topic of unsteady Stator/Rotor interaction of a high-expansion ratio organic Rankine cycle (ORC) turbine. Gustavo achieved his goal when, in 2014, he received his MSc degree. After this period, Gustavo went to the industry where he worked for a year at an ORC manufacturer (Tri-O-Gen B.V.). After this experience, Gustavo wanted to return to the university and decided to pursue a Ph.D. under his MSc thesis supervisor, Dr. R. Pecnik.